



HAL
open science

Highly coherent III-V-semiconductor laser emitting phase-, amplitude- and polarization-structured light for advanced sensing applications: Vortex, SPIN, Feedback Dynamics

Mohamed Seghir Seghilani

► **To cite this version:**

Mohamed Seghir Seghilani. Highly coherent III-V-semiconductor laser emitting phase-, amplitude- and polarization-structured light for advanced sensing applications: Vortex, SPIN, Feedback Dynamics. Other. Université Montpellier, 2015. English. NNT: 2015MONTTS207 . tel-02049651

HAL Id: tel-02049651

<https://theses.hal.science/tel-02049651>

Submitted on 26 Feb 2019

HAL is a multi-disciplinary open access archive for the deposit and dissemination of scientific research documents, whether they are published or not. The documents may come from teaching and research institutions in France or abroad, or from public or private research centers.

L'archive ouverte pluridisciplinaire **HAL**, est destinée au dépôt et à la diffusion de documents scientifiques de niveau recherche, publiés ou non, émanant des établissements d'enseignement et de recherche français ou étrangers, des laboratoires publics ou privés.

THÈSE

Pour obtenir le grade de
Docteur

Délivré par l'UNIVERSITE DE MONTPELLIER

Préparée au sein de l'école doctorale Information,
Structures et Systèmes
Et de l'unité de recherche Institut d'Électronique et des
Systèmes

Spécialité : Électronique

Présentée par Mohamed Seghir SEGHILANI

Highly coherent III-V-semiconductor laser
emitting phase-, amplitude- and
polarization-structured light
for advanced sensing applications: Vortex,
SPIN, Feedback Dynamics

Soutenue 07 October 2015 devant le jury composé de :

Anne C TROPPER	Professeur Univ of Southampton, UK	Rapporteur
Eric LACOT	Professeur Univ Grenoble Alpes	Rapporteur
Isabelle SAGNES	DR CNRS LPN (Marcoussis)	Examineur
Philippe LALANNE	DR CNRS LP2N (Bordeaux)	Examineur
Salvador BALLE	Professeur IMEDEA , Spain	Examineur
Denis SCALBERT	DR CNRS L2C (Montpellier)	Examineur
Arnaud GARNACHE	CR-CNRS IES (Montpellier)	Directeur de thèse
Ryad BENDOULA	CR Irstea (Montpellier)	Co-directeur
Mikhaël MYARA	MC IES (Montpellier)	Co-encadrant



THÈSE

pour obtenir le titre de

DOCTEUR DE L'UNIVERSITÉ DE MONTPELLIER

École doctorale : Information Structures Systèmes

Discipline : Électronique, Composants et Systèmes

Présentée et soutenue publiquement le 07 October 2015 par

Mohamed Seghir SEGhilani

Highly coherent III-V-semiconductor laser emitting phase-, amplitude- and polarization-structured light for advanced sensing applications: Vortex, SPIN, Feedback Dynamics

jury

Anne C TROPPER	Professeur Univ of Southampton, UK	<i>Rapporteur</i>
Eric LACOT	Professeur Univ Grenoble Alpes	<i>Rapporteur</i>
Isabelle SAGNES	DR CNRS LPN (Marcoussis)	<i>Examineur</i>
Philippe LALANNE	DR CNRS LP2N (Bordeaux)	<i>Examineur</i>
Salvador BALLE	Professeur IMEDEA , Spain	<i>Examineur</i>
Denis SCALBERT	DR CNRS L2C (Montpellier)	<i>Examineur</i>
Arnaud GARNACHE	CR-CNRS IES (Montpellier)	<i>Directeur de thèse</i>
Ryad BENDOULA	CR Irstea (Montpellier)	<i>Co-directeur</i>
Mikhaël MYARA	MC IES (Montpellier)	<i>Co-encadrant</i>

Acknowledgments

First and foremost, I would like to express my sincere gratitude to my advisor Dr. Arnaud Garnache and my co-advisors Dr Mikhaël Myara and Dr Ryad Bendoula for the continuous support of my Ph.D. study and research, for their motivation, enthusiasm, and patience. Their guidance helped me in all the time of research and writing of this thesis

I would like to thank my thesis examiners Professor Anne Tropper from School of Physics and Astronomy, University of Southampton, UK, And Professor Eric Lacot from Laboratoire Interdisciplinaire de Physique Université Joseph Fourier, Grenoble, France for their interest in my work.

I thank Professor Denis Scalbert from Laboratoire Charles Coulomb, University of Montpellier, France who has kindly accepted to chair my committee.

I gratefully acknowledge Professor Isabelle Sagnes from Laboratoire de Photonique et de Nanostructures Marcoussis, France for the great semiconductor structures that she had grown.

I acknowledge sincerely, Professor Philippe Lalanne from Laboratoire Photonique, Numérique et Nanosciences, Bordeaux, France for his supply of the RCWA simulation code, and for his guidance on metamaterials, his interest in this work and his critical spirit.

I acknowledge Professor Salvador Balle from University of the Balearic Islands, Spain for the constructive and stimulating discussions and his precious help on polarization dynamics modeling.

Thanks to all the members of the group Nanomir who make my three years in the laboratory colorful.

Last but not least, I would like to thank my friends and my family for their love and support.

“Les grandes vocations se prolongent au-delà du lieu de travail. Même au lit, même fiévreux, je fonctionne. ce métier-là, d’ailleurs, on ne l’exerce pas, on le respire à toute heure.”

— Albert Camus, La chute

Contents

Introduction	1
Chapter 1 Principles of mode selection in a laser cavity	5
1.1 Introduction	5
1.2 Longitudinal modes	6
1.3 Transverse modes of a passive cavity	7
1.3.1 What is a transverse mode	7
1.3.2 Modes of an optical cavity with curved mirrors	8
1.3.3 Gaussian modes propagation	11
1.3.4 Optical resonator stability	12
1.3.5 Calculation of generalized cavity modes	14
1.3.5.1 The Fox-Li iterative method	15
1.3.5.2 The matrix method, with Huygens Kernel formulation	16
1.3.5.3 Resonator with an arbitrary phase/amplitude mask	17
1.3.5.4 Comparison: when to use each method	19
1.3.5.5 Some practical mode calculation examples	19
1.4 Polarization modes of a passive cavity	20
1.4.1 Polarization of plane waves	20
1.4.2 Polarization representation tools	21
1.4.2.1 Jones matrices formalism	21
1.4.2.2 Stokes parameters	22
1.4.3 Polarization eigenstates of an optical resonator	23
1.4.4 Eigenstate calculation of some resonators of interest	23
1.4.4.1 A resonator with linear dichroism	24
1.4.4.2 A resonator with circular birefringence	25
1.4.4.3 A resonator with linear birefringence	25
1.5 Laser dynamics and mode selection	26
1.5.1 Class of lasers	26
1.5.2 The laser rate equations	27
1.6 Mode competition	29
1.6.1 Qualitative treatment: Darwin survival of the fittest	29
1.6.2 Quantitative treatment: the Lamb model	30
1.6.3 Longitudinal mode selection	30
1.6.4 Polarization mode selection	31
1.6.5 Transverse mode selection	32
1.7 Noise, coherence and mode purity	33
1.7.1 Relative noise intensity expression	35
1.7.2 Frequency noise expression	36
1.7.3 Importance of noise characterization in laser applications . .	37
1.7.4 Noise measurement for eigenstates's purity characterization .	37

1.8	Conclusion	39
Chapter 2 A laser source for structured light generation: VECSELs		41
2.1	Semiconductor lasers	41
2.1.1	Edge emitting semiconductor lasers	42
2.1.2	Surface emitting lasers	43
2.2	Solid state lasers	44
2.3	VECSELs, lasers of choice	46
2.3.1	Power, Coherence and Functional versatility	46
2.3.2	A prime candidate for structured light generation	47
2.4	How to make a VECSEL: the building blocks	48
2.4.1	The gain medium	49
2.4.1.1	The quantum wells	50
2.4.1.2	The optical gain	51
2.4.1.3	Spectrum of the optical gain	52
2.4.1.4	Amplitude of the optical gain	54
2.4.1.5	Gain dichroism	55
2.4.2	Pumping the gain medium	55
2.4.2.1	Carrier generation	55
2.4.2.2	Carrier lifetime	56
2.4.3	Design of multi-quantum well gain mirror	57
2.4.3.1	The Bragg mirror	57
2.4.3.2	Positioning the quantum wells	59
2.4.3.3	Optimization of quantum wells number	59
2.4.4	Design of the micro cavity	61
2.4.4.1	Resonant configuration	61
2.4.4.2	Anti-resonant configuration	61
2.4.4.3	Anti-reflective coated microcavity	63
2.5	Conclusion	64
Chapter 3 VECSEL integrating metasurfaces for intracavity mode-control		67
3.1	Introduction	67
3.2	What are photonic metamaterials	69
3.3	Some basic principles and properties	70
3.3.1	Material vs structural dispersions	70
3.3.2	Metamaterial or photonic crystal?	71
3.4	Metamaterials integration in VECSEL: principle and implementation	72
3.4.1	Advantages	72
3.4.2	Design principle	73
3.4.3	Materials choice	75
3.4.4	Design and fabrication procedure	75
3.4.4.1	Design	75
3.4.4.2	Fabrication	76

3.4.5	Some examples of fabricated masks	77
3.4.6	Laser test procedure	79
3.4.7	Limitations of the technology	79
3.5	Related work: intracavity mode control technologies	81
3.5.1	Intracavity conventional thick optics	81
3.5.2	Subwavelength structures in laser cavities	82
3.6	Demonstration and characterization of a VeCSEL integrating meta- material based flat-optics	83

Chapter 4 Generation of phase and amplitude-structured coherent photon states 99

4.1	What is phase and amplitude-structured light	99
4.2	phase-structured light generation methods	102
4.2.1	Extra-cavity generation of phase-structured light	102
4.2.2	Intra-cavity generation of phase-structured light	104
4.3	Modes carrying OAM: properties and applications	104
4.3.1	Properties	104
4.3.2	How to detect the OAM's charge and sign of a beam	107
4.3.3	Applications	107
4.4	Generation of coherent beams with OAM=0 using VeCSELs	109
4.4.1	Description of our approach	109
4.4.2	Design and fabrication of the 1/-VCSEL with integrated in- tensity masks	110
4.4.2.1	The gain mirror	110
4.4.2.2	The integrated intensity masks	110
4.4.2.3	Fabrication and characterization	112
4.4.2.4	Laser setup and obtained results	114
4.4.2.5	Discussion	117
4.5	Generation of beams carrying OAM	118
4.5.1	The handedness control problem	118
4.5.2	State of the art of intracavity vortex-beams generation	119
4.5.2.1	Amplitude only intracavity mode selection	119
4.5.2.2	Hybrid generation methods:	120
4.5.3	Vortex modes dynamics and random handedness selection	121
4.5.3.1	The general Maxwell-Bloch equations	121
4.5.3.2	Maxwell-Bloch equations in multi-transverse mode VeCSEL	123
4.5.3.3	Discussion on coupling via the loss term	127
4.5.3.4	Dual vortex mode class-A competition equations	128
4.5.3.5	Numerical results and discussion	128
4.6	The proposed solution: OAM charge and handedness control using a flat photonics element	131
4.6.1	Description of the flat-photonics element (FPE)	131
4.6.2	The operation principle	132

4.6.2.1	OAM charge control	132
4.6.2.2	OAM handedness control	133
4.6.3	Design and fabrication of the 1/2-VCSEL and the FPE	136
4.7	The article:Vortex Laser with III-V flat photonics	139
4.8	conclusion	159
Chapter 5 Generation and control of coherent polarization states in VECSELs		161
5.1	Introduction	161
5.2	Polarization properties of 1/2-VCSEL structure	162
5.2.1	Linear dichroism in [001] Quantum wells structures	162
5.2.2	Dichroism control	165
5.2.3	Linear birefringence in 1/2 VCSEL structure	165
5.2.3.1	Experiments	167
5.2.3.2	Birefringence control	169
5.2.4	Circular dichroism and circular birefringence	170
5.3	Generation of pure linear polarization	172
5.3.1	Inherent selection of linear polarization in VECSELs	172
5.3.2	The problem of the suppressed mode linewidth	172
5.3.3	Dynamics of polarization modes: the SFM model	173
5.3.4	Theoretical noise spectrum and polarization modes beating	176
5.3.4.1	Normalized dimensionless SFM equations	176
5.3.4.2	Linearization and noise spectrum calculation	176
5.3.4.3	Comparison with experiments	178
5.4	Generation of controlled circular polarization with electronic spin transfer	181
5.4.1	Preparing the cavity eigenstate	181
5.4.2	Experimental results and analysis	182
5.4.2.1	First observations	182
5.4.2.2	Perturbing the circular eigenstates to enable mode competition	184
5.4.2.3	Mode dynamics: numerical results	185
5.5	Conclusion	186
Chapter 6 Structured laser light for self-mixing sensing		189
6.1	Introduction	189
6.2	Presentation and theoretical elements of Laser-self-mixing	190
6.2.1	Presentation of the method	190
6.2.2	Equivalent cavity model	191
6.2.3	Feedback regimes	192
6.2.4	Self-mixing for sensing applications	193
6.2.4.1	Displacement measurement	193
6.2.4.2	Velocity measurement	194
6.2.5	How to choose a laser source for self-mixing	195

6.3	Article :Self-mixing in low noise semiconductor vortex laser for rotational Doppler shift detection in backscattered light	197
6.4	Feedback in a Hermite-Gaussian laser for particle sizing	206
6.4.1	Brief overview of conventional particle sizing techniques . . .	206
6.4.1.1	Phase Doppler Anemometry	206
6.4.1.2	Interferometric particle imaging	207
6.4.2	The proposed design: Spatially-resolved feedback for particle sizing	208
6.4.3	Self-mixing signal simulation	209
6.4.3.1	Simultaneous size and velocity measurement	213
6.5	Conclusion	214
 Conclusion		217
Appendices		223
Chapter A Jones vectors table and Jones matrices of polarizing optics		225
A.1	Jones vectors	225
A.2	Jones matrices	225
A.2.1	A wave plate	225
A.2.2	A polarizer	227
 Chapter B Derivation of Lamb model coefficients for dual transverse modes		229
 Bibliography		231

Introduction

2015 has been chosen as the international year of light and light based technologies (IYL2015) to highlight the importance of light and optical technologies for the social, economics, and scientific development of the world. It celebrates the 20 years since the first realization of atomic Bose-Einstein condensate, the 45 years since the invention of optical trapping, 150 years since Maxwell's theory of electromagnetic waves, 200 years since Fresnel's proposition of the wave nature of light, and 1000 years since Ibn AL-Haytham's treatise on optics.

Laser invention is one of the major events in the field of optics and optical physics. In the continuum of states of free-space, light waves can have any polarization (\vec{P}), take any spatial pattern ($k(\mathbf{r})$) and oscillate in time at any frequency ($Z(t)$). These are the three light axis \vec{E}, k, Z illustrated schematically in Fig 1. But inside a laser cavity light is confined and so quantized with respect to these

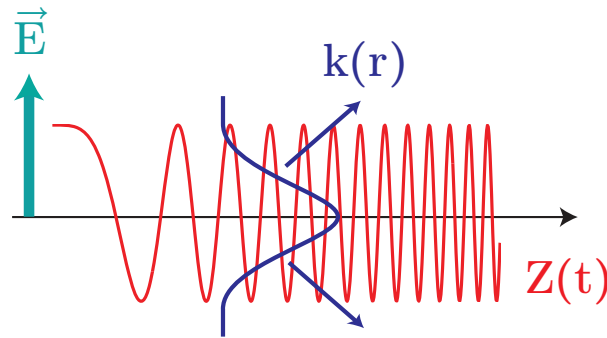


Figure 1: The three light axis: transverse (k), longitudinal (Z), and polarization (E).

axis. Because when a laser is turned on, light is generated spontaneously in all the directions by excited atoms, and only those light-waves that can stay long enough in the cavity can cause stimulated emission. As a result, only waves that are close to the cavity axis and have the same direction, wavelength, and polarization are amplified. The laser cavity exhibits a non-linear laser phase-transition that makes a strong discrimination between waves with respect to their frequency, intensity pattern and polarization. Only some of them are allowed to exist and form a discrete spectrum of modes.

Traditionally, laser sources are fabricated to emit on the fundamental mode of the cavity, characterized by a unique intensity lobe (such as Gaussian mode), a uniform spherical phase front, and a linear polarization state. However, in recent years other new coherent laser light-states with structured-phase, -amplitude and polarization are generating an increasing interest thanks to their unique properties.

Generation of such exotic states of light in a laser cavity is the main focus of this thesis.

Several other appellations are used in the literature to refer to this kind of beams, such as: complex light, exotic light, phase-structured beams, high order beams...etc. But in most cases, the phase-structured modes are referred to, using one of their main properties. For example Bessel Gauss beams are usually called self-reconstructing, or non-diffracting beams. Laguerre-Gauss beams with radial number $p = 0$ and azimuthal number $l \neq 0$ $LG_{p=0,l \neq 0}$ possess a helical wave front, and they are usually called helically-phased or donut-shaped beams, vortex modes, twisted light and twisted photons. Indeed, this diversity reflects the growing interest structured-light is raising, especially vortex beams that carry and orbital angular momentum (OAM) and to which we give a special focus in this thesis, together with spin angular momentum carried by circularly polarized light.

The study of the formation of these modes inside a laser cavity and their properties holds a certain interest from both fundamental and application points of view. For example, high order LG beams are considered for use in future gravitational waves detectors [Chelkowski 2009] and vortex modes carrying orbital angular momentum are at the center of widespread new fields ranging from the domain of infinitely small such as the manipulation of Bose-Einstein condensate [Andersen 2006], nano and micro-manipulation of particles [Galajda 2001, Galajda 2002b, Dienerowitz 2008], to the very large distances in astrophysics [Harwit 2003], free-space telecommunications [Gibson 2004a, Wang 2012, Bozinovic 2013, Lei 2015]. In addition to fundamental fields such as Quantum entanglement experiments [Mair 2001, Vaziri 2002], quantum communication [Molina-Terriza 2004, Langford 2004] and quantum cryptography [Gröblacher 2006].

Motivated by the emerging applications, generation of structured light directly inside a laser cavity has become the field of very active research work. Indeed, this method presents several advantages in terms of coherence, power, cost, and compactness, over the traditional extra cavity transforming of conventional beams, using, for example spatial light modulators.

Nevertheless, direct generation in a laser cavity presents several challenges, open-questions, poor understanding of the involved effect, and sometimes erroneous interpretations and to date unsolved bottlenecks. The most obvious one is that of controlling vortex's modes handedness inside the cavity, that we address, inter alia, within the framework of this thesis.

In a similar approach, the photon spin control through electronic injection has led to numerous works without successful solution [Holub 2007, Frougier 2013], in spite of great interest for spintronic applications like telecoms, data-storage...etc. The problem here comes from the fast spin reservoir relaxation in semiconductor media compared to the radiative lifetime.

It is an aim of this present work to contribute to the understanding of the main processes involved in intracavity structured laser-light generation. When possible, we tried to give answers to the open questions, supported by our experimental results, theoretical calculations and observations reported in the literature. Such as the efficient electronic spin transfer to a coherent photon state, or the random hand-

edness selection of vortex modes, observed by many researchers but not understood. In sum, direct laser generation requires to:

- Understand the fundamental physical mechanisms involved in mode formation in a laser cavity and their selection via laser mode dynamics.
- Have a well suited laser source concept, that enables to integrate mode control elements
- Develop a compact and accurate mode control technology suitable for integration inside the laser cavity.
- Studying the physical properties of the coherent generated light-state using powerful optical and RF (radio frequency) tools

These points outline the goals of this thesis (see Fig 2) which is divided into six chapters, as describe belows: The first one is dedicated to the study of the light

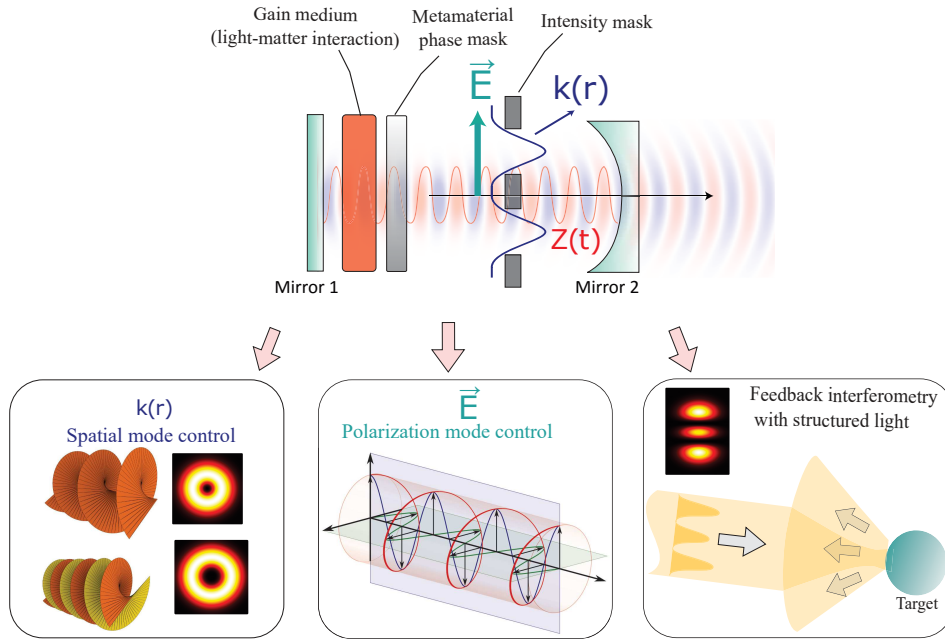


Figure 2: Summary of the main work lines.

eigenstates in high-finesse laser cavities. We start by describing these eigenstates with respect to the three axis of the light that define the photon state: longitudinal (frequency), transverse (spatial), and polarization. For each one of these axis we study the physical ingredients governing modes formation, and develop the theoretical tools required to the calculation of the eigenmodes in non-conventional cavities. In a second step, as the mode selection in a laser involves light-matter interaction, we focus on the laser dynamics study by writing the semi classical Maxwell-Bloch equations for our lasers. These equations allow us to study the role of temporal dynamics in laser mode selection, and the path to a possible steady state.

In the second and the third chapters, we address the development and the characterization of a III-V semiconductor-based technology that enables us to efficiently select the wanted mode in the eigenbasis. We adopt an approach based on highly coherent III-V semiconductor laser sources containing multi-quantum wells (InGaAs/GaAs/AlGaAs) Vertical-External-Cavity-Surface-Emitting-Laser (VeCSEL), operating in the near infra-red (IR). Chapter two, is dedicated to the development of these sources, we first show why they are ideal candidates for structured light generation, then we present some elements of design and fabrication.

The third chapter is dedicated to the development of integrated mode control technology. It consists in stacked subwavelength-thick layers acting as phase and intensity masks. The phase masks are based on 2D subwavelength grating with artificial refractive index that can be controlled by design. These gratings are commonly called metamaterials. The intensity masks, for their part, consist in a subwavelength metallic layer that we use to introduce highly selective transverse loss patterns.

In the fourth chapter we use the previously developed sources with integrated mode control technology to generate and characterize, structured-phase modes. We focused on Laguerre-Gauss (LG) with and without orbital angular momentum (OAM $\neq 0$ and OAM=0, respectively), and also Hermite-Gauss (HG) beams. In this chapter we propose a solution to the unsolved problem of the handedness control of degenerate contra-rotating vortex modes. We do this by introducing a weak "orbital birefringence" using a meta-surface. The induced azimuthal symmetry breakdown allows to select the vortex handedness by exploiting H. Haken's principle "Darwin's survival of the fittest" in non-linear laser dynamics, that always favors a homogeneous intensity pattern [Haken 1985]. At the end we characterize the generated exotic light-states.

The fifth chapter deals with polarization mode selection in a laser. We start by studying the polarization properties of the optical cavity and the quantum-well-based gain medium: the birefringence near the semiconductor surface; the dichroism and the spin-flip time in the quantum wells. We make use of these elements to generate and characterize the wanted polarization state: highly coherent linear and circular polarization state carrying a spin angular momentum (SAM) controlled via electronic spin injection.

In the last chapter new integrated and highly sensitive sensor concept is presented. This sensor design is based on feedback interferometry (self-mixing) in III-V semiconductor structured-light laser sources developed in this work. The first design, takes advantage of the rotational Doppler shift that occurs in beams carrying angular momentum to measure both translational and angular velocities. The second design uses the spatial structure of the laser mode for particle sizing. These new sensor concepts show examples of measurements, inaccessible using conventional laser sources

Principles of mode selection in a laser cavity

1.1 Introduction

In this chapter we deal with light eigenstates (modes) of a laser cavity. We address longitudinal, transverse and polarization modes. For each case, we give some basics and theoretical tools that will allow us to tackle the central issue of this work: how to generate and control high coherence unconventional modes with structured phase and intensity profiles.

The light field inside an optical cavity is quantized with respect to the three light axis (longitudinal, transverse and polarization). It forms then, a discrete spectrum of modes as shown schematically in Fig 1.1, and to deal with them one has to adopt two important approximations: the rotating wave approximation, and the slowly varying envelope approximation. By doing so, we can write the electric field inside the optical cavity in slowly varying sinusoidal form, and in terms of the cavity eigenstates [Khanin 1995] as follows:

$$\vec{\mathcal{E}}(\vec{r}, t) = \text{Re} \left(\sum_{n,q,i} \tilde{E}_{nq}(\vec{r}, t) e^{-j\omega_{nqi} t} \vec{x}_i \right) \quad (1.1)$$

where $\tilde{E}_{n,q,i}(\vec{r}, t)$ is the complex amplitude of the electric field of transverse index n , longitudinal index q and projected on the polarization axis defined by the unit vector \vec{x}_i . We assume that the spatial and temporal components of the electric field can be treated separately, thus: $\tilde{E}_{nq}(\vec{r}, t) = u_{nq}(\vec{r}) E_{nq}(t)$.

By the end of this chapter we shall answer two main questions: (1) how to determine the modes of a passive optical resonator. (2) How to describe the mode selection process and dynamics operated by the laser.

To answer the first one we start by treating the classical case of longitudinal modes in a Fabry-Perot resonator. Then we move to transverse modes using generalized resonator theory which will allow us to determine the eigenmodes and eigenvalues of a resonator, including resonators with an arbitrary phase and amplitude transverse function, in order to describe unconventional optical elements.

The second question, requires the use of laser dynamics, which can be treated rigorously using the semi-classical Maxwell-Bloch theory. However, for the pedagogical requirement, this first chapter starts with the classical rate equations, to

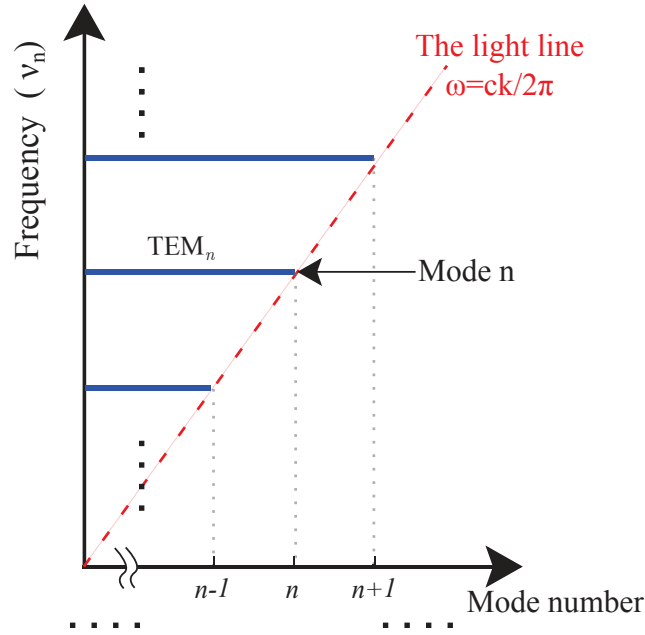


Figure 1.1: Schematic illustration dispersion relation of transverse modes in a concave-type cavity.

give an intuitive understanding of the different dynamic processes involved in mode selection by the laser. We postpone then the semi-classical approach to the forthcoming chapters where a more rigorous approach is required. We end the chapter by describing the noise and coherence properties of lasers and highlight their importance to us.

1.2 Longitudinal modes

The longitudinal mode selection is usually achieved using an optical cavity with two facing mirrors¹ with reflectivities r_1, r_2 close to 1. The tangential component of the electric field at each mirror surface must vanish, which creates a boundary condition. This condition is fulfilled by the electric field when it forms a standing wave with a node on each mirror. In this case the phase shift after one round-trip must satisfy the condition: $2kL_c = q\pi$ where q is an integer, $k = 2\pi/\lambda$ is the wave-vector and L_c is the cavity length. The resonator creates strong wavelength discrimination and allows only a set of discrete and periodic longitudinal modes to exist. The transfer function of such a resonator can be written as:

$$T_f(\lambda) = \left| \frac{t_1 t_2 \exp(-kL_c)}{1 - r_1 r_2 \exp(-2kL_c)} \right|^2 \quad (1.2)$$

¹Other arrangements using more than two mirrors can be used, but as we will see next (Sec 2.4) these arrangements can always be reduced to an equivalent two-mirror cavity.

where $t_i = \sqrt{1 - r_i^2}$ is the mirror transmission. These longitudinal modes of the cavity have a finite lifetime τ_{ph} ¹, because of the cavity losses, mainly due to transmission of the mirrors, and possible absorption losses. τ_{ph} is given by:

$$\tau_{ph} = \frac{\mathcal{F}}{\pi FSR} \quad (1.3)$$

where $FSR = c/(2n_c L_c)$ is the free spectrum range of the cavity with n_c the refractive index inside it, and \mathcal{F} is the finesse of the cavity given for mirrors transmission $R < 10\%$ as [Siegman 1986]:

$$\mathcal{F} = \frac{\pi\sqrt{R}}{R} \quad (1.4)$$

By means of the finite lifetime the amplitude of the mode is damped, which gives rise to a frequency width, with a full width half maximum (FWHM) value $\Delta\nu_c$ given by:

$$\Delta\nu_c \simeq \frac{FSR}{\mathcal{F}} \quad (1.5)$$

It should be noted that the laser mode linewidth is much lower than the one of the unloaded cavity, thanks to the laser process itself

It is possible to predict longitudinal mode selection behavior, by merely comparing the FSR of the cavity and the gain bandwidth of the laser medium. For example, in microcavity vertical surface emitting lasers (VCSELs) the semiconductor quantum wells provide a gain with a wide bandwidth in the order of 3 THz. And the typical cavity length is in the range 1 – 3 μm , which gives a FSR of 50 THz for an emission wavelength $\lambda = 1 \mu\text{m}$. This means that there is only one longitudinal mode in the gain bandwidth. However, for a cavity length of 5mm, for example, the $FSR \simeq 30 \text{ GHz}$ and more than 100 modes are contained within the gain bandwidth, the frequency selection introduced by the cavity is then not sufficient to select a single longitudinal mode. In this case, single mode selection comes as a result of laser dynamics, or more precisely through mode competition in the gain medium that we will discuss next (see section 1.6).

1.3 Transverse modes of a passive cavity

1.3.1 What is a transverse mode

Transverse modes of an optical resonator are related to the transverse form of the traveling waves inside it. We refer to this part of the wave using the complex phasor amplitude $u(x, y)$ which describes the transverse amplitude and phase variation of the waves:

¹The mode lifetime is the time in which the mode intensity inside a cavity without amplification, drops down to $1/e$ of its initial value.

To understand the transverse mode notion, we consider a wave with a given initial transverse profile $u^{(0)}(x, y)$, after a complete round trip inside the optical resonator, we expect the transverse profile $u^{(1)}(x, y)$ to be different from the initial one, because of losses, diffraction, reflection and mirror edges (aperture) effects. We call transverse eigenmode of the optical cavity, any transverse profile that conserves exactly the same form after one round trip, with possible amplitude reduction due to diffraction and other losses. This condition can be written as [Siegman 1986]:

$$u^{(n+1)}(x, y) = \gamma u^{(n)}(x, y) \quad (1.6)$$

where γ is the complex eigenvalue, whose argument represents the round trip phase shift, and $1 - |\gamma|^2$ represents the power fractional loss experienced by the eigenmode in one round trip.

1.3.2 Modes of an optical cavity with curved mirrors

In optical cavities with curved mirrors (Fig 1.2), several modes satisfying the self-reproducing condition occurs. The most known ones are those belonging to the Gaussian modes family, which forms a complete basis set of orthogonal modes. Such as the Laguerre-Gauss (LG) basis (see Fig 1.3) in resonators with circular symmetry, and the Hermite-Gauss basis (HG) in resonators with rectangular symmetry. The general expressions of non-degenerate LG modes and HG modes are given by Eq 1.7, and Eq 1.9, respectively [Siegman 1986].

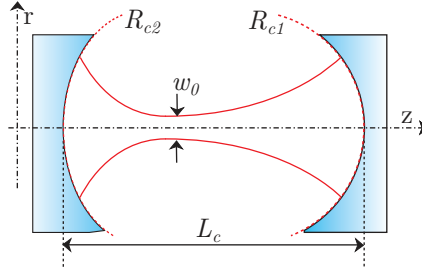


Figure 1.2: Optical cavity with curved mirrors.

$$u_{pl}^*(r, \theta, z) = \frac{1}{w(z)} \sqrt{\frac{2p!}{\pi(p+|l|)!}} \left(\frac{\sqrt{2}r}{w(z)} \right)^{|l|} L_p^{|l|} \left(\frac{2r^2}{w(z)^2} \right) \exp \left[-jk \frac{r^2}{2\tilde{q}(z)} \right] \quad (1.7)$$

$$\times \exp[j(-kz + l\theta)]$$

where r, θ are radial and azimuthal coordinates respectively, z is the propagation distance, $p \geq 0$ is the radial mode number and l is the azimuthal one. The beam parameter $q(z)$ and the Gaussian beam waist $w(z)$ are described next, when we discuss the propagation properties of Gaussian beams. $L_p^{|l|}$ is the generalized Laguerre polynomial given by

$$L_p^{|l|}(x) = \sum_{i=0}^p (-1)^i \binom{p+|l|}{p-i} \frac{x^i}{i!} \quad (1.8)$$

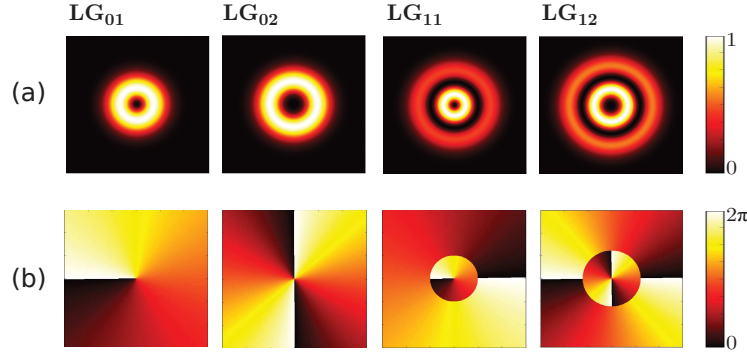


Figure 1.3: Intensity (a) and phase (b) patterns of the the first LG modes.

Modes with radial number $p = 0$ and azimuthal number $l \neq 0$, have a donut-shaped intensity profile and helical wavefront. The handedness of the helical wavefront (right-handed or left-handed) depends on the sign of the azimuthal mode number (+ or -). The center of such beams presents a phase singularity, therefore, these beams are sometimes called vortex beams. The helical wavefront confers to these beams an orbital angular momentum, which is a property of a great importance that has led to a new widespread applications. Indeed, these beams are the subject of a very active research work. We will pay a special attention to the generation and control of such exotic light states in chap 4.

Hermite-Gaussian beams expression is given by:

$$u_{nm}(x, y, z) = \frac{1}{w(z)} \sqrt{\frac{1}{(2^{n+m-1} n! m! \pi)}} H_n \left(\frac{\sqrt{2}x}{w(z)} \right) H_m \left(\frac{\sqrt{2}y}{w(z)} \right) \times \exp \left(-jk \frac{(x^2 + y^2)}{2q(z)} \right) \exp(-jkz) \quad (1.9)$$

where $H_n(x)$ are the Hermite polynomials of order n . The first Hermite polynomial, without normalization, can be written as:

$$\begin{aligned} H_0(x) &= 1 & H_1(x) &= 2x \\ H_2(x) &= 4x^2 - 2 & H_3(x) &= 8x^3 - 12x. \end{aligned} \quad (1.10)$$

Further orders can be computed recursively since:

$$H_{n+1}(x) = 2xH_n(x) - 2nH_{n-1}(x) \quad (1.11)$$

Gaussian modes with different mode numbers (p, l) have different resonance frequencies in the optical resonator¹, because of the Gouy phase shift and its dependence on the mode numbers. This resonance frequency for a transverse mode LG_{pl} is given by [Siegman 1986]:

$$\omega_{qpl} = 2\pi FSR \left[q + (1 + 2p + |l|) \frac{\cos^{-1}(\sqrt{g_1 g_2})}{\pi} \right] \quad (1.12)$$

where $g_i = 1 - L_c/R_{ci}$ are the cavity parameters, and q is the longitudinal mode number. This means that for each longitudinal mode q there is an associated set of discrete frequencies corresponding to transverse modes with different mode number as shown in figure 1.4. Here we point out an important property of LG modes, which is that donut modes LG_{0l} having the same azimuthal number module l , but with opposite handedness $(+/-l)$, have a degenerate resonance frequency in the optical resonator. This can be seen from equation 1.12. This frequency degeneracy along with the fact that such modes have the same intensity profile, make them very hard to discriminate inside the optical resonator. Furthermore, these two modes can be combined coherently and form a degenerate mode (Eq 1.13). This happens very often in laser resonators, because non-degenerate modes need good symmetry, which requires special attention when fabricating the resonator. For example the presence of optical defects on one mirror or in the gain medium favors the locking of non-degenerate modes to give a degenerate one as we will see with more details in section (4.5.3.3).

$$u_{pl}(r, \theta, z) = \frac{1}{\sqrt{2}} \left[u_{pl}^*(r, \theta, z) + u_{p(-l)}^*(r, \theta, z) \right] \quad (1.13)$$

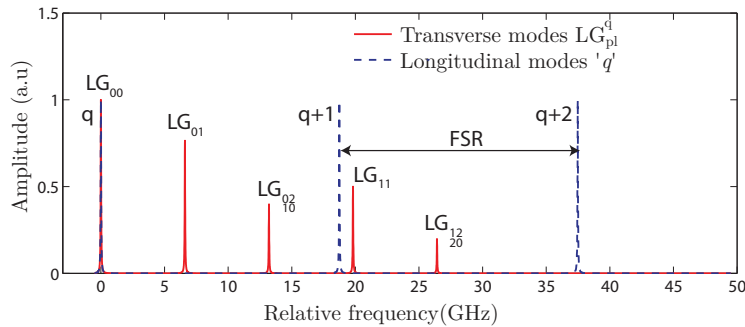


Figure 1.4: Transverse modes frequencies in a 8 mm long plano-concave cavity, with $R_c = 10$ mm.

Optical resonator modes with different mode numbers have also different diffraction losses. These losses are due to the finite diameter of the end mirrors, thus in conventional resonators higher order modes with higher order radial variations have

¹Except in the case of confocal configuration

always larger diffraction loss. However, it should be noted that in practice the mirrors diameter are usually much larger than the mode one, thus the few first modes have very small diffraction losses ($\ll 1\%$) with very close values, which cannot be used to discriminate these modes.

1.3.3 Gaussian modes propagation

After this brief description of optical resonators' transverse modes, it is useful to describe their propagation properties. For the sake of simplicity, we deal with the fundamental Gaussian mode, but the discussed properties are applicable to other higher order modes. If we consider a Gaussian beam propagating in $+z$ direction, starting from a plane at $z = 0$, at this point the beam diameter contracts to its minimum value w_0 called the waist, and the phase front is plane. The normalized field expression $u(r, z)$ is given by:

$$\begin{aligned} u(r, z) &= \left(\frac{2}{\pi}\right)^{1/2} \frac{q_0}{w_0 q(z)} \exp\left[-jkz - jk\frac{r^2}{2q(z)}\right] \\ &= \left(\frac{2}{\pi}\right)^{1/2} \frac{\exp[-jkz + j\varphi(z)]}{w(z)} \exp\left[-\frac{r^2}{w(z)^2} - jk\frac{r^2}{2R(z)}\right] \end{aligned} \quad (1.14)$$

where the complex radius of curvature $q(z)$ is related to the spot size w ¹ and the radius of curvature of the wavefront $R(z)$ at any plane z by:

$$\frac{1}{q(z)} = \frac{1}{R(z)} - j\frac{\lambda}{\pi w^2(z)} \quad (1.15)$$

The beam parameter at the waist is purely imaginary:

$$q_0 = j\frac{\pi w_0^2}{\lambda} = jz_R \quad (1.16)$$

Where z_R is the Rayleigh range, a distance at which the beam area doubles. And at a distance z away from the waist this parameter is given by:

$$q = q_0 + z. \quad (1.17)$$

From Eq1.15 and Eq1.17 one obtains all the important parameters of the beam at any plane z :

$$w(z) = w_0 \sqrt{1 + \left(\frac{z}{z_R}\right)^2}, \quad (1.18)$$

$$R(z) = z + \frac{z_R^2}{z} \quad (1.19)$$

and finally the Gouy shift $\varphi(z)$ is given by:

$$\varphi(z) = \tan^{-1}\left(\frac{z}{z_R}\right) \quad (1.20)$$

¹ w is the distance at which the amplitude is 1/e times that on the axis.

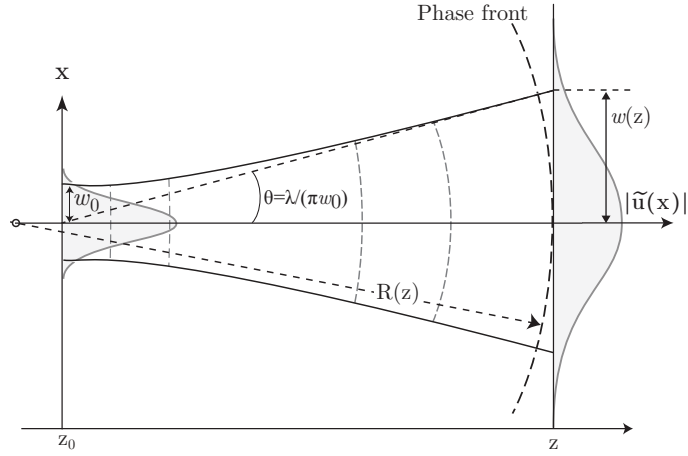


Figure 1.5: Gaussian beam parameters and propagation.

Figure 1.5 shows the expansion of the beam according to Eq 1.14, for $z \gg z_R$ (far field) this expansion is quasi linear with a divergence angle θ given for an ideal beam by :

$$\theta = \frac{\lambda}{\pi w_0} \quad (1.21)$$

However, real-world beams have a higher divergence given by:

$$\theta_{Laser} = M^2 \frac{\lambda}{\pi w_0}, \quad \text{with } M^2 > 1 \quad (1.22)$$

where the M^2 factor, also called beam propagation factor, is a common measure of the beam quality. Beams are often said M^2 times diffraction limited, thus an ideal beam has an $M^2 = 1$. An ideal high order beam LG_{pl} has an $M^2 = 2p + |l| + 1$. We note that the M^2 factor cannot be considered as a complete characterization of the beam quality, however, in practice it allows us to predict the evolution of real beams using a simple extension of an ideal Gaussian one.

1.3.4 Optical resonator stability

An optical cavity is considered as stable if it allows a self-reconstructing mode to exist within it. We have seen that for a Gaussian beam, all the propagation information are contained in the beam parameter $q(z)$. Therefore, in a stable optical cavity, we can always find a beam parameter $q_m(z)$ that does not change after one round trip propagation. This q_m represents then, the properties of the Gaussian mode of this cavity.

Stability analysis is usually performed using ray transfer matrices [Yariv 2007]. This method allows to propagate the slope (θ_1) and the displacement (h_1) of an optical ray through a paraxial optical system (see Fig 1.6) using a matrix operation as follows:

$$\begin{pmatrix} h_2 \\ \theta_2 \end{pmatrix} = \begin{pmatrix} A & B \\ C & D \end{pmatrix} \begin{pmatrix} h_1 \\ \theta_1 \end{pmatrix} \quad (1.23)$$

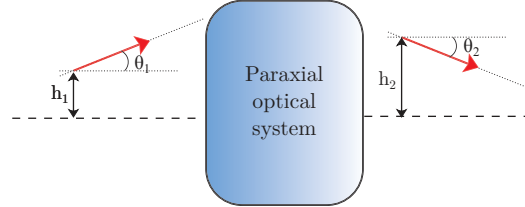


Figure 1.6: Parameters of ABCD optical system.

This method is used to describe the propagation of spherical waves, including Gaussian beams through paraxial optical systems, and can be used to analyze the stability of an optical cavity with curved mirrors. An optical cavity in which the light is propagating back and forth between the mirrors can be represented by a periodic sequence of focusing elements (Fig 1.7) (curved mirrors or their equivalent focusing lenses with a focus length $f = R_c/2$) [Yariv 2007]. The self-reproducing

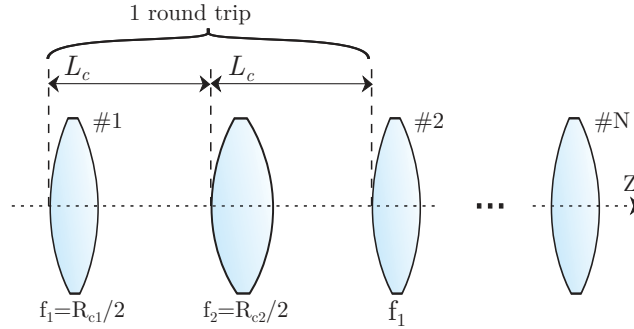


Figure 1.7: Equivalent periodic ABCD system of an optical resonator.

solution $\vartheta_i = \begin{pmatrix} h_i \\ \theta_i \end{pmatrix}$ can be written for N round trip, in matrix form as follows:

$$\begin{pmatrix} A & B \\ C & D \end{pmatrix}^N \vartheta_i = \gamma^N \vartheta_i \quad (1.24)$$

This periodic system is stable if:

$$-1 \leq \frac{A+D}{2} \leq 1, \quad \text{or} \quad 0 \leq \frac{A+D+2}{4} \leq 1 \quad (1.25)$$

For the typical example of two curved mirrors cavity, this condition gives:

$$0 \leq g_1 g_2 \leq 1 \quad (1.26)$$

When this stability condition is fulfilled, the mode sizes on each mirror w_1, w_2 are given by:

$$w_1^2 = \frac{L\lambda}{\pi} \sqrt{\frac{g_2}{g_1(1-g_1g_2)}}, \quad \text{and} \quad w_2^2 = \frac{L\lambda}{\pi} \sqrt{\frac{g_1}{g_2(1-g_1g_2)}} \quad (1.27)$$

1.3.5 Calculation of generalized cavity modes

Gaussian modes described above are valid in the case of ideal resonators with infinite mirror diameters. This ideal case can be satisfactorily approached in high finesse conventional resonators where the mirror radius is much larger than the mode waist. However, the exact transverse eigenmodes and eigenvalues of stable Gaussian resonators with finite apertures, or with additional optical elements, must be calculated numerically, as analytical solutions are generally not available. This numerical mode calculation is of great practical importance to describe the transverse mode selection. It is important to note that optical resonators are usually described in scalar or quasi plane-wave terms, with an emphasis on diffraction effects at apertures and mirrors edges, rather than in vector terms with emphasis on matching boundary conditions. Therefore, transverse mode calculation methods are based on the diffraction integral through the optical resonator. For a given stable resonator having a set of eigenmodes $u_{nm}(x, y)$ and eigenvalues γ_{nm} , the round-trip propagation integral must satisfy the condition in Eq 1.6, and can be written as:

$$u_{nm}^{(1)}(x, y) = \iint K(x, y, x_0, y_0) u_{nm}^{(0)}(x_0, y_0) dx_0 dy_0 = \gamma_{nm} u_{nm}^{(0)}(x, y) \quad (1.28)$$

where $u_{nm}^{(0)}$ is the initial field distribution and $u_{nm}^{(1)}$ is the field distribution after one round trip, the linear operator $K(x, y, x_0, y_0)$ is the propagation kernel from the plane (x_0, y_0) to (x_1, y_1) , and commonly called the propagator. This kernel depends on the chosen reference plane and the optical components of the resonator, for an arbitrary ABCD system the propagation kernel between the starting plane (1) and the arrival plane (2) is given by [Siegman 1986]:

$$\begin{aligned} K &= K(x_1, x_2) K(y_1, y_2) \\ &= \sqrt{\frac{j}{\lambda B_x}} \exp \left[-\frac{j\pi}{\lambda B_x} (A_x x_1^2 - 2x_1 x_2 + D_x x_2^2) \right] \\ &\quad \sqrt{\frac{j}{\lambda B_y}} \exp \left[-\frac{j\pi}{\lambda B_y} (A_y y_1^2 - 2y_1 y_2 + D_y y_2^2) \right] \end{aligned} \quad (1.29)$$

This allows to write the propagation kernel for any paraxial optical resonator by writing its ABCD matrix, or the round-trip matrix of the equivalent periodic focusing elements. For example, the conventional optical resonator shown in Fig 1.2 has an ABCD matrix given by:

$$M_{ABCD} = \begin{pmatrix} 2g_1g_2 - 1 & 2g_2L_c \\ 2g_1/L_c & 2g_1g_2 - 1 \end{pmatrix} \quad (1.30)$$

Equation 1.28 can be written in a more general form by introducing an amplitude or/and phase mask, using a complex function $\rho(x, y)$:

$$\gamma_{nm}u_{nm}(x, y) = \iint K(x, y, x_0, y_0)u_{nm}(x_0, y_0)\rho(x_0, y_0)dx_0dy_0 \quad (1.31)$$

In order to calculate the eigenmodes of a given resonator, one has to find wave functions $u_{nm}(x, y)$ and their associated eigenvalues γ_{nm} that satisfy the condition in Eq 1.31. This can be done using an iterative approach such as the Fox-Li method, to calculate the mode having the lowest diffraction losses (dominant mode), or the matrix method with Huygens Kernered formulation, which is a more powerful one that allows to calculate the higher order modes too. In the following we describe these two methods, and discuss the advantages and limitations of each one, to understand how to use them properly depending on the resonator configuration we want to analyze.

1.3.5.1 The Fox-Li iterative method

To understand this approach, we consider that a starting field with an arbitrary distribution $u^{(0)}(x, y)$ is launched inside a stable optical resonator. If we assume that this resonator possesses a set of orthogonal eigenmodes u_{nm} , this starting field can be expanded as follows:

$$u^{(0)}(x, y) = \sum_{nm} C_{nm}u_{nm}(x, y) \quad (1.32)$$

after N round trip, and from Eq 1.31 each transverse mode u_{nm} will be attenuated as $|\gamma_{nm}(x, y)|^N$, because $u_{nm}^{(N)}(x, y) = \gamma_{nm}^N u_{nm}^{(0)}(x, y)$, thus the intra-cavity field becomes:

$$\begin{aligned} u^{(N)}(x, y) &= \sum_{nm} C_{nm}\gamma_{nm}^N u_{nm}(x, y) \\ &= \underbrace{C_{00}\gamma_{00}^N u_{00}}_{\text{dominant mode}} + \underbrace{C_{01}\gamma_{01}^N u_{01} + C_{10}\gamma_{10}^N u_{10} + C_{02}\gamma_{02}^N u_{02} + \dots}_{\text{weak for large N values}} \end{aligned} \quad (1.33)$$

This equation tells us that, whatever is the initial field distribution, after a sufficient number of round trips, the mode with the smallest loss per transit (with closest $|\gamma|$ to 1) will become dominant. In conventional resonators this mode is usually the fundamental TEM_{00} one. This mode calculation procedure is called the Fox-Li approach ¹, after A.G Fox and T. Lee who first used it [Fox 1961] in the earliest days of the laser to calculate the modes of some simple laser resonators. The numerical procedure of this method consists in propagating a given initial field $u^{(0)}(x, y)$ using the round trip integral (Eq 1.28), and after each iteration (or few iterations) the overall amplitude level is rescaled to compensate the diffraction loss.

¹When applied to solve the mode of a resonator, but generally speaking this approach is known as the power method in linear algebra [Arbenz 2012].

The iteration is repeated until the establishment of a steady state: unchanging field pattern, which represents the eigenmode distribution. The eigenvalue is calculated as follows:

$$\gamma = \lim_{k \rightarrow \infty} \frac{u^{(k+1)}(x, y)}{u^{(k)}(x, y)} \quad (1.34)$$

so in practice, after N total iterations:

$$\gamma = \frac{u^{(N)}(x, y)}{u^{(N-1)}(x, y)} \quad (1.35)$$

1.3.5.2 The matrix method, with Huygens Kernel formulation

The matrix method is very powerful and allows to calculate the eigenvalues and the associated eigenvectors (modes pattern) of the fundamental, and also the higher order modes at the same time. To describe this method we start from the main equation of optical resonator theory (Eq 1.31). However, for the sake of simplicity we first consider the 1D case :

$$\gamma_n u_n(x) = \int K(x, x_0) u_n(x_0) \rho(x_0) dx_0 \quad (1.36)$$

If we apply the Legendre-Gauss quadrature scheme $\int_{-1}^1 f(x) dx \simeq \sum_{j=1}^N L_j f(\chi_j)$ to approximate the definite integral of Eq 1.36 by a discrete kernel weighted by Legendre polynomials L_j , with abscissas χ_j given by the roots of L_j [Zwillinger 2003]. The equation then takes the form:

$$\gamma_n u_n(\chi_u) = \sum_{j=0}^N L_j K(\chi_u, \chi_j) \rho(\chi_j) u_n(\chi_j) \quad (1.37)$$

where $u_n(\chi_u)$ is the discretized eigenmode evaluated at abscissa χ_u describing the spatial axis (see Fig 1.8). This equation represents a matrix eigenproblem given by:¹

$$\gamma u_u = H_{uj} u_j \quad (1.38)$$

where H_{uj} is a complex symmetric matrix given by:

$$H_{uj} = \begin{pmatrix} \dots & \dots & \dots \\ \dots & L_j K(\chi_u, \chi_j) \rho(\chi_j) & \dots \\ \dots & \dots & \dots \end{pmatrix} \quad (1.39)$$

The eigenvalues of H_{uj} and their associated eigenvectors are the eigenvalues γ_n and the modes patterns $u_n(x)$ of the optical resonator. They can be calculated using any numerical matrix eigenvalue calculation procedure.

¹Note that we drop the mode order subscript n in matrix writing u_n . The new subscript denotes the discretized field at an abscissa χ : $u_{u,j} = u(\chi_{u,j})$

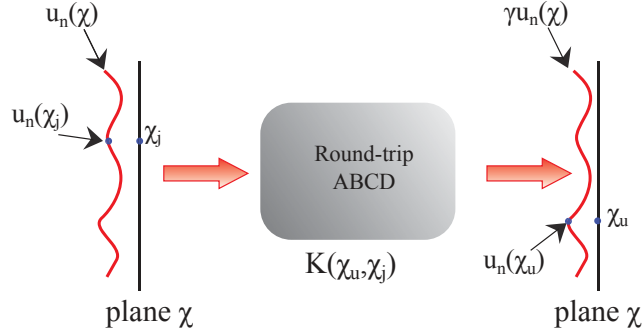


Figure 1.8: Schematic illustration of the discretized matrix-kernel of the optical cavity.

For more than two decades, the matrix method has been limited to 1D modes calculation. Because as we can see from the above description, starting from an 1D problem we obtained a 2D matrix kernel. However, very recently F.Morrissey and H.Chou proposed a substitution technique to write a 2D cavity problem in 1D problem fashion [Morrissey 2011]. The general 2D problem of Eq 1.28 is discretized as:

$$\gamma_{nm}u_{nm}(x_u, y_v) = \sum_{i=1}^N \sum_{j=1}^M K_{iu}K_{jv}u_{nm}(x_i, y_j) \quad (1.40)$$

if we put $\alpha = N(i-1)j$ and $\beta = N(u-1) + v$ and for all combinations of iterating variables¹, Eq 1.40 can be rewritten as a single sum and takes the same form as in the 1D case (described by Eq 1.37): where $S = N \times M$, $\beta = 1 \dots S$ and $\alpha = 1 \dots S$. Using this substitution we rearranged the 2D mode pattern represented by an $N \times N$ complex matrix into a 1D vector having the dimension $1 \times N^2$, and rearranged the kernel matrix according to this.

1.3.5.3 Resonator with an arbitrary phase/amplitude mask

The matrix method allows to add a phase and/or an amplitude mask through $\rho(\beta)$. This can be very useful, for example to determine the eigenmodes of resonators with arbitrary thermal lens, aberrations, tilted mirrors, non uniform reflectivity pattern... etc. However, the method as presented in [Morrissey 2011] allows to apply the ρ function at the first plane of the resonator only. Consequently there are many practical situations where it cannot be used, the most simple one is resonator with double aperture, and also when we need to introduce one or more phase and (or) amplitude mask somewhere between the two mirrors rather on the first one. In this paragraph we show how to generalize the method by splitting the resonator kernel into several sub-kernels and cascading them.

The limitation discussed above stems from the properties of the optical diffraction theory. Because we can calculate the diffraction integral through a paraxial

¹ i and u range over $[1 \dots N]$ while j and v range over $[1 \dots M]$

system as long as there is no aperture in the propagation path (or more generally no arbitrary amplitude or phase function), otherwise one has to split the integral into two parts: from the first plane to the aperture, apply the aperture function, and then propagate to the second plane. One can make the same reasoning when deriving the kernel-matrix expression. For example the system shown in Fig 1.9(a) can be divided into three parts as we show in the equivalent periodic system in Fig 1.9(b). To accomplish a round trip propagation we need to perform a first propagation through the paraxial system defined by M_1 , then apply the function ρ . We next propagate the resulting field through M_2 , apply ρ a second time, and finally propagate to the first mirror (through M_3), with M_1, M_2, M_3 given by:

$$M_1 = \begin{pmatrix} 1 & 0 \\ -2/R_{c1} & 1 \end{pmatrix} * \begin{pmatrix} 1 & d_1 \\ 0 & 1 \end{pmatrix}, \quad M_2 = \begin{pmatrix} 1 & d_2 \\ 0 & 1 \end{pmatrix} * \begin{pmatrix} 1 & 0 \\ -2/R_{c2} & 1 \end{pmatrix} * \begin{pmatrix} 1 & d_2 \\ 0 & 1 \end{pmatrix},$$

$$M_3 = \begin{pmatrix} 1 & d_1 \\ 0 & 1 \end{pmatrix}$$

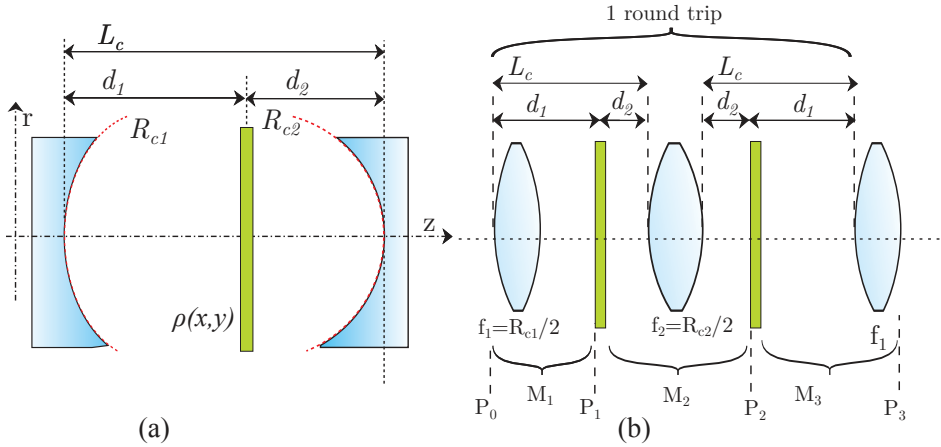


Figure 1.9: (a) Cavity with curved mirrors, incorporating an arbitrary phase/amplitude function. (b) Equivalent periodic system.

The fields u^{P1}, u^{P2}, u^{P3} calculated at the planes $P1, P2, P3$, respectively, are given by:

$$u^{P1}(x_1) = \int K_1(x_0)u^{P0}dx_0; \quad u^{P2}(x_2) = \int K_2(x_1)u^{P1}dx_1;$$

$$u^{P3}(x_3) = \int K_3(x_2)u^{P2}dx_2;$$

By writing these equations in the matrix form one can write:

$$u^{P3} = (H^3 * H^2 * H^1)u^{P0}$$

With H^1, H^2, H^3 are complex kernel matrices corresponding of each subsystem and whose elements are given by Eq 1.39: $H_{uj}^1 = L_j K_1(\chi_u, \chi_j)$, $H_{uj}^2 = L_j K_2(\chi_u, \chi_j)\rho(\chi_j)$ and $H_{uj}^3 = L_j K_3(\chi_u, \chi_j)\rho(\chi_j)$. The global matrix kernel of the resonator is given by $H_{uj} = H_{uj}^3 * H_{uj}^2 * H_{uj}^1$

1.3.5.4 Comparison: when to use each method

In the present work we use both the matrix-kernel and the Fox-Li methods. The first one is very powerful, and converges rapidly even when the eigenvalues are closely spaced (well confined modes). It allows to extract the lowest N modes and eigenvalues at the same time, its accuracy is determined by the size N of the matrix. And as shown above this method can be extended to analyze resonators with arbitrary phase and amplitude functions placed anywhere inside the optical resonator. The Fox-Li approach allows to calculate the lowest order mode only. And when the loss discrimination among modes is weak it requires a large number of iterations, and often in such a case, it does not converge. However, this approach is very useful and still widely used, because it is very close to the real physical situation in an optical resonator. Moreover, it is very practical when analyzing the behavior of unstable perturbed resonators, because it allows to observe the field evolution after each round trip, rather than giving just the final result.

1.3.5.5 Some practical mode calculation examples

In the following examples we are interested in a plano-concave optical resonator, we used an in-house eigenmode solver¹ based on the matrix method described above to calculate the modes of the 2D resonator illustrated schematically in Fig 1.10b, this resonator has $g_1 = 1, g_2 = 0.4$. In Fig 1.10a we plot the calculated fractional power loss per round trip for the lowest four modes of this cavity as a function of the Fresnel number $Nf = a^2/(\lambda L_c)$. This parameter is approximately equal to the number of Fresnel zones seen on one mirror from the center of the other mirror. The first thing we can notice, is that the greater Nf , the lower the power loss, which is easy to understand, because high Nf means well confined modes (large mirror diameters or small resonator length). This figure also allows us to predict, the mode selection behavior of the laser. If we take a practical example of a high finesse laser resonator where the transmission loss $t \simeq 1\%$, and the active medium can provide a gain of 2% per round trip, we can plot a horizontal line to divide the plot in Fig 1.10a into two regions: an upper one (Power loss $> 1\%$) where laser operation is not possible, because the available gain is not sufficient to compensate the total losses in the resonator. And a lower zone where laser operation is possible. For example the LG_{00} falls below 1% when $Nf > 1.7$, and LG_{01} when $Nf > 2.4$ which corresponds to mirror diameters of 100 μm and 120 μm , respectively, for $L_c = 6\text{mm}$. Thus, when $1.7 < Nf < 2.4$ only the fundamental mode can reach the threshold, the cavity is then intrinsically single mode. This strong mode discrimination can be achieved in practice by using an aperture with variable diameter to control the Nf of the resonator. For high Nf values, several modes see their power loss reduced below 1%, and the eigenvalues become closely spaced. In this case the mode selection cannot be achieved by the threshold condition, but by means of mode competition

¹The developed solver is provided as an open-source python package that can be downloaded from the following link: <http://seghil.github.io/OpenCavity/index.html>.

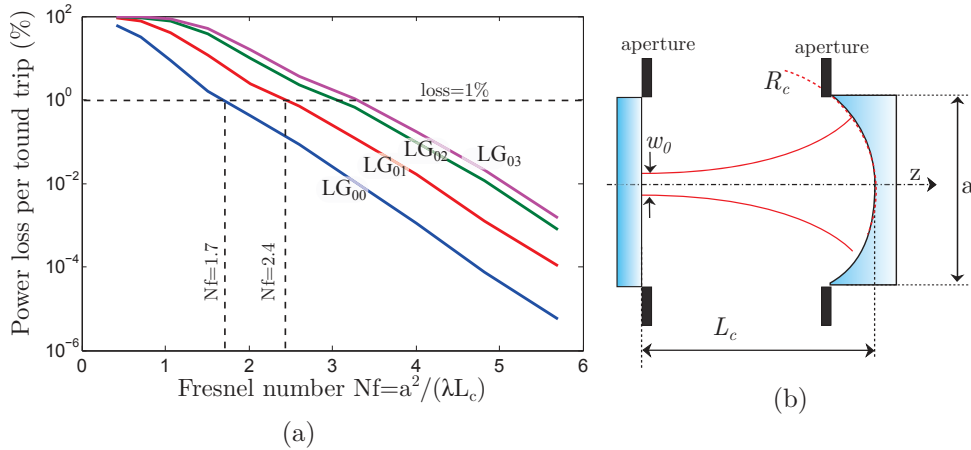


Figure 1.10: (a) Round trip loss of first modes of the double aperture cavity shown in (b). (b) Double aperture limited plano-concave optical cavity.

in the laser medium. This is a more complex dynamic process which depends on the gain medium properties, the power loss and the intensity pattern of the modes, we will address this process in sec 1.6.

In Fig 1.11, we performed the same mode calculation, but this time we used an amplitude mask to introduce an opaque disk with a radius ($a_d = 4 \mu\text{m}$) located at the flat mirror center. The goal of this configuration is to change the natural order of appearance of the modes. This is shown in Fig 1.11a, this time the lowest mode is the LG_{01} rather than the LG_{00} which has dropped to the last place with very high power loss. This is an example of how to prevent the selection of the fundamental mode and favor another higher order one, because this change in the mode configuration, greatly influences the mode competition process.

1.4 Polarization modes of a passive cavity

1.4.1 Polarization of plane waves

The polarization state of a beam is completely characterized by its electric field vector. In the case of plane waves, this vector lies in the transverse plane and can be written as a combination of two mutually independent components.

$$\begin{aligned} E_x &= A_x \exp(-kz + \phi_x) \\ E_y &= A_y \exp(-kz + \phi_y) \end{aligned} \quad (1.41)$$

The polarization state of the electric field depends on the phase difference $\Delta\phi = \phi_x - \phi_y$ between the two components. The electric field vector oscillates linearly along one direction at an angle ψ with respect to the x-axis, when the two components are either in phase ($\Delta\phi = 0$) or have opposite signs ($\Delta\phi = \pi$). The light is circularly polarized when $\Delta\phi = \pm\pi/2$, in this case vector field describes a circle as the time evolves. If we look in the direction of propagation, the field rotates in clockwise

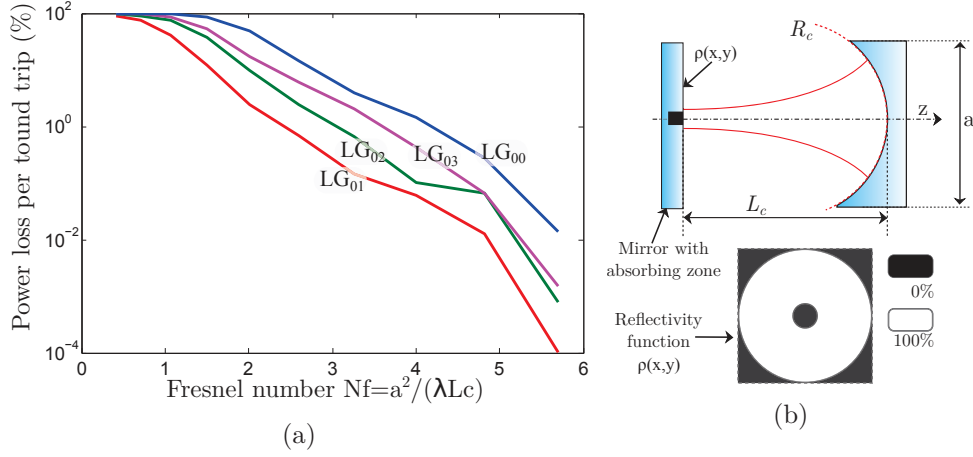


Figure 1.11: (a) Round trip loss of first modes of the double aperture cavity shown in (b). (b) Double aperture limited plano-concave optical cavity plus an absorber placed at the plane mirror's center.

direction (right handed) for $(\Delta\phi = +\pi/2)$ and in counterclockwise direction for $(\Delta\phi = -\pi/2)$. For any other phase difference value the polarization of the light is elliptical.

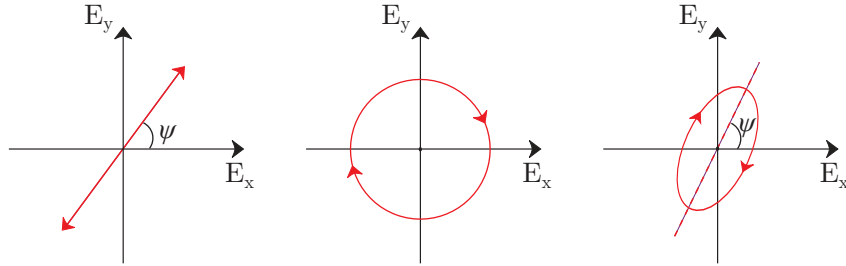


Figure 1.12: Different polarization states, from the left to the right: linear, circular and elliptical.

1.4.2 Polarization representation tools

1.4.2.1 Jones matrices formalism

The two complex amplitudes can be expressed as a column vector, called Jones vector [Yariv 2007]:

$$J = \begin{pmatrix} A_x \exp(j\phi_x) \\ A_y \exp(j\phi_y) \end{pmatrix} \quad (1.42)$$

We usually use the normalized Jones vector representation. If we put

$$\chi = \exp(j\Delta\phi) \tan(\psi) = \frac{A_x}{A_y} \exp(j\phi_y - j\phi_x) \quad (1.43)$$

with ψ defined between 0 and 2π , the Jones vector can be then written in the following form:

$$J(\psi, \Delta\phi) = \begin{pmatrix} \cos(\psi) \\ \exp(j\Delta\phi) \sin(\psi) \end{pmatrix} \quad (1.44)$$

A Jones vector can be propagated through a sequence polarizing optics (polarizers, birefringent media, Brewster plates and Faraday rotator... etc.) using a powerful matrix technique known as the Jones matrix method. The principle of this method is similar to the one of ABCD matrices: the polarization state out of an optical system is obtained from the matrix product of the input Jones vector, and a 2×2 Jones matrix representing the optical system.

$$\begin{pmatrix} J_1^{out} \\ J_2^{out} \end{pmatrix} = \begin{pmatrix} Mj_{11} & Mj_{12} \\ Mj_{21} & Mj_{22} \end{pmatrix} \begin{pmatrix} J_1^{in} \\ J_2^{in} \end{pmatrix} \quad (1.45)$$

1.4.2.2 Stokes parameters

By definition a monochromatic wave must be polarized, however in practice laser light is quasi-monochromatic. Such a wave can still be described by 1.41 but can be partially polarized, because the field vectors can change their orientation randomly and in a short time compared to the detection time. To describe the polarization state of this type of light we usually use the Stokes parameters given by the time average quantities:

$$\begin{aligned} S_0 &= \langle A_x^2 + A_y^2 \rangle \\ S_1 &= \langle A_x^2 - A_y^2 \rangle \\ S_2 &= \langle A_x A_y \cos(\Delta\phi) \rangle \\ S_3 &= \langle A_x A_y \sin(\Delta\phi) \rangle \end{aligned} \quad (1.46)$$

were the averages are performed over the detection time. The Stokes parameters are usually normalized such that $S_0 = 1$, thus the three other parameters lies between -1 and 1. Although these parameters were initially introduced to describe partially polarized light, they can be used to describe the polarization states of polarized light. The Stokes parameters for a polarized light with a complex representation given in Eq 1.44 are given by:

$$\begin{aligned} S_0 &= 1 \\ S_1 &= \cos(2\psi) \\ S_2 &= \sin(2\psi) \cos(\Delta\phi) \\ S_3 &= \sin(2\psi) \sin(\Delta\phi) \end{aligned} \quad (1.47)$$

The parameter S_1 describes the linear polarization along x or y axis, $S_1 = 1, -1$ corresponds to a complete polarization in these directions, respectively. In a similar

manner $S_2 = \pm 1$ describes the linear polarization along directions at angles of ± 45 deg to the x axis. And S_3 represents the degree of circular polarization, $S_3 = 1$ means that the light is completely circularly polarized, with right handedness when $S_3 = +1$ and left handedness when $S_3 = -1$

1.4.3 Polarization eigenstates of an optical resonator

Polarization eigenstates of an optical resonator are polarization states that remain unchanged after one round trip. When an optical resonator contains only highly reflective mirrors, any arbitrary polarization state can reproduce itself in a round trip. Because highly reflective mirrors generally does not influence the polarization properties of the beam. However, when polarizing elements are introduced, one must determine the Jones matrix of one round trip in the resonator, and the eigenstates are given by the two eigenvectors of this matrix. If we denote these eigenvectors as Jp , and the Jones matrix of the resonator as Mj_r we can write:

$$\mu p Jp = Mj_r Jp \quad (1.48)$$

where μp is the eigenvalue associated with the eigenstate Jp . As in spatial modes $1 - |\mu p|^2$ represents the power fractional loss due to polarizing optics experienced by the eigenmode in one round trip. For a given Jones matrix Mj :

$$Mj_r = \begin{pmatrix} m_{11} & m_{12} \\ m_{21} & m_{22} \end{pmatrix} \quad (1.49)$$

The characteristic polynomial of this 2 matrix is quadratic, thus its eigenvalues can be expressed in terms of the matrix elements as follows [Golub 1996, Hodgson 1997]:

$$\mu p_{1,2} = \frac{m_{11} + m_{22}}{2} \pm \sqrt{\left(\frac{m_{11} - m_{22}}{2}\right)^2 + m_{12}m_{21}} \quad (1.50)$$

and the corresponding eigenvectors as follows:

$$Jp_i = \begin{pmatrix} 1 \\ \frac{\mu p_i - m_{11}}{m_{12}} \end{pmatrix} ; \quad i = 1, 2 \quad \text{if } m_{12} \neq 0 \quad (1.51)$$

$$Jp_1 = \begin{pmatrix} 1 \\ 0 \end{pmatrix}, \quad Jp_2 = \begin{pmatrix} 0 \\ 1 \end{pmatrix} ; \quad i = 1, 2 \quad \text{if } m_{12} = 0 \quad (1.52)$$

1.4.4 Eigenstate calculation of some resonators of interest

To end with polarization modes, we give three practical examples of polarization eigenstates calculation in optical resonators with polarizing optics. The first one is a resonator containing a linear loss dichroism, this case can occur in resonators with Brewster window, a Bragg cell, or alternatively gain dichroism. The second

one is a resonator with circular birefringence, which is usually obtained by placing a Faraday rotator inside the cavity. And in the last example, we will determine the eigenmodes of a cavity with linear birefringence. These practical examples are of particular interest to us, because they represent practical cases that we will encounter in chapter 5 when studying the polarization properties of VeCSELs.

1.4.4.1 A resonator with linear dichroism

As a practical example we consider a resonator with a Brewster plate. This resonator is obtained by placing a dielectric plate with an index of refraction n_p arranged at the Brewster angle $\theta_B = \text{atan}(n_p/n_{air})$, with the surface normal in the $y - z$ plane as shown in Fig 1.13.

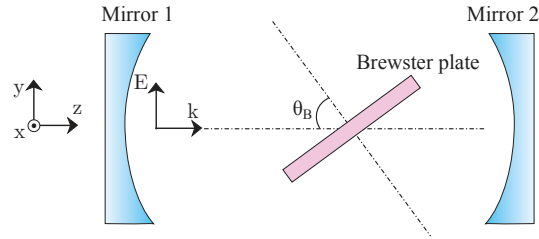


Figure 1.13: Optical resonator with Brewster plate.

In this configuration, light polarized along y axis passes the plate without loss, and the field component polarized in the perpendicular direction (along x -axis) experiences a fractional amplitude reduction of $t_p = 2n_p/(n_p^2 + 1)$. Using the Jones matrix of a Brewster plate (see Appendix A), we can write the round trip Jones matrix of this resonator as:

$$M_{J_r} = \begin{pmatrix} \left[\frac{2n_p}{n_p^2 + 1} \right]^4 & 0 \\ 0 & 1 \end{pmatrix} \quad (1.53)$$

Using equations 1.50 – 1.52 the eigenvectors and eigenvalues of this resonator are:

$$\begin{aligned} Jp_1 &= \begin{pmatrix} 1 \\ 0 \end{pmatrix}, & \mu p_1 &= \left(\frac{2n_p}{n_p^2 + 1} \right)^4 \\ Jp_2 &= \begin{pmatrix} 0 \\ 1 \end{pmatrix}, & \mu p_2 &= 1 \end{aligned} \quad (1.54)$$

These polarization eigenstates are linear along the x and y axis. The first one exhibits a round trip loss of $1 - \left[2n_p/(n_p^2 + 1) \right]^8$. And the second one has no loss. It is important to note that a polarized laser beam can only be generated if the loss for one polarization eigenstate is lower than that for the other one. In this case the polarization with the lowest losses is preferred (see section 1.6.4). This is commonly referred to as dichroism, however, we note that for simplicity, we also call a laser resonator with two polarization states experiencing a different optical gain as a gain

dichroism. The resonator discussed here will allow us (in sec 5.2.1) to measure the gain dichroism between the crystal axis of semiconductor quantum wells structure. We will use a plate made of CaF_2 which has at our working wavelength (1 μm) a refractive index $n_p \simeq 1.43$. Thus, by using this plate as a Brewster window, one polarization mode experiences no loss while the orthogonal one experience round trip loss of the order 40%.

1.4.4.2 A resonator with circular birefringence

This case is merely obtained by placing a Faraday rotator inside a resonator. As we did above, using Jones matrix for rotation (see Appendix A we can write the round trip Jones matrix of this resonator as:

$$M_{j_r} = \begin{pmatrix} \cos(\beta)^2 - \sin(\beta)^2 & -2 \cos(\beta) \sin(\beta) \\ 2 \cos(\beta) \sin(\beta) & \cos(\beta)^2 - \sin(\beta)^2 \end{pmatrix} \quad (1.55)$$

Where β is the rotation angle of the Faraday rotator. The eigenvectors and eigenvalues are:

$$\mu_{p_{1,2}} = \cos(\beta)^2 - \sin(\beta)^2 \pm j2 \cos(\beta) \sin(\beta) \quad (1.56)$$

and

$$J_{p_1} = \begin{pmatrix} 1 \\ j \end{pmatrix}; \quad J_{p_2} = \begin{pmatrix} 1 \\ -j \end{pmatrix} \quad (1.57)$$

These are two circularly polarized eigenstates with a fractional power loss $1 - |\mu_p|^2$ that can be written using trigonometry rules as:

$$loss_{1,2} = 1 - |(\cos(2\beta) \pm j \sin(2\beta))|^2 = 1 - |\exp(\pm 2j\beta)| = 0. \quad (1.58)$$

Indeed, this resonator has left and right circularly polarized eigenstates presenting null round-trip loss. We will use this resonator in Sec 5.4.1 were we address the circularly polarized laser.

1.4.4.3 A resonator with linear birefringence

This case can be obtained by inserting a birefringence element (such as a wave-plate inside a resonator (see Fig 1.14). It is also the case of lasers using a gain medium with a crystalline structure, because most of crystals present a natural birefringence. And as we will see in Chap 5, VeCSELs gain structures also present an intrinsic birefringence. The Jones matrix of a resonator with linear birefringence is given as (see Appendix A):

$$M_{j_r}(\alpha) = \begin{pmatrix} \cos(\alpha)^2 + \exp(j\delta\phi) \sin(\alpha)^2 & \sin(\alpha) \cos(\alpha) [1 - \exp(j\delta\phi)] \\ \sin(\alpha) \cos(\alpha) [1 - \exp(j\delta\phi)] & \sin(\alpha)^2 + \exp(j\delta\phi) \cos(\alpha)^2 \end{pmatrix} \quad (1.59)$$

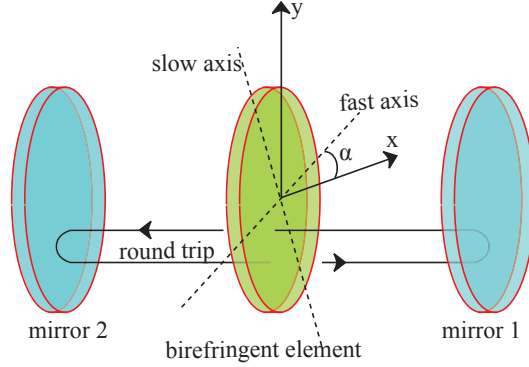


Figure 1.14: Optical resonator with a birefringent element.

where $\delta\phi$ is the phase difference between the fast and the slow axis of the birefringent element. And α is the orientation of the element with respect to the reference axis. The eigenvalues and eigenvectors of this matrix are:

$$\begin{aligned} Jp_1 &= \begin{pmatrix} \cos(\alpha) \\ \sin(\alpha) \end{pmatrix}, & \mu p_1 &= 1 \\ Jp_2 &= \begin{pmatrix} -\sin(\alpha) \\ \cos(\alpha) \end{pmatrix}, & \mu p_2 &= 1 \end{aligned} \quad (1.60)$$

The eigenstates are linear polarization oriented along the two axis of the birefringent element. And both the eigenvalues have a module equals to 1 because the birefringent element do not introduce any loss. This example shows that the introduction of a birefringence inside a laser cavity defines two linear polarization eigenmodes oriented parallel to the ordinary and the extraordinary axis, regardless of the birefringence value.

1.5 Laser dynamics and mode selection

1.5.1 Class of lasers

Laser dynamics treats the interaction between the intracavity electromagnetic field $\vec{\mathcal{E}}(\vec{r}, t)$, and the atoms of the active medium. The electric field in the gain medium generates through the active atoms population $N(t)$, a macroscopic polarization $\vec{\mathcal{P}}(\vec{r}, t)$. The medium polarization acts in turn as a source for the electromagnetic oscillations. This mutual influence will determine the spatial, temporal, spectral and polarization properties of the laser emission.

In what follows we assume that the slowly varying amplitude and the rotating wave approximations are valid, and that all the equations are given for large photon number [Haken 1985]. Thus, we will be interested in studying the evolution of the envelope and the spatial pattern: $E_n(t)$, $u_n(r, \theta)$ respectively. Within this context, laser dynamics is described by a system of nonlinear equations called the Maxwell-Bloch equations, where the light field is treated as a classical electro-magnetic field

which obeys to Maxwell's equations, and the motions of the electrons in the matter are described using a quantum mechanical treatment (Bloch equations). This system of equations describes the time evolution and the coupling between the E-field, the polarization of the medium and the population inversion. To complete the semi-classical physical model, one needs to inject the Langevin noise sources $F_{n,p}$ in order to take into account of the fundamental stochastic nature of spontaneous emission events (for N and \vec{P}) [Mandel 1995]. The fundamental thermal noise source for the E-field is thus negligible in the optical domain.

The dynamic behavior is governed by the relaxation processes of these three quantities, to which three relaxation rates are associated: respectively, the resonator mode photon decay rate γ_c , the atomic polarization relaxation rate γ_\perp , and the population inversion relaxation rate γ_e . According to how γ_c compares to the two material relaxation rates, four dynamical classes are defined [Khanin 1995]:

- Class A: $\gamma_c \ll \gamma_e, \gamma_\perp$ (1 degree of freedom)
The laser medium follows without delay the field variations inside the resonator. Material variables can be adiabatically eliminated from the equations. The turn-on transient is aperiodic and the laser has no relaxation oscillation. We find in this family VCSELs with long cavity ($> mm$), atomic gas lasers and dye lasers.
- Class B: $\gamma_e \ll \gamma_c \ll \gamma_\perp$ (2 degrees of freedom)
Only the atomic polarization follows the field without delay and can be eliminated from the equations. The system has thus two degrees of freedom and presents a resonance frequency, and the transient can be oscillatory. This is the most common class of lasers, it comprises solid state lasers, short cavity VCSELs ($< mm$), monolithic VCSELs, edge emitting laser diodes, and molecular gas lasers.
- Class C: $\gamma_c \sim \gamma_\perp$ (3 degrees of freedom)
In this class, no variable can be eliminated and the dynamics of such a system can be very complex and sometimes chaotic.
- Class D: $\gamma_c \gg \gamma_e, \gamma_\perp$ (2 degrees of freedom)
This class is an exotic one that concerns only some types of MASERS, where the field follows the medium variations and can be eliminated from the equations.

1.5.2 The laser rate equations

Rate equations in photon number are purely classical equations that can be derived from the semi-classical Maxwell-Bloch theory or heuristically, and in which, the process of light-matter interaction is restricted to stimulated emission and absorption/loss. In what follows we consider the case of class-A,B lasers operating on a single longitudinal, transverse, and polarization modes at high photon number.

Thus, in their simplest form the rate equations reads:

$$\begin{aligned}\frac{dn}{dt} &= BN(\mathcal{N} + \xi) - \gamma_c n_p \\ \frac{dN}{dt} &= \rho - \gamma_e N - BNn_p\end{aligned}\tag{1.61}$$

where n_p is the intracavity photon number in the oscillating mode, and N is the population inversion. B is Einstein coefficient for stimulated emission, ξ is the spontaneous emission factor¹ (unity for four level systems [Mandel 1995]), and ρ is the pumping rate. The steady state photon number $n_{p_{ss}}$ of Eq 1.61 is given by:

$$n_{p_{ss}} = \frac{\rho}{N_{th}} - \frac{\gamma_e}{B} = (\eta - 1) \frac{\gamma_e}{B}\tag{1.62}$$

where N_{th} is the population inversion at laser threshold, and η is the pumping rate above threshold. γ_e/B represents the saturation photon number I_{sat} .

In a semiconductor gain medium, the gain factor depends on N , this is usually approximated by a linear dependence. Furthermore, the gain variations are accompanied by variations in the refractive index of the material, as demonstrated by Henry [Henry 1982] and described by the following expression:

$$\alpha_h = -\frac{4\pi}{\lambda} \frac{dn_{sc}/dN}{dg/dN}\tag{1.63}$$

Photons can also be absorbed to generate an electron-hole pair when N is lower than the transparency carrier density N_{tr} .

In sum, in the case of semiconductor lasers we need to modify the rate equations given in Eq 1.61 to take account of the transparency effect (N_{tr}), and the phase-amplitude coupling effect (α_h). But in their form given above, the equations don't allow to take account of the phase. To resolve this, we write them this time using the evolution of complex electric field E oscillating in the cavity, and use a complex gain factor to take account of α_h . We also introduce the Langevin noise sources F_E , F_N that allow to take account of the random nature of carrier generation and photon density fluctuation due to spontaneous emission noise [Mandel 1995]. The rate equations take the following form:

$$\begin{aligned}\frac{dE}{dt} &= -\frac{\gamma_c}{2}E + \frac{B}{2}(1 - j\alpha_h)(N - N_{tr})E + F_E \\ \frac{dN}{dt} &= \rho - \gamma_e N - B(N - N_{tr})|E|^2 + F_N\end{aligned}\tag{1.64}$$

If we multiply the electric field equation by $2E$ and separate real and imaginary part of the field we obtain three equations describing the time evolution of the intensity

¹By adding the spontaneous emission factor ξ we count "one extra photon" in the laser mode, we note that this changes the threshold condition. The validity of this point is extensively discussed in [Siegmán 1986]

(photon number), the population inversion and the phase φ as follows:

$$\begin{aligned}\frac{dI}{dt} &= -\gamma_c I + B(N - N_{tr})(I + \xi) + F_I \\ \frac{dN}{dt} &= \rho - \gamma_e N - B(N - N_{tr})I + F_N \\ \frac{d\varphi}{dt} &= -\alpha_h \frac{B}{2}(N - N_{tr}) + F_\varphi\end{aligned}\tag{1.65}$$

These equations allow the treatment of several problems such as: laser condition, turn-on transient, relaxation oscillation and Q-switching. They can be extended to account for specific effects such as optical feedback [Lang 1980], and multi mode competition between simultaneously (or potentially) oscillating longitudinal, transverse or polarization modes, leading in the general case to a strongly multimode equation system with a large degree of freedom with possible irregular pulsing, chaotic state [Siegman 1986].

1.6 Mode competition

Rate equations can be extended to take account of more than one mode. In what follows, however, we will treat the case of pure intensity competition between two potential oscillating modes. We focus our attention on a class-A laser resonator with homogeneous gain medium, our goal is to illustrate the main physical ingredients involved in this process with a particular interest in VeCSEL-type laser cavities.

1.6.1 Qualitative treatment: Darwin survival of the fittest

The mode competition stems from the fact that all the modes of an optical cavity share the available population inversion (or gain), and thus will compete for it. Oscillation in one mode will generally reduce the available gain for other modes. Hermann Haken used the biological natural selection analogy in his book *Laser light dynamics* [Haken 1985] to explain this process: if we visualize the different photon kinds (modes) as animals, and the inversion of population as food which is continuously fed into the system. The kind of animal that has a better access to the food grows more quickly and can eat more food. The other kinds cannot compete in eating and eventually perish. If we follow this line of thinking, two different kinds can coexist if they live from separated resources of food. This separation may be due to the fact that each animal kind eat a different food type, or they eat the same food type but live in separate regions. With the laser, the coexistence can be achieved when the different modes don't share the same population inversion. This can happen, for example, in a laser where there are two spatial modes that don't overlap.

1.6.2 Quantitative treatment: the Lamb model

Quantitative treatment of mode competition can be performed using the Lamb model, which represents rate equations written for two oscillating modes in a class-A laser and, in the small-saturation approximation ($I < I_{sat}$), these equations are given by:

$$\begin{aligned} dI_1/dt &= (\alpha_1 - \beta_1 I_1 - \theta_{12} I_2)(I_1 + \xi) + F_{I1} \\ dI_2/dt &= (\alpha_2 - \beta_2 I_2 - \theta_{21} I_1)(I_2 + \xi) + F_{I2} \end{aligned} \quad (1.66)$$

where $\alpha_{1,2}$ represent the unsaturated gain minus loss (net gain) for each mode, θ_{12} and θ_{21} are called cross-saturation coefficients, whereas $\beta_{1,2}$ are the self-saturation coefficients. The four saturation coefficients depend on the inverse of the saturation intensity $I_{sat} = B/\gamma_e$, and the spatial overlaps of the modes with the gain medium and with each other. These coefficients can also contain beat terms representing the modulation of the population inversion at the frequency difference between the two modes, the beat terms can be neglected however, when the frequency difference is too high so that the population inversion cannot follow the variations [Siegman 1986]. In the three following subsections we will see how to use this model to describe some simple cases of longitudinal, polarization and transverse mode selection in a laser.

1.6.3 Longitudinal mode selection

To illustrate longitudinal mode selection by the laser we consider two longitudinal cavity modes and a semiconductor gain medium (*GaInAs* Quantum wells) having a homogeneous gain with a parabolic profile and a typical bandwidth $\Delta\nu_{gain} = 3$ THz (Fig 1.15a). We assume that the spatial patterns of the two modes are essentially identical in the gain medium. In this case all the spatial overlap terms in the cross- and self-saturation coefficients are identical. The only difference between the two modes is due to the gain curvature, which translates into different net-gains. The mode with larger net-gain will, obviously, reach the threshold first and saturates the population inversion, which reduces the available gain for the second mode as shown in Fig 1.15b. In this case the side mode suppression ration (SMSR) for the mode number q from the central laser frequency is approximated using a simple analytical expression:

$$SMSR_q \simeq 10 \log \left[\frac{q^2 P_{out}}{Q^2 \xi \gamma_c h \nu} \right] \quad (1.67)$$

where Q denotes the number of modes in the gain curve (HWHM). For a typical VeCSEL with 5mm long cavity and an output coupler transmission $T_{oc} = 1\%$ one obtains $SMSR = 45dB$.

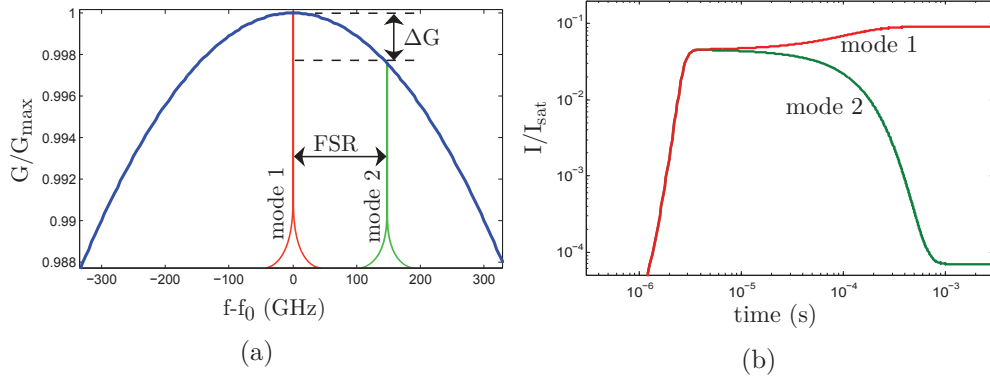


Figure 1.15: (a) Calculated parabolic gain profile of quantum well based gain medium with gain bandwidth=3 THz, and two successive longitudinal modes of 1 mm length resonator. (b) Time evolution of the two longitudinal modes intensity, for pump rate $\eta = 1.1$.

1.6.4 Polarization mode selection

A similar selection process occurs with polarization modes in VeCSELs. Indeed, the semiconductor gain structures in VeCSELs have an intrinsic birefringence with the slow and fast axis oriented along the $[110]$ and $[1\bar{1}0]$ semiconductor crystal axis. We have seen in section 1.4.4.3 that such a cavity has two linear polarization eigenstates oriented along the birefringence axis. Furthermore, the quantum wells' gain along the $[110]$ axis is slightly higher than the gain along $[1\bar{1}0]$ axis ($\frac{\Delta G}{G} \sim 10\%$). This gives rise to a mode competition situation similar to the one we obtained with the longitudinal modes (see Fig 1.16), thus the mode with higher net-gain (linear along $[110]$) wins the competition.

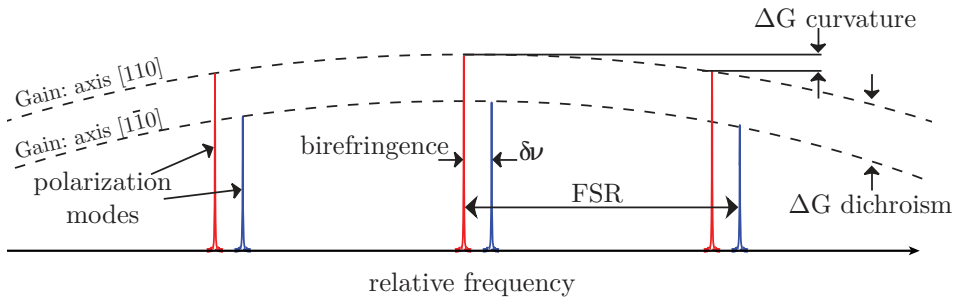


Figure 1.16: Illustration of the gain dichroism between the $[110]$ and the $[1\bar{1}0]$ axis of a semiconductor VeCSEL gain structure.

The polarization extinction ratio (PER) can also be approximated by:

$$PER \simeq 10 \log \left[\frac{P_{out} \lambda \Delta G}{hc \gamma_c \xi G} \right] \quad (1.68)$$

With the previous VeCSEL example, for $\Delta G/G \sim 10\%$ and $P_{out} \simeq 20mW$ one obtains $PER \simeq 80dB$

1.6.5 Transverse mode selection

In case of transverse mode competition, the frequency difference between the modes (Gouy shift) is smaller than the FSR, thus the gain curvature is usually negligible. The important parameters one must take into account are the loss and the spatial intensity pattern of each mode, these two parameters are defined by the resonator theory presented earlier (Sec 1.3.5). One could also to a certain extent create a gain difference between the modes, by means of the overlap between the active zone (pumped) and the modes patterns, indeed the modal gain of each mode is proportional to the overlap integral. The gain/loss -based selection methods are

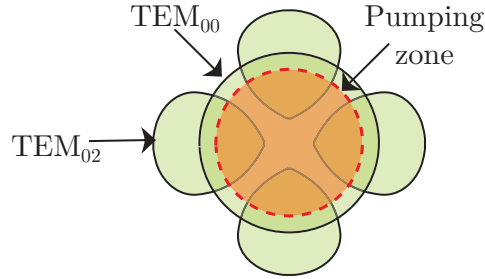


Figure 1.17: Illustration of the optimization of overlap between the mode and the active zone, in this example TEM_{00} mode has a better overlap and thus a higher modal gain.

usually used to obtain the fundamental mode by optimizing the overlap with the active zone (see Fig 1.17) or inserting an aperture. But here we discuss other effects, namely the non-linear self- and the cross-saturations due to modes patterns. For this purpose we consider a resonator with two potential oscillating modes, the LG_{01} and the LG_{01}^* shown in Fig 1.18.a and Fig 1.18.(b), respectively. The two modes have identical diffraction losses, and the same resonance frequency. The difference between them is that the second one is degenerate and thus has azimuthal intensity modulation known as a petal like intensity profile, whereas the first one has a more homogeneous intensity profile. This petal like pattern translates in a larger self-saturation coefficient. To derive the coefficient of Eq 1.66 we wrote the Maxwell-Bloch equations for dual transverse mode, class-A laser, with linearized saturation terms (see Appendix B) the obtained coefficients read:

$$\alpha_i = -\gamma_c + \gamma_c \eta \int_S |U_i|^2 ds \quad (1.69)$$

$$\theta_{12} = \theta_{21} = \gamma_c \frac{B}{\gamma_e} \eta \int_S |U_1|^2 |U_2|^2 ds \quad (1.70)$$

$$\beta_i = \gamma_c \frac{B}{\gamma_e} \eta \int_S |U_i|^4 ds \quad (1.71)$$

where U_i is the normalized transverse wave function of the mode 'i'. In Fig 1.18.c we plot the simulated time evolution of the two modes (LG_{01} and LG_{01}^*).

The simulation result show that, although the two modes have the same gain and loss factors, the mode with homogeneous distribution wins the competition, because it is the one that allows the most efficient use of the gain. The mode suppression ratio is again limited by spontaneous emission like for polarization and longitudinal modes, with a value for a typical TEM_{00} VeCSEL of more than 30 dB even close to threshold (low power) [Lacot 1996].

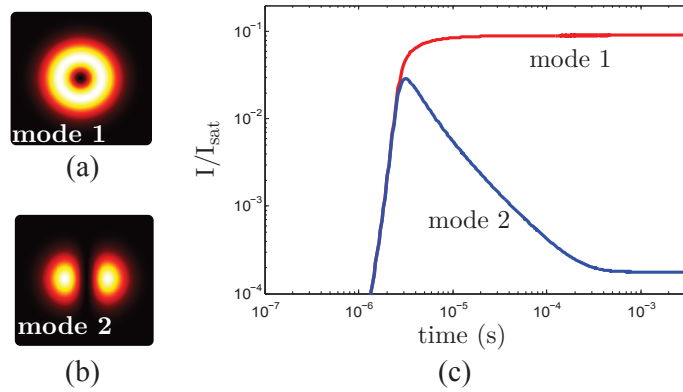


Figure 1.18: (a,b) LG_{01} , LG_{01}^* mode pattern. (c) Time evolution of the intensity of the two transverse modes. We considered a cavity with $\gamma_c = 2 \cdot 10^8$ for both modes, $\gamma_e = 3 \cdot 10^8$ and a pump rate $\eta = 10^{-1}$.

The key point we learn here is that, the laser always favors the mode with the more homogeneous intensity pattern, because it is the one that permits the most efficient use of the gain. One can have an intuitive feel for this process by using the analogy presented in Sec 1.6.1, because the most efficient way to use food that is continuously fed all over a given area (say a growing grass) is clearly not to cluster the animals in limited regions, but to homogeneously distribute them all over the area. This is an important point that we will discuss with more details using the more rigorous semi-classical approach (Maxwell-Bloch equations), because this selection principle will enable us to bring a solution to the unsolved problem of handedness control in LG_{0l} vortex modes. This is one of the main issues we will address in chapter 4.

1.7 Noise, coherence and mode purity

Now that we have seen how the laser mode builds up using temporal dynamics, we are interested in the fluctuation of the stationary state. Both of carrier and photon number of a given laser mode, present small fluctuations which are the result of several contributions commonly called noise sources, such as spontaneous emission noise and the pump induced noise. These fluctuations produce two types of noise: a phase noise, most commonly described using the spectrum density of frequency

noise $S_f(f)$, and an amplitude noise usually described using the relative intensity noise RIN defined as follows [Coldren 2012]:

$$RIN(f) = \frac{S_p(f) - 2h\nu\langle P_{out} \rangle}{\langle P_{out} \rangle^2} \quad (1.72)$$

Where $S_p(f)$ is the amplitude noise spectrum density, $\langle P_{out} \rangle$ is the average output power, and $2h\nu\langle P_{out} \rangle$ is the photons shot noise.

Both noises are fundamentally related to the addition of spontaneously emitted photons with random phase, to the quasi-coherent oscillating cavity mode. This effect is illustrated by the Henry phasor [Henry 1982] shown in Fig 1.19 where the coherent sum of photons with random phase gives rise to amplitude fluctuations and broadens the laser linewidth.

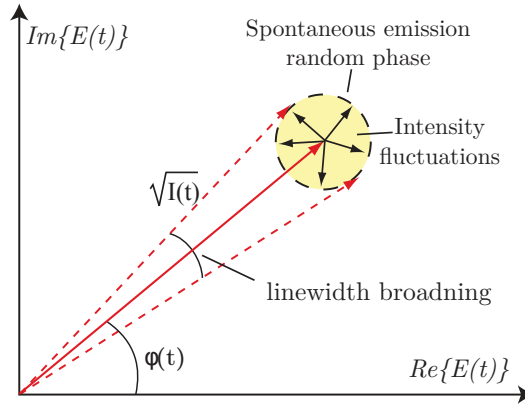


Figure 1.19: Henry phasor illustrating the effect of spontaneous emission random phase on the field amplitude fluctuations, and linewidth broadening (frequency fluctuations).

Furthermore, in semiconductor lasers, carrier density fluctuations also contribute to frequency noise, because both of the imaginary part (the gain) and the real part of the refractive index in semiconductors are affected by the carrier density, as described by the linewidth enhancement factor α_h in Eq 1.63. We note that other environmental noise sources such as thermal fluctuations, mechanical vibrations, pumping noise...etc. could contribute the total noise of the laser. The scheme in Fig 1.20 summarizes the interrelated noise sources in semiconductor lasers.

In order to describe the intensity and phase laser noises, one must determine their spectral densities of fluctuations. The noise sources can be considered as a modulation sources and introduced in the rate equations using the Langevin noise sources. The equations can be then written in the Fourier space and resolved in small signal regime (neglecting second order terms). The power spectral density of intensity noise and frequency noise can be deduced thanks to the autocorrelation functions of their respective Langevin noise sources.

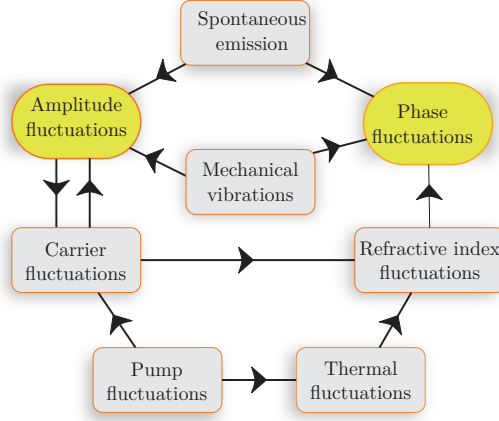


Figure 1.20: Interrelated noise sources in semiconductor lasers.

1.7.1 Relative noise intensity expression

In this section we will focus on noise expressions of class-A,-B lasers, and more particularly of VeCSELs which is the laser technology we adopted in the present work as we will see in more details in the following chapter. The RIN expression is given by [Laurain 2010a, Myara 2013]:

$$\begin{aligned}
 RIN(\Omega) &= \frac{4\xi\gamma_c}{\bar{I}} \left| \frac{j\Omega - \varsigma}{\Omega_r^2 - \Omega^2 - j\Omega\varsigma} \right|^2 + RIN_p \left| \frac{\varsigma\gamma_c}{\Omega_r^2 - \Omega^2 - j\Omega\varsigma} \right| \\
 &= RIN_Q + RIN_p \times |H(\Omega)|^2
 \end{aligned} \tag{1.73}$$

where I is intracavity photon number, Ω_r represents the relaxation oscillations frequency of class-B lasers, and ς is the damping rate of this oscillations, given by:

$$\begin{aligned}
 \Omega_r^2 &= \gamma_c\gamma_e(\eta - 1) \\
 \varsigma &= \gamma_c\eta
 \end{aligned} \tag{1.74}$$

RIN_p is the pump induced noise, and $H(\Omega)$ is the laser transfer function, and RIN_Q is the quantum noise due to the random nature of spontaneous emission. In the laser bandwidth, the quantum noise can be written in the simple form [Laurain 2010a]:

$$RIN_Q = \frac{2hc}{\pi\lambda} \frac{1}{P_{out}} \xi \left(\frac{\eta}{\eta - 1} \right)^2 \tag{1.75}$$

Figure 1.21 shows the RIN spectrum with the different contributions according to Eq 1.73 using the typical parameters of a class-A VeCSEL.

The quantum noise of VeCSELs is relatively low (<170dB for an output power of the order of 10 mW) thus, the RIN in the laser bandwidth reproduces the pumping noise. And thanks to the relatively low cutoff frequency f_c , the noise spectrum shows a large spectral range (from $f_c \sim MHz$ to $ISL \sim 10 GHz$) with very low RIN limited by the noise. This latter is due to the screening process performed by the output coupler.

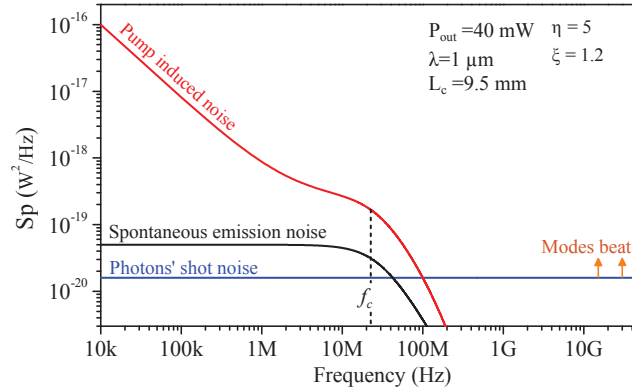


Figure 1.21: Theoretical RIN spectrum according to Eq 1.73 showing the contributions of the main noise sources in the case of VeCSELs. For the pump we considered a typical noise of a single mode optical pump diode.

1.7.2 Frequency noise expression

The expression of the frequency noise spectral density is given by [Laurain 2010a, Myara 2013]:

$$S_{FN}(\Omega) = \frac{\pi\xi\gamma_c}{I} \left(1 + \alpha_h^2 \left| \frac{\Omega_r^2}{\Omega_r^2 - \Omega^2 + j\Omega\varsigma} \right|^2 \right) + RIN_p \left| \frac{\alpha_h\gamma_c\varsigma\Omega}{4\pi(\varsigma\Omega + j\Omega^2 - \Omega_r^2)} \right|^2 + S_T(\Omega) + S_M(\Omega) \quad (1.76)$$

The first term of Eq 1.76 represents the fundamental limit due to spontaneous emission, this term can be simplified and gives the Schawlow-Townes-Henry linewidth limit defined at FWHM as follows:

$$\Delta\nu_{limit} = \frac{\pi h\nu(\Delta\nu_c)^2}{P_{out}} \xi(1 + \alpha_h^2) \quad (1.77)$$

Where $\Delta\nu_c$ is the cold cavity linewidth. The second term of Eq 1.76 corresponds to frequency fluctuations induced by the pumping noise via the α_h factor. The third term represents frequency fluctuations due to the thermal noise. This noise is mainly induced by temperature fluctuations caused by the pumping process, and depends on the thermal characteristics of the gain medium which are usually determined numerically. The last term represents mechanical noise source, which are usually difficult to describe theoretically. This technical noise is the dominant one in VeCSELs, as shown in Fig 1.15 where the main contributions are plotted in the case of a VeCSEL with the typical parameters shown in the inset.

From this figure, we can see that the frequency noise in VeCSELs can be divided into three main spectral regions of different dominant noise contributions. In the $10Hz - 1MHz$ interval, the noise is dominated by the thermal fluctuations originating from the pumping process. In the $[1MHz - f_c]$ range, the dominant source

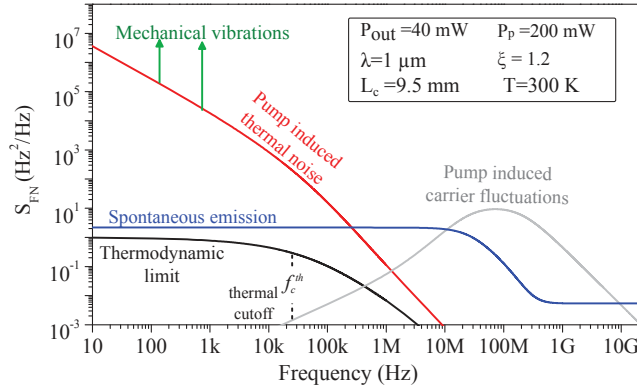


Figure 1.22: Theoretical frequency noise spectrum according to Eq 1.76 showing the contributions of the main noise sources in the case of VeCSELs.

is the spontaneous emission. And after the cutoff frequency we see the contribution of carrier fluctuations via the α_h factor, but this contribution is rapidly damped leaving place to the Schawlow-Townes limit at high frequencies. The Schawlow-Townes limit in VECESLs is of the order of $1Hz$, this limit can be considered with short observation time. However, for observation time ($> \sim 1ms$) one must take all the technical contributions into account.

1.7.3 Importance of noise characterization in laser applications

Characterizing the noise produced by the laser is an important step for several applications. For example, in optical telecommunications, for data rates lower than 10 Gbits/s a bit error rate of less than 10^{-9} is required, which requires a laser with a $RIN \sim -120dB/Hz$ [Coldren 2012]. The Opto-Microwave links also requires lasers with wide spectral range with flat RIN at shot-noise level [Baili 2008]. In sensing applications, the RIN determines the sensitivity limit, for example, in Chap 6 we will show rotational and translational velocity sensor based on VeCSEL with very high sensitivity of $10^{-15}Hz^{-1}$, and quantum limited capability of $10^{-17}Hz^{-1}$ thank to the low RIN of the laser. The frequency noise determines the coherence length of the laser light, this length defines the maximum achievable range of interferometric measurements. The typical values of frequency noise presented above translates into a coherence length of the order of $10km$ because of all the technical noise sources [Laurain 2010a]. However, the fundamental limit in VeCSELs is larger than $90\,000km$.

1.7.4 Noise measurement for eigenstates's purity characterization

The noise spectrum of a laser carries many additional information of great relevance for the purity analysis of laser eigenstates. Indeed, the mode that "loose" the competition don't disappear completely, this is well known in the case if longitudinal modes where the degree of extinction of between the "winner" and the residual

modes is described using the SMSR or the PER in with polarization modes, and one could obviously define an extinction ratio for transverse modes. The SMSR is usually measured using an optical spectrum analyzer, the PER with polarization filters and the spatial modes purity with beam profilers based on CCD cameras.

However, the problem arises when we want to measure these ratios in a highly coherent laser where the residual modes are very weak, because of apparatus limitations. For example, commercially available polarization filters allow to measure extinction ratios of the order of $20 - 25dB$. CCD cameras are limited by the pixel dynamic range with similar values, which limits the suppression ratio one can measure using an optical grating spectrometer (typical resolution limit FWHM few GHz).

Characterization of an eigenstate purity can be achieved using the noise spectra of the laser in two steps:

- Characterization of the state's coherence: it is the classical use of laser noise spectra, the goal here is to measure the intensity and the frequency noise of one state to determine its temporal coherence, by measuring the RIN and frequency noise in the RF domain with electronic apparatus.
- Characterization of the purity of the state: Here the goal is to determine quantitatively to what extent the selected mode is unique, by measuring an extinction ratio. This can be achieved using the RIN of the laser in the RF (radio frequency) domain using fast sensitive detector and RF spectrum analyzer (electronic apparatus). For example, the existence of more than one longitudinal mode in the laser cavity produces an optical beat note at the FSR, and when the residual mode is sufficiently weak, its power can be deduced from the measured beat peak. The same measurement can be achieved with transverse modes and polarization modes, provided that we find a way to mix the dominant and the suppressed modes which are in principle orthogonal. During this work, every time we build a laser generating a light state of interest, we will use the noise spectrum as a 'magnifying glass' to thoroughly study its purity, rather than just giving an intensity map in the case of transverse modes, or the Stokes parameters for polar modes. And as we do the measurements in the RF domain we benefit from several advantages over optical methods, mainly:
 - High resolution ($< 1Hz$).
 - High dynamic ranges (several decades).
 - High sensitivity (few photons).

As we shall see in Chap 4 and Chap 4 this technique will allow us to measure transverse and polarization modes extinction ratios superior than $70dB$.

1.8 Conclusion

In this chapter we have provided the theoretical framework required to tackle the main issue of this work: how to generate and control high purity, highly coherent unconventional laser-cavity eigenstates. This issue can be treated in two steps. In the first one the modes of the passive resonator (i.e. without the gain medium) are determined. Then in the second step, mode selection in the active resonator is described by means of laser dynamics, to determine the light-state after laser phase transition. It is important to note that this procedure can be used only with high-Q modes [Haken 1985].

We have addressed the first step by presenting a generalized resonator theory that allows to determine the following points:

- The stability of the resonator,
- The eigenstates (modes patterns) and eigenvalues (modes losses and resonance frequencies) of the resonator, including resonators with arbitrary transverse phase and amplitude masks.

We also presented the Jones matrices formalism to calculate the polarization eigenstates and eigenvalues of an optical resonator.

Then we have addressed the second step by presenting laser dynamics equations and mode competition. For the sake of simplicity, we preferred to start by the laser rate equations and extend them to intensity-only dual-mode competition Lamb model. A more rigorous approach would have been to start from the semi-classical Maxwell-Bloch model and derive mode competition equations from them. We will use this approach in chapter 4, because it allows to describe mode competition more rigorously, for example it allows to take account of the phase of the modes, mode beating, backscattering...etc. The presented intensity-only mode competition model, although simple, allowed us to determine the main parameters involved in mode selection:

- Gain and loss of the modes: mode with higher net-gain has a lower threshold, grows faster and is the most likely to be selected
- Self- and cross-saturation coefficients: they describe the gain saturation of each mode by its own intensity, and gain saturation of each mode by the intensity of the other one. We have seen that the laser always favors the mode with the most homogeneous intensity profile, because it is the one that makes the most efficient use of the gain.

At the end of each part we presented some practical examples of modes calculation and mode competition. These examples will be very useful for us, because they present practical situations that we will encounter in the forthcoming chapters, and thus, give the main physical ingredients required to deal with every situation.

The two following chapters are dedicated to the description of the laser technology we will use to achieve intracavity mode control: VeCSELs integrating phase and intensity masks, based on subwavelength metasurfaces and metallic layers, respectively.

A laser source for structured light generation: VECSELs

Vertical external cavity surface emitting lasers (VECSELs) is a relatively new semiconductor laser family first demonstrated in mid-90s [Kuznetsov 1999], it owes its existence to researchers efforts to overcome the limitations of the existing laser technologies: semiconductor lasers and solid-state lasers. The goal was to achieve a compact source generating laser emission at watt level or more, with circular high quality beam, and wide wavelength coverage. The problem researchers were facing is that each laser type excels in some of the laser properties, while exhibiting shortcomings in others. The most important of these properties are the output power; the emission wavelength; the spatial and temporal coherence; the device size; the pumping method and modulation capability. More recently, with the development of new applications some other exotic properties became of interest, such as the polarization properties, the mode control capability, ultra-short pulse, the orbital momentum of the beam... etc. In this part we present the existing laser families with their advantages and limitations. We end with VECSELs to show that they are a technology of choice for several demanding applications. Their unique advantages: power, coherence, compactness and great versatility make them a prime candidate for structured light generation.

2.1 Semiconductor lasers

In this laser family the active region is usually a quantum well formed by placing a layer of semiconductor material between two others having a higher energy gap to confine particles. When the layer thickness is comparable to the De Broglie wavelength of carrier [Zory 1993] the effects of quantum confinement take place leading to discrete energy levels of carriers in conduction and valence bands. The optical gain is obtained thanks to radiative recombination between these levels (inter-bands or inter sub-bands) through stimulated recombination mechanism. Semiconductor lasers are very compact, have good efficiency and wide range of emission wavelength coverage as summarized in Fig 2.1. Using GaAs, InP and GaSb semiconductor material systems, semiconductor lasers operating in CW at the ambient temperature can access 0.8 μm , 1.5 μm and 2.0 μm wavelength regions respectively. The accessible regions can be extended to 0.4 μm using GaN-based material systems and to 4.5-5 μm using PbTe and PbSe . Thanks to inter sub-band recombination in cascade lasers, emission wavelengths from 3 μm to THz domain can be

achieved [Williams 2005]. Beside these directly generated wavelengths, non-linear optical conversion has tremendously broadened the wavelength accessible range to 0.24 μm -0.65 μm ultraviolet and visible [Calvez 2009]. Semiconductor lasers family can be divided into two major laser types: edge emitting and surface emitting, both share the above-mentioned features that stem from the properties of semiconductor structures, but differ in other ones as we will see in the two following sections.

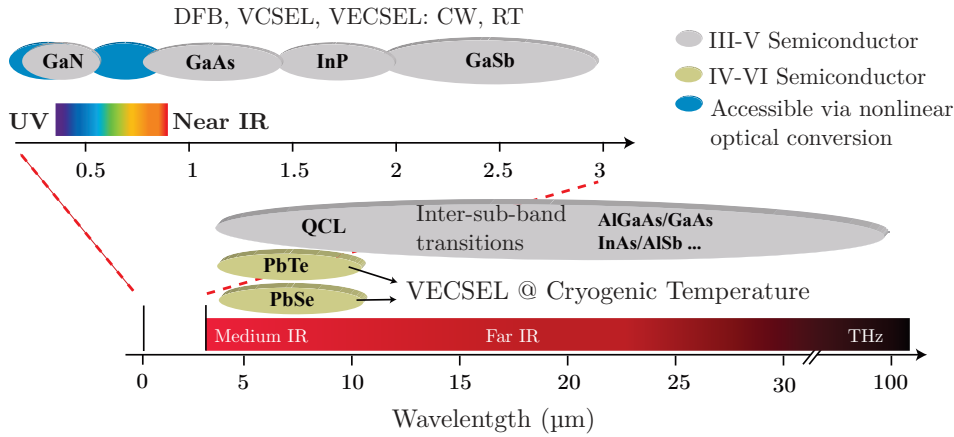


Figure 2.1: Spectral regions accessible by the main semiconductor material-systems used in semiconductor lasers.

2.1.1 Edge emitting semiconductor lasers

In edge emitting lasers the light is confined in the plane of the semiconductor chip using a waveguide (see Fig 2.2), the optical resonator can be formed by two mirror facets obtained by cleaving the wafer along the crystal planes. The resulting reflectivities are 30% due to the semiconductor-air interface. This is usually sufficient to reach the lasing threshold thanks to the high gain per pass (50%). The waveguide transverse dimensions are typically in the order of the wavelength to ensure single transverse mode operation. These lasers operate in multi longitudinal-mode regime, because of the long cavity (100 μm to few millimeters) and the large bandwidth of the optical gain. Thus a lot of non-linearly coupled longitudinal modes can exist within the gain bandwidth. Single frequency operation can be obtained by incorporating a wavelength selective diffraction grating coupled to the optical waveguide. The laser is then called DFB (Distributed Feedback) laser. DFB lasers can generate single frequency laser emission with SMSR>30 dB and a linewidth of the order of 1 MHz. The wavelength can be tuned using thermal or current effect to change the grating's index of refraction. These lasers are very widely used in applications that need single frequency operation, such as telecommunications at 1.55 μm and spectroscopy in the mid-infrared. However, Because of the waveguide geometry, these edge emitting sources generate highly astigmatic and asymmetric beams, that require sophisticated mode-converting optics in order to be manipulated, for example to be coupled into single-mode optical fibers.

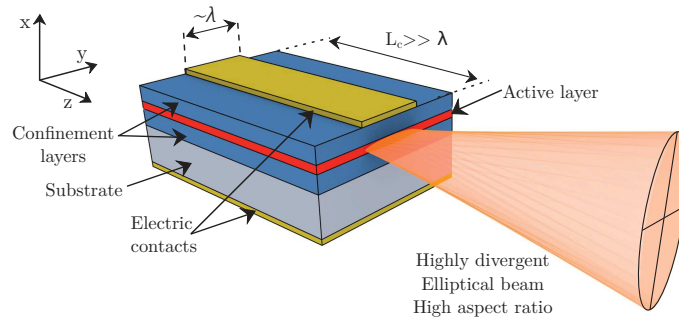


Figure 2.2: Schematic illustration of an edge-emitting laser. The laser cavity is in the substrate plane along the axial direction z and have a length L_c in the range 300-2000 μm .

The maximum output power of edge-emitting lasers in single mode behavior (longitudinal and transverse) is of the order of 100 mW at $\lambda = 980 \mu\text{m}$. Scaling up the output power to watt level raises many problems, the most important ones are: heat dissipation due to the high thermal impedance of the active strip; catastrophic optical damage of the mirror facets due to high optical density; and the filamentation phenomenon: parasitic waveguides created in the hot regions of the active strip (refractive index increased) which destroy the transverse mode profile. Overcoming these problems requires a wider waveguide with a larger area beams, this reduces the thermal impedance of the active strip and decreases the optical density. But the waveguide is then highly multi-mode and the beam is further elongated with very high aspect ratio.

2.1.2 Surface emitting lasers

In vertical cavity surface emitting lasers (VCSELs) the optical propagation (cavity axis) is normal to the substrate surface (see Fig 2.3) and the gain is provided by a set of quantum wells sandwiched in the optical cavity. The effective cavity length is very short (few microns) allowing the existence of one longitudinal mode within the gain spectral bandwidth. This cavity configuration limits the amplification zone to the thickness of the quantum wells, which results in low gain per pass of the order of few percents. Thus, in order to reach laser threshold high reflectivity mirrors close to 100 % are required, which is usually achieved using Bragg reflectors. These reflectors consist of epitaxially grown semiconductor layers having a thickness of a quarter wavelength and alternating high and low refractive index.

VCSELs have entirely replaced edge emitting laser diodes for use in multi-mode fiber-based data transmission applications, for the interconnection of various kinds of networks and computer clusters at several Gbit/s data transmission speed. This success arises from the combination of many properties, the most important are:

- Highly effective coupling to optical fibers thanks to circular beam profile with

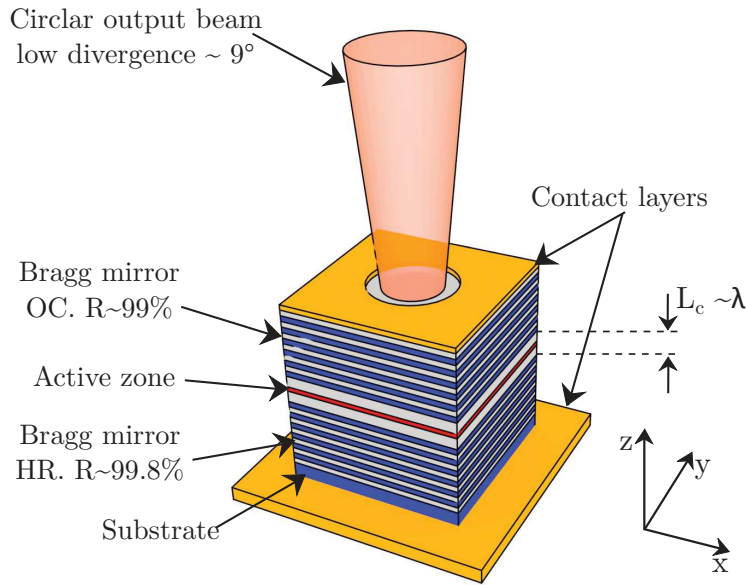


Figure 2.3: Schematic illustration of a VCSEL. The laser cavity is perpendicular to the substrate plane. The mirrors reflectivities are close to 100% and the cavity length $L_c \sim \lambda$.

small divergence angle. (this also simplifies the design of beam shaping optics)

- Very low threshold current in the order of 1 mA (reduced active zone)
- Very high reliability with projected lifetime of the order of 10 million hours at room temperature

These lasers can emit few milliwatts in single transverse mode operation with a linewidth comparable to that of DFBs (\sim few MHz). Single transverse mode operation limits the active zone diameter to few microns ($< 4 \mu\text{m}$) [Diehl 2000], however as in EEL this limits the output power because of the heat dissipation. Scaling up the output power demands larger active areas which raises two major problems: the laser operates then in multi-transverse mode regime and uniform current injection over large areas is difficult.

2.2 Solid state lasers

These lasers are based on solid state gain media, which consist of host crystals (YAG ($\text{Y}_3\text{Al}_5\text{O}_{12}$), YVO (YVO_4), Sapphire (Al_2O_3)...) or glasses (optical fibers), doped with rare earth ions (Nd^{3+} , Yb^{3+} , Ti^{3+} , Er^{3+} ...) or transition metal ions (Cr^{3+} , Ti^{3+} ...) usually called activators. The most used active media in solid state lasers are those having absorption bands in 800 nm and 940-980 nm spectral zones, such as Neodymium (Nd) and Ytterbium (Yb) doped media. This is due to the availability of adequate high power AlGaAs/GaAs and InGaAs/GaAs pump laser

diodes. The optical cavity in diode-pumped solid state lasers (DPSSLs) is usually formed by a dielectric concave output coupler and a flat mirror usually obtained by HR coating of one facet of the active medium (see Fig 2.4).

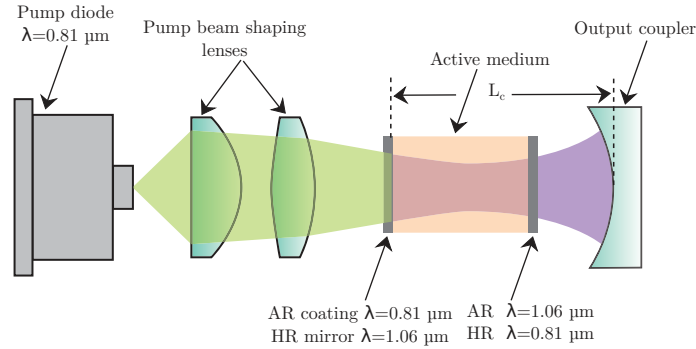


Figure 2.4: Schematic illustration of an Nd:YAG DPSSL with end pumping scheme. Adequate layers should be deposited on the end surfaces of the active material to ensure high transmission at the pump wavelength and low resonator losses at emission wavelength.

These lasers can achieve high output power, and the extended cavity permits high spatially coherent beams. Furthermore, the open cavity enables the use of functional intracavity elements such as frequency filters for single frequency operation, and polarizers or Brewster windows to control the polarization state. And more recently new elements have been used to control the intracavity light structure: phase plates, absorbers and spatial light modulators. However this laser family suffers from some shortcomings that come mainly from the gain medium. For example the emission wavelength is limited to discrete values of electronic transitions in ions such as 1064 nm of Nd:YAG, This leaves large inaccessible spectral regions, and also restricts the pumping wavelengths. The spectral width of the pump light absorption is usually very narrow, for example it is close to 1 nm in the very widely used Nd:YAG, thus accurate regulation and temperature stabilization of the pumping diode should be ensured for efficient pumping. Another shortcoming is the low absorption of active media, for example the material absorption $\alpha = 8 \text{ cm}^{-1}$ in Nd:YAG [Jankiewicz 2001], while in semiconductor structures the absorption is of the order of $10^4 \text{ cm}^{-1} = 1 \mu\text{m}^{-1}$ for pump photon energies above the band gap (this means that 86% of pump light is absorbed in 2 μm only). Because of low absorption in solid state media, a much thicker gain medium is required (100 – 300 μm) and multiple pump-beam passes, which requires a pump beam with good depth of field to absorb it along all the gain medium, and complex optics to handle the beam on multiple passes. Furthermore, thicker gain medium means stronger thermal effects, such as thermal lensing which deteriorates the beam quality. Overcoming these limitations results in cumbersome and costly laser systems unsuitable for integration, which is increasingly sought by researchers in both academia and industry.

2.3 VECSELs, lasers of choice

2.3.1 Power, Coherence and Functional versatility

The desire to generate high power laser emission with high quality beams and wide wavelength coverage, has led to the appearance of Vertical External Cavity Surface Emitting Lasers (VECSELs) [Kuznetsov 1999], which is a relatively new family that uniquely combines many of these desirable laser properties simultaneously. VECSELs can be pumped electrically or optically using a semiconductor laser-diode. They form a hybrid between traditional semiconductor and solid-state lasers, and can be viewed as solid-state lasers, where the gain medium, instead of the traditional active ions in a transparent host materials, uses band-gap-engineered semiconductor structures. Figure 2.5 shows a basic configuration of an optically pumped VECSEL.

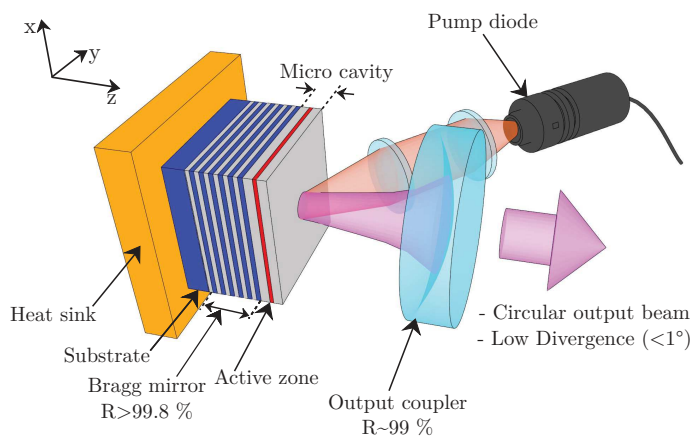


Figure 2.5: Schematic illustration of an optically pumped VECSEL. The cavity is formed by the Bragg mirror and dielectric concave mirror. As in monolithic VCSELs, the cavity is perpendicular to the plane of the active layer. The cavity length L_c is in mm-cm range.

It is based on a thin semiconductor gain structure in surface emitting configuration, in order to achieve symmetric and low divergence output beam. This gain structure usually called 1/2-VCSEL or gain mirror, consists of highly reflective Bragg mirror and multi-quantum-well active zone, both epitaxially grown on the same semiconductor chip. An anti-reflection coating is usually introduced to reduce the etalon effect, produced by the bottom Bragg mirror and the semiconductor-air interface on the top surface of the gain mirror. A concave mirror is used as an output coupler to form a stable (mm-cm) length optical cavity.

For high-power, good beam quality operation with wavelength versatility, optically pumped VECSELs have many significant advantages compared to both the traditional semiconductor laser diodes and solid-state lasers, and have become lasers of choice for a wide range of laser applications.

By using semiconductor gain structure, VECSELs take advantage of more than 40 years of compound semiconductor technology which allows to develop reliable

band-gap engineered multilayer structures. Such band-gap engineering allows VECSELs to access a wide emission wavelength range by design, and also to control the gap-energy of pump absorption layers. Thus VECSELs can access all wavelength ranges of compound semiconductor systems discussed in Sec 2.1. A further advantage of semiconductor gain structures is the availability of pump laser diodes, because any laser diode with photon energy higher than band-gap of the absorption layers can be used. Furthermore, thanks to the low thickness of semiconductor chip, thermal lensing and other beam phase profile distortions caused by thermally induced refractive index gradients are very weak. This results in a highly symmetric cavity, suitable for generation of modes with rotational symmetry such as vortex modes with high spatial coherence.

The Polarization state in optically pumped VECSELs is usually linear and stable, because of the gain dichroism and the birefringence, both naturally occur in the semiconductor structures.

The transverse modes in VECSELs are stabilized by the external cavity optics, which allows independent control of the mode size that can be matched to the pump spot by changing the cavity length. This allows to achieve multi-watt operation in the fundamental transverse mode [Laurain 2010b], using large mode size ($> 100 \mu\text{m}$). Because spatially wider higher-order modes experience larger diffraction losses, and higher excess loss from the unpumped regions. The external cavity also enables broad continuous wavelength tunability, by changing the cavity length [Laurain 2009].

In contrast with monolithic semiconductor lasers with lossy cavities and guided spontaneous emission, VECSELs with their high finesse cavities and thin gain medium, have very low spontaneous emission noise. Hence, laser emission with high temporal coherence (laser linewidth $\ll \text{MHz}$) can be generated.

The open cavity gives tremendous versatility to VECSEL device configurations and functions. For example it allows the insertion of saturable absorbers to achieve passive mode locking [Garnache 2002]; transparent intracavity heat spreaders in direct contact with the active zone [Alford 2002, Kim 2007]; intracavity absorption cells such as gas cells for laser absorption spectroscopy (ICLAS) [Garnache 2000, Garnache 1999a]. Thanks to the high finesse of VECSEL cavities, equivalent absorption length as long as 130 km has been achieved [Picqué 2003] with real absorption length of the order of 1 m. The external cavity also allows the insertion of non-linear optical crystals, for non-linear optical conversion of the output wavelength. For example, using second harmonic generation VECSELs can cover the whole visible spectrum range [Calvez 2009, Rautiainen 2007, Seelert 2005, Fallahi 2008, Raymond 1999], which is of great interest for bio-photonic, medicine and laser projection applications.

2.3.2 A prime candidate for structured light generation

Usually in most traditional laser applications (material processing, laser medicine, metrology...) one wants to obtain the low order fundamental beam with Gaussian

intensity profile and spherical wave-front. However, the increasingly growing interest in laser beams having complex phase and intensity structure (e.g. high order LG, HG, Bessel-Gauss beams....etc.) has led to several research works that address direct generation of such beams in a laser cavity. Generation of such states of light requires symmetric stable cavity inside which we place intensity/phase/polarization control elements. From the previous description of most used laser families two things become clear: first, monolithic semiconductor lasers are not suitable for this purpose. Second, thanks to the open cavity versatility both DPSSL and VECSELs meets these requirements and allow in principle structured light generation. Several works in the literature have been dedicated to this issue in DPSSL, as shown in the review article by Senatsky et al [Senatsky 2012] and other newer works [Ngcobo 2013, Kim 2013, Burger 2015]. However surprisingly enough, literature on generating such beams using VECSELs is very poor, despite the several advantages they offer over solid state lasers: in addition to those discussed earlier (wavelength coverage, power scaling, beam quality) other ones directly related to intracavity mode shaping capabilities are worth highlighting

- As in DPSSLs, the open cavity configuration in VECSELs enables introduction of functional element.
- The low thickness of the active medium ($\sim \lambda$) plus negligible thermal effects result in highly symmetric ideal optical cavity, that generates ideal states of light without any distortions.
- We also stress that the semiconductor structures allow to use integrated functional elements made in the same semiconductor material system, and can be grown in the same epitaxial growth step as the gain region itself. Which enables to achieve compact, auto-aligned, cost-effective and high quality elements, using a mature semiconductor technology

2.4 How to make a VECSEL: the building blocks

In this section we will go through the elements of a VECSEL to provide the necessary bases to understand how to design these laser sources, and their key properties. These elements are shown schematically in Fig 2.5, the VECSEL is formed by a concave mirror acting as an output coupler and the so-called gain mirror or 1/2-VCSEL, the two mirrors form a stable plane-concave optical cavity. Other cavity configurations can be used, such as V-shaped using two mirrors in addition the gain mirror (Fig 2.6(a)), or Z-shaped using three mirrors with the gain chip (Fig 2.6(b)). There are also other cavity arrangements where more than one gain chip are used, such as the five mirrors W-shaped cavity illustrated in (Fig 2.6(c)) . This arrangement allows to scale up the output power of the VECSEL. The output couplers used in VECSELs are usually commercially available dielectric mirrors, we therefore focus our attention on the description of the gain mirror, which

can be split into three main parts: the multi-quantum-well active zone; the highly reflective Bragg mirror, and the micro-cavity.

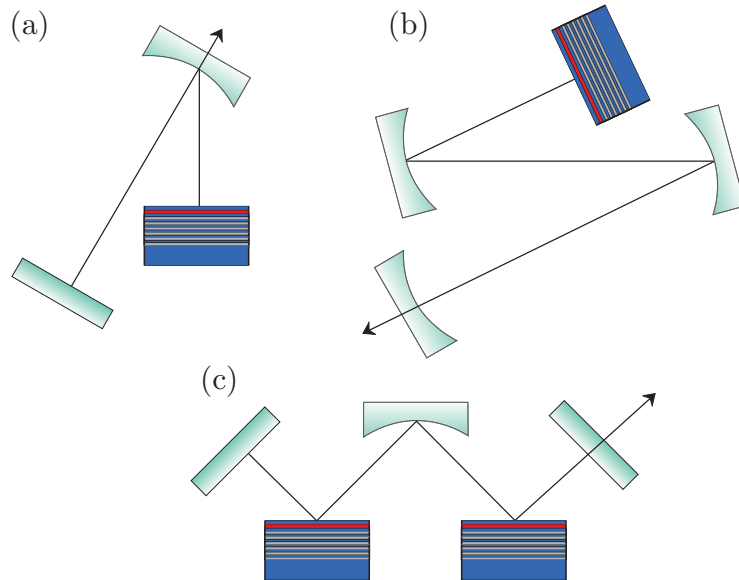


Figure 2.6: Examples of possible VECSEL cavities. (a) Three mirror V-shaped cavity. (b) Four mirror Z-shaped cavity. (d) W-shaped cavity with two gain chips.

2.4.1 The gain medium

The semiconductor gain chip is the main component of VECSELs, it is the part that ensures the amplification of light, which is a vital process for laser operation. In VECSELs as in any semiconductor laser, this gain structure can be made using different semiconductor material systems, with binary, ternary, quaternary and quinary alloys, allowing to cover different wavelength regions by changing the alloy composition, which modifies the properties of the alloy including the gap energy (Fig 2.7). This operation is usually called bandgap engineering. To make a good laser the semiconductor materials have to possess some properties, the most fundamental ones being:

- A direct gap in E-K space, which facilitates radiative transitions because the momentum is conserved in a vertical recombination (between electrons and holes having the same k).
- The semiconductor compounds must have the same crystal structure and nearly the same lattice constant, so that the alloys can be grown free of dislocations and defects that can inhibit a proper operation of the laser device.

Good quality crystals can also be grown with small lattice mismatch ($\Delta a/a$ 1%) [Coldren 2012], in this case the lattice of the deposited layer distorts to fit the lattice of the substrate, the layer is then strained (tensile or compressive). Strained

structures can show some interesting properties such as higher material gain, lower threshold and improved temperature dependence [Joachim 2003, Zory 1993]. However, the thickness of the deposited layer must not exceed the so-called critical thickness, above which the strain causes defects in the crystal [Matthews 1974]. But sometimes a thick strained multi-layered active zone is needed, in this case one should balance the strain by alternating between tensile and compressive stress to prevent dislocations.

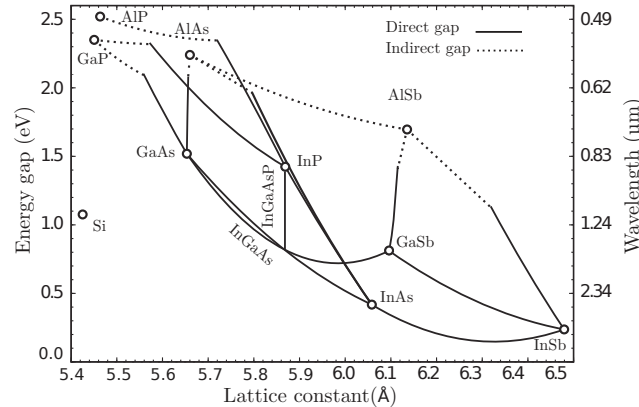


Figure 2.7: Energy gap vs. lattice constant of III-V semiconductor compounds materials at $T=0$ K.

In this PhD work, all the fabricated lasers contain a GaAs-based (GaAs/InGaAs) active zone, and emit at $\lambda = 1 \mu\text{m}$. We have chosen this material system because of its above-mentioned advantages, but clearly all the concepts developed within the framework of this thesis can be transposed to other material systems emitting at different wavelengths. We also use the strain balancing technique to maintain high crystal quality of the grown layers. In what follows we describe in more details the main elements of a VECSEL active zone, we start by describing the quantum wells, the optical gain, and also the pumping process. Then we describe how to optimize the quantum wells number and how to place them into the active zone in order to obtain optimal laser operation.

2.4.1.1 The quantum wells

A quantum well (QW) is obtained by embedding a planar semiconductor layer within two other layers of higher gap energy referred to as the barriers. This creates a potential well that 'traps' and confines carriers (Fig 2.8). Due to the low thickness of the quantum wells (<10 nm), the energy levels of both the conduction and the valence bands are quantized. Thus the emission wavelength is no longer set by the semiconductor band-gap alone, but rather it also depends on the well thickness, because the radiative transitions occur from the lowest quantized level of the conduction band to the highest quantized level of the valence band, and changing the well width changes these quantized levels. The transition energy can

be approximated by (Eq 2.1) [Zory 1993]:

$$E_c^n - E_v^n = E_g + \frac{1}{2m_r^*} \left(\frac{n\pi\hbar}{L_{QW}} \right)^2 \quad (2.1)$$

where $m_r^* = (1/m_e^* + 1/m_h^*)^{-1}$ is the reduced effective mass, related to electron effective mass m_e^* and hole effective mass m_h^* , and E_g is the gap-energy of the semiconductor material. There are two other important QW parameters one should optimize when designing the well, namely the inter sub-band spacing and the quantum-well depth. As a rule, the energy spacing between two sub-bands must be higher than the thermal energy k_bT ($=26$ meV at $T=300$ K) to prevent thermally populating energy levels with quantum number $n>1$ and thus ensure minimum transparency carrier density N_{tr} . And, barriers with high energy (deeper well) prevent thermal carrier leakage which reduces the thermal dependence of the threshold.

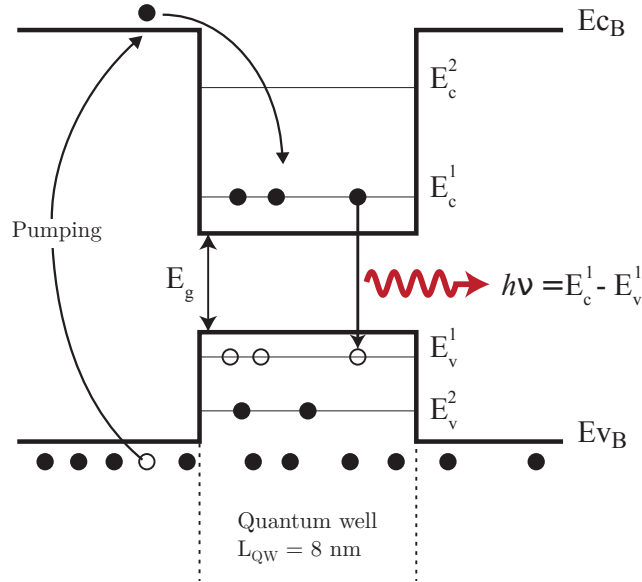


Figure 2.8: Schematic description of a quantum well optically pumped in the barriers. Full dots denote states occupied by electrons, whereas empty circles denote vacant states (holes).

2.4.1.2 The optical gain

The optical gain is defined as the growth ratio of light intensity (photon density) per unit length of light propagation, and is given in cm^{-1} . The gain is generated by stimulated recombination of an existing electron-hole pair, creating a second photon. The second photons exhibits the same wavelength and the same phase as the first one, doubling the amplitude of the monochromatic wave. Repetition of this process leads to a strong light amplification in the QW. The stimulated emission prevails when more electrons are present at the higher energy level (conduction

band E_c) than at the lower energy level (valence band E_v), and the optical gain is proportional to the probability that a given photon triggers a transition between these two bands. This leads to the simplified expression:

$$g = g_{max}(f_c - f_v) \quad (2.2)$$

where the maximum gain g_{max} is a property of the material ($g_{max} \lesssim 10^4 \text{ cm}^{-1}$ for 10 nm thick GaAs QW), f_c and f_v are the Fermi functions which give the probabilities that the energy levels E_c and E_v , respectively, are occupied by electrons, these functions are given as follows:

$$f_c = \frac{1}{1 + \exp\left(\frac{E_1 - E_{F_c}}{k_b T}\right)} \quad \text{and} \quad f_v = \frac{1}{1 + \exp\left(\frac{E_2 - E_{F_v}}{k_b T}\right)} \quad (2.3)$$

where $h\nu = E_1 - E_2$ is the energy of transition between high and low energy levels. The Fermi functions depend on carrier density N in the QW via the quasi-Fermi levels E_{F_c}, E_{F_v} . Assuming that only the first energy levels (E_c^1, E_v^1) participate in the gain process, E_{F_c}, E_{F_v} can be deduced from the carrier density as follows:

$$E_{F_c} = E_c^1 + k_b T \ln\left(e^{\frac{N}{N_{c,v}}} - 1\right) \quad \text{and} \quad E_{F_v} = E_v^1 - k_b T \ln\left(e^{\frac{N}{N_{c,v}}} - 1\right) \quad (2.4)$$

with

$$N_{c,v} = \frac{m_{c,v}^*}{\pi \hbar^2} k_b T \quad (2.5)$$

From the above description, it becomes clear that the gain of a semiconductor QW depends on the carrier density in the well and the radiative transition energy ($E_g = E_c - E_v$). Indeed, in the thermal equilibrium E_{f_c} and E_{f_v} are degenerate in the center of the energy-gap, the gain medium is then absorbent (transparent) for photons with energy higher (lower) than the band-gap. When we start pumping the QW, the carrier density increases and the quasi-Fermi levels E_{f_c}, E_{f_v} moves toward the conduction band and the valence band, respectively. In this case, the QW provides amplification (positive gain) for photons with energy $h\nu$ satisfying the Bernard-Duraffourg condition [Bernard 1961]:

$$E_g < h\nu < \Delta E_F = E_{F_c} - E_{F_v}. \quad (2.6)$$

In the particular case when the quasi-Fermi levels separation ΔE_F equals the energy gap of the QW, the Fermi factor equals '0' the material is then said transparent and the corresponding carrier density is called transparency carrier density N_{tr} .

2.4.1.3 Spectrum of the optical gain

In a quantum well the gain spectrum is broadened because of collisions between particles and, or phonons in the crystal. The curves in Fig 2.10 show the evolution of the gain with the wavelength for different carrier densities in a GaAs-QW. We

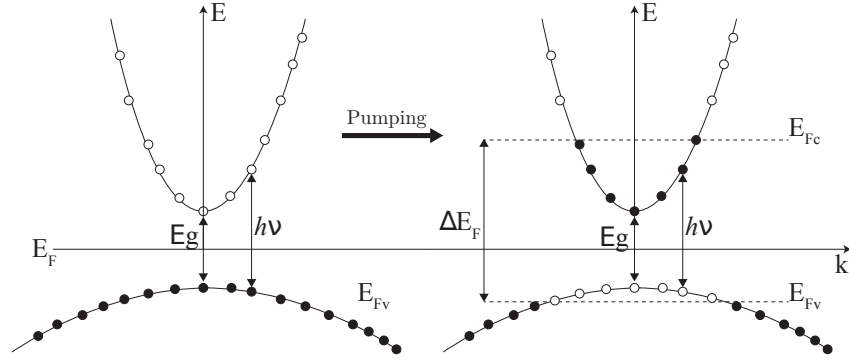


Figure 2.9: Band structure diagram of a direct energy-gap semiconductor in (left) and out (right) of thermodynamical equilibrium. Full dots denote states occupied by electrons, whereas empty circles denote vacant states.

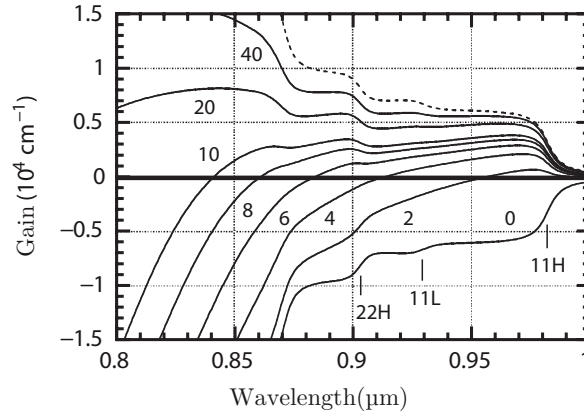


Figure 2.10: The gain spectrum vs. carrier density in strained $\text{In}_{0.2}\text{Ga}_{0.8}\text{As}/\text{GaAs}$ QW of 8 nm width [Coldren 2012].

can see that for low carrier density the gain spectrum can be approximated by a parabola, given by [Garnache 1999b]:

$$G(\sigma, N) = g(N) \left[1 - \left(\frac{\sigma - \sigma_0}{\Delta\sigma(N)} \right)^2 \right] \quad (2.7)$$

where $\sigma = 1/\lambda$ is the wave-number, and $\Delta\sigma(N)$ is the width of the parabolic gain given by

$$\Delta\sigma(N) = \Delta\sigma_{QW} \sqrt{N - N_{tr}} \quad (2.8)$$

where $\Delta\sigma_{QW}$ is a material property. For example, in a $\text{In}_{0.2}\text{Ga}_{0.8}\text{As}$ QW and carrier density $N = 1.6 \times 10^{12} \text{ cm}^{-2}$, $\Delta\sigma(N)$ is of the order of 100 cm^{-1} (3 THz) (by taking $N_{tr} = 1.2 \times 10^{12} \text{ cm}^{-2}$ and $\Delta\sigma_{QW} = 1.2 \times 10^4$). It is also important to note that the gain spectrum is usually shifted by the temperature and the carrier density. Indeed, increasing the temperature reduces the gap energy, and thus shifts

the gain spectrum to longer wavelengths ($\approx 0.3 \text{ nmK}^{-1}$), and it is well known that increasing the carrier density causes a band-gap shrinkage ($\approx 22 - 32 \text{ meV}$) called the *re-normalization*, hence the gain spectrum is red-shifted by a noticeable amount ($\approx 10 \text{ nm}$ at $\lambda = 1 \mu\text{m}$). These two effects are anticipated when we design the quantum wells so that the peak photoluminescence wavelength at low excitation density is $10 - 20 \text{ nm}$ shorter than the design wavelength of the laser.

2.4.1.4 Amplitude of the optical gain

The gain in the QW has approximately logarithmic dependence on the carrier density N

$$g = g_0 \ln(N/N_0) \tag{2.9}$$

where g_0 is an adjustable material gain parameter. The typical values for a InGaAs QWs are $g_0 \approx 2100 \text{ cm}^{-1}$ and $N_{tr} \approx 1.2 \times 10^{12} \text{ cm}^{-2}$ [Coldren 2012]. For moderate carrier density (typically $N < 2.5 \times 10^{12} \text{ cm}^{-2}$), the gain dependence on N can be approximated by a linear function:

$$g(N) \approx \left(\frac{dg}{dN} \right)_{N_{tr}} (N - N_{tr}) \tag{2.10}$$

When the carrier density in the well increases, the gain saturates, in general with GaAs-based QWs the gain could reach a maximum value of 5000 cm^{-1} (0.5% per pass) as shown in Fig 2.11. This implies that in VECSELs, a single quantum well is not sufficient to reach laser threshold with output coupler transmission of the order of 1%. To provide more gain the active zone must contain several QWs. In Sec 2.4.3 we see how to calculate the optimal QW number and where to place them for optimal laser operation.

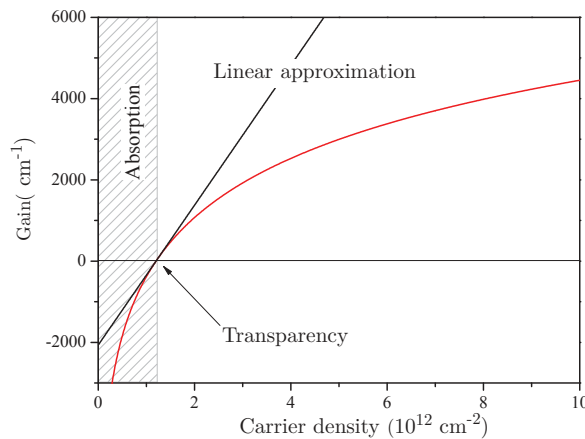


Figure 2.11: Modal gain of an 8 nm length InGaAs/GaAs QW as a function of the carrier density. g_0 is taken $\approx 2000 \text{ cm}^{-1}$ and $N_{tr} \approx 1.2 \times 10^{12} \text{ cm}^{-2}$.

2.4.1.5 Gain dichroism

Another important property of QWs is the gain difference between the $[110]$ and $[\bar{1}\bar{1}0]$ growth crystal axis in vertical geometry (see Fig 2.12) This property is explained by the fact that in 'Zinc blende' semiconductor structures, the anisotropy in the crystal results in a different carrier effective mass for each axis [Krebs 1996, Krebs 1997]. Therefore, the density of states is anisotropic, which leads to different material gain according to the polarization of light. Thanks to this property, VeCSELs are usually linearly polarized with an electric field oriented parallel to the $[110]$ axis. We shall study this property in more details in Chap 5, where we see how to measure the dichroism, how to control it, and describe its effect on the polarization state of VeCSELs.

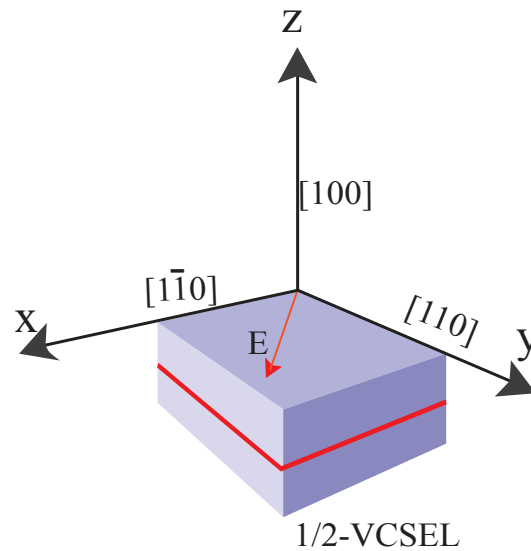


Figure 2.12: Vertical geometry of a 1/2-VCSEL structure.

2.4.2 Pumping the gain medium

2.4.2.1 Carrier generation

Carrier generation in the QWs usually called "pumping process" can be achieved using optical or electrical pumping. Despite the fact that electrical pumping allows to achieve very compact laser sources, optical pumping of VECSELs presents several advantages, we summarize the most important ones:

- Optical pumping allows uniform transverse carrier excitation over large areas which enables linear power scaling through larger active zone surface.
- No need to dope the structures, and thus no free-carrier absorption and no heavy and expensive post growth lithographic processing is required.

56Chapter 2. A laser source for structured light generation: VECSELs

- Pump wavelength flexibility because semiconductors absorb light for all wavelengths shorter than the material bandgap, this also implies that there is no need to stabilize the diode pump temperature as is DPSSLs.
- Poor quality pump beam can be used, thanks to the short absorption depth of semiconductor structures. The pump spot dimensions have to be right in a very thin plane and it does not matter how the pump beam diverges before or beyond this plane
- Optical pumping adds an additional degree of freedom (great versatility) to transverse mode control because it allows to separately control transverse size and shape of the active region.

As the quantum wells are very thin (<10 nm), most of pump power is absorbed in the barriers. The pump beam absorption in barriers follows an exponential profile given by the Beer-Lambert formula:

$$A_b = 1 - e^{-\alpha_p L} \quad (2.11)$$

where A_b is the fraction of the photons absorbed, L is the length of the absorption zone and α_p is the absorption coefficient of the barrier at the pump wavelength λ_p .

2.4.2.2 Carrier lifetime

Carrier created in the continuum state of the barriers are confined using a confinement layer (Fig 2.13), and thanks to the diffusion process they travel to the QWs where they are trapped. The carrier lifetime in the wells, $\tau(N)$ depends on the

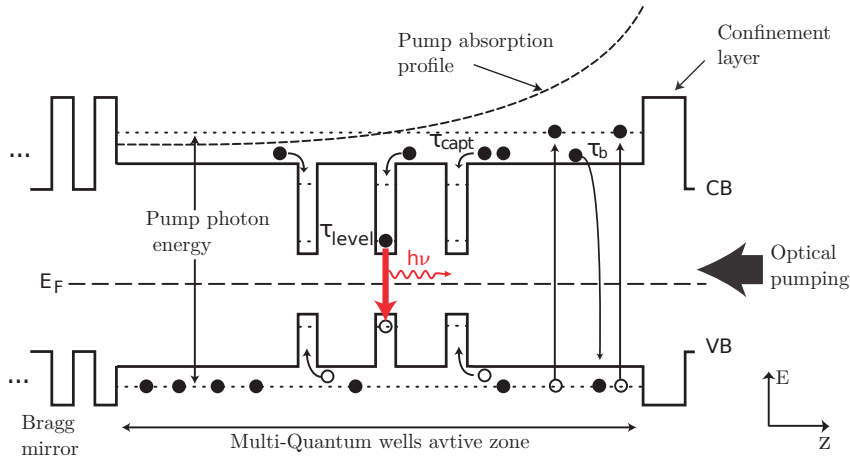


Figure 2.13: Schematic description of a MQWs active zone of a VECSEL under optical pumping.

carrier concentration, the relationship is approximated by [Coldren 2012]:

$$\frac{1}{\tau(N)} = A + BN + CN^2, \quad (2.12)$$

where A , B , C are the monomolecular, bimolecular, and Auger recombination coefficients. A characterizes the non-radiative recombinations due to crystal defects and impurities, $A \sim 10^7 \text{ s}^{-1}$ for a good quality structure. C depends strongly on the temperature and on the emission wavelength, $C \sim 3 \times 10^{-30} \text{ cm}^6 \text{ s}^{-1}$ at $\lambda = 1 \text{ }\mu\text{m}$, and ten times larger at $\lambda = 2.3 \text{ }\mu\text{m}$ for example. The two coefficients A and C give the total non-radiative lifetime given by ¹:

$$\frac{1}{\tau_{nr}(N)} = A + C \left(\frac{N}{L_{QW}} \right)^2 \quad (2.13)$$

and B gives the radiative lifetime in spontaneous emission regime as follows:

$$\frac{1}{\tau_r(N)} = B \left(\frac{N}{L_{QW}} \right) \quad (2.14)$$

The carrier recombination time in the barriers $\tau_b \sim \text{ns}$ is much larger than the capture time in the QWs $\tau_{cap} \simeq 20 \text{ ps}$ [Steinkogler 2003], this allows us to assume that all the generated carriers are trapped in the QWs. Thus, the pump intensity required to maintain a carrier density N in the QWs depends upon carrier lifetime on the energy level of the QWs τ_{level} :

$$I_{inc} = \frac{N}{\tau_{level}} \frac{h\nu}{\lambda_p} \frac{1}{A_b T_r} N_{QW} \quad (2.15)$$

where N_{QW} is the number of quantum wells and T_r is the pump transmission coefficient at the semiconductor surface.

2.4.3 Design of multi-quantum well gain mirror

As its name implies, the gain mirror provides two main functions: high reflectivity and light amplification. The first function is achieved using a Bragg mirror, and the second one by means of a multi-quantum wells active zone. The design guidelines of the gain mirror can vary depending on the chosen laser system (pumping scheme, continuous or pulsed regime ...) and the targeted performances (efficiency, tuning ...). However, regardless of the laser system, the design guidelines usually aim to maximize the reflectivity of the mirror and the gain extraction from the active zone. In the following we show how to design and optimize the gain mirror by considering an optical pumping scheme.

2.4.3.1 The Bragg mirror

The Bragg mirror consists of epitaxially grown semiconductor layers having a thickness of a quarter the emission wavelength and alternating high and low refractive index. This mirror allows to achieve high reflectivity of more than 99% over large

¹In the expressions the carrier density is divided by L_{QW} because B and C coefficients are conventionally used with volume carrier density

spectral region called the stop-band, and serves as one of the mirrors of the laser cavity. The reflectivity of the Bragg reflectors is governed by the index contrast $\Delta n = n_H - n_L$ and the number of the stacked pairs N_p , the maximal reflectivity is given by:

$$R_{max} = \left(\frac{1 - \frac{n_s}{n_0} \left(\frac{n_L}{n_H} \right)^{2N_p}}{1 - \frac{n_L}{n_0} \left(\frac{n_L}{n_H} \right)^{2N_p}} \right)^2 \quad (2.16)$$

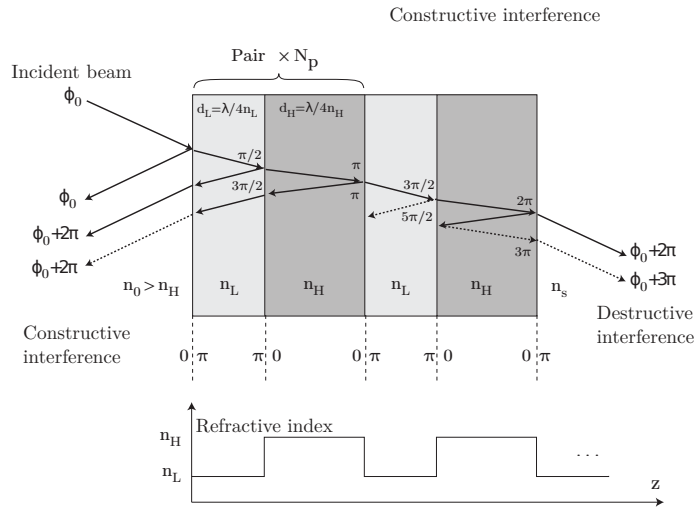


Figure 2.14: Schematic of a Bragg reflector with $n_0 > n_L$, The incident beam is drawn with an angle for better clarity.

To maximize the R_{max} one must use materials with high index contrast. However, the materials choice is limited to those satisfying the lattice-matching condition. Alternatively, one can increase the number of the pairs, but this is not a recommended solution because the mirror forms a thermal barrier between the active region and the heat sink, and a longer mirror implies higher thermal impedance. Other important properties of the Bragg reflectors are the width of the stop band and the absorption losses, given by:

$$\Delta\lambda = \frac{4\lambda}{\pi} \arcsin \left(\frac{\Delta n}{n_H + n_L} \right) \quad (2.17)$$

and

$$Loss = 2\alpha_b L_{pen} = 2\alpha_b \frac{\lambda}{4\Delta n} \quad (2.18)$$

where L_{pen} is the penetration length of the optical wave inside the Bragg mirror, for example at $1 \mu\text{m}$ using 27 pairs of lattice-matched *GaAs/AlAs* with $\Delta n = 0.56$ allows to reach a reflectivity of 99.88%, a $\Delta\lambda \simeq 110 \text{ nm}$ and $Loss < 0.02\%$.

2.4.3.2 Positioning the quantum wells

Given that the gain provided by a single quantum well ($\sim 0.2\%$) is not sufficient to reach the laser threshold, the active zone in VECSELs contains several QWs. In order to absorb the pump power efficiently, one must ensure that the active zone length is sufficient. For example, in a GaAs-based active zone, a barrier length of $7\lambda/2$ is required to absorb 85% of the incident pump power in a single pass. And to maximize the gain extraction, the QWs are placed at the antinodes of the standing wave of the electric field pattern established by the semiconductor mirror (Fig 2.15). This configuration is known as 'resonant periodic gain' RPG [Wilsem 2001], it enhances the gain around the design wavelength. However, the exponential pump absorption (Eq 2.11) provides a graded profile of carrier distribution, which results in non-uniform excitation of the QWs. This effect can be counterbalanced by varying the number of quantum wells at different antinodes, possibly skipping some antinodes. We note that this is valid because the carrier diffusion length is much smaller than the period of standing waves: $L_D \ll \lambda/(2n)$, in GaAs $L_D \simeq 20$ nm.

All the structures we use in this work are designed according to this principle. For example, in Fig 2.15 we show the QW's distribution we use in most of the structures we designed.

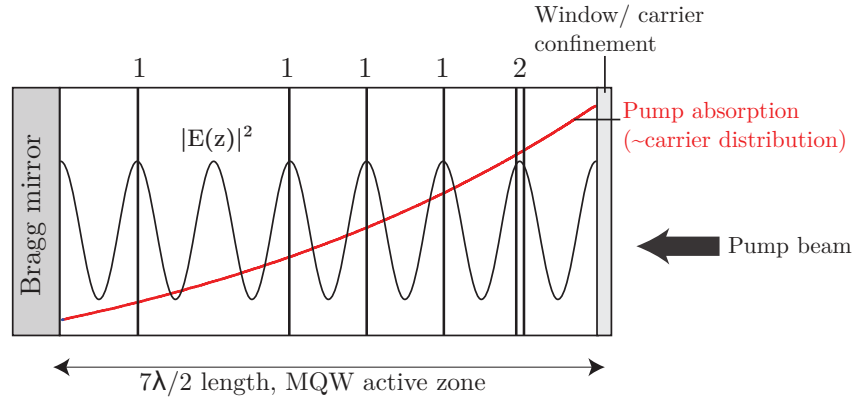


Figure 2.15: Schematic showing an example of QWs positioning in the active zone, in this example there are 6 QWs distributed in $7\lambda/2$ -length active zone.

2.4.3.3 Optimization of quantum wells number

Increasing the number of the QWs increases the gain provided by the active zone, but this also increases the QW's transparency carrier density N_{tr} . Consequently, the gain is limited due to stronger Auger effect. We therefore need to find an optimal QWs number that maximizes the gain using the minimum transparency carrier density. The total gain depends on the number of the QWs N_{QW} , their width L_{QW} and also their overlap with the intracavity optical standing waves. The gain is then referred to as the modal gain, and can be written for N_{QW} placed at the anti-nodes of the standing waves, and as a function of the carrier density N as

follows:

$$G_{mod}(N) = 4N_{QW}L_{QW}\Gamma_{\mu c}\Gamma_{xy}g_0 \ln\left(\frac{N}{N_{tr}}\right) \quad (2.19)$$

where $\Gamma_{\mu c}$ characterizes the resonance due to the sub-cavity etalon, formed by the on-chip Bragg mirror and the air/semiconductor interface reflection at the top surface of the gain structure [Tropper 2006]. $\Gamma_{\mu c} = 1$ when the surface is anti-reflection coated. Γ_{xy} is the transverse confinement factor characterizes overlap between the laser transverse mode and carrier distribution related to the transverse pump profile. To reach the laser threshold on one round-trip the modal gain must be equal to the total losses in the laser cavity given by:

$$Loss^{op} = -\ln(R_{oc}) + \Gamma_{\mu c} [2\alpha_{\mu c}L_{\mu c} - \ln(R_{HR})] \quad (2.20)$$

Where R_{oc} is the reflectivity of the output coupler, $\alpha_{\mu c}$ characterizes the total losses inside the sub-cavity mirror due to absorption, $L_{\mu c}$ is the sub-cavity length, and R_{HR} is the Bragg mirror reflectivity. Putting Gain = Losses gives the following threshold carrier density :

$$N_{th} = N_{tr} \exp\left(\frac{Loss}{4N_{QW}L_{QW}\Gamma_{\mu c}\Gamma_{xy}g_0}\right) \quad (2.21)$$

It is more convenient to write this expression in terms of the incident pump density conventionally used in the experiments. From Eq 2.15 one can write:

$$I_{th} = \frac{N_{th}}{\tau_{level}(N_{th})} \frac{hc}{\lambda_p} \frac{1}{A_b T_r} N_{QW} \quad (2.22)$$

This value changes with the temperature due to the shift of the gain spectrum, and also to the temperature dependence of Auger effects which affect the quantum efficiency. The global temperature dependence of threshold intensity I_{th} can be expressed using the so-called characteristic temperature T_0 as:

$$I_{th}(T_2) = I_{th}(T_1) e^{\frac{T_2 - T_1}{T_0}} \quad (2.23)$$

where $I_{th}(T_1)$ and $I_{th}(T_2)$ are the power densities at temperature T_1 , T_2 , respectively.

Figure 2.16 plots the evolution of the incident pump density as a function of the quantum wells number N_{QW} for different output coupler transmissions. These curves were calculated using Eq 2.22 and typical GaAs-QWs parameters summarized in Table 2.1. The curves show that 5-6 QWs are required to compensate output losses of the order of 2% while keeping moderate pump intensity (1–2 kW/cm²). This is mainly, the typical QWs number we use in our structures.

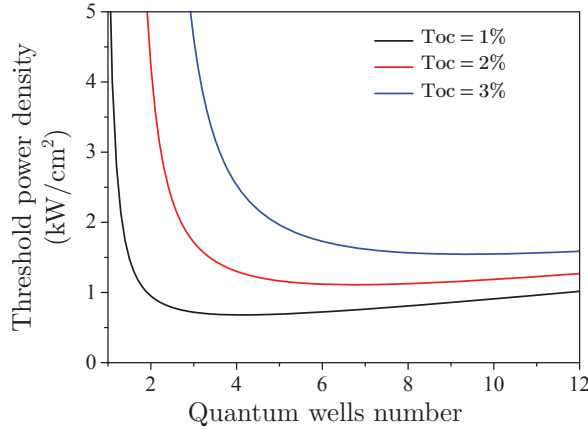


Figure 2.16: Threshold power density vs. InGaAs/GaAs QWs number for different output coupling losses.

2.4.4 Design of the micro cavity

2.4.4.1 Resonant configuration

In this configuration the length of the active zone is a multiple of $\lambda/2$, the phase shift after one round trip is then $0[2\pi]$ which gives rise to constructive interferences (antinode) on the chip surface. This increases the electric field intensity in the active zone (Fig 2.17a) and induces a filtering effect (Fig 2.17b) because when the lasing wavelength departs from the design one, the electric field intensity decreases in the active zone which reduces the overlap with the QWs ($\Gamma_{\mu c}$).

This configuration is interesting because it increases the modal gain by a factor $\Gamma_{\mu c}$. And, having an antinode on the gain mirror surface can be particularly useful, for example when functional elements such as phase and intensity masks are integrated on the gain-chip. This configuration maximizes the interaction between the electric field and the integrated elements. However, to ensure proper laser operation, one has to ensure that the maximum of $\Gamma_{\mu c}$ coincides with the maximum of the gain curve. This requires precise control of the growth process (Quantum wells composition and thickness of the epitaxial layers), in addition to the anticipation of the red-shift of the gain due to thermal effect and carrier density. Furthermore, the narrow spectral width restricts the gain bandwidth for tuning, and increases the thermal sensitivity [Tropper 2006].

2.4.4.2 Anti-resonant configuration

This configuration is obtained by adjusting the length of the active zone to an odd multiple of $\lambda/4$, Fig 2.18a shows the electric field intensity in an anti-resonant micro-cavity, it is characterized by reduced electric field intensity at the wells ($\sim 34\%$ less than in the air), and a node of the standing wave at the chip surface which minimizes the possible scattering losses due to contamination of the surface. This configuration also allows tuning of the wavelength over large opti-

Parameter	Description	Value	Units
g_0	Material gain coefficient	2000	cm^{-1}
N_{tr}	Transparency carrier density	$8,4 \times 10^{11}$	cm^{-2}
L_{QW}	Quantum well thickness	8	nm
N_c	Conduction band density of state	$7,7 \times 10^{11}$	cm^{-2}
A	Monomolecular recombination coefficient	$6,10^7$	s^{-1}
B	Bimolecular recombination coefficient	$2,10^{-10}$	cm^3s^{-1}
C	Auger coefficient	$3,10^{-30}$	cm^6s^{-1}
λ_p	Pump wavelength	~ 800	nm
A_b	Pump absorption coefficient	85	%
T_r	Pump transmission at chip surface	~ 95	%
$\Gamma_{\mu c}$	Micro-cavity confinement factor	1	—
$Loss_{\mu c}$	Loss in the Micro-cavity	$< 0,5$	%
R_{HR}	Bragg mirror reflection	99,9	%

Table 2.1: Laser and material parameters of InGaAs/GaAs structures at 300 K used in the gain and laser threshold calculations.[Coldren 2012].

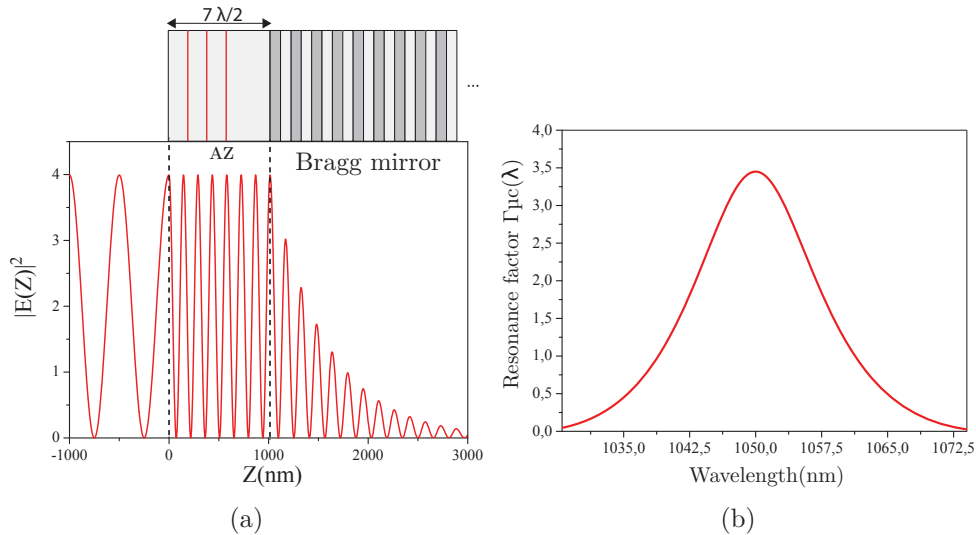


Figure 2.17: (a) electric field intensity profile in VECSEL gain mirror with a resonant micro-cavity. (b) Confinement factor of the micro-cavity as a function of the wavelength.

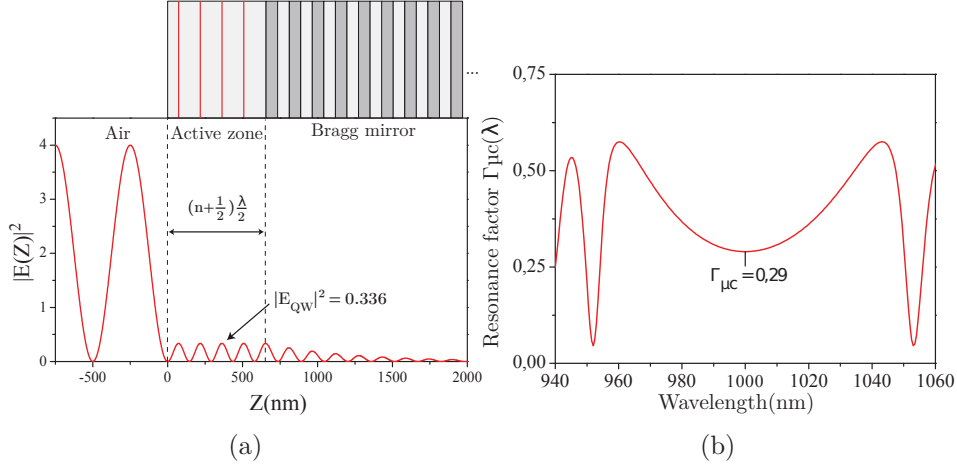


Figure 2.18: (a) electric field intensity profile in VECSEL gain mirror with an anti-resonant micro-cavity. (b) Confinement factor of the micro-cavity as a function of the wavelength.

cal band because the gain spectrum is not filtered. The effective gain bandwidth may even be larger than the intrinsic gain bandwidth since the curvature of the confinement factor $\Gamma_{\mu c}$ is opposite to that of the gain (Fig 2.18b).

2.4.4.3 Anti-reflective coated microcavity

Depositing an anti-reflective coating on the top surface of the 1/2-VCSEL structure allows to eliminate the resonance or the anti-resonance effect of the microcavity. For this purpose, we deposit a $\lambda/4$ -thick dielectric layer to make a progressive adaptation of the refractive index. In our GaAs-based structures the coating is made of Si_3N_4 layer followed by an AlAs window, both are $\lambda/4$ -thick. The refractive index of Si_3N_4 satisfies the condition: $n_{\text{dielectric}} = n_{\text{AlAs}} \sqrt{n_{\text{air}}/n_{\text{GaAs}}}$, which results in a resonance factor $\Gamma_{\mu c} \simeq 1$. This design is depicted in Fig 2.19.

We will be using these three micro-cavity configurations. The anti-reflective coated in the standard one, and most of the time we will use this configuration. However, sometimes we need to study some gain mirror properties (such as the birefringence in Chap 5) by varying the electric field intensity at the 1/2-VCSEL's surface, in such cases we design and fabricate two versions of the same structure: with and without anti-reflective coating. We will also use 1/2-VCSEL structures with an anti-resonant micro-cavity in Chap 4 because we will integrate a metasurface-based phase and intensity masks, and we want their effects to be perturbative, thus we minimize the electric field intensity at the surface by using an anti-resonant microcavity.

To end this part, we give in Fig 2.20 two complete design examples with detailed material information and real thickness values. We gave these two structures two references in order to identify them later. We will use two versions of the Gas680: with / without anti-reflective coating. This structure is mainly used in phase-

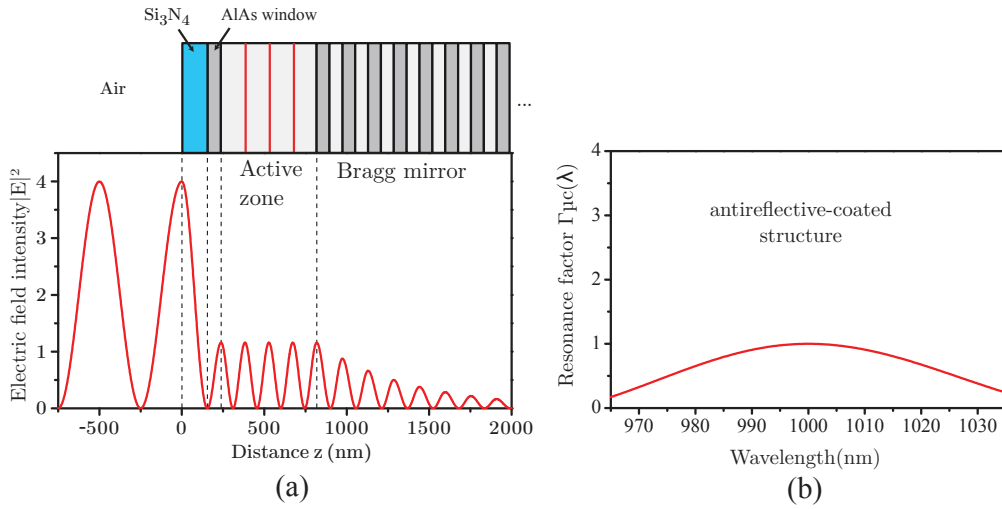


Figure 2.19: (a) Electric field intensity profile in VECSEL gain mirror with an anti-reflective coated micro-cavity. (b) Confinement factor of the micro-cavity as a function of the wavelength.

structured beams generation addressed in Chap 4, and in polarization modes study and control addressed in Chap 5.

The second structure Gas656, contains an additional moderately reflective Bragg reflector that acts as longitudinal mode filter, and ensures robust single frequency operation. We will mainly use this structure under feedback when we address feedback-interferometry measurement in Chap 6. The last structure shown in Fig 2.21 is a Bragg reflector (without quantum wells) its reference will be Gas620. We will use this reflector as an output coupler in Chap 3 and in Chap 5, in the former to demonstrated a focusing ability of metasurfaces, and in the latter to balance the birefringence of 1/2-VCSEL structures.

2.5 Conclusion

In this chapter we presented the VeCSEL laser sources, and compared them with other laser families with the idea of using VeCSELS as a laser source with integrated mode control technology. We have seen that they take advantage of band-engineered compound semiconductor materials which confers to them wide wavelength coverage, compactness, pump flexibility and high efficiency. Furthermore, the extended cavity allows to pump VeCSELS with large spots and thus to generate high power in single mode emission.

More importantly to us, the open cavity configuration and the low thickness of the QW-based active medium ensure high homogeneity and prevent distortion effects induced by thermal lensing in thick gain media. This makes VeCSELS ideal candidates for structured light generation with high spatial coherence.

In the second part we presented the building blocks of a VeCSEL, we described

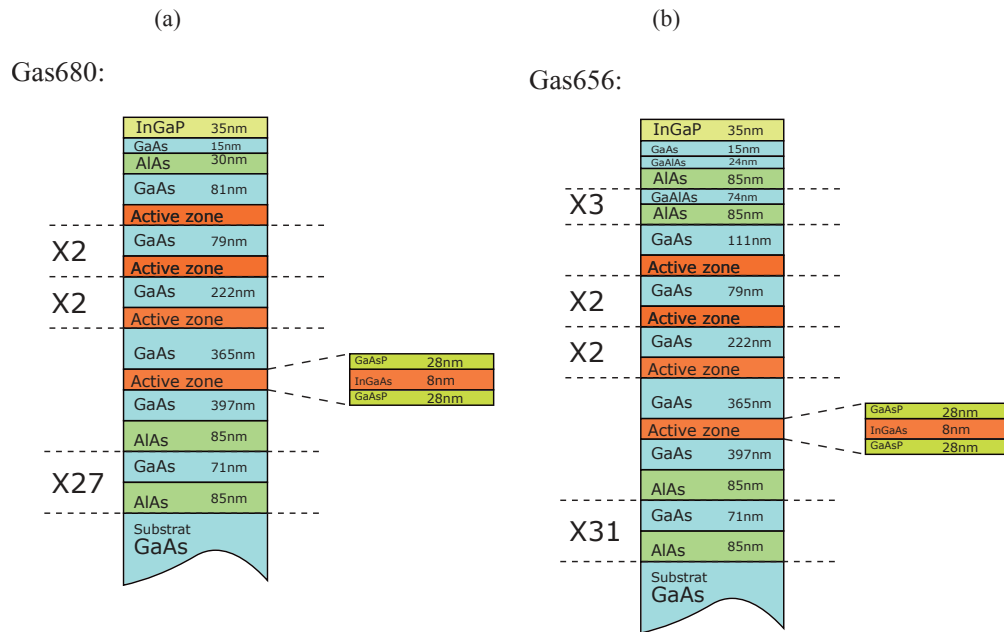


Figure 2.20: Two detailed examples of 1/2-VCSEL structures.

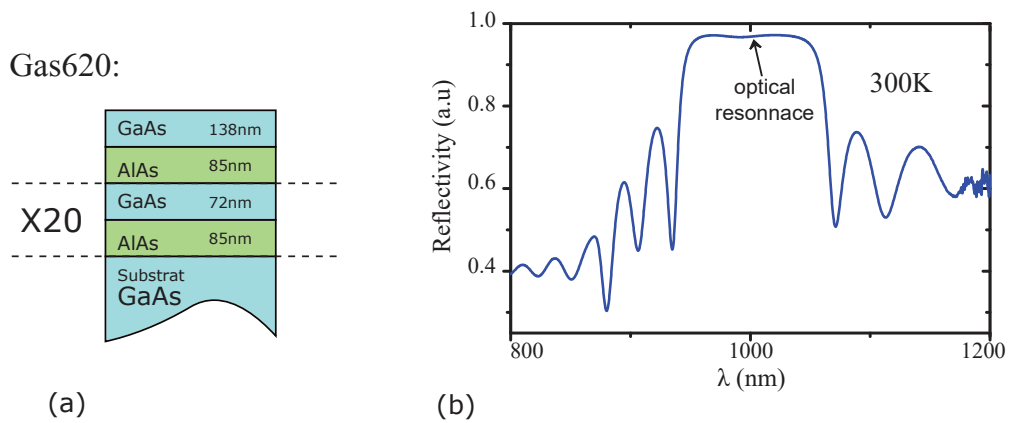


Figure 2.21: (a) Gas620 structure: highly reflective broad band Bragg reflector. (b) Its measured reflectivity spectrum

66Chapter 2. A laser source for structured light generation: VECSELs

the gain medium and its properties, then we show how to calculate the optimal number of QWs and how to place them in the active zone in order to optimize the performances of the VeCSEL.

An InGaAs/GaAs quantum well, in the vertical cavity geometry of V(E)CSELs, provides a typical gain of $\sim 0.2\%$ per pass. Thus we have seen that for output coupling of $\sim 2\%$, and to have a reasonable threshold density ($\sim 1 \text{ kW/cm}^2 - 2 \text{ kW/cm}^2$) the optimal number of required quantum wells is $\sim 5 - 6$.

In the last part we presented three micro-cavity configurations: resonant, anti-resonant and antireflective coated. The main difference between them is the intensity of the electric field on the top surface of the 1/2-VCSEL structure. This is particularly important to us, because in the following chapters we will use phase and amplitude masks integrated on this very top surface. Thus, by choosing one of these structures we will control the intensity of the electric field on the integrated masks and thus control the strength of the interaction.

The following chapter is dedicated to the development of an integrated mode control technology, for intra-cavity mode control with VeCSELs.

VECSEL integrating metasurfaces for intracavity mode-control

3.1 Introduction

This chapter aims at finding an answer to the issue: how to control the intracavity light state in a VECSEL. To fully answer this question one must address two points, the first one is the understanding of the cavity light states formation and properties, that could allow to select a given state with some desired qualities. And the second point is the development of an appropriate technology that enables such mode control in VECSELs. The first issue has been addressed in Chap 1, we have seen that in a laser cavity the modes are quantized, they have different resonance frequencies and different spatial wave functions. We have also seen that as they share the same gain medium, they compete for the available gain. This dynamic effect is governed by the light-matter interaction process, and the main parameters that defines the competition result are: the modal gain, the loss, and dynamical cross and self-saturations coefficients. Thus, if one wants to constrain the competition process to select a given mode, one has to modify one of the these four parameters in a way that favors the wanted mode, this latter must experience higher net gain or (and) weaker saturation in comparison with unwanted modes.

Our main focus in this chapter is to develop a technology that allows such mode control. It is easy to understand how to change the gain or the loss for a given mode, for example one can merely put an absorbent or an opaque element inside the cavity. This method has been traditionally used to force the laser operation on the fundamental TEM_{00} mode by placing a variable aperture inside the cavity [Piche 1983]. However we can use more complex intracavity loss distribution to select other higher order modes of interest.

It is less obvious to visualize how to the modify the dynamical parameters (mainly the self-saturation) of a given mode. In fact, these coefficients are related to the mode pattern, so in order to change them we need a method that enables us to modulate the phase in addition to the amplitude of the transverse intracavity field. We shall describe this point in details in Chap 4 when we address the generation of vortex modes with controlled handedness (Sec 4.6).

It is helpful at this point to summarize the main criteria that the mode control technology we aim to develop here should meet, namely:

- Very low loss, because the gain in VECSELs is of the order of 1% this allows to use output coupler transmission up to 1% for power extraction. Therefore in order to reach laser threshold, VECSELs are unable to tolerate any extra-losses.
- Enable efficient and accurate intracavity transverse phase and intensity shaping.

Beside these two vital criteria for laser operation and mode control, there are other ones of major importance. Namely: mode control elements must have a compact size (transverse dimensions of the order of the mode waist $\sim w_0$) in order to preserve the compactness of VECSELs which is a feature of great interest for integration. Furthermore, the positioning and the alignment of such component can be very critical, because the quality of the generated state of light depends heavily on them. Consequently, the used technology must enable very accurate positioning of the functional elements (transverse $\ll w_0$, longitudinal $< \lambda$). From the description of

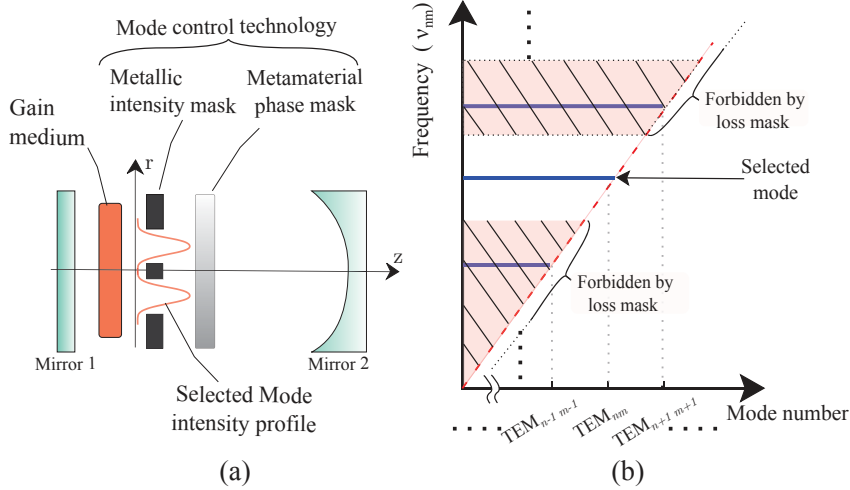


Figure 3.1: Principle of intracavity mode selection technology developed in this chapter.

the required criteria, it becomes clear that some new techniques used in solid state lasers for intracavity phase and intensity shaping, such as LCD-spatial light modulators [Ngcobo 2013], are not completely adapted for our application requirements because of pixilation, diffraction losses, bulkiness, positioning accuracy, power limitation and so on. We shall return to this point with more details in Sec 3.5 to compare the existing technologies with ours. But before we do that, we will present our approach which consists in using integrated flat optics based on metamaterial for intracavity mode control. Its principle is described in Fig 3.1. It consists in using two stacked layers to spatially modulate the intensity and the phase of the intracavity field. The intensity masks are based on subwavelength metallic layer, and phase masks are based on 2D dielectric subwavelength grating, acting as a

metasurface (thin metamaterial layer whose refractive index can be controlled by design).

This chapter is organized as follows: The following section starts by defining metamaterials and gives some of their basic principles and properties. Then, we discuss the advantages of integrating metamaterials in VECSELs for mode control, and illustrate the principle of the method we developed, we also give some examples of realized mode control masks integrated on 1/2-VCSEL structures. At this stage we will be ready to compare our technology to the existing ones, for this purpose, we will give an overview of laser-mode control technologies' state of the art. We end the chapter by putting all the blocks together to build and characterize the first VECSEL integrating metasurface-based intracavity mode control elements as proof of concept.

3.2 What are photonic metamaterials

Optical devices manipulate light by altering its phase, amplitude and polarization. In conventional optical components, these functionalities are based on reflection, refraction and diffraction, which are achieved by elaborating geometries and structures using the available materials of a given refractive index to control the light path. The achievable functionalities are limited by the scope of the available materials and the very restrictive ability to control their properties at will. For example the simple functionality of an anti-reflective coating can be achieved using a single layer of quarter-wavelength thick whose refractive index is the square root of that of the substrate. Most common optical glasses have a refractive index in the region of 1.55, thus an optimal single layer coating would have to be made of a material with an index of about 1.245. Unfortunately, there is no known material with such low reflective index. Metamaterials were borne out of a need for a functional materials with tailorable properties to overcome the limitations of the conventional materials. The definition of a metamaterial in the literature is still nebulous, for example, some experts include photonic crystals and other not. But it is universally admitted that metamaterials are an arrangement of artificially structured units made of conventional materials in order to achieve advantageous and unusual electromagnetic properties, that can be tailored by changing the structural design [Cai 2010]. The material units sometimes called meta-atoms are usually (but not necessarily) arranged in a periodic fashion, and the structural period must be smaller than the wavelength of interest. Therefore, metamaterials were first used in microwave domain of the electromagnetic spectrum [Zouhdi 2008]. Recently, photonic or optical metamaterials became possible thanks to the current maturity of nanofabrication techniques.

Photonic metamaterials are particularly necessary when the desired functionality requires a gradient in the material property, such as in Luneburg lens [Luneburg 1944] and optical cloak [Cai 2006]¹ where a variable refractive index is

¹A the time of this writing the proof of principle was demonstrated, but there is no practical

required. This ability of creating a given refractive index distribution is of a key importance in our context as it enables efficient and accurate intracavity shaping of the lasing field.

3.3 Some basic principles and properties

3.3.1 Material vs structural dispersions

In conventional materials a piece of crystal consists of atoms arranged in a periodic manner with a lattice constant of a few angstroms. When light propagates in the medium it is slowed down because the energy is stored in atomic polarization (material dispersion): in each atom or molecule there are electric dipoles that can be excited by the electric field of incident light, subsequently, the dipoles radiate the energy with a certain delay. However, at the macroscopic scale light does not feel the atoms, nor the oscillations of the dipoles and their radiation, but all these phenomena are averaged and described with the absorption, transmittance, reflectance and a certain retardation using the refractive index of the material. In a similar fashion, when the lattice constant a of the artificial structure in a metamaterial is much smaller than the wavelength of interest $a \ll \lambda$, light feels a homogeneous medium, and the material response to the electromagnetic field can be described using effective parameters including the refractive index or more globally two parameters: the permittivity ϵ and the permeability μ . However, it is important to note that here light is slowed down because of multiple scattering, rather than atomic polarization. This is called structural dispersion. The resulting effective properties depend on the properties of the involved materials and the structural design. Thus, all the used materials must be transparent to light at the wavelength of interest. The properties of the resulting metamaterial can be calculated using different methods depending on the lattice constant of the artificial structure and how it compares to the wavelength. Fig 3.2 summarizes the possible situations. Metamaterials belong to the subwavelength domain which can be divided into two

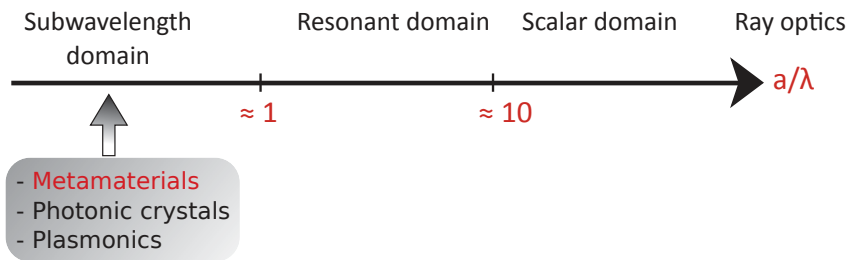


Figure 3.2: Periodic structures behavior depending on the period-wavelength ratio.

parts:

optical cloaks yet.

- **When $a \ll \lambda$** : In this case the optical properties of the metamaterial are usually investigated using the effective medium approaches, such as Maxwell-Garnett theory and the Bruggeman effective medium theory first developed for composite materials with random distributions [Cai 2010]. These homogenization methods rely on spatial averaging of the permittivity and does not take the structural geometry into account, thus they are quite intuitive, but give only an approximate value of the effective parameter ε when $a_s/\lambda \rightarrow 0$. The effective refractive index n_{eff} of a two-material composite is bounded by the Wiener bounds [Aspnes 1982, Joannopoulos 2007]:

$$(f_1\varepsilon_1^{-1} + f_2\varepsilon_2^{-1})^{1/2} \leq n_{eff} \leq (f_1\varepsilon_1 + f_2\varepsilon_2)^{1/2} \quad (3.1)$$

where f_1, f_2 are the volume fractions of the materials with refractive indexes $\sqrt{\varepsilon_1}, \sqrt{\varepsilon_2}$. We note that $f_1 + f_2 = 1$. These bounds tell us that the refractive index can be continuously tuned between the indexes of the two materials of the composite. This general analytical constrain expression is very useful as it applies for all artificial material structures.

- **When $a < \lambda$** : In this case we are very close to resonance domain, thus to determine the properties of the effective medium rigorous calculation of the microscopic field is required. Photonic metamaterial based on regular periodic structure belong to this wavelength domain, and one of the advantages of using such structures is that theoretical analysis has been made easier thanks to Bloch theorem. Indeed, several methods can be used to study metamaterials based on periodic subwavelength structures, the most used ones are those based on Fourier expansion of the periodic function of the permittivity, such as the plane-wave method usually used to calculate band-structures (dispersion relation) of photonic crystals [Ho 1990, Zhang 1990] (see Fig 3.3.a,b), and the rigorous-coupled-wave analysis (RCWA) method [Moharam 1995, Lalanne 1996], which is the one we use to design our structures as it is more suited to multilayer periodic structures (Fig 3.3.c,d).

3.3.2 Metamaterial or photonic crystal?

As a unique and unambiguous definition for metamaterials is still to be established, and for the purpose of clarity, we note that in general a given structure could have different behaviors such as photonic crystal, diffraction grating, and of course a homogeneous artificial dielectric so-called metamaterial. These behaviors depend on the structure geometry and also the illumination axis, a very useful way to obtain a global view of all the possible behaviors, is to calculate the dispersion diagram of the structure. To illustrate this, we calculated the band diagram of the periodic structure shown in Fig 3.3a for wave-vector parallel to x-axis (or y-axis) and z-axis. We represented the obtained results in Fig 3.4. From this figure, we can see that when the impinging light is on the z-axis a photonic bandgap appears. Whereas, when the structure is illuminated by incident waves along Z-axis there is no band-gap and we notice that for small values of 'a' ($\frac{ka}{2\pi} = \frac{a}{\lambda} \ll 1$) the dispersion relation

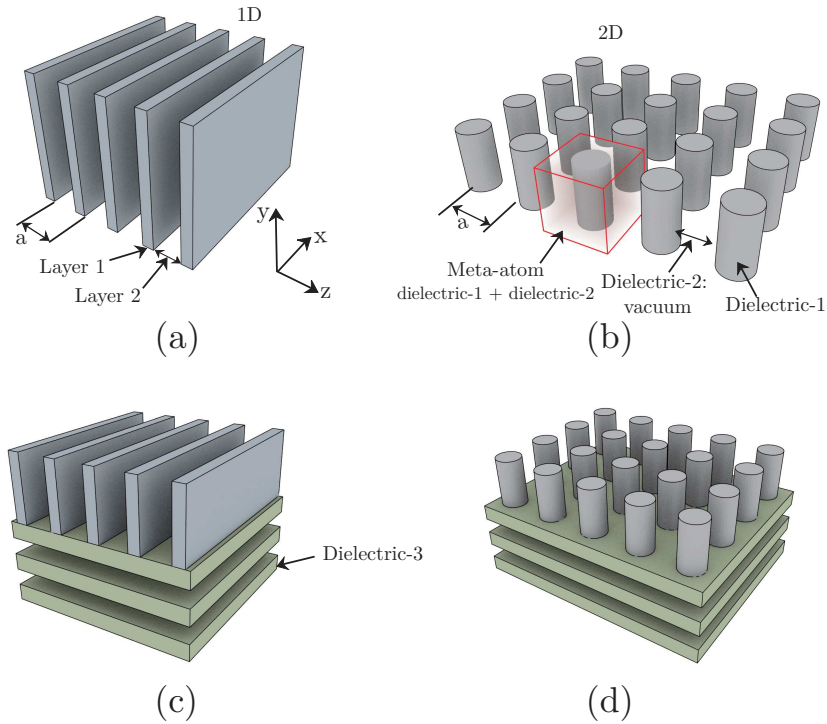


Figure 3.3: Examples of 1D, 2D periodic structures. In (a) and (b) the structures are either periodic or invariant in every direction, therefore their band diagram can be calculated with the plane-wave method. (c,d) Related structures with a finite thickness and stacked on other layers, in this case the RCWA method is more suitable for simulations.

is quasi-linear. This means that the structure behaves like a homogeneous artificial dielectric with an effective refractive index. The value of the effective index (slope of the dispersion curve) depends on the volume fractions f_i . We note that as one of the two materials here is vacuum, f_i is called the filling factor and denoted ff .

3.4 Metamaterials integration in VECSEL: principle and implementation

3.4.1 Advantages

This brief overview of metamaterials and their main properties shows that they possess several features that makes them ideal candidates that meet our application requirements, the main advantages are:

- Subwavelength dimension of the periodic structure means that there are no diffraction losses as is SLMs and other diffractive elements. The only losses that may exist are the absorption losses in the materials, which can be avoided by choosing the right materials for the wavelength of interest.

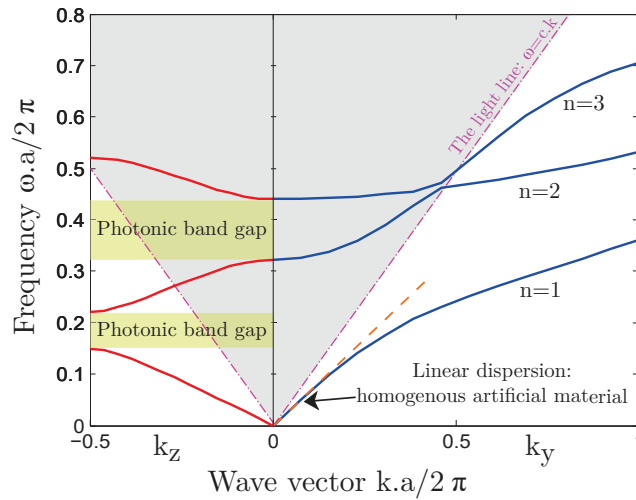


Figure 3.4: The band diagram of the multilayer periodic structure shown in Fig 3.3a. The left side shows the on-axis band, i.e the wave-vector of the impinging light k_z is parallel to the z -axis. And on the right side the wave-vector is parallel to the y -axis. The electric field is in the yz plane.

- The effective refractive index can be controlled locally by changing the structural geometry (filling factor, the layer thickness...). This feature enables us to create two dimensional refractive index profiles with high accuracy, in order to modulate the phase and the intensity of the intracavity waves.
- Metamaterials are fabricated using micro-lithography and associated semiconductor technologies, which present two advantages: First, this is the same technology used to fabricate the VECSELs' semiconductor gain chip itself. This enables to achieve compact, auto-aligned, cost-effective and high quality elements. Second, this technology allows accurate longitudinal placement of metamaterial functional elements, thanks to accurate control of layer thicknesses (at nanometer scale) whereas our beam dimensions $w \gg \lambda$. This provides a very effective way to control the intensity of interaction between the intracavity field and the metamaterial. For example, placing the metamaterial at an antinode of the intracavity standing wave maximizes the interaction, whereas placing the element at an anti-nod lowers it.

Fig 3.5 illustrates the dimensions of the metamaterial elementary cell, both its thickness and transverse dimensions are sub- λ , which results in a total volume of the meta-atom $V_{cell} \ll \lambda^3$

3.4.2 Design principle

Figure 3.6 illustrates the principle of the method we developed in the present work. It consists of subwavelength-thick stacked layers that plays the role of intracavity transverse phase and / or amplitude masks. And to implement transverse phase

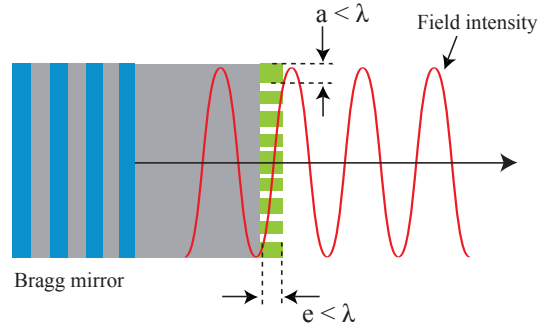


Figure 3.5: Dimensions of the metamaterial elementary cell (meta-atom).

functions, we use a 2D metamaterial layer and vary the artificial refractive index by design according to the desired phase profile. To implement transverse amplitude functions there are two possible options: the first one is to use subwavelength-thick absorbing metallic layer. By varying the layer thickness we can precisely control the absorption, and thus the amplitude of the transmitted electric-field, and as with phase masks, we can implement the desired transverse amplitude function using an adequate transverse pattern. The second option, is to use a phase function that introduces localized high diffraction losses. This is achieved, using an abrupt phase step, the amplitude loss can then, be estimated according to the value of the phase step using the complex plane method illustrated in Fig 3.7 [Dudley 2012].

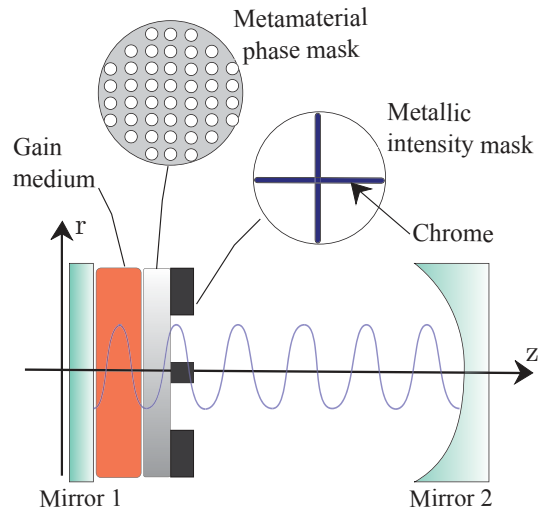


Figure 3.6: Principle of the developed intracavity phase and intensity control technology.

The stacked layers are placed inside the laser cavity, almost all the fabricated masks are integrated on a 1/2-VCSEL structure, except one phase mask that we integrated on a separate HR Bragg mirror because we used it as an output coupler as we will show in Sec 3.6. Fig 3.8 shows a schematic of a 1/2-VCSEL structure integrating a metamaterial layer. We can also stack another metallic layer which

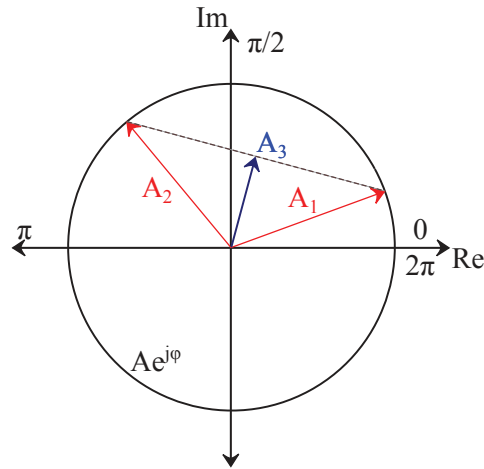


Figure 3.7: Complex plane method: in this technique the vectors A_1 and A_2 represent the phase values on each part of the phase step, the resulting local field is given then by the vector sum of A_1 and A_2 , for example when the phase difference $\Delta\varphi = \pi$ the field amplitude is null.

adds more flexibility to the method.

3.4.3 Materials choice

The metamaterial layer can be fabricated using III-V semiconductor or dielectric materials, we choose Si_3N_4 for three main reasons: (1) It is a material that has a good adhesion on GaAs, and that can be deposited using chemical vapor deposition (CVD) techniques. SiN is usually used in III-V semiconductor structures as an anti-reflective coating. (2) It is transparent at our working wavelength. (3) It allows selective etching over GaAs structures, which is very important for the accuracy of technological process and structures quality.

To fabricate the metallic layers we choose to use the chromium because it has a high absorption coefficient $\alpha = 4 \times 10^5 \text{ cm}^{-1}$ [Rakic 1998]. Thus a very thin subwavelength layer ($\sim 10 \text{ nm}$) allows us to achieve the desired attenuation ($>40\%$). This is of high interest to us because a thick layer may introduce diffraction losses which deteriorates the spatial quality of the mode.

3.4.4 Design and fabrication procedure

3.4.4.1 Design

In concrete terms, designing a mask consists in calculating the holes profile required to implement the desired phase function. To do this we follow these steps:

- We determine the expression of the required transverse phase function as a function of space coordinates: $\Delta\varphi = f(x, y)$.

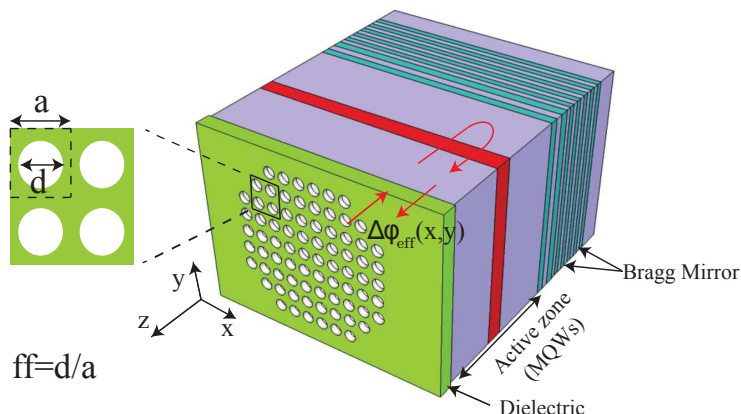


Figure 3.8: Schematic of a 1/2-VECSEL structure integrating a metamaterial layer on its top-surface.

- As the mask is integrated on the gain mirror, we calculate the effective refractive index or directly the phase shift $\Delta\varphi$ experienced by reflected waves as a function of the fill factor ff , for this we use the RCWA method by taking into account the multilayer configuration of the 1/2-VECSEL structure (see Fig 3.9), we obtain $\Delta\varphi(ff) = g(ff)$ (see Fig 3.10).
- Using the two above-mentioned parameters, we calculate the ff spatial pattern required to achieve $\Delta\varphi$: $ff(x, y) = g^{-1}[\Delta\varphi(x, y)]$. The hole size pattern is then $d(x, y) = a \times ff(x, y)$.
- Knowing $d(x, y)$ we draw the 2D lithography photomask and encode it in GDSII format which is the industry standard for integrated circuit layouts¹. This photomask will be used in the fabrication step.

3.4.4.2 Fabrication

All the structures we designed are fabricated and processed in the technological facility LPN (Laboratory for Photonics and Nanostructures) by Pr Isabelle Sagnes and her team.

To describe the fabrication procedure, we consider the general case of two stacked metallic and metamaterial layers, because it describes the fabrication process of both. The process can then be divided into two major steps:

Metallic mask fabrication Figure 3.11 depicts the technological process used to fabricate the metallic mask. Firstly a polymethyl methacrylate (PMMA) resist is spin-coated on the wafer and patterned by electron beam lithography (Vistec EBPG 5000 at 100 kV) with a resolution of 1.25 nm. After PMMA development in methylisobutylketone (MIBK) solution, a thin layer (5 nm – 20 nm) of chromium

¹We used the python package IPKISS to encode the masks.

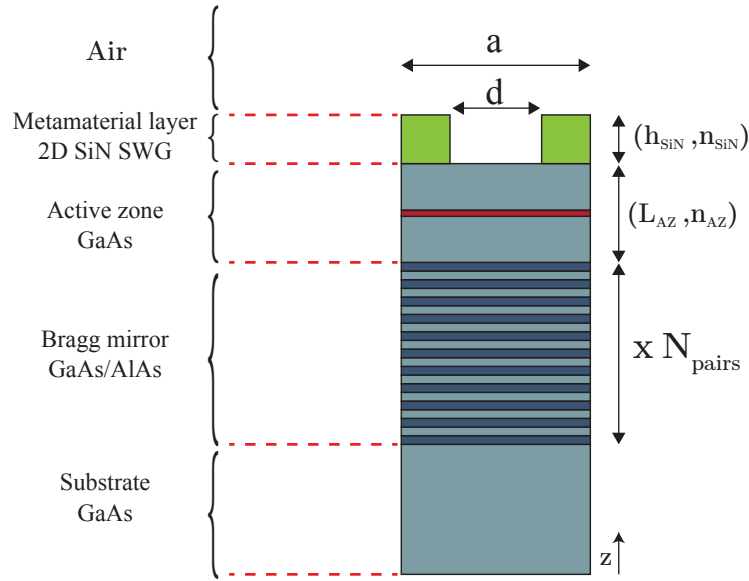


Figure 3.9: Multilayer 1/2-VECSEL structure integrating an elementary cell of the 2D subwavelength grating (meta-atom).

is deposited using physical vapor deposition (PVD), and finally the structure is cleaned from residual chromium and PMMA.

Meta-material layer fabrication The technological process used to fabricate the meta-material layer is depicted in Fig 3.12. Firstly, a sub-wavelength thick Si_3N_4 is deposited by ion-beam-assisted electron-beam vacuum evaporation. Then a PMMA resist is spin-coated on the wafer and patterned by electron beam lithography. After PMMA development in MBIK solution, the SWG holes are transferred to the SiN layer by Reactive Ion Etching (RIE), and finally the PMMA is removed.

3.4.5 Some examples of fabricated masks

Fig 3.13a shows an optical microscope photograph of a double-layered set of masks (metallic + dielectric metamaterial), the optical microscope is equipped with a polarizing filter in order to accent the details. We note that even if these patterns were designed to work at $\lambda = 1 \mu\text{m}$ we still see the effect in the visible wavelengths. We usually implement several masks in the same technological process to efficiently use the available surface of the 1/2-VECSEL structure, and also to be able to test different functions without changing the experimental conditions (the structure, the pump, the cavity configuration and so on). Each mask in the set, has a typical surface of $\sim 200 \mu\text{m} \times 200 \mu\text{m}$ ($\sim 3 \times 3$ times the fundamental mode surface $\sim 40 \mu\text{m}$) which ensures that each mask overlaps sufficiently with the cavity transverse mode.

Each mask implements a specific phase or (and) amplitude function, such as the one shown in Fig 3.13b which consists of crossed lines surrounded by a bright

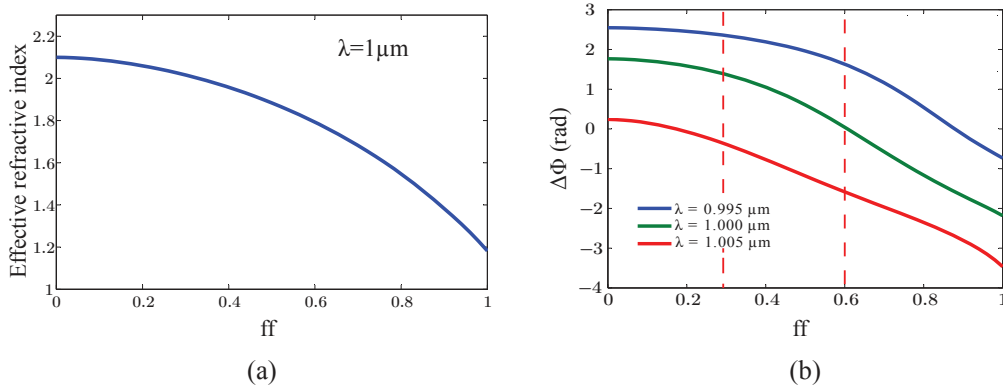


Figure 3.10: (a) Effective refractive index, and (b) phase-shift experienced by reflected waves, calculated as a function of the fill factor for the multilayer structure shown in Fig 3.9.

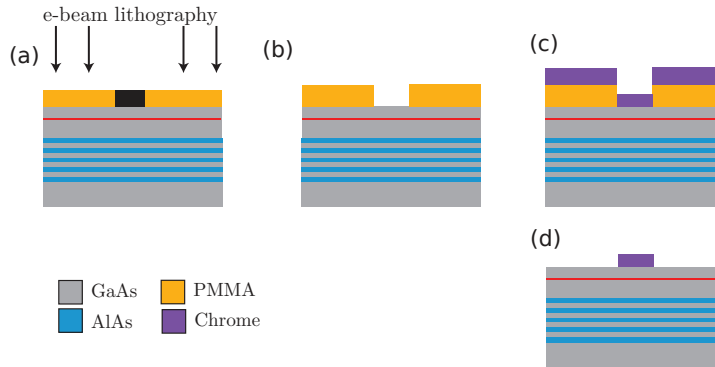


Figure 3.11: Technological process of fabrication of the metallic mask integrated on the VECSEL gain-mirror. a) e-beam lithography; b) PMMA development; c) chromium deposition; d) lift-off.

rectangular pattern. This crossing lines are diffraction grating with high diffraction loss, it plays the role of an amplitude mask by introducing high diffraction loss. The outer rectangular pattern consists of a 15 nm thick chromium layer, its purpose is to limit the active zone by introducing high absorption where we don't want light emission. The elements of this mask are shown in the SEM photograph of Fig 3.14a, the whole set is represented in Fig 3.14a, while Fig 3.14b, and Fig 3.14c show two successive zooms in the crossed-lines mask.

The second mask example we take is shown in Fig 3.13c, we can recognize the bright surrounding chromium region which has the same role as in the previous mask. If we go to the mask center, we can see an azimuthal gradient (from bright to dark orange) produced by a gradient of the artificial refractive index, implemented by varying the fill factor of periodic holes as shown in the SEM photograph of Fig 3.14d,e And in the center of the mask there is a phase step that introduce high diffraction loss locally. We will use the two mask examples shown here, in Chap 4,

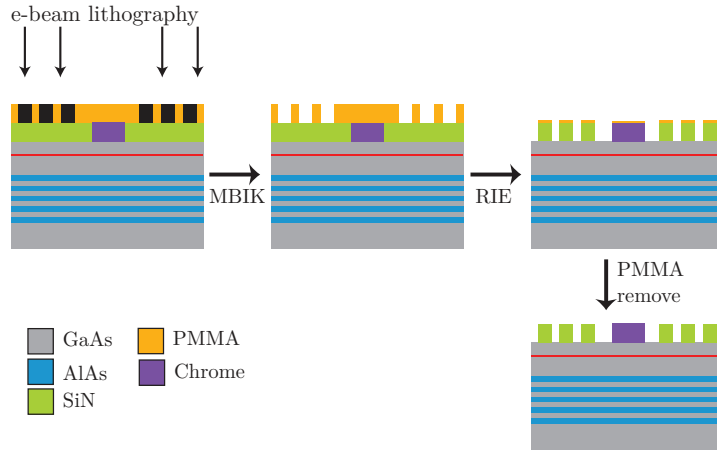


Figure 3.12: Technological process of fabrication of stacked phase and intensity masks integrated on the VECSEL gain-mirror.

where we shall describe what is the role of each mask in mode selection. But, for the time being, let us discuss the main limitations of this technology and how we may overcome them.

3.4.6 Laser test procedure

Most of these masks are visible using the photoluminescence light produced by pumping the 1/2-VCSEL, this is very useful because it will help us to precisely place the right mask in the pumped region. To do this we use an in-house two-lenses plus a 2D camera imaging system with a resolution of $\sim 1 \mu\text{m}$. To filter out the pump light's scattering, we use a high-pass optical filter ($\lambda > 980 \text{ nm}$). This enables us to see the pumped region and the overlap with the mask. This is illustrated in Fig 3.15a and Fig 3.15b where we show two examples of recorded 2D photoluminescence charts with a large pump spot illuminating a mask with azimuthally varying artificial refractive index in (a), and focused pump spot illuminating a two-crossed lines mask in (b).

3.4.7 Limitations of the technology

The technology we demonstrated here allows to introduce in principle an arbitrary phase and amplitude pattern to modulate the wavefront and the intensity of the intracavity lasing field. Using subwavelength metallic layer, we realized large masks of the order of few $100 \mu\text{m}$ with good thickness homogeneity (of the order of few nanometers). And using a metamaterial layer allows in principle to introduce any phase function, but for this, the achievable total phase difference must reach 2π . The refractive index variations are bounded by the Weiner bounds Eq 3.1. In our case the meta-atom consists of air plus dielectric material with a thickness $e = \lambda/2$ ($\simeq 300 \text{ nm}$). The refractive index has then a lower limit $n_{eff}^{min} = n_{air}$ and an upper

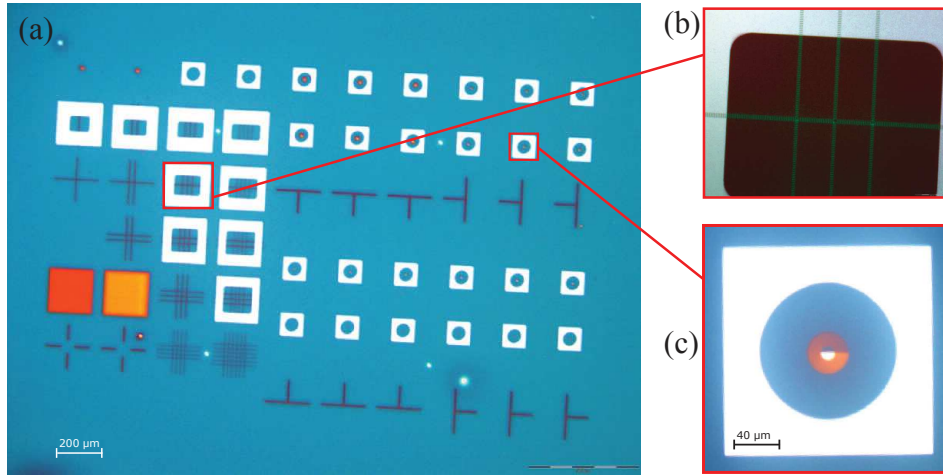


Figure 3.13: (a) Optical microscope photograph of a double-layered set of masks (10 nm thick patterned Chromium layer + 280 nm thick SiN-based metamaterial layer) fabricated on the Gas680 1/2-VCSEL. (b) Zoom on a mask example, the crossed lines are highly lossy diffractive gratings and the bright surrounding pattern is made of an absorbing chromium layer. (c) Zoom on an example of a mask with azimuthal refractive index gradient.

limit $n_{eff}^{max} = n_{SiN}$. This can be also seen from RCWA simulations of the artificial refractive index shown in Fig 3.10a, calculated with the structure illustrated in Fig 3.9. However, these bounds are reduced by some technological limits. For example the e-beam lithography imposes a minimum hole diameter, in our case this limit is 20 nm. And one has to leave a distance of ~ 50 nm between two adjacent holes in order to ensure that there is a sufficient amount of material to prevent the structure from collapsing. We also choose to work in a region where the n_{eff} show linear dependence with ff, this limits the $ff \in [0.3 - 0.6]$. At the end, with our material choice and with a metamaterial layer placed on the top of a resonant 1/2-VCSEL structure we obtain a total phase difference $\simeq \pi/2$. To extend this phase difference range, although not without difficulty, several solutions can be considered, like increasing the metasurface thickness: the challenge here is to make very deep holes while keeping a good homogeneity, which is quite challenging with wet-etching techniques. Other options would be to choose another material with higher refractive index, this material has to offer the possibility of selective etching as well, like GaAs on AlAs.

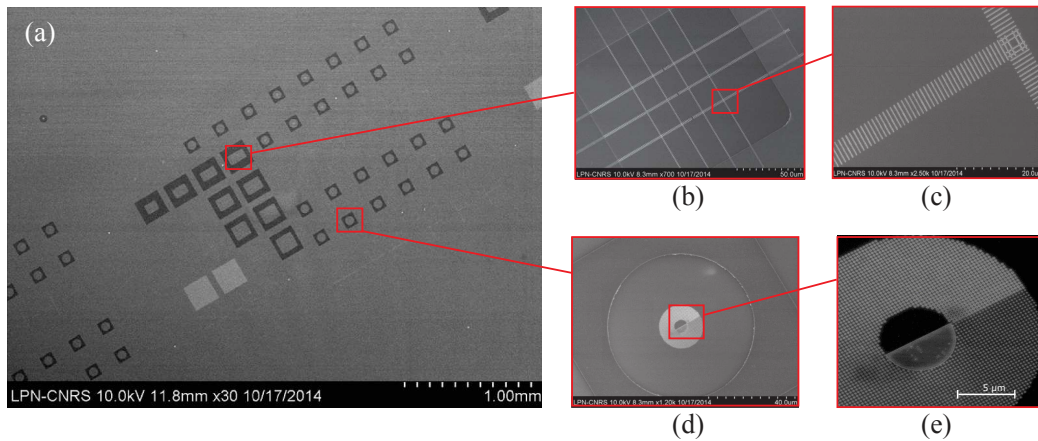


Figure 3.14: Scanning electron microscope photograph of the same masks set shown in Fig 3.13 (a) the whole set of masks, (b,c) zoom in the crossed lines mask, (d,e) zoom in the mask with azimuthal refractive index gradient and a phase step at the center.

3.5 Related work: intracavity mode control technologies

3.5.1 Intracavity conventional thick optics

This method consists in introducing conventional optical elements such as lenses, axicons, apertures, absorbers and phase elements in plano-concave cavity (supporting LG basis), or conical-concave cavity (supporting Bessel-Gauss basis), to alter intracavity wavefront. This approach has been investigated through an impressive set of experimental work. Various techniques have been studied, such as shaping the pump beam to match the wanted mode profile [Bisson 2004, Bisson 2005, Chen 2001, Kim 2011, Kim 2013] or adding intracavity absorbers (e.g. opaque disk on the output mirror [Harris 1994a, Naidoo 2011], a spot-defect mirror [Ito 2010]). A mirror with modulated reflectivity has also been used to obtain high order LG mode [Kozawa 2008, Hamazaki 2008], or high order Bessel-Gauss mode [Putnam 2012]. In other works researchers reported using intracavity spherical aberrations to alter the mode wavefront, these aberrations were obtained by intracavity lens [Senatsky 2009, Thirugnanasambandam 2010], or thanks to thermal lens in the gain medium [Okida 2007, Okida 2009, He 2011]. These methods are very popular within open-cavity-lasers community, such as solid state lasers, and have provided the basis for many successful demonstrations. However, their main disadvantage is that very often the mode quality (purity and spatial coherence) is greatly deteriorated by misalignments of the intracavity elements, which are most of the time movable, leading to strong distortions in the mode profile, and sometimes to strong differences between the near-field and the far-field of the generated modes, which implies strong perturbation of the cavity eigen-basis. Another limitation of

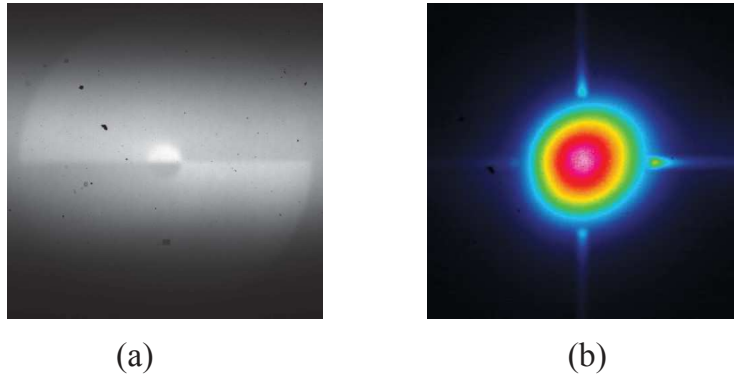


Figure 3.15: 2D photoluminescence charts obtained with (a) large pump spot illuminating a mask with azimuthally varying artificial refractive index, (b) focused pump spot illuminating a two-crossed lines mask.

these selection methods, is that the accessible set of modes is limited by optical functionalities achievable by conventional optics.

More recently intracavity mode control using a spatial light modulator (SLM) has been demonstrated in a DPSSL [Ngcobo 2013, Burger 2015]. In this method an SLM, which is a computer-controlled reconfigurable phase hologram, is used as one of the cavity mirrors. Then, by altering the digital hologram, a phase and/or amplitude modulation can be implemented. This method presents two main advantages, the first one is that it enables to implement any phase or amplitude function in principle. The second is the current availability of these devices. It should be noted, however, that SLMs introduce high losses (15 – 20%), due to the overall diffraction efficiency as well as the losses due to the fill factor (useful surface/total surface). Furthermore, these devices are usually based on liquid crystals (LC), therefore, maximum intracavity power is limited by the boiling temperature of these LC (Maximum power density $\sim 1\text{W}/\text{cm}^2$) [Beck 2010]. Moreover, the device size makes the laser systems cumbersome and unsuitable for integration.

3.5.2 Subwavelength structures in laser cavities

To our best knowledge, there is no work reporting the use of metamaterials for wavefront shaping inside a laser cavity. Reported work related to intracavity subwavelength structures, focuses on using photonic crystal mirrors, for example to replace the bulky Bragg mirror in VCSELs [Boutami 2007, Huang 2007], or to make polarization selective reflectors [Kim 2012]. Therefore we describe here some wavefront shaping devices based on subwavelength structures, demonstrated extracavity. Our goal is to discuss the potential for using these approaches in intracavity mode control scheme.

Metamaterial based devices have been first achieved in the microwave domain of the electromagnetic spectrum, to develop lightweight microwave antennas and radar absorbers [Zouhdi 2008]. More recently an optical photonic crystal-based flat lens,

operating in the near-field has been reported [Fabre 2008]. A flat dielectric grating reflector with focusing abilities has also been demonstrated [Fattal 2010]. This device uses non-periodic patterning of one dimensional grating to achieve the focusing ability (see Fig 3.16). However, the demonstrated reflector shows significant losses (10 ~ 20%), and the technique used to alter the wave front, severely restricts the achievable phase functions. Metamaterials based on a two-dimensional lattice of subwavelength metallic elements (meta-atoms) usually called meta-surfaces, provide a large capacity (2π coverage) of wave front manipulation [Yu 2014]. However, the biggest obstacle between these novel devices and real world applications is their low efficiency, due to dissipative losses¹.

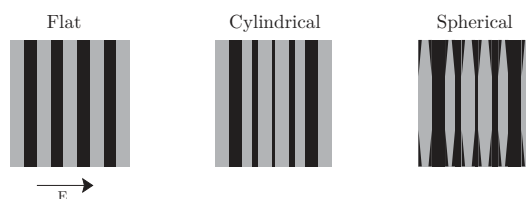


Figure 3.16: Schematic of the flat reflector with focusing ability proposed in [Fattal 2010] it shows the groove distribution for the three structures: flat (left), cylindrical (middle) and spherical (right) SWG mirrors.

3.6 Demonstration and characterization of a VeCSEL integrating metamaterial based flat-optics

In this part we present our paper that aims to demonstrate the potential of the novel method we developed here, the next step is to build a VECSEL with an integrated intracavity flat optics using metamaterials. A good point where to start to prove the feasibility of this concept is to replace the traditional curved output coupler by a flat semiconductor mirror with integrated flat optics that reproduces the spherical phase function required to achieve intrinsically single-mode, stable plano-concave cavity. This will allow us to accurately verify the implemented phase function by merely studying the stability of the cavity. Furthermore, by analyzing the spatial coherence of the beam (its wavefront fluctuations) any aberrations could be detected. Moreover, the finesse of the cavity can be determined by measuring the RIN of the laser, which will allow us to accurately determine the intracavity losses.

¹A novel all dielectric meta-surface type to enhance the overall efficiency has been investigated [Decker 2015], this work has not been published yet when we proposed our approach.

Photonic Crystal-based flat lens integrated on a Bragg mirror for High-Q external cavity low noise laser

M. S. Seghilani,¹ M. Sellahi,¹ M. Devautour,¹ P. Lalanne,³ I. Sagnes,²
G. Beaudoin,² M. Myara,¹ X. Lafosse,² L. Legratiet,² J. Yang,³
and A. Garnache^{1,*}

¹ Institut d'Electronique du Sud, CNRS-UMR 5214, Université Montpellier 2, France

² Laboratoire de Photonique et de Nanostructures, CNRS-UPR 20, 91460 Marcoussis, France

³ Laboratoire Photonique, Numérique et Nanosciences, Institut d'Optique d'Aquitaine,
Université Bordeaux, CNRS, 33405 Talence, France

*arnaud.garnache@ies.univ-montp2.fr

Abstract: We demonstrate a high reflectivity ($> 99\%$), low-loss ($< 0.1\%$) and aberrations-free (2% of λ rms phase fluctuations) concave Bragg mirror (20mm radius of curvature) integrating a photonic crystal with engineered spherical phase and amplitude transfer functions, based on a III-V semiconductors flat photonics technology. This mirror design is of high interest for highly coherent high power stable external cavity semiconductor lasers, exhibiting very low noise. We design the photonic crystal for operation in the pass band. The approach incorporates spatial, spectral (filter bandwidth = 5nm) and polarization filtering capabilities. Thanks to the mirror, a compact single mode TEM_{00} 2mm-long air gap high finesse (cold cavity Q-factor $10^6 - 10^7$) stable laser cavity is demonstrated with a GaAs-based quantum-wells 1/2-VCSEL gain structure at $1\mu m$. Excellent laser performances are obtained in single frequency operation: low threshold density of $2kW/cm^2$ with high differential efficiency (21%). And high spatial, temporal and polarization coherence: TEM_{00} beam close to diffraction limit, linear light polarization ($> 60dB$), Side Mode Suppression Ratio $> 46dB$, relative intensity noise at quantum limit ($< -150dB$) in 1MHz-84GHz radio frequency range, and a theoretical linewidth fundamental limit at 10 Hz (Q-factor $\sim 3.10^{13}$).

© 2014 Optical Society of America

OCIS codes: (140.3570) Lasers, single-mode; (140.5960) Semiconductor lasers; (140.7260) Vertical cavity surface emitting lasers; (050.5298) Photonic crystals; (230.1950) Diffraction gratings; (140.3300) Laser beam shaping.

References and links

1. M. Kuznetsov, M. Stern, and J. Coppeta, "Single transverse mode optical resonators," *Opt. Express* **13**, 171–181 (2005).
2. N. Laurand, C. L. Lee, E. Gu, J. E. Hastie, S. Calvez, and M. D. Dawson, "Microlensed microchip VECSEL," *Opt. Express* **15**, 9341–9346 (2007).
3. A. Laurain, M. Myara, G. Beaudoin, I. Sagnes, and A. Garnache, "Multiwatt-power highly-coherent compact single-frequency tunable vertical-external-cavity-surface-emitting-semiconductor-laser," *Opt. Express* **18**, 14627–14636 (2010).
4. A. Garnache, A. Ouvrard, and D. Romanini, "Single-frequency operation of external-cavity VCSELs: Non-linear multimode temporal dynamics and quantum limit," *Opt. Express* **15**, 9403–9417 (2007).

5. S. Boutami, B. Benbakir, X. Letartre, J. L. Leclercq, P. Regreny, and P. Viktorovitch, "Ultimate vertical Fabry-Perot cavity based on single-layer photonic crystal mirrors," *Opt. Express* **15**, 12443–12452 (2007).
6. M. C. Y. Huang, Y. Zhou, and C. J. Chang-Hasnain, "A surface-emitting laser incorporating a high-index-contrast subwavelength grating," *Nat. Photonics* **1**, 119–122 (2007).
7. J.-H. Baek, D.-S. Song, I.-K. Hwang, H.-H. Lee, Y. Lee, Y. -G. Ju, T. Kondo, T. Miyamoto, and F. Koyama, "Transverse mode control by etch-depth tuning in 1120-nm GaInAs/GaAs photonic crystal vertical-cavity surface-emitting lasers," *Opt. Express* **12**, 859–867 (2004).
8. T. Czuszanowski, M. Dems, H. Thienpont, and K. Panajotov, "Optimal radii of photonic crystal holes within DBR mirrors in long wavelength VCSEL," *Opt. Express* **15**, 1301–1306 (2007).
9. N. Fabre, L. Lalouat, B. Cluzel, X. Mélique, D. Lippens, F. de Fornel, and O. Vanbésien, "Optical near-field microscopy of light focusing through a photonic crystal flat lens," *Phys. Rev. Lett* **101**, 073901 (2008).
10. F. Brückner, D. Friedrich, T. Clausnitzer, M. Britzger, O. Burmeister, K. Danzmann, E.-B. Kley, A. Tünnermann, and R. Schnabel, "Realization of a monolithic high-reflectivity cavity mirror from a single silicon crystal," *Phys. Rev. Lett.* **104**, 163903 (2010).
11. M. M. Vogel, M. Rumpel, B. Weichelt, A. Voss, M. Haefner, C. Pruss, W. Osten, M. A. Ahmed, and T. Graf, "Single-layer resonant-waveguide grating for polarization and wavelength selection in Yb:YAG thin-disk lasers," *Opt. Express* **20**, 4024–4031 (2012).
12. D. Fattal, J. Li, Z. Peng, M. Fiorentino, and R. G. Beausoleil, "Flat dielectric grating reflectors with focusing abilities," *Nat. Photonics* **116**, 1–5 (2010).
13. V. Lousse, W. Suh, O. Kilic, S. Kim, O. Solgaard, and S. Fan, "Angular and polarization properties of a photonic crystal slab mirror," *Opt. Express* **12**, 1575–1582 (2004).
14. S. Boutami, B. Benbakir, H. Hattori, X. Letartre, J. L. Leclercq, P. Rojo-Romeo, M. Garrigues, C. Seassal, and P. Viktorovitch, "Broadband and compact 2D photonic crystal reflectors with controllable polarization dependence," *IEEE Photonics Technol. Lett.* **18**, 835–837 (2006).
15. P. Lalanne, S. Astilean, P. Chavel, E. Cambriil, and H. Launois, "Blazed binary subwavelength gratings with efficiencies larger than those of conventional échelette gratings," *Opt. Lett.* **23**, 1081–1083 (1998).
16. The free-software used for the calculation can be downloaded at <http://www.lp2n.institutoptique.fr/Membres-Services/Responsables-d-equipe/LALANNE-Philippe>.
17. M. G. Moharam, E. B. Grann, D. a. Pommet, and T. K. Gaylord, "Formulation for stable and efficient implementation of the rigorous coupled-wave analysis of binary gratings," *J. Opt. Soc. Am. A* **12**, 1068–1076 (1995).
18. P. Lalanne and G. M. Morris, "Highly improved convergence of the coupled-wave method for TM polarization," *J. Opt. Soc. Am. A* **13**, 779–784 (1996).
19. L. Li, "New formulation of the Fourier modal method for crossed surface-relief gratings," *J. Opt. Soc. Am. A* **14**, 2758–2767 (1997).
20. C. Ribot, M. S. L. Lee, S. Collin, S. Bansropun, P. Plouhinec, D. Thenot, S. Cassette, B. Loiseaux, and P. Lalanne, "Broadband and efficient diffraction," *Adv. Opt. Mater.* **1**, 489–493 (2013).
21. A. E. Siegman, *Lasers* (University Science Books, 1986).
22. A. Laurain, M. Myara, G. Beaudoin, I. Sagnes, and A. Garnache, "High power single-frequency continuously-tunable compact extended-cavity semiconductor laser," *Opt. Express* **17**, 9503–9508 (2009).
23. A. Garnache, A. Ouvrard, L. Cerutti, D. Barat, A. Vicet, F. Genty, Y. Rouillard, D. Romanini, and E. A. Cerda-Méndez, "2–2.7 μm single frequency tunable Sb-based lasers operating in CW @ RT: Microcavity and external-cavity VCSELs, DFB," *Proc. SPIE* **6184**, 61840N (2006).
24. M. Devautour, A. Michon, G. Beaudoin, I. Sagnes, L. Cerutti, and A. Garnache, "Thermal management for high-power VCSEL emitting in the near- and mid-IR," *IEEE J. Sel. Top. Quantum Electron.* **19**, 1701108 (2013).
25. L. A. Coldren and S. W. Corzine, *Diode Lasers and Photonic Integrated Circuits* (John Wiley, 1995).
26. K. Petermann, *Laser Diode Modulation and Noise* (Kluwer Academic, 1991).
27. M. Myara, M. Sellahi, A. Laurain, A. Garnache, A. Michon, and I. Sagnes, "Noise properties of NIR and MIR VCSELs," *Proc. SPIE* **8606**, 86060Q (2013).
28. C. Henry, "Theory of the phase noise and power spectrum of a single mode injection laser," *IEEE J. Quantum Electron.* **19**(9), 1391–1397 (1983).
29. F. Riemenschneider, M. Maute, H. Halbritter, G. Boehm, M.-C. Amann, and P. Meissner, "Continuously tunable long-wavelength MEMS-VCSEL with over 40-nm tuning range," *IEEE Photonics Technol. Lett.* **16**, 2212–2214 (2004).
30. F. Riemenschneider, I. Sagnes, G. Böhm, H. Halbritter, M. Maute, C. Symonds, M.-C. Amann, and P. Meissner, "A new concept for tunable long wavelength VCSEL," *Opt. Commun.* **222**, 341–350 (2003).

1. Introduction

High quality factor (high-Q) spatially stable optical cavities are key elements in achieving highly coherent high power semiconductor laser sources [1] required in many advanced applications such as coherent laser detection, high resolution spectroscopy, lidar ...etc. Those high-Q

cavities are usually realized using polished dielectric concave mirrors or micro-lenses [2], in a concave-type stable cavity, and applied mostly in high finesse extended-cavity lasers, as for example Vertical-External-cavity-Surface-Emitting-Lasers, which offer the possibility to add some functionalities like spectral filtering and polarization control, by introducing movable optical-elements into the cavity. However, such a design usually results in a bulky and complex optical system. Moreover, it induces extra losses, which is at the expense of the cavity finesse, and the mechanical noise is usually large. All these features thus limit the temporal coherence, and exclude a broad continuous spectral tunability. Another solution to realize a stable plano-concave cavity is to use the thermal lens-based stability [3], but thermal lenses are difficult to control and introduces aberrations in the laser beam. These two solutions become very limited when accurate control of phase and intensity profile of the wave in the cavity is needed, for the purpose of thermal lens compensation or wavefront correction, lossless transverse mode selection, frequency or polarization filtering...etc.

Our goal is to develop an integrated III-V semiconductor flat photonic technology which allows to design a high finesse air gap stable paraxial optical cavity, with a large transverse mode area ($\gg \lambda^2$) for high power laser operation. For high spatial, temporal and polarization coherence, such a high-Q laser cavity has to stabilize or to dynamically select a single eigenstate of light in the optical cavity orthogonal basis functions, with high weak state suppression ratio: a unique transverse mode (in Laguerre-Gauss basis e.g.), a single (linear e.g.) polarization state, a single longitudinal mode for single frequency operation. To reach such a high coherent state, we push the laser cavity design to exhibit weak quantum noise for photon intensity (close to shot noise limit), and photon phase or frequency (at the Hz level), so to be free of amplified spontaneous emission thanks to free space propagation in a mm to cm-long air gap cavity (thus tunable). The cold cavity can be designed to be single transverse mode [1], with intracavity birefringence and loss dichroism regarding linear polarization eigenstates [3]. Exploiting quantum-well VCSEL technology, the active laser cavity can be designed to exhibit a homogeneous gain dynamics, free of complex non-linear dynamic behavior, to strongly select a unique longitudinal mode and single linear polarization state [3, 4].

In recent years there has been a growing interest in Photonic Crystal Mirrors (PCM), which have been extensively studied for realizing high-Q cavities, essentially used in Vertical Cavity Surface emitting Lasers (VCSELs), for example by introducing a photonic crystal (PC) slab instead of conventional DBR mirror [5], or by using a hybrid top mirror combining High-index Contrast Grating (HCG) and a conventional DBR [6], to reduce the thickness of the top mirror. A hybrid PCM for transverse single mode stabilization in VCSELs has been also reported [7, 8], the mode stabilization was done by introducing PC pattern into the top DBR mirror. In all these works the PCM was used in monolithic VCSEL called PC-VCSEL, and to our best knowledge there is no report of high-Q PC-based external cavity semiconductor lasers. In the field of nanophotonic devices, a highly lossy cylindrical PC lens operating in the near field [9] have been demonstrated; however this is not usable for external cavity lasers operating in the far-field.

Other subwavelength grating reflectors based on SiO₂/Si have been reported, like highly reflective flat broadband mirror [10] and flat narrowband mirror with moderate reflectivity [11]. A flat mirror with focusing ability has been also realized by modulating the groove width of non periodic subwavelength grating [12] based on SiO₂/Si and amorphous silicon, but the reflectance of the mirror was in the range 80-90% making it not suitable for high finesse cavities. Furthermore, in contrast to III-V semiconductor based PCMs which can be integrated directly on active devices, integrating SiO₂/Si-based mirrors is more challenging and need additional technological processes.

In this work using a 2D PC on Bragg mirror, operating in the far field domain (diffractive optics), we demonstrate a low-loss, high reflectivity and aberrations-free PCM with engineered

spherical phase transfer function and amplitude transfer function, based on a III-V semiconductor flat photonics technology. This PCM is used for the development of a highly coherent, high power stable external cavity single frequency semiconductor laser, stabilizing a unique transverse mode. Its operation differs from the usual operation of PCs. Indeed, in most PC-based devices PCs are used in their photonic band gap regime. However, the virtue of PCs is not only to provide photonic band gaps, they also allow an accurate control of the transverse profile of the phase and the intensity of transmitted (reflected) waves. In addition PCs present additional assets, like the introduction of spectral filtering and polarization filtering (birefringence and loss dichroism) in the optical response, depending on the lattice type [13, 14]. In this report we firstly explain the principle and the design of the PC mirror; then we present the fabrication process and the characterization of the PC-based flat mirror, with spherical phase function. Finally, we use our beam shaping PCM in a mm-long single transverse mode Vertical External Cavity Surface Emitting Laser (VECSEL), and demonstrate a compact, highly coherent low noise high power single frequency tunable semiconductor laser.

2. Design of the PCM and principle

2.1. Principle

The objective is to generate a flat optics having various optical functionalities to stabilize a single light state in a high-Q stable optical cavity: like a concave mirror with aperture, spectral filter and linear polarization filter. To design the elementary PC cell, we used the method developed in [15] for diffractive elements composed of graded subwavelength features. As depicted in Fig. 1(a), the PCM consists of a conventional 1D Bragg mirror made of GaAs/AlAs layers on a GaAs substrate (the reflectivity is $R = 98.8\%$), and a multiple of $\lambda/2$ -thick GaAs spacer above the Bragg mirror. On top of the thin film stack, a single Si_3N_4 layer is perforated by a 2D array of holes placed on a square grid, of period a . The holes diameters h_r vary and implement a precisely-controlled graded-phase profile at the lasing wavelength, and a radially-dependent reflection profile, acting as an amplitude mask.

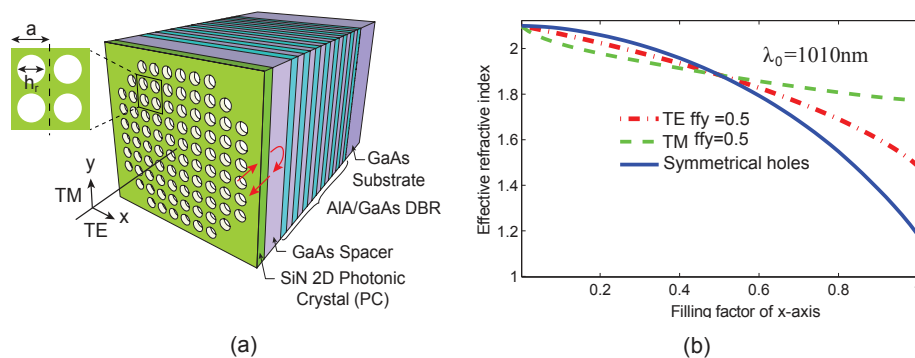


Fig. 1. (a) Schematic representation of the PCM structure investigated in this study. The arrows represent path of optical waves. (b) Effective refractive index of the PC artificial material made of a Si_3N_4 layer perforated by a 2D periodic array of air holes placed on a square lattice. For circular holes (blue curve) and for elliptical holes (red and green curves).

Generally two-dimensional arrays of subwavelength indentations support several propagative Bloch modes and do not behave as artificial materials with a well-defined effective index. However, when the period a of the array is smaller than the structural cutoff period $a_s = \lambda_0/n_{\text{Si}_3\text{N}_4}$ [15], only a single fundamental Bloch mode carries energy for every polar-

ization, with all the other ones being evanescent, and the array can be considered as an artificial material with an effective refractive index equal to the normalized propagation constant of the fundamental Bloch mode. In addition, as the perforated dielectric thin film acts as a diffraction grating at normal incidence, two additional conditions have to be fulfilled to ensure that only the zeroth-orders in transmission and reflection are diffracted: $a < \lambda_0/n_{air}$ and $a < \lambda_0/n_{spacer}$. Actually, since $n_{spacer} > n_{SiN} > n_{air}$, the upper bound for the period is given by:

$$a \leq \lambda_0/n_{spacer} \quad (1)$$

Providing that the condition of Eq. (1) is fulfilled at the lasing wavelength, the laser wave experiences an artificial material with an effective index n_{eff} as it propagates through the PC. Figure 1(b) shows the dependence of n_{eff} with the fillfactor. The effective indices have been calculated by assuming that the holes are regularly placed on a square lattice with a period a , using a free software [16] based on the Rigorous Coupled Wave Analysis (RCWA) [17–19]. Tiny air holes correspond to a dense artificial dielectric with a large effective index close to the refractive index of the bulk Si_3N_4 material, whereas large hole areas implement low refractive-index artificial dielectrics. Through a careful control of the hole diameters h_r , the transverse phase-transfer-function of the PCM can be engineered to be spherical, and the PCM then operates in a similar manner as a concave mirror. Moreover, the transverse amplitude transfer function is also affected; it is not flat and it generates an amplitude mask acting as an aperture as well. Polarization control may be introduced by using elliptical PC-holes, so that TE and TM-polarized waves experience different refractive indices. This is shown in Fig. 1(b) where we calculated the effective refractive index of the PC with asymmetrical holes. The holes diameter along the y-axis f_y is set to 0.5, while the filling factor f_x along the x-axis is varied. The curves show that, except for $f_x = 0.5$ (which means that we fall on the symmetrical case), the effective refractive indices are different for TE and TM-polarized waves, making the meta-material birefringent.

As shown in Fig. 2 and Fig. 3 the dependence of the reflected beam's phase with the filling factor is strongly impacted by other parameters, such as the PC thickness and the high index semiconductor spacer thickness. To enhance the phase/amplitude variation with the filling factor, we can choose the spacer thickness and the PC-layer thickness as multiple of $\lambda_0/2$ for a fixed f (we choose $f = 0.55$), thus the multilayer structure between the DBR and the air exhibits longitudinal Fabry-Perot resonance as shown in Fig. 2(a), for comparison Fig. 2(b) shows an anti-resonant structure. In the resonant case the PC effect is maximized, i.e fast induced phase-difference with f and higher intensity transmission.

2.2. Design and simulation

To obtain the adequate indentation distribution we performed RCWA simulation by varying the filling factor of the PC. Figure 3 shows the PCM reflectivity and phase-difference of the reflected wave as a function of the filling factor f with $\lambda/2$ -thick PC layer. The reflectivity remains high for all filling factors, and importantly the phase varies monotonically with the filling factor, and it depends on the PC-layer thickness. Figure 4 shows that with a $3\lambda/2$ -thick PC layer we can achieve more than 2π phase differences, so the first Fresnel zone can be reached. The phase-difference is also wavelength dependent (see Fig. 3(b)). The chromaticity has been recently exploited to fabricate diffractive optical elements that remains blazed over one octave [20]. In the present case, it offers an extra degree of freedom to enhance the spectral-filtering capability to the PCM.

We took advantage of above-mentioned features of the PCM, to design a high-Q stable laser resonator, see Fig. 5(a). It consists of a highly reflective gain mirror, and a PCM with spherical phase function, and a finite deflection acting like an aperture, which add a transverse intensity

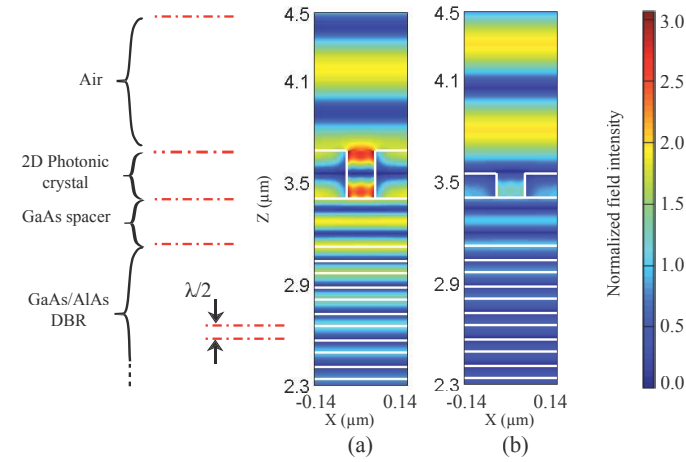


Fig. 2. Simulated amplitude of the transverse E-field in the PCM (at $\lambda = 1.01\mu\text{m}$ Spacer thickness=142nm, $a=280\text{nm}$): (a) Resonant PCM structure, PC-layer thickness=280nm. (b) Anti-Resonant PCM structure, PC-layer thickness=140nm

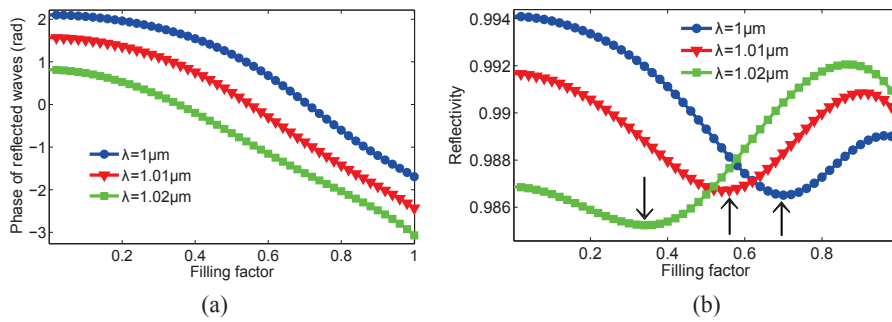


Fig. 3. (a) Phase of the reflected plane waves by PCM as a function of the filling factor at work wavelength $\lambda_0 = 1010\text{nm} \pm 10\text{nm}$ (PC thickness=280nm, Spacer thickness=142nm, $a=280\text{nm}$). (b) Corresponding PCM reflectivity, black arrows show the optical resonance effect moving when the wavelength changes.

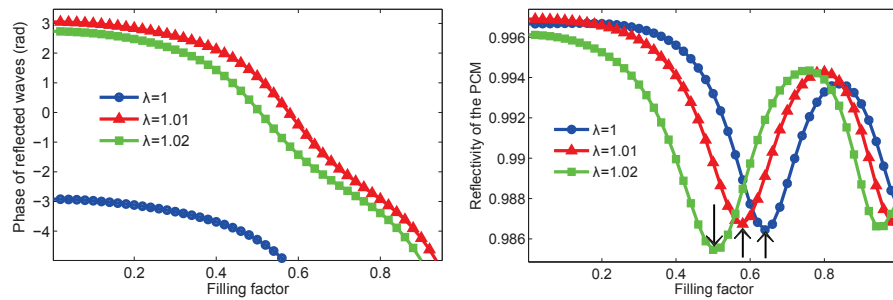


Fig. 4. (a) Phase of the reflected plane waves by PCM as a function of the filling factor at work wavelength $\lambda_0 = 1010\text{nm} \pm 10\text{nm}$ (PC thickness=840nm, Spacer thickness=142nm, $a=280\text{nm}$). (b) see caption in 3.

filtering of high order modes in the resonator. Figure 5(b) shows the equivalent intrinsically single transverse mode optical cavity, based on a finite deflection mirror [1].

This resonator is stable if the cavity length L_c is lower than the radius of curvature of the concave mirror R_c : $L_c < R_c$ see Fig. 5(c). The resonator length and the waist W_0 on the flat mirror of the TEM_{00} mode of the resonator, are fully governed by the radius of curvature of the concave mirror. Gaussian beam optics determines the Gaussian beam parameter q , which is related to the waist $W(z)$ and the radius of curvature of the wave front $R(z)$ at any plane z by the relation [21]

$$\frac{1}{q(z)} = \frac{1}{R(z)} - j \frac{\lambda}{\pi W^2(z)} \quad (2)$$

This Gaussian beam parameter must repeat after one round trip. At the plane mirror, one finds

$$q = -j\sqrt{L_c R_c - L_c^2} \quad (3)$$

The minimum waist for the Gaussian component of the beam occurs at the plane mirror and can be determined from $q = -jz_R$ where $z_R = \pi W^2/\lambda$. For the following calculations we chose a radius of curvature $R_c = 20mm$ and a resonator length $L_c = 1.8mm$ which results in $W_0 = 45\mu m$ for the working wavelength $\lambda_0 = 1010nm$. These parameters were selected as they give an intracavity beam with weak divergence, because we are within the Rayleigh range ($L_c < z_R$). This gives a total phase variation at the external mirror $\Delta\phi = 1.3rad$ over $r = 100\mu m$, and beam waist at the PCM $W(L_c) = 47\mu m$, which allows to reduce the constraints on the total needed phase-difference variations range, and to realize a compact design with PCM radius $r_{PCM} = 2W(L_c) \simeq 95\mu m$. Thanks to Gaussian beam optics, we have the exact transverse phase profile of the TEM_{00} mode of the cavity. The PCM must be engineered to conjugate the phase of this mode.

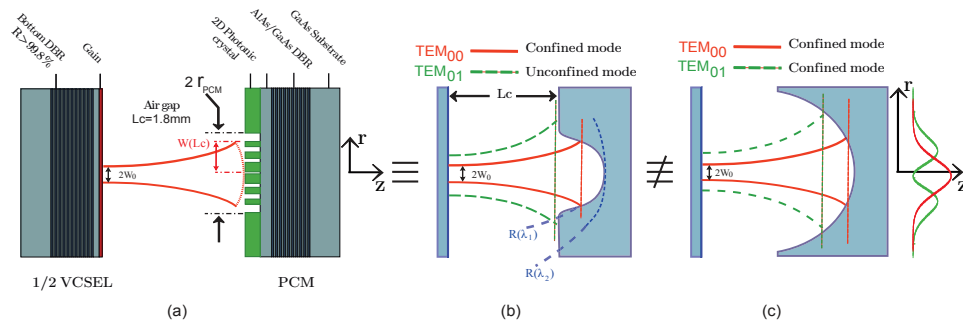


Fig. 5. (a) Schematic of the optical resonator: based on the gain mirror and PCM with spherical phase-difference transfer function. (b) Schematic of the equivalent intrinsically single mode optical resonator. (c) Classic multimode plano-concave optical resonator; Intensity profile of the 2 first Laguerre-Gauss resonator modes.

The last step before fabrication is the calculation of the filling factor distribution over the PCM, to realize the spherical phase function that conjugate TEM_{00} mode in the cavity. The curves in Fig. 6(a) show this distribution, and the simulated resulting phase difference, at the lasing wavelength $\pm 10nm$. This design is obtained using symmetrical holes. Figure 6(b) shows the corresponding PCM reflectivity, it shows a very high reflectivity, that varies very slowly all the way from the PCM center up to $100\mu m$. In Fig. 7 we show a design with elliptical holes to introduce polarization effect as discussed in the previous section. Thanks to the birefringence of the PC (see Fig. 1), the TE-polarized waves and TM-polarized waves experience different

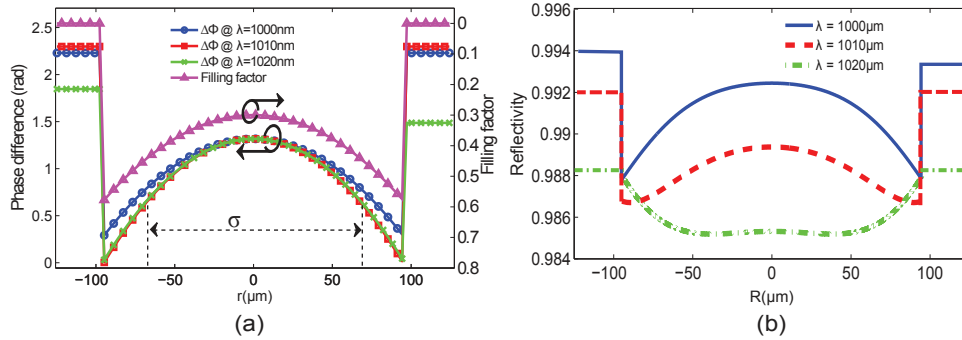


Fig. 6. (a) Filling factor profile needed to realize the spherical phase function as a function the radial distance from PCM center; the simulated resulting phase difference profile at work wavelength $\lambda_0 = 1010\text{nm} \pm 10\text{nm}$. (b) The resulting PCM reflectivity at work wavelength $\lambda_0 = 1010\text{nm} \pm 10\text{nm}$. (PC thickness=280nm, Spacer thickness=142nm, $a=280\text{nm}$)

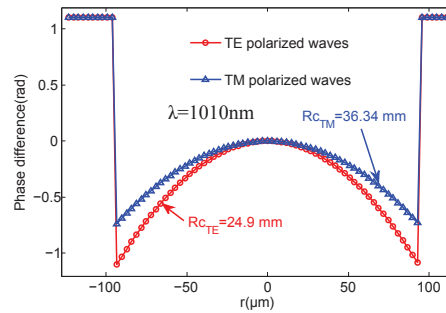


Fig. 7. Simulated resulting phase difference profile at work wavelength $\lambda_0 = 1010\text{nm}$ using elliptical holes ($f_x = 0.6$ and varying f_y). PC thickness=280nm, Spacer thickness=142nm, $a=280\text{nm}$. TE / TM-polarized waves experience different radius of curvature.

radius of curvature which means that the two polarization states will be stabilized with different mode's waist (here $W_0^{TE} < W_0^{TM}$) and experience different net modal gain ($Gain_{TE} > Gain_{TM}$). Thus for any cavity length $L_c < \min(R_{c_{TE}}, R_{c_{TM}})$ only the polarization state with higher net modal gain can reach threshold.

2.3. Advantages and limitations

As shown in Fig. 3(b) the phase of the reflected beam rapidly varies with the wavelength. The rapid variation is due to the highly dispersive nature of the artificial material; n_{eff} is highly chromatic, especially when operated at wavelengths close to the structural cutoff [20]. The rapid variation offers an extra degree of freedom to enhance the spectral-filtering capacity of the PCM, because at a fixed cavity length as the wavelength departs from the lasing wavelength, strong chromatic diffraction losses are introduced at the concave mirror and the cavity experiences additional losses, that would not be implemented with a classical refractive lens. To illustrate our purpose, Fig. 8(a) shows the evolution of the waist on the PCM for the fundamental mode of the optical cavity, as a function of the cavity length. Because the finite PCM diameter is acting as an aperture. We designed the cavity such that the waist of the fundamental transverse mode on the PCM equals half the mirror radius ($W_{TEM_{00}} = R_{PCM}/2$). so that the

99% aperture-criterion is fulfilled [21]. Thus, for waists below this radius more than 99% of the beam power is within the PCM surface, which is the case of our cavity at $\lambda_0 = 1010nm$. However at $\lambda = 1000nm$ for exactly the same cavity, this criterion is not fulfilled as the waist on the PCM is $8\mu m$ larger, and the mode is not well confined anymore in this high finesse cavity. This criterion defines a spectral bandwidth of the optical cavity stability with a Half Width Half Maximum = $5nm$ for $L_c = 2mm$ (see Fig. 8(b)), this bandwidth can be further reduced by increasing the cavity length.

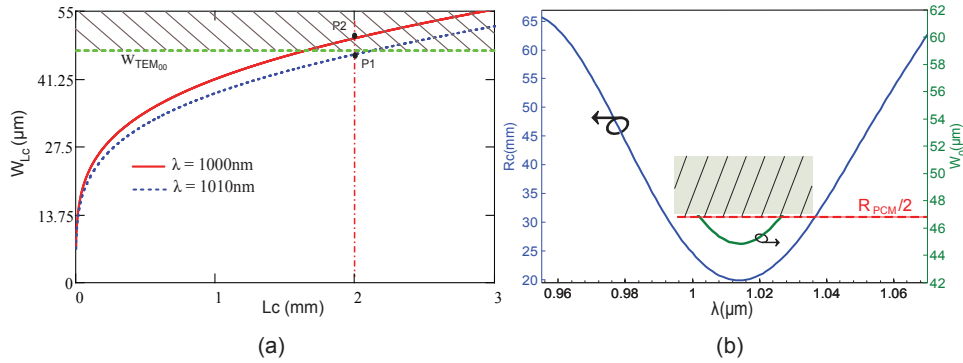


Fig. 8. (a) Evolution of the TEM_{00} 's waist on the PCM as a function of the cavity length at two lasing wavelengths $\lambda = 1010nm$ and $\lambda = 1000nm$. Dashed horizontal line shows the waist size corresponding to the 99% aperture-criterion due to the finite diameter of the PCM, the gray-shaded region is a forbidden stability region. P1 (resp.P2) shows the case where the 99% criterion is (resp. is not) fulfilled. (b) Evolution of the PCM radius of curvature as a function of the wavelength; Beam radius of the fundamental cavity mode for L_c , dashed horizontal line shows the same 99% criterion as in (a), it defines the cavity stability spectral bandwidth, this bandwidth can be reduced by increasing L_c .

Furthermore, the PCM offers the possibility to make the resonator intrinsically single transverse-mode, i.e it supports only the TEM_{00} mode, and to keep out all the higher order transverse Laguerre-Gauss (LG) modes which have a larger spatial extent (see Fig. 5(c)). This new class of intrinsically single transverse mode optical free-space resonators, were first introduced by Kuznetsov et al [1] using a quantum mechanical analogy: a potential well with an infinite potential barriers has an infinite number of confined energy states, and it is possible to confine only one state by reducing sufficiently the deepness or/and the width of the potential well. Analogously in optical resonators, if the depth of the mirror or the gradient index is limited, giving rise to the so-called finite deflection mirror, it is possible to obtain a resonator which fundamentally supports only a single confined mode as illustrated in Fig. 5(b). Following this principle, he established a criterion to get a single-mode resonator [1]

$$V \equiv \frac{\pi\sigma}{\lambda} \sqrt{d_0/L_c} < 2 \quad (4)$$

Where d_0 is the depth and σ is the Full Width Half Maximum FWHM of the finite depth mirror. However, it is worth noticing that for a realistic description of the cavity behavior the condition in Eq. (4) have to be used by taking the finesse into account. Because high finesse resonators can be intrinsically single mode, even for $V > 3$ [1]. As a conclusion, thanks to the PCM features the cavity can be designed to intrinsically provide single frequency and single transverse mode operation.

It is possible to adapt the design for other working wavelengths or to use other materials. Obviously one should take into account the properties of the materials involved, these materials

have to provide a very low absorption at the working wavelength, and to allow selective etching process on the semiconductor Bragg for high fabrication accuracy. For example it is possible to use a thicker SiO₂ PC layer with a lower index on GaAs, or GaAs PC on an oxide layer but this is a more challenging process. A GaAs PC would offer a higher index medium which allows a larger phase shift.

The maximum phase difference variation range depends upon the PC-layer thickness, and the filling factor variation range (see Fig. 3(a), Fig. 4(a)). The latter depends directly on the period (a) and the holes size, the typical technological limit gives a minimum thickness of 50nm between adjacent holes, to ensure that there is a sufficient amount of material and prevent the structure from collapsing. And the typical minimum hole size a_{min} is 20nm. Knowing that $f = h_r/a$ this two conditions can be written as follows:

$$\frac{20nm}{a} \leq f \leq 1 - \frac{50nm}{a} \quad (5)$$

But as shown in Fig. 3(a) the phase variation curves remain flat until $f \simeq 0.2$. In this work and for practical purposes we choose to work after this zone ($f \geq 0.2$).

In practice the designed filling factor profile has to be discretized before the implementation, to obtain laser-quality surface flatness: the step-phase due to discretization $\Delta\phi_{step}$ has to be smaller than $\lambda/10$. In our case $\Delta\phi_{step} \simeq \lambda/150$ thanks to the high resolution of the e-beam lithography.

3. Fabrication and characterization

The semiconductor structure holding the PC is grown on a GaAs substrate in a low pressure (70Torr) metal-organic chemical vapor deposition (MOCVD) VEECO D180 by using hydrogen as a carrier gas. It consists of a high reflectivity AlAs/GaAs Bragg mirror (20.5 pairs) with a $\lambda/2$ thick GaAs spacer on top. The technological process used to fabricate the PC holes is depicted in Fig. 9(a). Firstly a $\lambda/2$ thick Si₃N₄ was deposited by ion-beam-assisted electron-beam vacuum evaporation. Then a polymethyl methacrylate (PMMA) resist was spin-coated on the wafer and patterned by electron beam lithography (Vistec EBPG 5000 at 100kV) with 1.25nm of resolution. After PMMA development in methylisobutylketone (MIBK) solution, the PC holes are transferred to the SiN layer by Reactive Ion Etching (RIE), and finally the PMMA is removed. Figure 9 shows the reflectivity spectra of the DBR structure, it is centered at 1010nm. Figure 10(a) shows the scanning electron microscope (SEM) top view of the fabricated PCM with two filling factors $f = 0.3$ and $f = 0.6$. This PCM image was chosen to show the effect of the PC filling factor on the obtained meta-material refractive index, we can clearly see the difference in the Fig. 10(b) showing the same PCM using an optical microscope. Figure 10(c) shows the fabricated PCM with spherical phase profile, designed to match the phase profile of the beam in the stable cavity described in the previous section. The diameter of the PCM is $2r_{PCM} = 190\mu m$. In this figure we can clearly see the effect of the filling factor in the visible spectral range, it gives a good appreciation of the realized phase function, but this is not precise enough to be used as an accurate characterization method (GaAs is not transparent in the visible spectral range).

4. PC-based External-Cavity VCSEL

We used the PCM with a gain mirror to form a stable TEM₀₀ high-Q laser cavity. The GaAs-based gain mirror structure was also grown by MOCVD. It is composed of an epitaxial high-reflectivity (99.9%) bottom AlAs/GaAs Bragg mirror (31.5 pairs), and an active layer of $13\lambda/2$

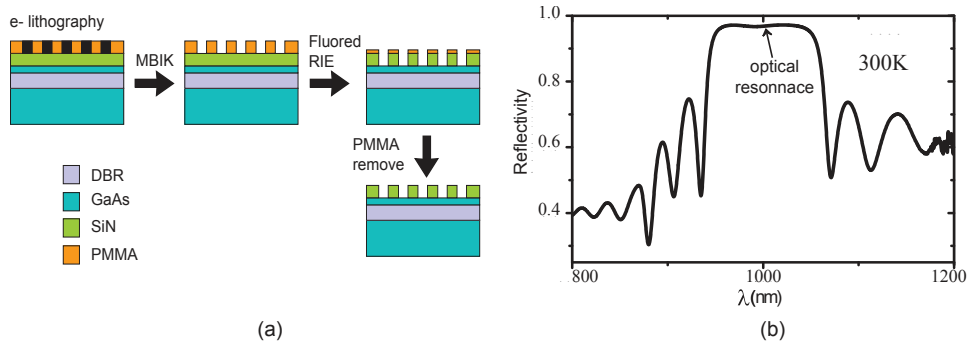


Fig. 9. (a) Technological process of fabrication of the PCM. (b) Reflectivity of the fabricated DBR structure holding the PC, the black arrow shows the optical resonance in the structure.

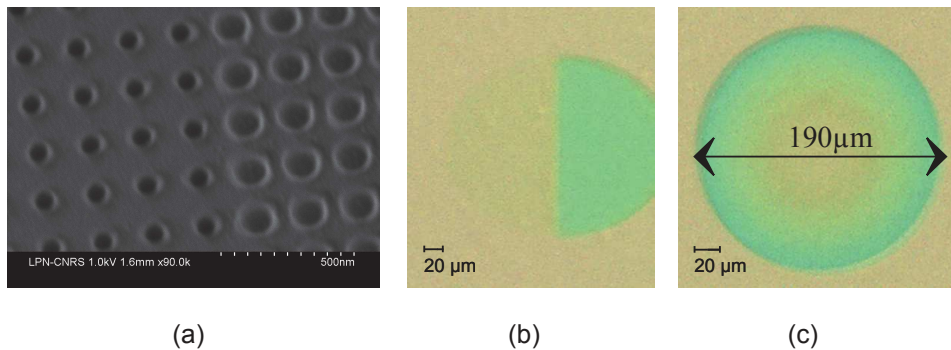


Fig. 10. (a) SEM top view of one fabricated PCM with 2 filling factors ($f_1 = 0.3$, $f_2 = 0.6$). (b) Optical microscope image of the PCM shown in (a). (c) Optical microscope image of the fabricated PCM with parabolic phase profile.

thick containing 6 strain-balanced InGaAs/GaAsP quantum wells (QW's). Each QW is placed at an antinode of the optical standing-wave, with an inhomogeneous longitudinal distribution ensuring equal QW's carrier excitation. This ensures a low threshold current density and a homogeneous gain dynamic behavior, free of strong non-linear longitudinal mode coupling [4, 22], for stable single frequency operation. A 30nm thick AlAs layer is deposited after the QW's barriers, to enhance the carriers confinement, and finally a 35nm of lattice matched InGaP cap layer is deposited on top to prevent oxidation of the overall structure.

As depicted in Fig. 11 the PC-VECSEL is formed by the gain mirror, a 1.8mm long air-gap and the PCM. The gain mirror is bounded on a Peltier element to stabilize its temperature. And it is optically pumped using a commercial single transverse mode GaAs-laser diode ($P_p = 300mW @ 780nm$), at an incidence angle of 64 deg. This angle allows to compensate the strong ellipticity of the pump beam, and to minimize reflection on the gain-mirror/air interface as it is very close to the Brewster angle. The pump beam is then focused on a spot size of $2W_p = 90\mu m$ ($@ 1/e^2$) using two commercial achromatic lenses.

Single frequency operation was obtained in CW at room temperature, with low threshold density ($2kW/cm^2$), differential efficiency of 21% and maximum output power of 18mW limited by the pump power. The SMSR is $> 46dB$ (apparatus limited, calculated quantum limit at 64dB [4]), and the beam is circular TEM_{00} close to diffraction limit with $M^2 < 1.2$ and

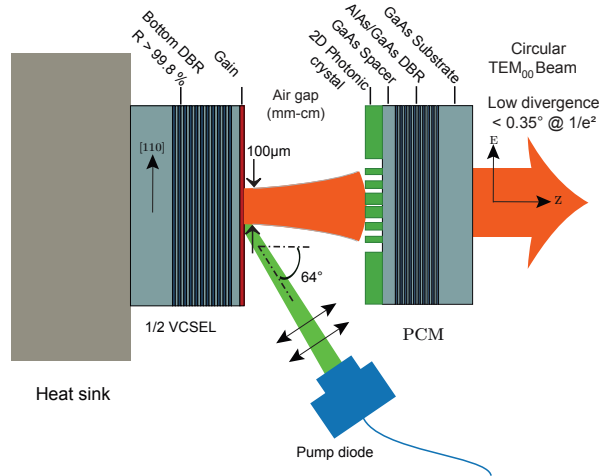


Fig. 11. Schematic of PCM based VECSEL design.

wave-front rms fluctuations of 2% of λ see Fig. 12(a). This shows that the PCM does not introduce optical aberrations in the beam, thanks to the high accuracy of the technological process, and good surface quality of the PC. The light polarization is linear and follows the [110] crystal axis of the gain mirror, thanks to gain dichroism in QW's and birefringence in the structure [4, 22, 23]. The orthogonal polarization extinction ratio is > 60dB (apparatus limited, calculated quantum limit at 70dB [4]).

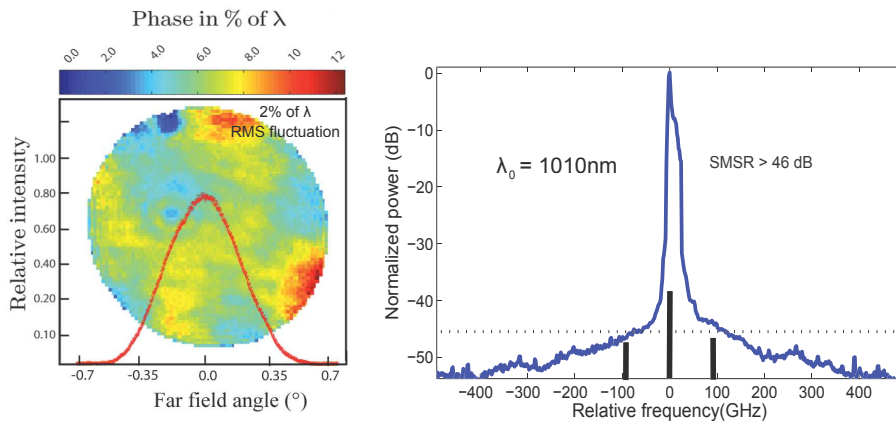


Fig. 12. (a) Far field phase map recorded with a wavefront sensor (field curvature Zernike term removed); intensity profile recorded with a beam profiler, the beam intensity profile is perfectly fitted by a gaussian shape (1.2% rms). (b) Laser spectrum recorded with an optical spectrum analyzer (6 GHz resolution). Solid vertical lines show the longitudinal mode positions.

Figure 13 shows the PCM-based cavity stability analysis (blue curve) compared to the thermally stabilized cavity, using the same mirror but outside the PC area (dashed red curve).

To perform the thermally stabilized cavity analysis we simulated the thermally induced radius of curvature generated by the Gaussian pump beam, taking a thermal resistance $R_{th} \simeq$

70K/W for pump beam waist $W_p = 45\mu\text{m}$ and an average index change in the gain mirror $dn/dT = 2.4 \times 10^{-4}K^{-1}$ as measured in similar structures in previous works [3, 24]. The thermally induced radius of curvature depends strongly upon the incident pump power and the beam waist, thus the thermal-lens based stability in Fig. 13 is valid for a one given pump power $P_{pump} = 270\text{mW}$ in our case, which is the maximum power allowed by the used pump diode. This way the thermal effect is the strongest possible in our configuration. Whereas the PCM based stability curve is valid for any pump power above the threshold.

To discuss the characteristics of our laser cavity we highlighted two important regions in Fig. 13: the first one (gray-shaded) is a non-lasing zone because of the finite PCM size as explained in the caption of Fig. 8. The second one (green-shaded) shows the validity zone of thermally-stabilized plano-plano cavity curve, because of the finite size of the pump beam radius, thus the thermal lens does not exist out of the region delimited by W_{th} which is the maximum width that allows to approximate the thermally induced graded-index to a parabola with a good accuracy [1], W_{th} is also the maximum allowed width of confined cavity fundamental mode. We experimentally observed a lasing regime in a plano-plano configuration for cavity lengths $L_c \leq 200\mu\text{m}$ which is in good agreement with this analysis. This shows that the obtained high quality beam is the fundamental LG mode of the stable PCM-based cavity and that the thermal lens effect is negligible.

From the far field beam phase and intensity profile, we deduced a measured radius of curvature of the PCM $R_c \simeq 20\text{mm} \pm 1.4\text{mm}$ with our laser at 1010nm close to the designed value (21mm at 1010nm).

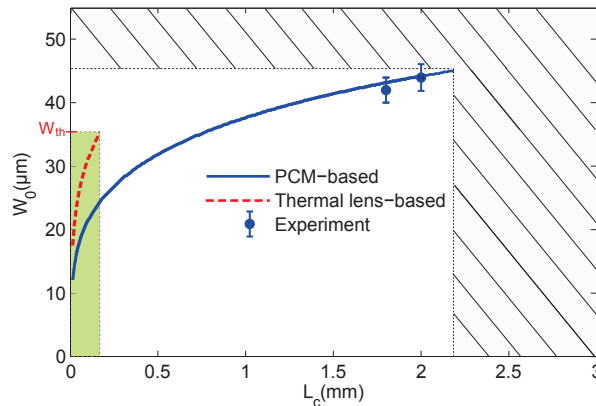


Fig. 13. PCM-based and thermal lens-based cavity stability: experimental and calculated Gaussian waist W_0 (@1/e²) on the VECSEL gain mirror varying with L_c . Green shaded region: validity zone of the thermal lens-based stability due to the finite size of the thermal lens. Gray-shaded region see caption of Fig. 8

Using the PCM in a laser cavity allowed us to validate the designed phase function profile, and the high accuracy of the fabrication process as the generated beam has high spatial coherence. Furthermore the laser threshold density and efficiency give a rough assessment of the cavity losses and thus its finesse. To get a more accurate estimation of the losses in this high-Q cavity we measured the relative intensity noise (RIN) of the laser, the obtained curves (Fig. 14) show a very low RIN at quantum limit above 1MHz and at shot noise from 100MHz up to cavity Free Spectral Range FSR = 84GHz. The RIN shows also a transitional regime from class-A to class-B at high pumping rate, and exhibits a weak relaxation oscillations at $f_r \simeq 127$ MHz. For low pumping rate the laser is closer to class-A regime. The theoretical expression

of oscillation frequency f_r for a class-B laser is given by Eq. (6) where η is the pumping rate, and the cavity losses rate $\gamma = FSR \cdot (T + Losses) = 2.5 \times 10^9 s^{-1}$ with the PCM transmission $T = 1\%$ and finally $A = 3.2$ ns is the carriers lifetime.

$$f_r = \frac{1}{2\pi} \sqrt{\gamma \cdot A \cdot (\eta - 1)}. \quad (6)$$

A more advanced analytical RIN expression is developed in [25–27] we used it to fit our experimental RIN curves and extract the transmission plus losses value in the cavity, taking into account quantum Langevin forces for carriers and photons and neglecting the pump noise. The obtained value is in good agreement with simulated one in the design section, see Fig. 9(b). This value is the sum of gain mirror internal losses, diffraction and material losses in the PCM ($< 0.1\%$) and the PCM transmission. To end we would like to note that the obtained laser coherence fundamental limit is given by quantum noise as it can be seen on the RIN above $1 MHz$. Thus the Langevin forces acting on the laser electric field limits its phase and amplitude fluctuations [4, 28]. It means that the theoretical fundamental laser linewidth is at Hz level, giving the minimum linewidth limit at short integration time. This quantum limit lead to a Q-factor limit of $3 \cdot 10^{13}$. However for long integration time technical, thermal and mechanical noises will limit the linewidth [3]. Thus a linewidth similar to a diode-pumped solid-state lasers one can be reached, far below a DFB-diode laser value.

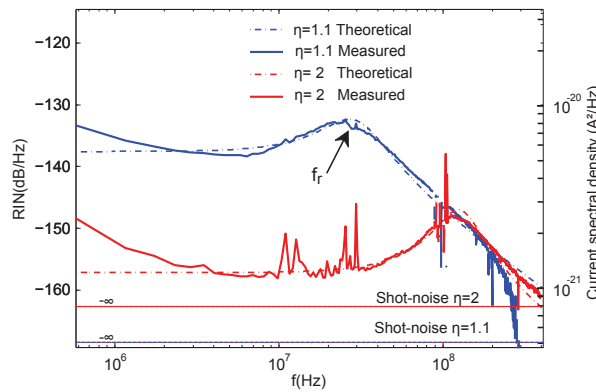


Fig. 14. Measured and simulated relative intensity noise curves of the PCM-based VECSEL for cavity length $L_c = 1.8 mm$ and two pumping rates $\eta = 1.1$, $\eta = 2$. The simulation only takes into account quantum noise forces on carriers and photons. Left axis: current fluctuations spectral density for $\eta = 2$.

5. Conclusion

We demonstrated a low loss ($< 0.1\%$) high reflectivity ($> 99\%$) and aberrations-free concave Bragg mirror ($20 mm$ radius of curvature) integrating a PC with spherical phase transfer function, based on planar III-V semiconductor flat photonics technology. The presented design is an alternative to micro-lenses and curved Bragg mirrors (dielectric glass mirrors or membrane type mirrors [29, 30]) for concave-type stable laser cavities. It also provides spatial, spectral and polarization filtering capabilities. The mirror is designed for highly coherent external cavity semiconductor lasers exhibiting very low quantum limit.

The PCM is designed with RCWA calculations, and once designed and fabricated is integrated into a compact single frequency TEM_{00} stable laser cavity, with GaAs-based quantum-well as $1/2$ -VCSEL gain mirror (emission wavelength $\lambda_0 = 1.01 \mu m$). We demonstrated a high

coherence single frequency PC-VECSEL with a TEM_{00} beam close to diffraction limit (2% of λ rms fluctuations). This shows that the fabricated mirror does not introduce any optical aberrations, thanks to the high accuracy of the III-V technological process. Then by studying the relative intensity noise of the laser, exhibiting a low quantum limit (below -150 dB above 1MHz), we show that the PCM does not introduce extra-losses (material and diffraction losses $< 0.1\%$) which make it suitable for high-Q cavities (cold cavity Q-factor in the range $10^6 - 10^7$ for a 2-mm long cavity). With the chosen VECSEL design, the theoretical fundamental limit for the laser linewidth is at 10 Hz (laser Q-factor of $\sim 3 \cdot 10^{13}$). This demonstration paves the way to highly coherent, high power compact semiconductor laser with embedded functionalities, like exotic beam generation, thermal lens compensation, polarization control and spectral filtering..etc. Furthermore, PC-VECSELs present big potential for applications that need high compactness, like Laser arrays which are currently reserved for monolithic VCSELs. For example one can imagine an array of PC-VECSEL using electrical pumping, or optical pumping across the PCM which is already mature for lasers at $1.5\mu m$ (transparent medium for pumping at $980nm$), for shorter wavelengths we need to use PC mirror grown or bonded on transparent substrate like Sapphire. This will offer the possibility to combine the compactness and the high coherence of PC-based free-space cavities.

Acknowledgments

This work was supported by the French ANR Micphir program, and the French RENATECH network.

Generation of phase and amplitude-structured coherent photon states

The aim of this chapter is to build high power VeCSEL sources generating phase and amplitude-structured modes. The targeted modes are high order degenerate and non-degenerate Laguerre-Gauss modes (LG, LG*, respectively), and high order Hermite-Gauss (HG) modes. We will give a special focus to beams carrying orbital angular momentum (OAM). In fact, intracavity generation of these beams raises a formerly unsolved problem which is the control of the handedness, and to which we will propose a solution in this chapter. This chapter is organized as follows: we first start with a brief overview of phase/amplitude-structured light, discuss its main properties and how to generate it. Then we address modes carrying OAM and present their properties, their applications and a detailed state of the art of intracavity generation of this kind of beams.

Next, we move to experiments which consist in two parts, the first one is dedicated to mode without OAM (HG and degenerate LG), and the second one to mode carrying OAM ($LG_{0,\pm 1}$). In both sections, we describe the design and show the fabricated intracavity masks, in addition to the obtained beams. The second section contains an additional part dedicated to the handedness control problem, where we explain it and give an overview of the reported works attempting to solve it. Then we propose a solution to the problem in two steps: first we use the semi classical Maxwell Bloch dynamics equation to understand the parameters governing the handedness selection in lasers. Second, we present a solution based on an integrated metamaterial base flat-photonics element to perturb the cavity eigenstates and allow to select one handedness.

4.1 What is phase and amplitude-structured light

Structured light is a general term by which we mean, all states of light with complex phase front and intensity pattern. High order modes of several transverse mode families fall under this definition, such as Hermite-Gauss, Laguerre-Gauss, Bessel-Gauss (BG) and Ince-Gauss modes. Each one of these mode families forms a set of orthogonal modes having different intensity and phase patterns. For example, we plot in Fig 4.1 the phase and intensity patterns of the few first non-degenerate LG modes. And in Fig 4.2 the first HG modes. The third example we take is the BG

basis plotted in Fig 4.3. The modes of these three basis have a structured phase and intensity profiles, but differ in their geometry and usually in their propagation properties. This greatly influences their existence conditions and the way one can generate them.

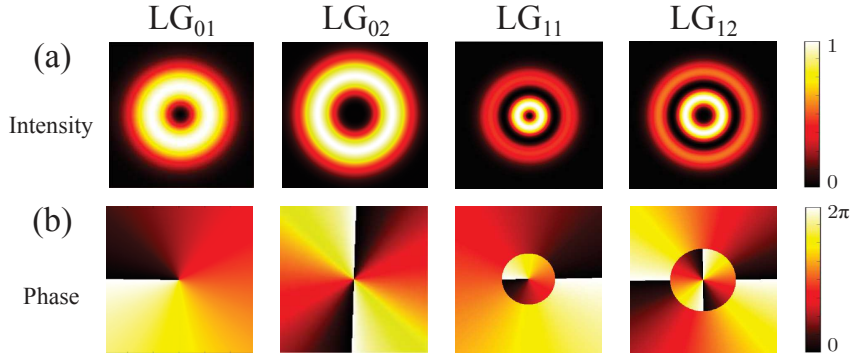


Figure 4.1: (a) Intensity, (b) phase, of the few first modes of the Laguerre-Gauss basis.

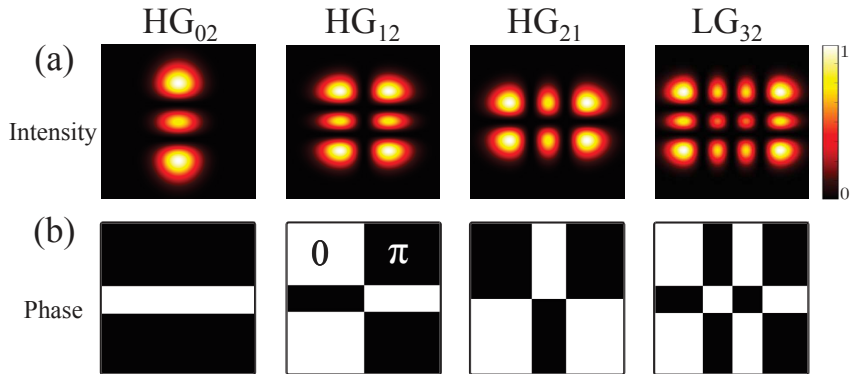


Figure 4.2: (a) Intensity, (b) phase, of the few first modes of the Hermite-Gauss basis.

All the modes can exist in the continuum states of the free space, They can also be obtained, in confined systems such as free-space or guided optical resonators. However, in this case, other conditions apply. For example, LG and BG modes have a cylindrical symmetry, while the HG modes have a rectangular one, they can therefore exist in free-space optical cavities or guided systems with cylindrical or rectangular geometry, respectively.

The main difference between free-space and guided-mode optical cavities is in the spatial spread of the modes. In free-space optical cavities, the mode waist increases as the square root of the mode order ($\propto \sqrt{n}$) [Siegman 1986], this property is very important in mode selection using phase or intensity masks, because one can almost always find an intensity or a phase mask to discriminate between modes without affecting the desired one. For example, one can suppress high order modes by

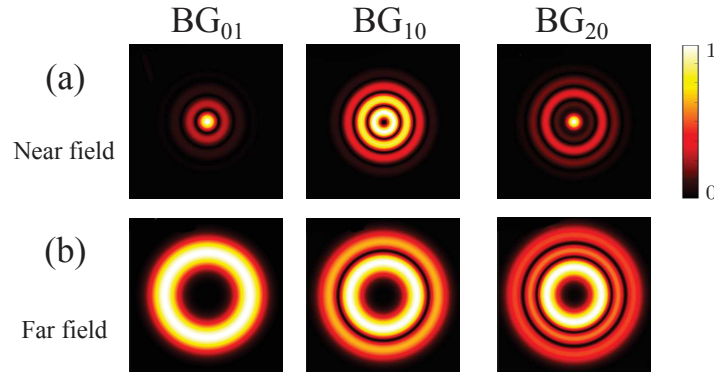


Figure 4.3: (a) Near-field, (b) far-field, of the few first modes of the Bessel-Gauss basis.

adapting the pumped zone to the fundamental beam waist or introduce an intracavity pinhole. This property is not valid for laser with guided modes, such as monolithic VCSELs and edge emitting diodes. Because in a step-index waveguide all the modes have approximately the same spatial spread, the difference between the two cases is illustrated in Fig 4.4.

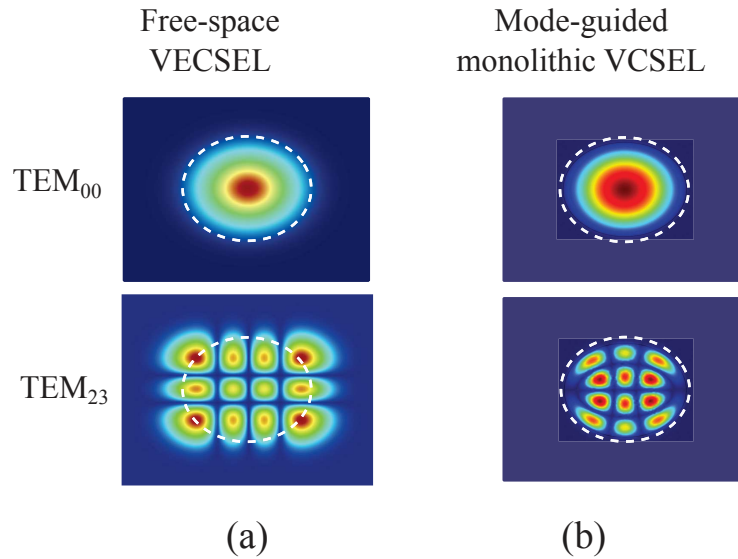


Figure 4.4: TEM_{00} and TEM_{23} modes of: (a) Free-space VeCSEL cavity. (b) Guided-modes optical cavity. the latter is simulated in a monolithic VCSEL having a waveguide diameter of $50 \mu\text{m}$ an effective index-step of 0.05, and an aspect ratio of 1 : 3.

In our case we are interested in intracavity generation of HG modes, in addition to degenerate (see Sec 1.3.2) and non-degenerate LG modes. The free-space VeCSEL cavity possesses a cylindrical symmetry which implies that its natural basis is the LG one providing that the pump profile and the mask geometry possess

the same rotational symmetry. In order to generate the HG modes, we impose a rectangular symmetry in the cavity by means of intensity masks, as illustrated in Fig 4.5.

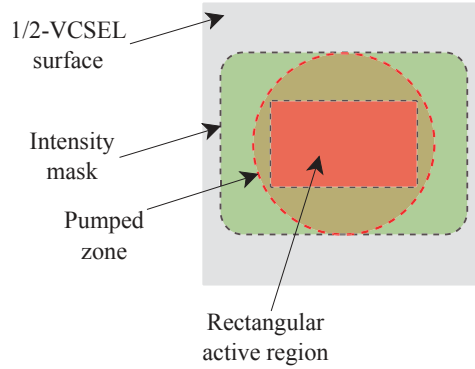


Figure 4.5: Illustration of rectangular symmetry imposed in a circular active zone, using an intensity mask.

4.2 phase-structured light generation methods

The generation of phase-structured beams can be divided into two major categories: (1) Extra-cavity transforming of conventional beams using beam shaping optics. (2) Generation of the structured-phase beam directly from a laser. Although our focus is on direct laser generation, it is useful to introduce the extra cavity beam transforming approach to discuss its main advantages and limitations and how it compares to direct generation method.

4.2.1 Extra-cavity generation of phase-structured light

There are many techniques that fall within this category, but regardless of the technique the idea is always the same: using phase transforming optics to transform a conventional beam with parallel wavefront into an exotic one with structured phase. This can be achieved using refractive optics (phase plates). For example, a spiral phase plate can be used to generate a LG_{01} mode with a helical wavefront (Fig 4.6). The optical thickness of the plate with the azimuthal position is given by $s(\theta) = l\theta(n - 1)/k$, where n is the refractive index of the material used to make the phase plate [Yao 2011], k is the wavevector, and $l \in \mathbb{Z}$ is the OAM charge.

A similar result can be obtained using diffractive optics instead of making complex refractive components. Indeed, if we take the interference between a plane wave and the desired structured beam and use it as a hologram, once illuminated by a plane wave, this hologram produces a first order diffracted beam with intensity and phase patterns of the desired one (Fig 4.7). This holographic approach is particularly popular, because the holograms can be calculated and implemented using computer driven spatial light modulators (SLMs) based on pixilated liquid

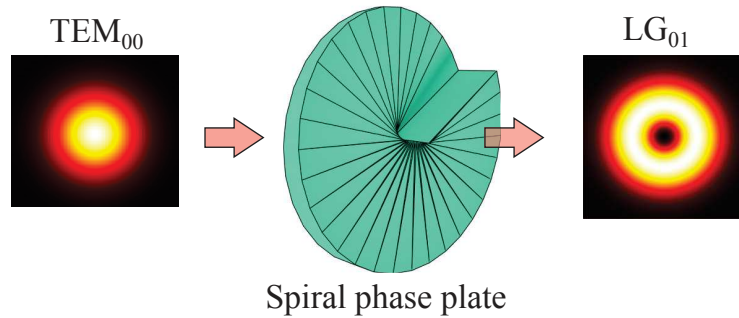


Figure 4.6: Transformation of TEM_{00} Gaussian beam to helically phase one using spiral phase plate.

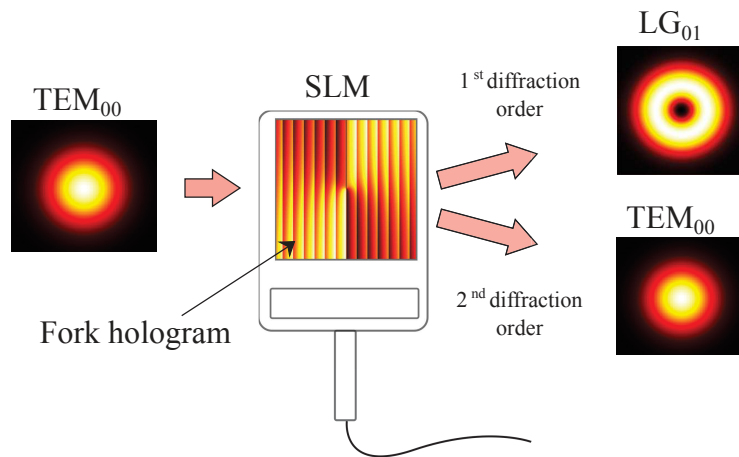


Figure 4.7: 'Fork-hologram' implemented with a spatial light modulator for the production of helically phased beam, the latter is obtained in the 1st order diffraction, and second order gives the fundamental beam.

crystals. What makes this method very appealing is the commercial availability of SLMs. It is also a general technique that can be used in principle to generate any exotic beam with structured phase.

SLMs can be used to directly mimic the phase profile of the wanted beam, however, because of the pixilation and linearity imperfections in these devices the obtained beam is a superposition of several diffraction orders which reduces the spatial coherence of the beams. The advantage of using holograms is to create an angular deviation between the diffracted orders, and thus the unwanted ones can be filtered spatially. There is an alternative method specific to generation of helically phased beams, called astigmatic mode converter, it consists in using a pair of cylindrical lenses to transform an HG_{01} beam to an LG_{01} . It is the method used by Allen and coworkers in 1992 to demonstrate the first production of beam carrying OAM in a laboratory [Allen 1992]. However, this technique requires a specific HG mode, and the range of achievable LG modes is also limited. Thus, the computer generated hologram approach has become the most commonly used technique.

The main limitation of extra cavity generation methods in general is that the generated beam quality depends strongly on the alignment of the transforming optics, in practice this usually penalizes the spatial coherence of the beam. Using SLMs introduces high losses (15-20%) due to the diffraction efficiency, and the pixel fill-factor. Furthermore, the boiling temperature of the liquid crystals limits the maximum usable power. And using these devices, usually results in cumbersome and onerous systems.

4.2.2 Intra-cavity generation of phase-structured light

In Sect 3.5 we have presented several intracavity mode selection methods reported in the literature. We have shown however, that these methods suffer from many limitations, and we have proposed a novel approach based on integrated subwavelength metamaterial and metallic layers well suited for efficient mode control in high-Q and compact laser cavities. However, beside this technical drawbacks, these methods present a fundamental limitation when it comes to generate vortex modes, which is the control of the wavefront handedness (OAM sign). Understanding this issue requires us to clearly understand the properties of vortex modes and their formation in the laser cavity. For this reason we postpone the state of the art analysis of direct generation of vortex modes until Sec 4.5.2.

4.3 Modes carrying OAM: properties and applications

4.3.1 Properties

From a historical point of view, it has been known for many decades that light can carry an angular momentum AM in addition to linear one. Indeed, in 1909 Poynting [Poynting 1909] pointed out that a circularly polarized light should have an AM to energy ratio equal to σ/ω where $\sigma = \pm 1$ is the spin of photons and ω is the pulsation of the light wave. This AM is commonly called the Spin angular momentum of light (SAM). But light can also possess an orbital angular momentum, related to the phase structure of the beam and independent from the spin of photons. As shown in the seminal paper by [Allen 1992], the OAM is present in beams whose expression contains an l -dependent azimuthal phase term: $\exp(jl\theta)$ as in $LG_{p=0,l \neq 0}$ modes given by Eq 1.7. This field can be written in a simplified form as follows:

$$u(r, \theta, z) = u_0(r, \theta, z) \exp(-ikz) \exp(jl\theta) \quad (4.1)$$

This class of beams is characterized by a helical wavefront and a donut shaped intensity pattern, with a dark core usually called the optical vortex because of the phase singularity at the beam center (see Fig 4.8).

As for SAM, it can be shown that the $\exp(jl\theta)$ term in vortex beam's expression results in an angular momentum to energy ratio of l/ω , multiplication of the numerator and the denominator of this ratio by \hbar gives an OAM per photon of $\hbar l$

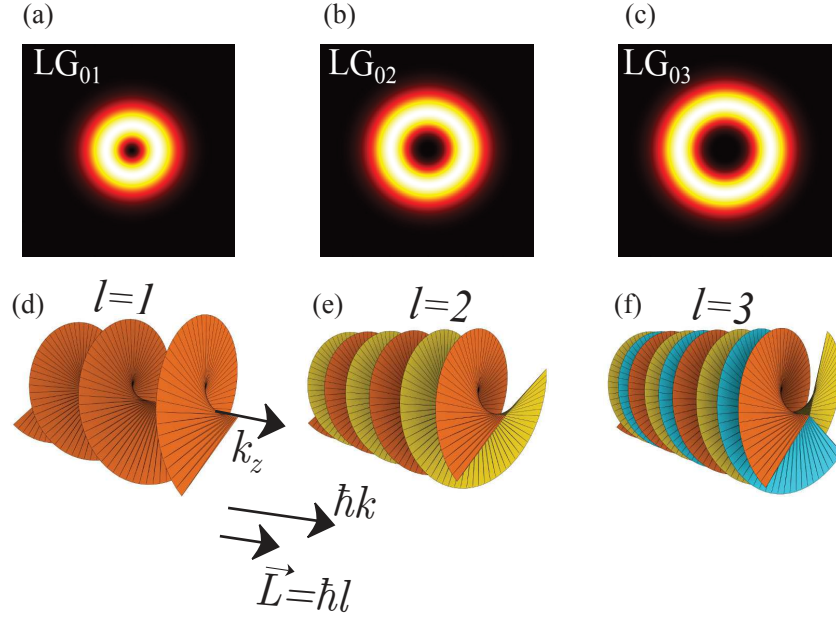


Figure 4.8: (a-c) Intensity patterns of vortex beams with the a charge $l = 1, 2, 3$.(d-e) Their respective helical wavefronts.

[Allen 1992]. This can be derived geometrically from the inclination of the wavefront due to the helical phase term [Padgett 2004] (see Fig 4.9). The inclination angle of the wavefront and thus of the Poynting vector is $\theta = l/(kr)$. The linear momentum of light has then an azimuthal component given by $\hbar k \sin(\theta)$, by letting $\sin(\theta) \simeq \theta$ the OAM is obtained by $r\hbar kl/(kr) = l\hbar$.

The same result can be obtained more formally [L.Andrews 2008] by calculating the cycle-averaged linear momentum density \vec{p} , and the angular momentum density, \vec{j} , of a light beam from the electric field, $\vec{\mathcal{E}}$, and the magnetic field, \vec{B} [Jackson 1962]:

$$\begin{aligned}\vec{p} &= \varepsilon_0 \langle \vec{\mathcal{E}} \times \vec{B} \rangle \\ \vec{j} &= \varepsilon_0 (\vec{r} \times \langle \vec{\mathcal{E}} \times \vec{B} \rangle) = (\vec{r} \times \vec{p})\end{aligned}\quad (4.2)$$

where ε_0 is the vacuum permittivity. The total linear and angular momentum per unit length may be found by integrating these expressions over the area of the beam. In this classical treatment, Eq 4.2 encompasses both the spin and orbital angular momenta of a light beam. The spin angular momentum of light is, of course, very often expressed as resulting from the spin of individual photons, but the approaches are equivalent.

For there to be angular momentum j_z in propagation direction z , the light field must have linear momentum in the azimuthal direction. This requires a z -component to the electromagnetic field. As emphasized by [Simmons 1970], an idealized planewave of infinite extent, which has only transverse fields, does not carry angular momentum, irrespective of its degree of polarization. However, for beams of finite extent, a z -component of the electromagnetic field can arise in

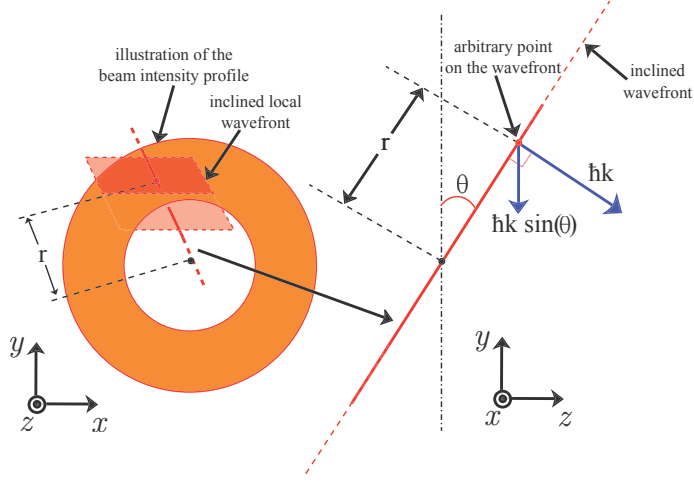


Figure 4.9: Illustration of Helically phased beam's inclined wavefront and geometrical relation with the Poynting vector.

two distinct ways. Because the electric field is always perpendicular to the inclined phase-front, a beam with helical phase-fronts has an oscillating component in the propagation direction. Less obviously, it appears that a circularly polarized beam, where \mathcal{E}_x is in quadrature with \mathcal{E}_y , has an electric field in the propagation direction proportional to the radial intensity gradient. This is, consistent with the argument with respect to the notional plane wave, as its gradient is then zero.

If we consider a linearly polarized light, within the paraxial approximation, $\vec{\mathcal{E}}$ and \vec{B} can be written as:

$$\begin{aligned}\vec{\mathcal{E}} &= ik \left[u \vec{x}_i + \frac{i}{k} \frac{\partial u}{\partial x} \vec{z}_i \right] \exp(ikz) \\ \vec{B} &= \mu_0 H = ik \left[u \vec{y}_i + \frac{i}{k} \frac{\partial u}{\partial y} \vec{z}_i \right] \exp(ikz)\end{aligned}\tag{4.3}$$

where μ_0 is the vacuum permeability, $u \equiv u(r, \theta, z)$ is the complex scalar function describing the distribution of the field amplitude, and $\vec{x}_i, \vec{y}_i, \vec{z}_i$ are unit vectors oriented along x, y, z axis respectively. One can evaluate the time-averaged Poynting vector, namely:

$$\begin{aligned}\vec{p} &= \frac{\varepsilon_0}{2} (E^* \times B + E \times B^*) \\ &= i\omega \frac{\varepsilon_0}{2} (u^* \nabla u - u \nabla u^*) + \omega k \varepsilon_0 |u|^2 \vec{z}_i\end{aligned}\tag{4.4}$$

For a field such as $u(r, \theta, z) = u_0(r, z) \exp(+il\theta)$ the θ -component of linear momentum density is:

$$p = \varepsilon_0 \omega l |u|^2 / r\tag{4.5}$$

while its cross product with \mathbf{r} gives an angular momentum density of magnitude $j_z = \varepsilon_0 \omega l |u|^2$. The energy density of such a beam is

$$W = c\varepsilon_0 \langle E \times B \rangle_z = c\varepsilon_0 \omega k |u|^2 = \varepsilon_0 \omega^2 |u|^2 \quad (4.6)$$

Thus,

$$\frac{j_z}{w} = \frac{l}{\omega} \quad (4.7)$$

We note that for circularly polarized light and additional term given by:

$$\vec{p}_\sigma = \omega \sigma \frac{\varepsilon_0}{2} \frac{\partial |u|^2}{\partial r} \vec{\theta}_i \quad (4.8)$$

appears in Eq 4.4, where $\vec{\theta}_i$ is a unit vector. This term encompasses the spin angular momentum density component arising from polarization, and dependent upon σ and on the intensity gradient.

To end this part, we note that the OAM property is present at the single photon level, and along with energy and linear momentum, it is one of the fundamental conserved quantities.

4.3.2 How to detect the OAM's charge and sign of a beam

One may wonder, how to make sure that a given beam carries an OAM. In fact, it is not enough to rely on the intensity distribution, for example Bessel-Gauss beams have an annular intensity distribution in the far field, but these beams do not possess necessarily an OAM. To verify the structure of the wave front, one solution is to observe the interference pattern of the helically phased beam with a reference plane wave. The interference gives the fork pattern shown in Fig 4.10 in the near field, and the spiral fringes shown in Fig 4.11b-e in the far-field. These spiral fringes are very useful, because the number of starts is a direct indication of the OAM charge [Harris 1994b], while the spiral sense indicates the handedness of the helical phase front. In Fig 4.11a we show an example of an interferometer setup that allows to obtain the spiral interference fringe, and by removing the lens (f2) the same interferometer gives the fork fringe.

4.3.3 Applications

The applications of beams carrying OAM stems from their unique properties. The most important one is that the OAM can be transferred to optically trapped particles, which enables to rotate the particles without restriction to birefringent ones only, as it is the case with SAM. The first experimental demonstration by [He 1995] opened the path to more sophisticated features in optical manipulation in several fields, such as bioscience, microfluidics and micro-mechanics. What distinguishes the novel optical tweezers achieved with beams carrying OAM is the ability to exert

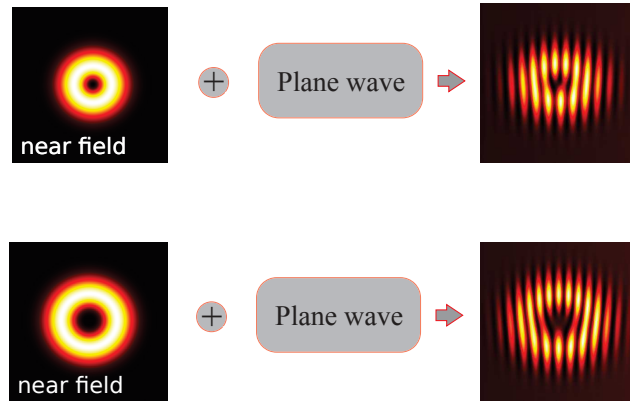


Figure 4.10: Interference of helically phased beam with a plane wave gives 'fork interference fringe'.

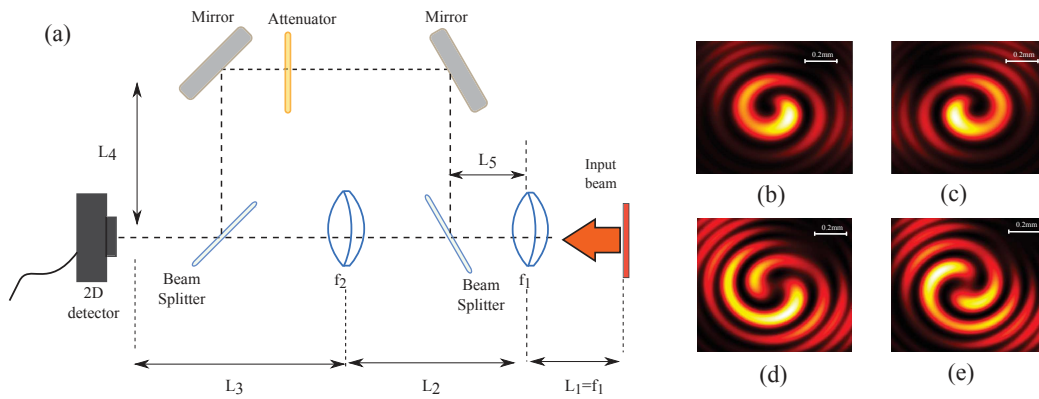


Figure 4.11: (a) Interferometer scheme for OAM's charge and sign characterization. (b,c,d,e) Simulated interference results using LG_{01} beams with $l = +1, -1, +2, -2$ respectively. The setup parameters are: $L_1 = f_1 = 50$ mm, $L_2 = 19$ mm, $f_2 = 60$ mm, $L_3 = 120$ mm, $L_4 = 140$ mm.

torques in addition to the linear force, which allows for example to drive micromachines [Galajda 2001, Galajda 2002b] and micro propellers [Galajda 2002a], or to actuate micrometer-scale hydraulic pumps and valves [Grier 2003].

It has also given rise to new techniques in the micro-rheology field [Bishop 2004], torsional AND manipulation [Oroszi 2006], and allowed measurement of viscoelastic parameters in picoliter volumes [Knöner 2005, Parkin 2007].

Trapping atoms and nano particles, is a more challenging task than tweezing micron-sized particles. Anderson et al [Andersen 2006] demonstrated the first transfer of the OAM from and LG beam to atoms trapped and cooled in the dark region (optical vortex) of the beam creating a Bose-Einstein condensate. Other works show trapping and rotating of nano-sized metallic particles [Dienerowitz 2008] and femtoliter-volume droplet in the optical vortex [Lorenz 2007].

The donut shaped intensity of helically phased beams, is used as a basis for

the sub-diffraction resolution microscopy [Hell 1994, Klar 1999], for which Hell received the Nobel prize in chemistry in 2014 [Hell 2014]. And more recently this technique was extended to endoscopy by demonstrating a fiber supporting OAM states [Gu 2014].

The OAM can be also be used as a multiplexing channel in optical telecommunications, channels with capacities in the range of Terabit/s have been achieved [Gibson 2004b, Wang 2012, Bozinovic 2013, Lei 2015]. Helically phased beams are also a good candidate for free space optical link, thanks to their good propagation properties through turbulent atmosphere [Tyler 2009, Cheng 2009, Djordjevic 2010, Krenn 2015]. They can also be used in imaging, using a technique called spiral resolved imaging, which enables remote probing of structural properties of a turbid and disordered media [Torner 2005].

In a similar way to the linear Doppler shift, rotating either the OAM beam or the observer with respect to the beam axis, gives rise to a rotational Doppler shift. This property has been predicted for the SAM by Poynting [Poynting 1909], and observed experimentally for the first time by Beth [Beth 1936]. However, unlike for the SAM, the rotational Doppler shift due to OAM is not accompanied by alteration of its charge. This has been first demonstrated in the microwave region of the electromagnetic spectrum [Courtial 1998] since it is an extremely challenging task at optical frequencies. And more recently, this effect has been used to detect spinning objects, by observing this rotational Doppler shift in scattered light [Lavery 2013], and used to measure the angular velocity of a spinning micro-sized particle [Phillips 2014]. We will return to this property in more details in Chap 6.

The Light with OAM also finds applications in astrophysics [Harwit 2003], and fundamental physics, for example in quantum entanglement experiments [Mair 2001, Vaziri 2002], quantum communication [Molina-Terriza 2004, Langford 2004] and quantum cryptography [Gröblacher 2006].

4.4 Generation of coherent beams with OAM=0 using VeCSELs

4.4.1 Description of our approach

We have already shown (see Sec 1.6) that mode selection inside a laser cavity involves competition of transverse modes, assuming single longitudinal mode and single polarization state. This competition relies on two dynamical parameters: (1) self and cross saturation terms; (2) the net-gain of each mode. However, the selection strategy we adopt here consists in using an amplitude mask and place it in such a way that unwanted modes experience very heavy loss (β_{kl}) inside the cavity, which prevents them from reaching the threshold, while the induced loss for the wanted mode (β_{ij}) stays negligible. This condition can be written in two points:

$$\begin{aligned} \text{Wanted modes : } \beta_{ij} + T_{OC} &\ll \text{available gain} \sim 2\% \\ \text{Unwanted mode : } \beta_{kl} + T_{OC} &\gg \text{available gain} \sim 2\% \end{aligned} \tag{4.9}$$

where T_{OC} is the transmission of the output coupler. In this case, the selection is done via the laser threshold condition, which implies that one can neglect the non-linear coupling (cross- and self-saturation effects) as the unwanted mode never cross the threshold. This is possible thanks to modes orthogonality and the weak spatial overlap between them in free-space cavities as discussed previously. In this case the cavity can be considered as intrinsically single transverse mode as illustrated schematically in Fig 4.12.

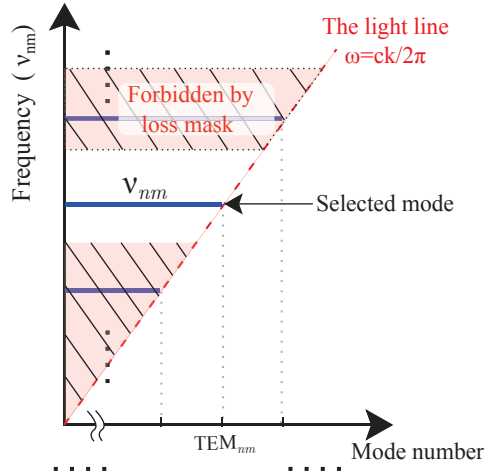


Figure 4.12: Diagram of modes in a stable concave-type optical cavity integrating loss mask.

4.4.2 Design and fabrication of the 1/-VCSEL with integrated intensity masks

We used a 1/2-VCSEL gain chip integrating mode selection elements, this structure consists of two main parts: a multi-quantum well based gain mirror and subwavelength thick amplitude masks.

4.4.2.1 The gain mirror

The gain mirror consists of a resonant periodic gain active zone optimized for emission at $\lambda = 1 \mu\text{m}$, containing 6 strain-compensated quantum wells, placed at the antinodes of the standing waves, with non-uniform distribution to ensure a homogeneous carrier excitation. The HR Bragg reflector is made of 27.5 pairs which results in a reflectivity ($R > 99.5\%$). This structure can provide a maximum gain $g \simeq 2\%$. The detailed design of the structure is given in Fig 4.13.

4.4.2.2 The integrated intensity masks

The loss masks can be achieved using an absorbing subwavelength metallic layer, or high loss diffraction grating. Fig 4.14 shows an example of loss mask containing two

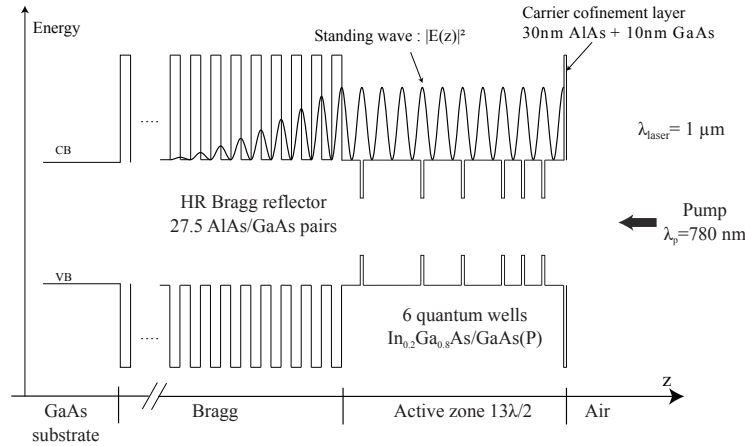


Figure 4.13: 1/2-VCSEL structure design.

crossed lines for the selection of degenerate LG_{02} , the mask is placed on the surface of a resonant gain structure (Fig4.13). The mask location and its subwavelength

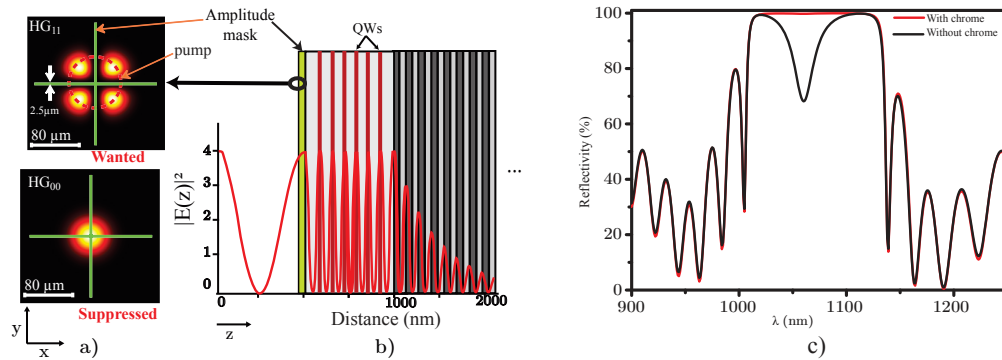


Figure 4.14: (a) Illustration of integrated chromium mask pattern. (b) Mask position on a field anti-node. (c) Simulated reflectivity spectra of the structure with and without chromium mask. We considered a mask thickness $e = 10$ nm, a Bragg mirror of 27.5 pairs.

thickness are of a key importance for us, because as its thickness is $\ll \lambda$ it does not introduce any diffraction loss which prevents the degradation of the spatial coherence. But this also means low absorption loss per pass, and that is why we used a resonant 1/2-VCSEL to maximize the interaction of the E-field with the mask. This is illustrated in Fig 4.14c where we plotted the simulated reflectivity of the structure with and without the mask. Furthermore, by placing the mask on the gain mirror surface, one ensure that it always coincide with an anti-node of the E-field independently of the lasing longitudinal mode as they are all in-phase on the gain mirror surface.

We note that pumping the gain mirror on a limited region, introduces an additional filtering function, because the unpumped region not only doesn't provide a gain, but is absorber too. This filtering function prevents higher order modes with

Mode	$\Gamma_{r,\theta}^{loss}$	round-trip loss (%)
LG_{00}	0.131	31.3
LG_{01}	0.679	17.7
LG_{10}	0.097	24.2
LG_{11}	0.060	15.7
LG_{02}	$1.851 \cdot 10^{-4}$	0.053
LG_{03}	0.039	10.3
LG_{04}	0.074	18.6

Table 4.1: Metallic mask loss calculated for a two-crossed lines mask shown schematically in Fig 4.14. We considered a chromium mask thickness $e = 10$ nm and crossed-lines width of $2.5 \mu\text{m}$.

larger spatial spread from lasing. This outer filtering function can be alternatively achieved by introducing an absorbing mask.

The mask thickness and transverse dimensions are chosen to satisfy the conditions of Eq 4.9. The modal loss, introduced by the mask depends on the material absorption of the mask layer α_e , weighted by two factors: the amplitude of the intracavity standing waves (longitudinal overlap $\Gamma_{\mu c}$), and the overlap between the mode intensity pattern ($|u_n(r, \theta)|^2$) and the normalized transverse pattern $\rho(r, \theta)$ of the mask. After one round trip the loss induced by the mask can be written as ¹:

$$loss = \alpha_e \Gamma_{\mu c} e^S \frac{\int \rho(r, \theta) |u_n(r, \theta)|^2 dS}{\int_S |u_n(r, \theta)|^2 dS} = \alpha_e e \Gamma_{\mu c} \Gamma_{r,\theta}^{loss} \quad (4.10)$$

Where e is the thickness of the mask. The material loss α_e in our case is merely the absorbance of chromium ², or the local loss induced by the diffraction grating (see section 3.4). This simple expression allows us to choose the right mask dimensions that allow efficient mode selection. As an example Table 4.1 shows the loss induced by the chromium mask illustrated in Fig 4.14 for the first modes of the LG basis. These values are calculated for a chromium layer thickness $e = 10$ nm, and a width of the crossed lines of $2.5 \mu\text{m}$. From these results it is clear that the mask causes a strong mode discrimination and favors the mode LG_{02} .

4.4.2.3 Fabrication and characterization

Fig 4.15 and Fig 4.16 show a scanning electron microscope (SEM) photographs of the two fabricated masks-sets. In these figures, each item in the set is a mask designed to generate one given mode. In the first figure each mask has a typical surface area of $300 \mu\text{m} \times 300 \mu\text{m}$, and consists of an absorbing chromium layer of

¹For $\alpha_e < 0.2$ see [Siegman 1986] Chap 11

² $\alpha_{chromium} = 2 \frac{2\pi}{\lambda} \kappa$, with $\kappa \simeq 3.5$ is the imaginary refractive index

a thickness $e = 10$ nm and a width of $2.5 \mu\text{m}$, designed to selected LG modes. The amplitude filtering function can be alternatively achieved using a diffraction grating introducing high diffraction loss as shown in the masks in Fig 4.16. These gratings consist of 131 nm thick SiN layer, with a periodic structure (period of $1 \mu\text{m}$), alternating low index region (groove of $0.8 \mu\text{m}$ with a refractive index $=1$) and a high refractive index region ($n_{SiN} = 2$) of $0.2 \mu\text{m}$. These dimensions are designed to maximize the diffraction loss of the grating (loss $= 60\%$).

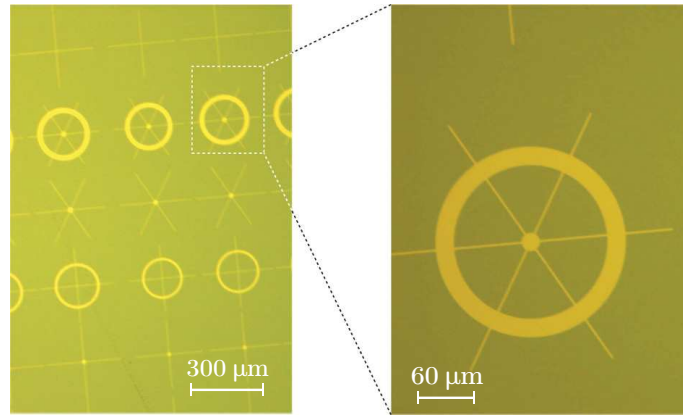


Figure 4.15: Optical microscope photograph of fabricated degenerate LG mask.

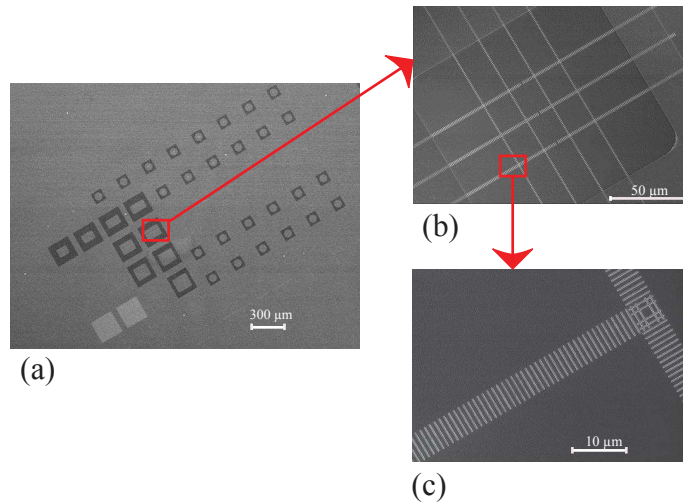


Figure 4.16: Scanning electron microscope photograph of fabricated mask: (a) Set of masks. (b) All-dielectric loss mask (c) Zoom in (b).

The structures characterization is achieved using the reflectivity and the photoluminescence spectra. The first one is measured by means of Fourier transform infrared spectroscopy (FTIR) (see Fig 4.17) and allows to verify the optical properties of the gain structure (thickness and refractive index of the different layers that form the structure, the reflectivity spectra of the DBR, and whether all the

elements are properly centered with regard to the working wavelength). The second

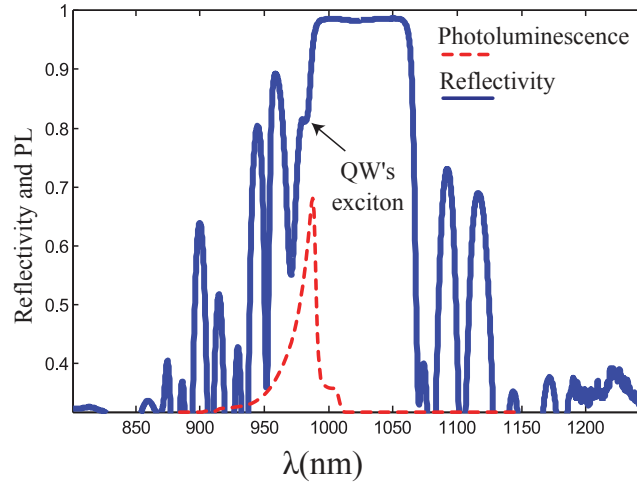


Figure 4.17: Measured reflectivity and photoluminescence spectra of the fabricated structure.

one gives the spectral position of the QWs gain curve. We also perform a 2D photoluminescence mapping of the gain chip, in order to check the crystal quality, this is achieved by a near field imaging of the spontaneous emission using a 2D CCD camera and an in-house imaging system. This allows to detect existing dislocations in the crystal structure which translates into dark spots or dark lines caused by the absence of the spontaneous emission as shown in Fig 4.18. We perform these three tests every time we have a new gain structure in order to validate its quality before using it in a laser setup.

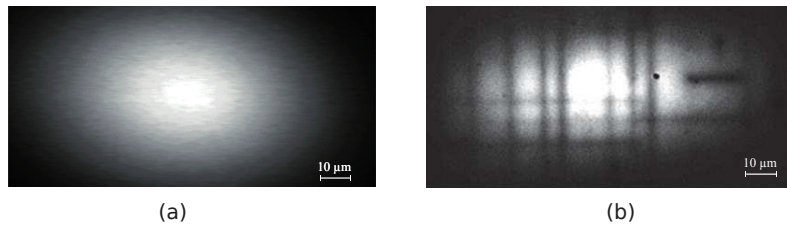


Figure 4.18: Near field imaging of the spontaneous emission: (a) Without dark lines (b) In presence of dark lines.

4.4.2.4 Laser setup and obtained results

We used the gain mirror integrating mode control elements to form a plano-concave cavity with a length L_c of few $mm(2 - 9)$. The gain mirror is bounded on a Peltier element to stabilize its temperature, and it is optically pumped using a commercial single transverse mode GaAs-laser diode emitting at $\lambda = 780$ nm, and generating a maximum output power of $230mW$. The pump spot is circular and has a Gaussian intensity profile.

In Fig 4.19 and Fig 4.21 we show some of the generated LG and HG modes, along with a schematic of the corresponding masks depicted in Fig 4.15 and Fig 4.16, respectively. And in Fig 4.20 and Fig 4.22 we show the cross section of some of these generated beams, superimposed with the theoretical LG and HG fit. These two figures show that the obtained mode are a pure LG and HG ones with circular and rectangular symmetry. We note that this symmetry is imposed by the masks geometry. The spatial modes have a divergence of $\simeq 0.8^\circ$ (FWHM).

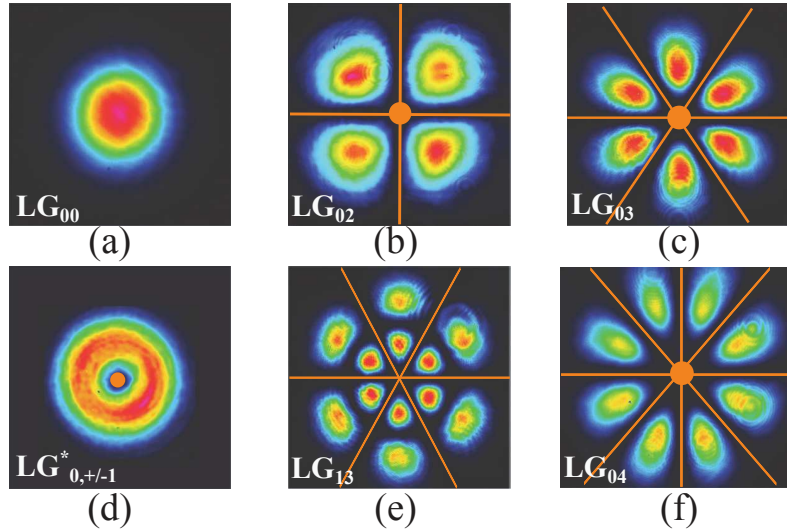


Figure 4.19: Intensity maps of obtained LG modes.

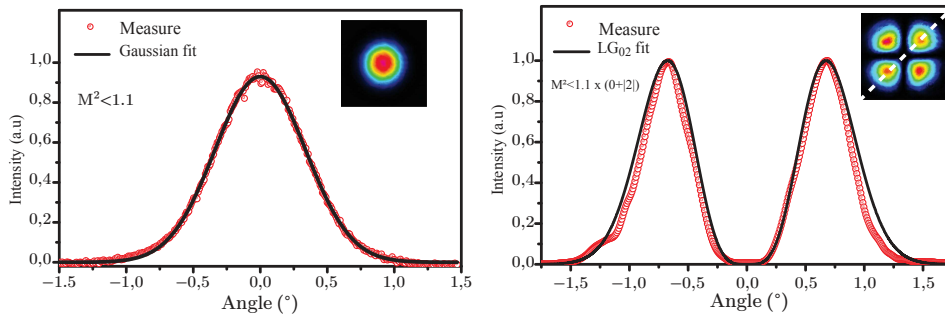


Figure 4.20: Laguerre-Gaussian fit of two obtained modes examples: (a) LG_{00} , (b) LG_{02} .

We also show an example of the measured output power as a function of the pump power density in Fig 4.23. These curves were obtained with an output coupler transmission $T_{OC} = 1\%$ and a temperature stabilized at 18°C . The power threshold density of HG_{00} is $\sim 0.61 \text{ kW/cm}^2$ and increases for higher order modes, the differential efficiency varies from 12% for high order modes fundamental mode to 16% for the fundamental mode. These differences in the efficiency and threshold between the modes is due to the difference of the modes overlap with the Gaussian pump

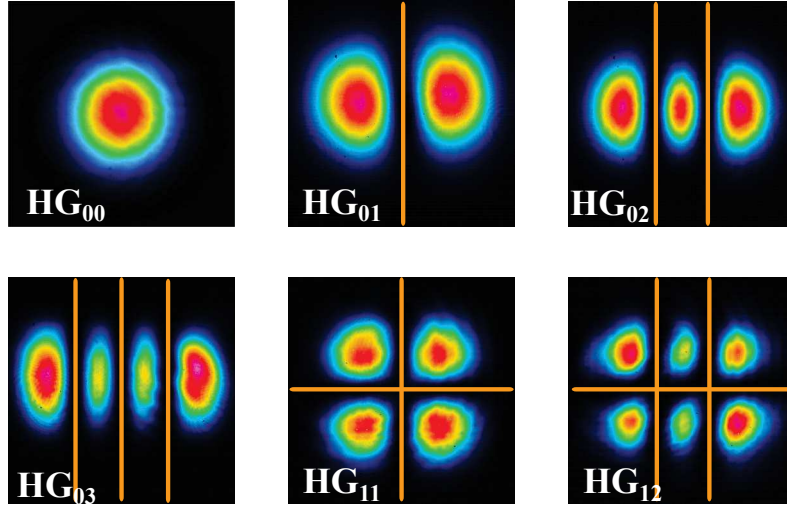


Figure 4.21: Intensity maps of obtained HG modes.

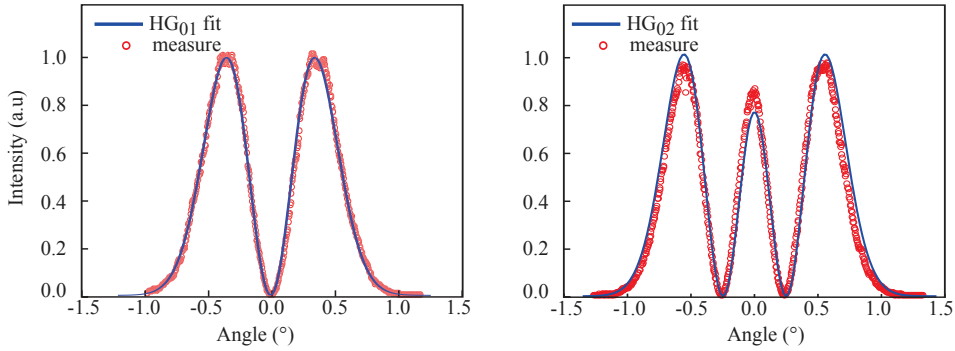


Figure 4.22: Hermite-Gaussian fit of two obtained modes examples: (a) HG_{00} , (b) HG_{02} .

beam and thus, the net-gain. The maximum output power in our experiments is limited by the available pump power (230 mW max). The laser operates in a single longitudinal mode regardless of the selected transverse one, with an SMSR > 45 dB measured using an optical spectrum analyzer with 10 GHz resolution (*Yokogawa AQ6370*), and with a scanning two-concave Fabry-Perot spectrum analyzer (*Coherent* with a resolution of ~ 60 MHz and a $FSR = 7.5$ GHz). In Fig 4.24 we give an example of a measured optical spectrum of our VECSEL emitting a degenerate LG_{02} mode. In this measurement the laser cavity length is 3 mm which results in a FSR of 50 GHz (0.2 nm at the working wavelength $\lambda = 1 \mu\text{m}$). It is worth noting that we have measured similar optical spectra for other high order modes, which suggests that the longitudinal state is independent from the transverse one.

The polarization of the modes is linear, parallel to the [110] semiconductor crystal axis with an extinction ratio of more than 70 dB measured using the beat-note between orthogonal polarization modes (selected and suppressed modes). This pure polarization state is obtained thanks to the birefringence and the gain dichroism

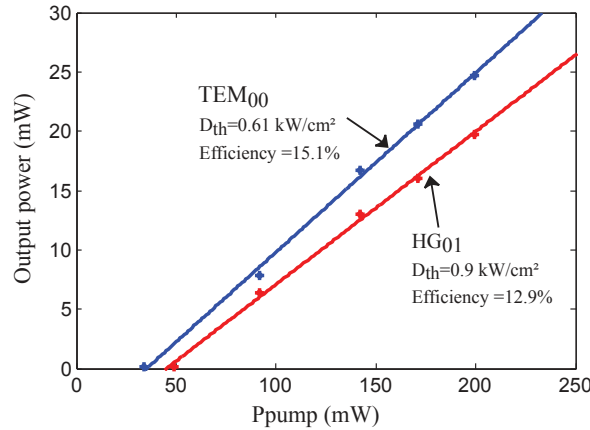


Figure 4.23: VeCSEL output power for HG_{00} and HG_{01} modes.

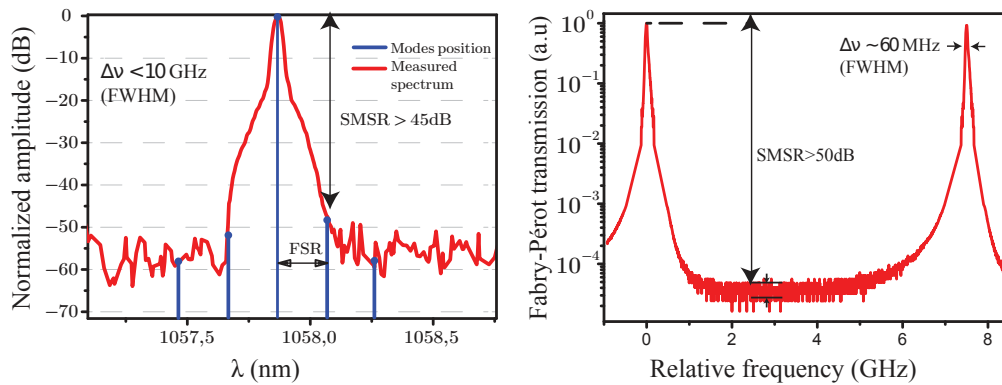


Figure 4.24: Optical spectrum of LG_{02} measured with: (a) Optical spectrum analyzer. (b) Fabry-Perot confocal, high resolution (60 MHz) spectrum analyzer. The laser output power is 20 mW.

between the two crystal axis, and is in a good agreement with our theoretical predictions as we will see in more details in Chap 5.

4.4.2.5 Discussion

We note that the laser behavior shown here (mode selection and power properties) is reproducible regardless of the selected mode. And the selection method we have shown allows in principle to select any higher order mode with a desired complex profile. In our experiments however, we were limited by the available pump power, because modes with very high order require large pumping zone and thus more power to reach the threshold density. It is also important to note that there are some particular cases where two modes have very close intensity profiles, which makes very difficult to find a mask design that enables to suppress one mode without strongly affecting the second one, this is the case for example of degenerate LG_{02} mode and LG_{12} . To describe the mode selection in such a case one should take

dynamic effect (self- and cross-saturation parameters) into account, for instance, in the example given above, this effect favors the LG_{02} mode according to the Lamb model (Eq 1.66). However, there are some particular situations where the intensity patterns of the modes are identical. This also implies that they have the same Gouy shift and thus degenerate resonance frequencies. This situation occurs with all resonator modes carrying an OAM of the same charge $|l|$ but opposite handedness $+l/-l$. This in fact, highlights the difficulty of selecting a mode carrying an OAM with controlled charge and more particularly, controlled handedness, which is the subject of the remaining part of this chapter.

4.5 Generation of beams carrying OAM

Generation of beams carrying OAM directly from a laser is a particularly interesting problem, because it raises a fundamental and to date unsolved bottleneck which is the control of the handedness of the helical wavefront. The literature treating this problem is relatively poor, nevertheless, there are some reported attempts to solve it. In some of the reported works, researchers have partially circumvented the problem by using hybrid approaches where the generated beam is not an eigenstate of the cavity, but obtained by transforming an eigenstate in small portion of the cavity or when coupling it out of the resonator. Other reports reveal misunderstanding of the handedness selection process and sometimes leads to erroneous interpretations. Therefore, we think that it is important to take time to discuss some methods reported in the literature. We describe some of the hybrid techniques which present sound and well understood results, but we also discuss some of the unexplained observations in order to compare them with our theoretical predictions and experimental results. Then we present our approach to solve the bottleneck of the handedness control in a laser cavity.

4.5.1 The handedness control problem

This problem stems from the intensity patterns of helically phased beams having the same OAM charge but opposite sign. As shown in Fig 4.25, the $LG_{0,+1}$ and $LG_{0,-1}$ modes have an identical intensity pattern and thus degenerate resonance frequencies. It is clear that these modes cannot be distinguished using an amplitude mask like the ones used the previously. For example, placing high loss mask in the dark regions of the beam may result in right handed or left handed vortex beam (see Fig 4.19d), or even the superposition of both. Indeed, it is interesting to determine which one of the three cases one may obtain in a completely symmetric cavity when nothing is done to control the handedness, this would help us to understand many of the literature results. We shall answer this question in Sec 4.5.3, but for the times being we describe some of the reported methods of intracavity generation of beams carrying OAM.

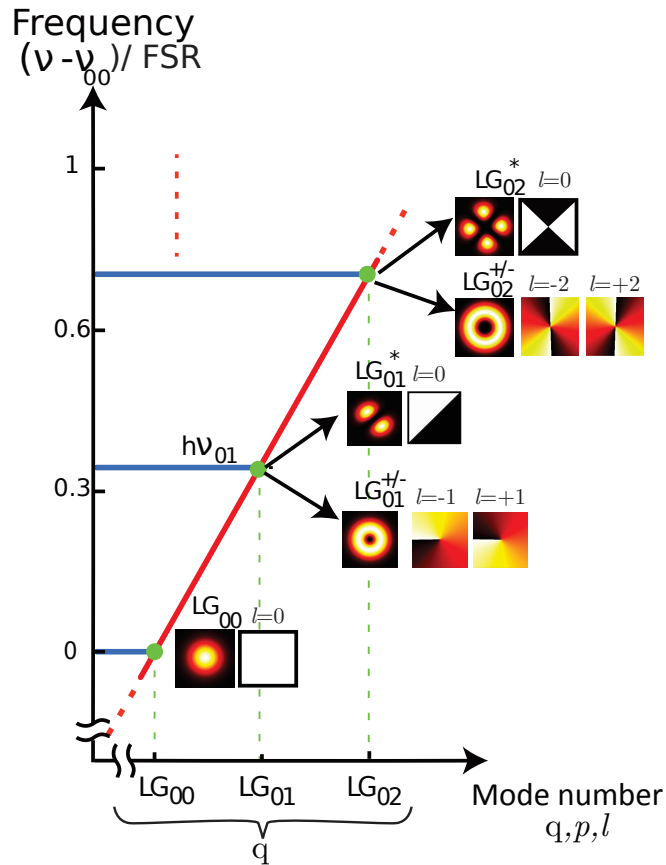


Figure 4.25: Diagram of LG modes in a stable concave-type optical cavity.

4.5.2 State of the art of intracavity vortex-beams generation

Reported methods of intracavity generation of modes carrying OAM are basically based on the same techniques as those discussed in Sec 3.5 and can be divided into two approaches: amplitude only selection methods and hybrid methods.

4.5.2.1 Amplitude only intracavity mode selection

In this case a circular high loss element is placed in the dark region of the helically phase beam to suppress the other non degenerate modes [Harris 1994a] (see Fig 4.26). The same effect can be achieved using an annular pumping profile

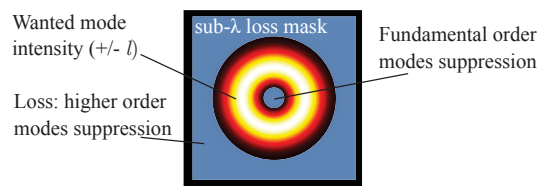


Figure 4.26: Loss mask for LG_{0l} mode selection.

[Kim 2013, Lin 2014], or by exploiting the spherical aberrations that severely affect the fundamental mode [Chard 2009]. In this case the handedness is not controlled, however, the authors reported a well-defined handedness. For example Harris et al [Harris 1994a] used a gas laser with highly symmetric cavity containing a circular absorber. The observed beam has a helical wavefront with a handedness that changes randomly every time the laser intensity builds up, with 50% occurrence probability for each one. In [Kim 2013] and in [Chard 2009] the authors observed a more stable handedness but that can be changed by touching some of the inserted intracavity elements. For example, by tilting an etalon in [Kim 2013]. In sum the handedness selection process is not understood.

4.5.2.2 Hybrid generation methods:

The aim of these approaches is to control the handedness of the OAM. For example, in [Li 2015] a refractive spiral phase plate has been inserted on the outer surface of a monolithic VCSEL. This approach is obviously closer to external transforming methods but we mentioned it here because it aims to obtain integrated emitters. [Cai 2012, Schulz 2013] have shown integrated ring resonator supporting whispering gallery modes carrying OAM with high charge, and to extract these modes researchers used an annular grating. We included this approach in the "hybrid" category because the OAM of the generated beam is different from the one of the resonator mode, due of the transformation caused by the extraction grating.

Another approach was very recently presented in a working paper by [Naidoo 2015] involves using a compound cavity shown schematically in Fig 4.27. In

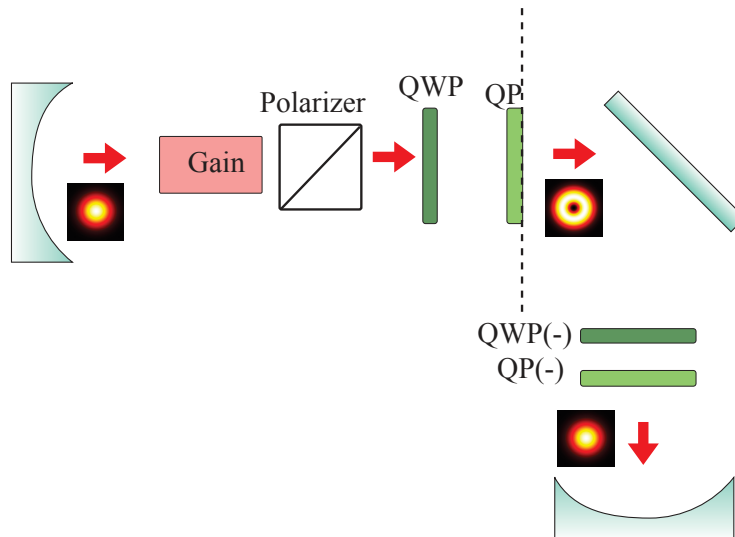


Figure 4.27: Illustration of handedness selection using a compound cavity [Naidoo 2015].

this cavity the two concave mirrors see a linearly polarized fundamental Gaussian beam. The polarization of the beam is transformed to circular one by the quarter

wave plate QWP then the Q-plate¹ transforms the beams to helically phased one [Marrucci 2006, Karimi 2009]. The beam must be extracted from this region of the cavity, because the couple QP(-) and QWP(-) will transform it back to linearly polarized fundamental Gaussian one. The handedness of the beams here is determined by the orientation of the QWP and the Q-plate. This system shows a functional and well understood way to control the handedness of the OAM, but suffers from the drawbacks of using a compound cavity. Because the beam is not an eigenmode of the cavity but transformed in a small section inside it, thus, this method encounters the same problems of the external generation in terms of alignment, beam quality, losses, and the system is clearly far from the compactness expected from direct generation.

4.5.3 Vortex modes dynamics and random handedness selection

Our goal here is to describe the vortex mode dynamics and explain the spontaneous handedness selection observed in amplitude only methods. This problem raises a key aspect of transverse modes selection by the laser, whose understanding brings us one step further to the method we propose. We analyze this problem using transverse mode competition equations. However, as here the two modes have identical intensity patterns ($|u(r, \theta)_{0l}| = |u(r, \theta)_{0-l}|$) and degenerate frequencies, the question cannot be treated using intensity-only mode competition equations presented in Sec 1.6.2. Indeed, a quick look at the involved coefficients (gain-loss, cross- and self-saturation) shows that the present situation results in a completely symmetric problem without the possibility of convergence to any of the two modes regardless of the initial conditions. This is obviously not the case in real lasers, the missing element here is that the two modes can also be coherently superimposed to form a degenerate petal-like mode with OAM = 0. To take account of this possibility we must use the semi classical mode competition equations that we derive in the following sections for a multi-transverse modes class-A VeCSEL. Afterward, we will resume our discussion on vortex mode dynamics, better equipped, in Sec 4.5.3.3.

4.5.3.1 The general Maxwell-Bloch equations

In what follows we assume that the slowly varying envelope approximation is valid for both the electric field and the macroscopic atomic polarization of the medium (the dynamic constants of the system $\gamma_e, \gamma, \gamma_\perp \ll \omega$ the optical frequency). We can then write the two quantities in slowly varying sinusoidal forms as follows:

$$\vec{\mathcal{E}}(\vec{r}, t) = \frac{1}{2} \left(\vec{E}(\vec{r}, t) e^{-j\omega t} + c.c \right) \quad \text{and} \quad \vec{\mathcal{P}}(\vec{r}, t) = \frac{1}{2} \left(\vec{P}(\vec{r}, t) e^{-j\omega t} + c.c \right), \quad (4.11)$$

where \vec{E} and \vec{P} are the slowly varying envelopes of the total cavity electric field and the polarization, respectively. We also make the assumption that the envelope

¹A Q-plate is an optical waveplate that transforms spin angular momentum to orbital one (see [Marrucci 2006]).

\vec{E} can be written as an expansion in a set of normal eigenmodes \vec{U}_i of the cavity in the form ¹:

$$\vec{E}(\vec{r}, t) = \sum_i \vec{U}_i(\vec{r}) E_i(t) \exp(-j\Delta_i t) \quad (4.12)$$

where \vec{r} represents the spatial variables and $\vec{U}_i = u_i(\vec{r}) \vec{x}_i$ are the spatial eigenmodes of the cavity with an electric-field polarization eigenmode parallel to the unit vector \vec{x}_i . The modes $\vec{U}_i(\vec{r})$ satisfy the Helmholtz equation for the electric field:

$$\left[c^2 \nabla^2 + \varepsilon(\vec{r}) \omega_i^2 \right] \vec{U}_i(\vec{r}) = \vec{0} \quad (4.13)$$

where ω_i is the resonance frequency of the mode $\vec{E}_i(\vec{r})$ in the unloaded resonator. $\varepsilon(\vec{r})$ is the dielectric constant (or a tensor if anisotropic) which can have a space dependence. $\Delta_i = \omega_i - \omega$ is the frequency detuning between the \tilde{u}_i mode frequency and the central frequency of the laser emission. The modes $\tilde{u}_i(\vec{r})$ satisfy the orthogonality condition:

$$\int_{V_c} \vec{U}_i(\vec{r}) \cdot \vec{U}_k^*(\vec{r}) d^3r = V_c \delta_{i,k} \quad (4.14)$$

where V_c is the volume of the cavity. The time dependent term $E_i(t)$ is the slowly varying envelope of the spatial mode number i , they are given by:

$$E_i(t) = \exp(j\Delta_i t) \int_{V_c} \vec{U}_i^*(\vec{r}) \cdot \vec{E}(\vec{r}, t) d^3r \quad (4.15)$$

Finally, if we assume that the medium is isotropic ², the Maxwell-Bloch equations can be written in the following form [Siegman 1986, Hodges 1997]:

$$\begin{aligned} \frac{dE_i(t)}{dt} &= -\frac{1}{2} \sum_k \gamma_{i,k} E_k(t) \\ &\quad - j \frac{\omega}{2V_c \varepsilon} \int_{V_a} \vec{P}(\vec{r}, t) \cdot \vec{U}_i^*(\vec{r}) d^3r \exp(j\Delta_i t) \end{aligned} \quad (4.16a)$$

$$\frac{d\vec{P}(\vec{r}, t)}{dt} = -(\gamma_{\perp} + i\Delta_a) \vec{P}(\vec{r}, t) + j \frac{d^2}{\hbar} \Delta n \vec{E}(\vec{r}, t) + F_P \quad (4.16b)$$

$$\frac{d\Delta n(\vec{r}, t)}{dt} = \rho(\vec{r}, t) - \gamma_e \Delta n(\vec{r}, t) - j \frac{1}{2\hbar} \left[\vec{E}^* \cdot \vec{P} - c.c \right] + F_{\Delta n} \quad (4.16c)$$

where V_a is the active volume, Δn is the population inversion, $\Delta_a = \omega - \omega_a$, and $\rho(\vec{r}, t)$ is the pump rate per unit volume. Δ_i (resp. Δ_a) is the frequency detuning between the mode $\tilde{u}_i(\vec{r})$ (resp. the mean value of the atomic transition ω_a) and the central frequency. d is the electric dipole moment of the laser transition, and $F_{P, \Delta n}$ are the Langevin Force for the atomic polarization, and for the population

¹In the general case this approximation is rigorous only when the active medium occupies all the cavity volume. However, in the case of VeCSELs, with a sub-wavelength thick active medium we can use this approximation in two dimensions.

² $\vec{\mathcal{E}}$ and $\vec{\mathcal{P}}$ are collinear.

inversion, respectively. The electric field damping terms in Eq 4.16 takes account of the non-uniform loss $\gamma(\vec{r})$ in the cavity which can couple the different electric-field harmonics (like backscattering in a bidirectional ring laser resonator [Khanin 1995, Schwartz 2008]). In the general case, $\gamma_{i,k}$ are time-dependent, and read:

$$\gamma_{i,k}(t) = \frac{1}{V_c} \int_{V_c} \gamma(\vec{r}) \vec{U}_k(\vec{r}) \cdot \vec{U}_i^*(\vec{r}) d^3r \exp(j\Delta_{i,k}t) \quad (4.17)$$

We note that when the laser system cannot respond to the spatial harmonics beating at high frequencies, the terms $\gamma_{i,k}$ can be neglected for $i \neq k$, the damping of each harmonics is constant in time and there is no coupling between the spatial harmonics of the electric-field.

The Maxwell-Bloch equations represent the starting point to analyze the temporal dynamics of most laser systems. The main difficulty in Eq 4.16 is to expand the population inversion and the atomic polarization in an adequate spatial basis in order to be able to integrate spatially and write the source term for each harmonic of the field. This difficulty stems from the fact that in most laser systems, the active medium don't fill the cavity volume. Consequently, if one expands \vec{P} and Δn on the basis of the electric field (Eq 4.12), one obtains spatial harmonics that are not slowly varying [Hodges 1997]. This difficulty should be dealt with on a case-by-case basis according to the considered laser system.

4.5.3.2 Maxwell-Bloch equations in multi-transverse mode VeCSEL

In this section we will write the Maxwell-Bloch equations for a multi-transverse mode Class-A, or Class-B VeCSEL.

When the laser is turned on, the gain curve contains a large number of modes (along all the light axis: longitudinal, transverse and polarization, see Fig 4.28) which makes the multi-mode dynamics too complex to be studied by considering all the light axis in a one model. Therefore, we will simplify the problem as much

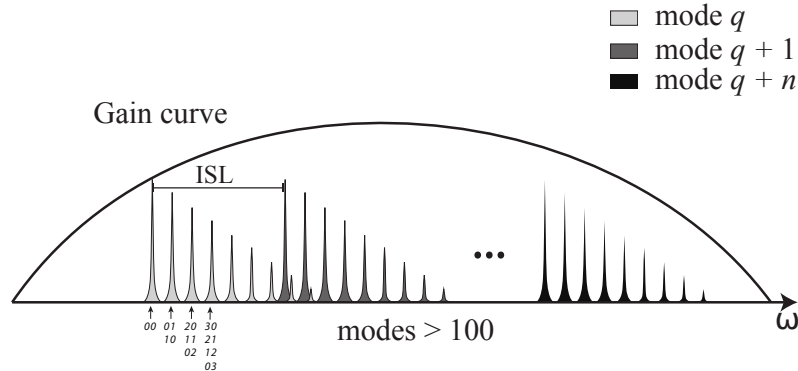


Figure 4.28: Illustration of the number of modes in the gain curve.

as possible by making the following assumptions:

1. The polarization of the medium is always in the steady state ($\frac{d\vec{P}}{dt} = 0$), as it follows adiabatically the electric field and the population inversion ($\gamma_{\perp} \gg \gamma_e$ and, γ). This means that we are in the case of class-A or -B laser.
2. The active medium being very small compared to λ , and as the quantum wells are located on an end mirror where all the waves are in-phase, we can consider that there is no longitudinal spatial hole burning. Thus, we assume that the transverse mode competition takes place on a 2D transverse plane (the active zone plane).
3. Several transverse modes can oscillate in the laser cavity, but each one oscillates on a single longitudinal mode. Put another way, we assume that the transverse modes dynamics is independent of longitudinal modes one (happens on different time scales).
4. In the case where the optical losses inside the cavity are distributed non-uniformly (because of an amplitude mask for example) the inter-mode beat at the frequency difference $\Delta_{i,k}$ may induce a modulation of the optical losses in time (Eq 4.17). As the VeCSEL has a short cavity $L_c < 10$ mm, the condition $\Delta_{i,k} \gg \gamma$ is fulfilled¹. This allows us to neglect the time dependence of the optical losses for each mode and consider that they are stationary and can be averaged over the mode volume.
5. The VeCSEL has a short cavity $L_c < 10$ mm. In this case we can neglect all the inter-mode beating terms with frequencies $\Delta_{i,j} > \gamma_e$ (see Fig 4.29). Indeed, when these modulations fall within the gain medium bandwidth, the modes will be non-linearly coupled by the gain medium. This effect is known as the four wave mixing [Yamada 1989, Garnache 2007].

Above the transparency, the semiconductor gain medium can be treated as a two-level system with a population inversion Δn . With assumption (1), according to Eq 4.16 we can write:

$$\vec{P}(\vec{r}, t) \simeq -j \frac{d^2}{\hbar \gamma_{\perp}} \frac{1}{1 + j \Delta_a / \gamma_{\perp}} \Delta n \vec{E}(\vec{r}, t) \quad (4.18)$$

By substitution \vec{P} in the electric-field and the population inversion equations, the

¹In the case of VeCSEL with a cavity length \sim few mm this condition is always fulfilled, because the available gain is of the order of few % which imposes to use a high finesse cavity.

system of equations reads:

$$\begin{aligned} \frac{dE_i(t)}{dt} = & -\frac{1}{2} \sum_k \gamma_{i,k} E_k(t) \\ & + \frac{B^*(\omega)}{2} \int_{V_a} \Delta n \vec{E}(\vec{r}, t) \cdot \vec{U}_i^*(\vec{r}) d^3r \exp(j\Delta_i t) + F_{E_i} \end{aligned} \quad (4.19a)$$

$$\frac{d\Delta n(\vec{r}, t)}{dt} = \rho(\vec{r}, t) - \gamma_e \Delta n(\vec{r}, t) - \frac{d^2}{2\hbar^2 \gamma_\perp} \frac{1}{(1 + \alpha_h^2)} |\vec{E}(\vec{r}, t)|^2 \Delta n(\vec{r}, t) + F_{\Delta n} \quad (4.19b)$$

where $F_{E_i(t)}$ is the Langevin source for the electric field induced from $F_P(t)$, and $B^*(\omega)$ is a complex Lorentzian gain term given by:

$$B^*(\omega) = B(\omega)(1 + j\alpha_h) \equiv \frac{2\omega d^2}{\varepsilon \hbar \gamma_\perp V_c} \frac{1}{1 + (\Delta_a/\gamma_\perp)^2} (1 + j\alpha_h) \quad (4.20)$$

with the Henry factor $\alpha_h \equiv \Delta a/\gamma_\perp$.

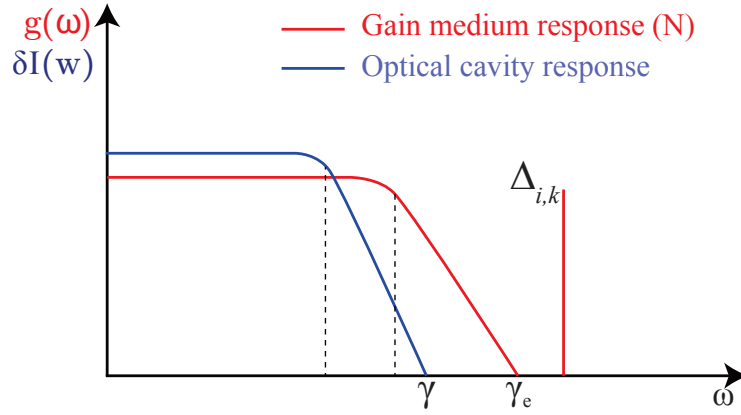


Figure 4.29: Schematic illustration of the gain medium and the optical cavity dynamic responses in a Class-A laser. As first order approximation, all the processes with a characteristic frequency beyond the laser system bandwidth can be neglected.

We can simplify further the system of equations 4.19 by integrating the spatial variables $\tilde{X}_i(\vec{r})$ over the z -axis (2nd assumption). Given that the quantum wells width is very small compared to the wavelength $L_{QW} \ll \lambda$ (the active medium is considered as a δ function at $z_0 = 0$), the spatial integrals in Eq 4.19 can be written as:

$$\int_{V_a} \tilde{X}_i(\vec{r}) d^3r = L_a \int_{A_a} \tilde{X}_i(\vec{r}) d^2r \Big|_{z=z_0} \quad (4.21)$$

where A_a is the active medium surface, and $L_a = N_{QW} \times L_{QW}$. Thus, in our case we can write the spatial variables in the mode basis defined by Eq 1.7 by putting $z = 0$:

$$\tilde{u}(r, \theta) \equiv \tilde{u}_{pm}(r, \theta, z = 0) = \Phi_{pm}(r, \theta) \quad (4.22)$$

At the end, the system of equations describing the transverse mode dynamics in a class (A,B) VeCSEL with assumptions 1,2,3 reads:

$$\frac{dE_i(t)}{dt} = \sum_k E_k(t) \left[\overbrace{-\gamma_{ik}}^{\text{Loss}} + \overbrace{B^*(\omega)L_a \int_{A_a} \Delta n(\vec{r}, t) \Phi_k(r, \theta) \Phi_i^*(r, \theta) dA e^{j\Delta_{ik}t}}^{\text{Gain}} \right] + F_{E_i} \quad (4.23a)$$

$$\begin{aligned} \frac{d\Delta n(\vec{r}, t)}{dt} &= \rho(\vec{r}, t) - \gamma_e \Delta n(\vec{r}, t) \\ &\quad - B^*(\omega) \frac{\varepsilon V_c}{4\hbar\omega} \Delta n(\vec{r}, t) \sum_k \sum_i E_k(t) E_i^*(t) \Phi_k(r, \theta) \Phi_i^*(r, \theta) e^{j\Delta_{ik}t} + F_{\Delta n} \end{aligned} \quad (4.23b)$$

In order to point out the terms mentioned in our discussions, this set of equations can be written in a more explicit form as follows:

$$\begin{aligned} \frac{dE_i(t)}{dt} &= E_i(t) \left[\overbrace{-\gamma_{ii}}^{\text{Loss (self)}} + \overbrace{B^*(\omega) \int_{A_a} \Delta n(\vec{r}, t) |\Phi_i(r, \theta)|^2 dA L_a}^{\text{Gain (self)}} \right] + F_{E_i} \\ &\quad + \sum_{k \neq i} E_k(t) \left[\overbrace{-\gamma_{ik}}^{\text{Loss (cross)}} + \overbrace{B^*(\omega) \int_{A_a} \Delta n(\vec{r}, t) \Phi_k(r, \theta) \Phi_i^*(r, \theta) dA L_a e^{j\Delta_{ik}t}}^{\text{Gain (cross)}} \right] \end{aligned} \quad (4.24a)$$

$$\begin{aligned} \frac{d\Delta n(\vec{r}, t)}{dt} &= \rho(\vec{r}, t) \overbrace{-\gamma_e \Delta n(\vec{r}, t)}^{\text{Spontaneous Emission}} \\ &\quad \overbrace{-B^*(\omega) \frac{\varepsilon V_c}{4\hbar\omega} \Delta n(\vec{r}, t) \sum_k |E_k(t)|^2 |\Phi_k(r, \theta)|^2 + F_{\Delta n}}^{\text{Stimulated Emission}} \\ &\quad \overbrace{-B^*(\omega) \frac{\varepsilon V_c}{4\hbar\omega} \Delta n(\vec{r}, t) \sum_k \sum_{i \neq k} E_k(t) E_i^*(t) \Phi_k(r, \theta) \Phi_i^*(r, \theta) e^{j\Delta_{ik}t}}^{\text{Stimulated Emission (cross coupling)}} \end{aligned} \quad (4.24b)$$

where $dA = r dr d\theta$.

With assumptions (4,5), only remains the cross coupling terms, in the E-field and population equations for degenerate modes with difference frequency $\Delta_{ik} \simeq 0 s^{-1}$ when $\Delta_{ik} \gg (\gamma_e, \gamma)$.

4.5.3.3 Discussion on coupling via the loss term

Let us take a moment to look at Eq 4.24, and discuss some important implications of remaining Loss-cross coupling terms in the electric field equation (Eq 4.24a), by considering two practical cases: HG and LG modes with degenerate frequencies¹.

In the first case, degenerate HG modes have different intensity profiles (see Fig 4.2), so when we select one of them using a loss mask, the other one experiences very high loss and doesn't reach the threshold. Therefore, the coupling due to the cross terms $E_k \gamma_{i,k}$ is very weak as all the modes $E_{i \neq k}$ are at the spontaneous emission level.

With LG modes the situation is a little more complex, because two LG modes LG_{nm} , LG_{pl} can be degenerate in two cases: (1) $|n|+|m|=|p|+|l|$ with $|n| \neq |p|$ and $|m| \neq |l|$. (2) $|n|+|m|=|p|+|l|$ but $|n|=|p|$ and $|m|=|l|$. In the first case we are in a situation similar to that of HG modes. The additional difficulty however, comes from the second case. It is a particular one, possible with LG modes because the azimuthal number l can be > 0 or < 0 : OAM's with different signs of same charge. Here if we use a mask that doesn't have the symmetry of LG modes (two crossed lines, for example) The cross terms γ_{ik} between LG_{p+l} and LG_{p-l} will be very strong and will lock the modes to give a petal-like mode (linear combination of LG_{p-l} and LG_{p+l}). We have already encountered this situation in our experiments (see Fig 4.19 b,c,e,f). When the mask does have symmetry of the modes (see Fig 4.26), in principle it does not introduce loss inhomogeneity, the 5th assumption is then valid, and there is no coupling between modes with $l > 0$ and $l < 0$. However in practice, the cavity elements can present intrinsic inhomogeneities (due to surface defects on mirrors for example) that can couple the two modes, this effect is called the backscattering. We neglected this question in the previous discussions because this effect is very weak when the other modes are at the spontaneous emission level, which is clearly not the case here as the intensity mask allows to select two vortex modes rather than only one.

The backscattering² effect is well known in bidirectional ring lasers where the presence of spot defects on the mirrors locks the two contra running modes, which results in standing wave usually unwanted in this type of lasers because it limits the minimum measurable angular velocity [Khanin 1995]. In our case this coupling can lock the two contra-rotating vortex modes to give a degenerate petal-like mode. In order to be close to experimental conditions, we will take it into account in our simulations. In summary, even when we use an intensity mask that has the symmetry of vortex modes, the two modes can coexist and can be locked by the backscattering effect. However, here we only discussed the effect of loss terms. A complete understanding requires to take account of inhomogeneity and cross coupling in the gain term too, thus to study the laser dynamics with gain saturation

¹As a reminder, two HG_{nm} , HG_{pl} modes are degenerate if they have the same total quantum number: $|n|+|m|=|p|+|l|$ (see Eq 1.12).

²More generally, in physics the backscattering is known as Huygens synchronization, when two oscillators have the same frequency and can exchange energy they will be locked.

dynamics and inhomogeneity: Spatial hole burning.

4.5.3.4 Dual vortex mode class-A competition equations

We can simplify the system of equations (4.23) by writing it for dual mode class-A VCSEL. The population inversion is considered in the stationary regime and can be eliminated adiabatically, the Dual mode system of equations reads:

$$\begin{aligned} \frac{dE_{1,2}(t)}{dt} = & \frac{E_{1,2}}{2} \left(-\gamma_{1,2} + L_a B^* \int_{A_a} \frac{\rho}{\gamma_e} |\Phi_{1,2}(r, \theta)|^2 \right) \\ & + \frac{E_{2,1}}{2} e^{\pm j \Delta_{21} t} \left(\tilde{\gamma}_b + L_a B^* \int_{A_a} \frac{\rho \Phi_{2,1}(r, \theta) \Phi_{1,2}^*(r, \theta)}{1 + \frac{D}{\gamma_e} |E_t|^2} \right) + F_{E_{1,2}}, \end{aligned} \quad (4.25)$$

where E_1, E_2 are the E-field of the two competing modes, $D = B \frac{\varepsilon V_c}{4\hbar\omega}$; $\tilde{\gamma}_b = \gamma_b e^{j\mu}$ is the backscattering coefficient, with μ a phase term that depends on loss inhomogeneities. E_t denotes the total electric field, and is given by:

$$E_t = \sum_{i=1,2} E_i U_i(r, \theta) e^{-j\Delta_i t} \quad (4.26)$$

In a high finesse cavity with laser-quality mirrors $\gamma_b \simeq 10^{-5} \gamma$ [Mignot 2008b]. We note that the photon number in a given spatial mode can be calculated from the Electric field using the following expression [Siegman 1986]:

$$I_i(t) = V_c \frac{\varepsilon}{2\hbar\omega_i} |E_i(t)|^2 \quad (4.27)$$

4.5.3.5 Numerical results and discussion

The system of equations (4.25) allows us to study the competition between two transverse modes, it takes account of the modes' intensity patterns, and importantly the phase patterns too. It also takes into account the overlap of the modes with the pumped zone, and the coupling due to the backscattering. In the simulations we use the pump rate η , defined as the pump rate above the threshold relative to the transparency, and given by:

$$\eta = \frac{P_p - P_{tr}}{P_{th} - P_{tr}} \quad (4.28)$$

where P_p, P_{tr}, P_{th} are the pump power, the threshold power and the transparency power respectively.

As a first example, let us consider the case where there are two potentially oscillating modes inside a 8mm length VCSEL cavity: LG₀₀ and LG₀₂, with modes waists on the 1/2-VCSEL structures $w_{00} = 36 \mu\text{m}$ and $w_{02} = w_{00}\sqrt{1+2}$. The structure is pumped with a Gaussian beam having a waist $w_p = 40 \mu\text{m}$, at a pump rate $\eta = 10^{-1}$.

In this case we expect the fundamental mode to win the competition because it has a higher net gain and the LG_{02} to not reach the threshold because of the excess loss coming from the unpumped region. Indeed, when we look at the simulation results in Fig 4.30 we can see that at the beginning, the two modes' intensities start growing, the LG_{00} one grows faster because of its higher net gain. On the other hand the LG_{02} intensity grows very slowly and almost does not exceed the spontaneous emission level. This is a classic example of selection by loss that we have used to select HG and degenerate LG modes (Sec 4.4).

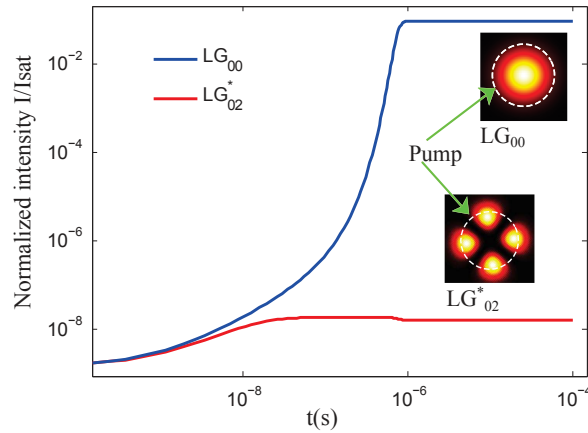


Figure 4.30: Dynamic simulation of dual mode competition in a class-A laser. Considered modes are LG_{00}, LG_{02} , simulation parameters: cavity length $L_c = 8\text{mm}$; loss = 1%; waists: $w_{00} = 36\ \mu\text{m}$ and $w_{02} = w_{00}\sqrt{1+2}$; pump waist $w_p = 40\ \mu\text{m}$; pump rate $\eta - 1 = 10^{-1}$.

We now move to the case of dual vortex modes, having the same intensity profile (donut) but opposite wavefront's handedness $LG_{0,+|l|}, LG_{0,-|l|}$. Fig 4.31a shows the simulation result we obtained in this case with a homogeneous pumping and a mode waist of $67\ \mu\text{m}$. When the laser is turned on, the two modes start growing at the same speed because they have the same net gain. However when the intensity gets much higher than the spontaneous emission level, the nonlinear cross and self-saturation effects come into play and prevent the coexistence of the two modes. In our simulations the mode that wins the competition is the one that has one additional photon at the starting, in real world lasers this additional photon may result from seeding by the spontaneous emission noise at the build up.

However, this is not the only possible result, in fact the backscattering always tends to lock the two modes, thus at low pumping rates when the laser intensity is too low, the nonlinear saturation effects are negligible and the laser output will be the coherent superposition of the two modes which results in a degenerate one with OAM=0 as we can see in Fig 4.31b. The pump rate value at which the nonlinear effects become significantly high to counterbalance the lock-in due to the backscattering depends on the strength of this latter, which is depends in turn on the defect density inside the cavity. In VeCSEL with good surface quality and

standard dielectric laser mirrors $|\gamma_b| \simeq 10^{-5} \gamma$ [Mignot 2008b, Mignot 2008a].

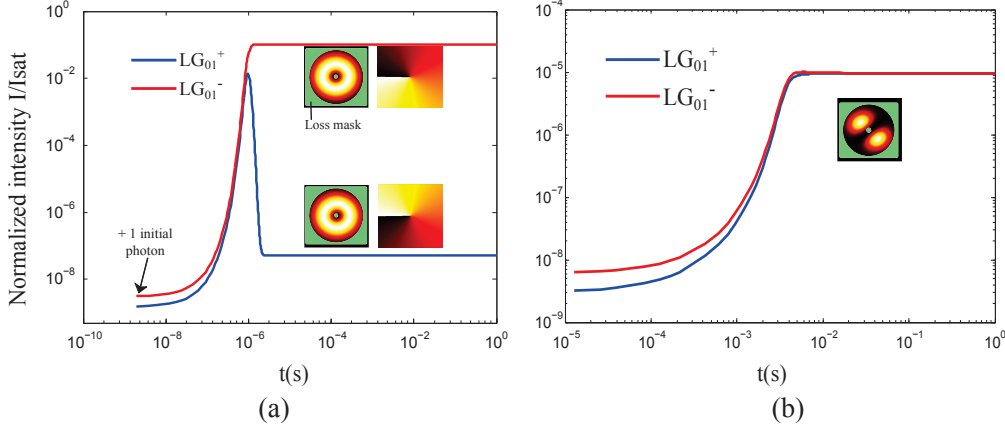


Figure 4.31: Dynamic simulation of contra-rotating vortex modes competition in a class-A laser by taking account of spontaneous emission and the backscattering $\gamma_b = 10^{-5} \gamma$, $L_c = 8\text{mm}$ at pumping rates: (a) $\eta - 1 = 10^{-1}$, (b) $\eta - 1 = 10^{-5}$. At low pumping rate the backscattering locks the two contra-rotating modes which results in a petal-like one.

Fig 4.32a,b summarizes these behaviors. In the first one we plot the steady state of the laser modes intensity as a function of the pump rate, and in the second one we plot the frequency difference between the modes. We can clearly distinguish the two operation regimes: the first one occurs for low pumping rates ($\eta - 1 \sim [0 - 10^{-6}]$), here the two modes are locked; if we look at the frequency plot (Fig 4.32(b)) we notice that they are degenerate. When the pumping rate increases the locking effect is counterbalanced by the nonlinear coupling between the two modes. (cross-saturation). And when we look at the frequency plot this time, we see that the degeneracy is now lifted due to the phase-amplitude coupling in the gain medium. We note that when the degeneracy lift is larger than the cutoff frequency of the laser cavity we consider that the two modes are independent. These simulation results are in good agreement with most of the experimental observations reported in the literature.

In our experiments, when the semiconductor chip has a very high surface quality, it is difficult to observe the first regime (the locking) because it occurs at very low pump rates. However, with some 1/2-VCSEL structures having lower surface quality, the two regimes are unambiguously observed as we show in the experimental beams patterns of Fig 4.33.

These simulations allowed us to explain the random handedness selection reported in the literature, The dynamic simulations we performed show that even when nothing is done to select the handedness, and in a completely symmetric cavity, non-linear coupling prevents the two contra-rotating vortex modes from co-existing. Thus, one of the two modes will always be selected and the laser will emit a beam with a well defined handedness. When the laser cavity has a good symmetry

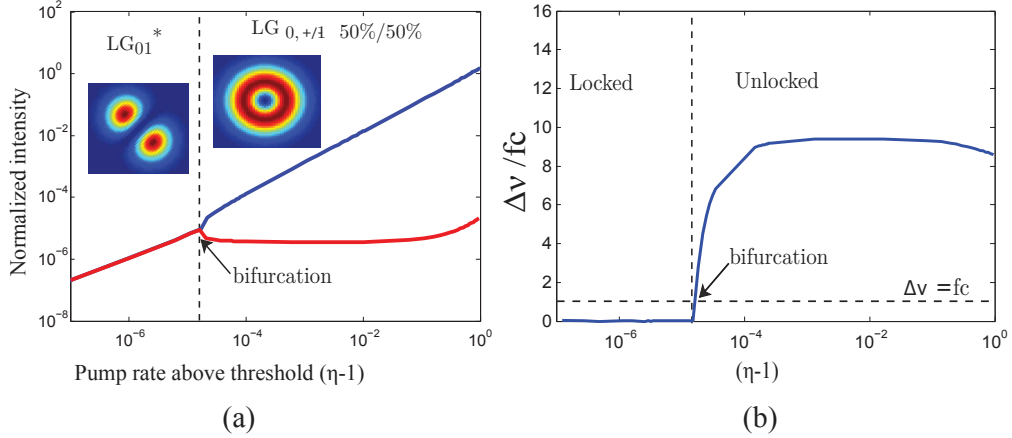


Figure 4.32: (a) Steady state diagram of the bi-transverse mode laser as a function of pumping rate η of two contra-rotating vortex modes by taking account spontaneous emission and the backscattering $\gamma_b = 10^4 s^{-1}$, and $\gamma = 2 \cdot 10^8 s^{-1}$ here the handedness is selected randomly. (b) Phase difference between the two modes.

the selection is done randomly because of the spontaneous emission seeding at the laser build-up.

In the following section, we propose to slightly perturb the cavity eigenstates using a phase mask to render this selection process deterministic, and controlled.

4.6 The proposed solution: OAM charge and handedness control using a flat photonics element

4.6.1 Description of the flat-photonics element (FPE)

The intracavity mode selection method we propose here allows to lift the degeneracy and break the symmetry of the contra-rotating modes' wave-functions $(u(r, \theta)^\pm)$ in a perturbative way like first order perturbation in quantum mechanics. At the same time the method must conserve the concave-type stability of the cavity and maintain the LG eigenmodes as its natural basis. To achieve these functions, our method relies on the perturbative handedness control mask shown in Fig 4.34. In what follows we call this mask 'the flat photonics element (FPE)'. This element is integrated on the top surface of the 1/2-VCSEL structure, and contains three parts: the first one is a phase step at the center, its role is to suppress the fundamental mode by introducing high diffraction loss. We note that the loss at the center can also be achieved using a metallic mask as shown earlier. This part of the FPE is hereafter referred to as 'the lossy disk'. The second part is a thin metamaterial layer (metasurface) that introduces an azimuthally varying refractive index, designed to introduce a perturbative azimuthal phase function $f(\theta)$ given by:

$$f(\theta) = \exp(\pm j\theta \delta m) \tag{4.29}$$

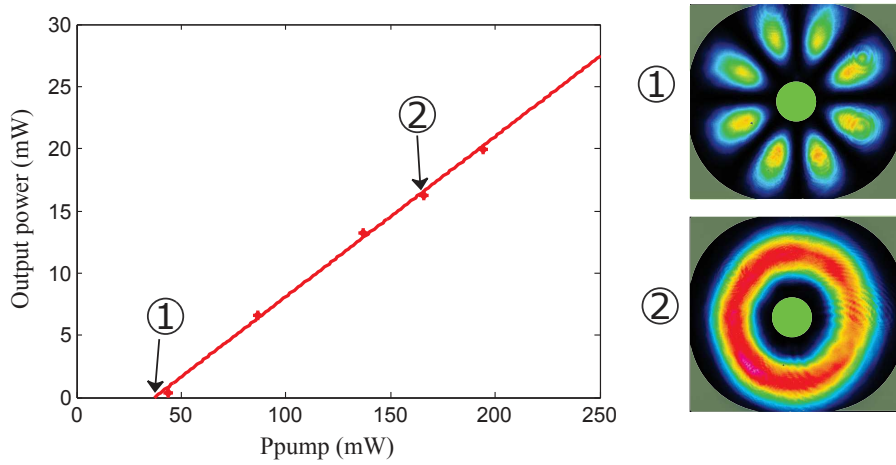


Figure 4.33: Experimental observation of contra-rotating vortex mode locking close to threshold.

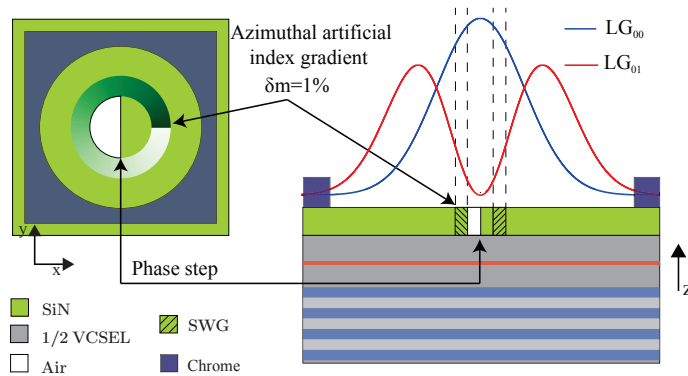


Figure 4.34: Schematic illustration of double-layered mask (chromium+ metasurface) designed to select right-handed vortex mode.

where the total phase shift δm is of the order of $2\pi/100$. We refer to this part as 'spiral phase element'. The last part of the FPE is a loss mask made of chromium and put at the periphery of the wanted mode to suppress higher order ones. The spatial distribution of the metamaterial is defined by $U_{FPE}(r, \theta)$.

4.6.2 The operation principle

4.6.2.1 OAM charge control

The lossy disk allows us to control the charge $|l|$ of the OAM, for example, in a given cavity with a constant length L_c , if one increases the diameter of the lossy disk, the selected mode will have a bigger dark region that fits the new disk diameter, and thus a bigger OAM charge. The same effect can be achieved using a lossy disk with a constant diameter, by changing the cavity length, which changes the waist of the eigenbasis according to Eq 1.27. (see the stability curves of Fig 4.35). In our

experiments we used both methods in order to release the constraints on the FPE dimensions and pump spot size.

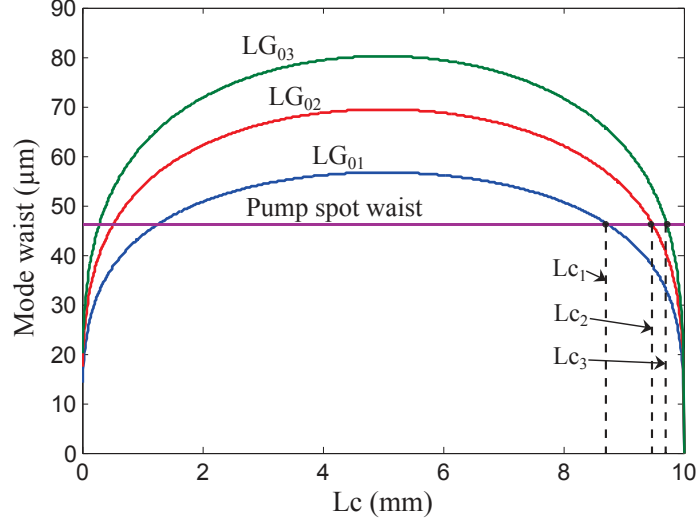


Figure 4.35: Stability curves of the first three vortex modes in a 10 mm length plano-concave cavity, with L_c the length of the cavity.

4.6.2.2 OAM handedness control

To describe how the perturbative spiral phase lifts the degeneracy and break the symmetry, we show schematically in Fig 4.36 an example of the overlap between the desired mode intensity $|\Phi(r, \theta)|^2$ and the FPE, this overlap is calculated using the overlap factor Γ as:

$$\Gamma = \frac{\iint_{\infty} |\Phi(r, \theta)|^2 U_{FPE}(r, \theta) dS}{\iint_{\infty} |\Phi(r, \theta)|^2 dS} \quad (4.30)$$

The typical Γ value we used is of the order of $\Gamma \sim 1\% - 5\%$. Such a low value is necessary not to break the eigenbasis of the cavity, because the mode experiences an azimuthal phase perturbation per pass, proportional to $\delta m \Gamma$, and one must ensure that the accumulated phase perturbation after several round-trip stays much smaller than 2π .

Let us consider the two possible situations according to the FPE and the mode handedness: When the FPE and the intracavity helically phased beam have the same handedness, the dark region of the beam is slightly expanded on each round trip, and thus the overlap with the FPE decreases until it becomes negligible. On the other hand, the beam the opposite handedness sees its dark region slightly narrowed after each round trip, which in turn increases the overlap with the FPE, the effect of the FPE on the mode is then bigger after each round trip, and the beam is somehow trapped in the vicious circle. The process cannot continue infinitely because of the finite cavity lifetime, but in the end, this mode will be strongly perturbed by the

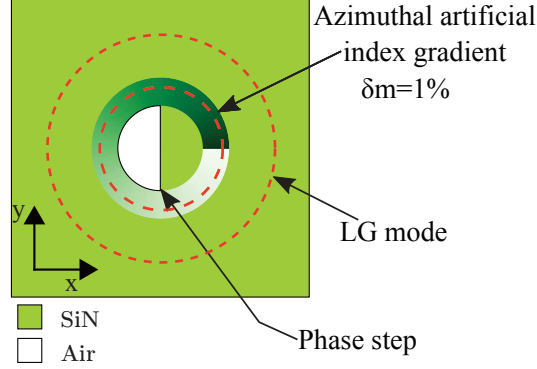


Figure 4.36: Schematic illustration of vortex mode overlap with metasurface-based phase and intensity mask (FPE), designed to control the handedness.

FPE, which results in noticeable modulations in its intensity profile (see Fig 4.37). The symmetry of the wavefunctions u_{0l} and u_{0-l} in the cavity is broken. This is accompanied by a degeneracy lift because the modes now have different resonance frequencies as illustrated schematically in Fig (4.38). To validate this method, we

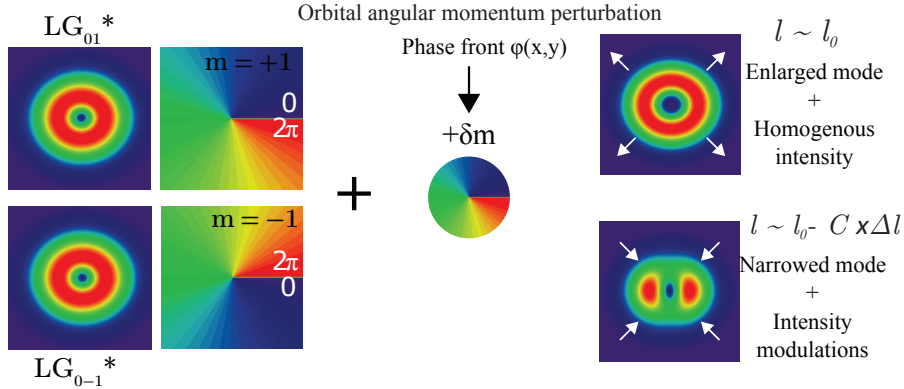


Figure 4.37: Operation principle of the perturbative spiral phase mask.

used numerical simulation of the perturbed cavity eigenstates, using an approach similar to the first order perturbation theory in quantum mechanics, i.e: first we calculated eigenvalues and the corresponding eigenmodes of the cavity incorporating the lossy disk placed on its axis. As expected we obtain two helically phased modes with the same intensity distribution (Fig 4.39 a2,b2) but opposite handedness (Fig 4.39 a1,b1). Thereafter, we re-injected the obtained degenerate contra-rotating vortex modes in the same cavity, but this time we added the perturbative azimuthal phase function, and used the Fox-Li iterative method to observe the evolution of each eigenmode to the steady-state. Simulation results are shown in Fig 4.39c,d, they are obtained for 1200 iteration in a plano-concave cavity with a length $L_c = 8mm$, Radius of curvature $R_c = 10$ mm, lossy disk radius $w_d = 2.5 \mu m$, mirrors radius of $200 \mu m$ and discretization step of $1 \mu m$.

These results support the explanations we provided at the beginning of this

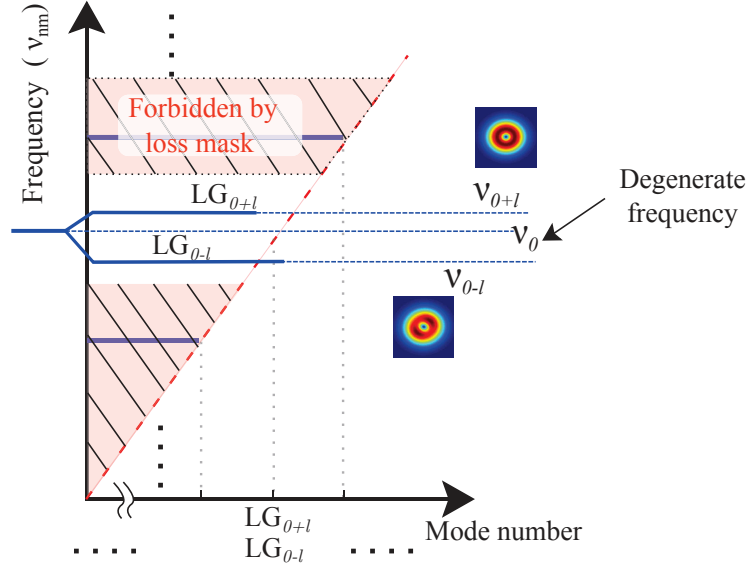


Figure 4.38: Degeneracy lift of between contra-rotation vortex modes in a cavity incorporating the FPE.

section: only the mode having a handedness opposite to the one of the FPE is strongly perturbed (Fig 4.39d). Furthermore, by observing the eigenvalues evolution we notice that the two modes still have basically the same loss but, importantly, different resonance frequencies. In sum, the FPE we integrated on the 1/2-VCSEL caused a symmetry breaking and a degeneracy lift between the left handed and right handed vortex modes. We note that the degeneracy lift is asymmetric with respect to the degenerate frequency (ν_0), the more perturbed mode get farther from it, this means that in the example of Fig 4.38 $|\nu_{0,+1} - \nu_0| < |\nu_{0,-1} - \nu_0|$. It is important to note that the degeneracy lift $\Delta\nu$ must be larger that the cutoff frequency of the laser cavity f_c so that the modes cannot be locked dynamically:

$$f_c < \Delta\nu = |\nu_{0,+1} - \nu_{0,-1}| \ll FSR \quad (4.31)$$

with f_c given by:

$$f_c = \frac{\gamma}{2\pi} \frac{\eta - 1}{\eta} \quad (4.32)$$

After the degeneracy lift and the symmetry breaking, the two vortex modes become now distinguishable, and based on the studies we conducted on mode competition, we can already predict that the one with the most homogeneous intensity distribution will "win" the competition in the gain medium, regardless of the initial conditions, thanks to the self-saturation effect (because the laser always tends to prevent the spatial hole burning). This is illustrated in Fig 4.40. These curves are computed by injecting the contra-rotating vortex modes that we obtained from the eigenmode calculation, in the dual mode competition Max-Bloch equations (Eq 4.25). We repeated the same simulation by varying the pump rate, the ob-

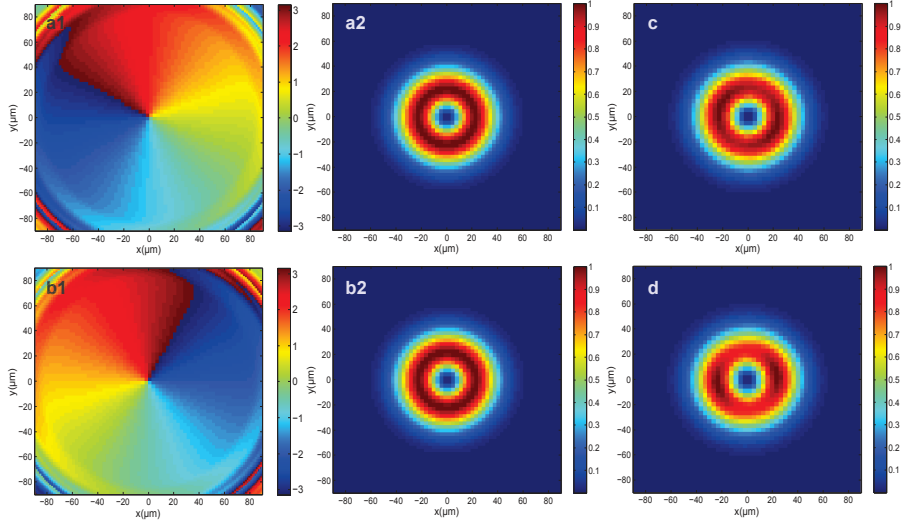


Figure 4.39: (a,b) Left- and right- handed, respectively, calculated first eigenmodes in a plano-concave cavity incorporating the lossy disk, the figure shows the obtained phase (a1,b1) and intensity (a2,b2) eigenfunction. (c,d): Fox-Li simulation results obtained by injecting modes obtained in (a,b) in a cavity incorporating the perturbative handedness control element shown in Fig 4.34.

tained curves are shown in Fig 4.41. We can see that unlike the case where the modes are degenerate, here the degeneracy lift prevents the locking of the modes, and this is true even at low pumping rates where we have two donut modes with opposite handedness. When the pumping rate increases, however, the intensity becomes high enough to enable the non-linear cross and self-saturation effects. And this time, the competition result is deterministic, as the most homogeneous mode always 'wins' regardless of the pumping rate or the initial conditions (Fig 4.41a). In Fig 4.41b we show the evolution of the frequency difference between the two vortex modes, we note that the negative slope of the curve is explained by the fact that frequency splitting is normalized to f_c which depends on the pump rate η . These results lead us to the conclusion that, using the FPE provided us an efficient and well understood method to select a given vortex mode with well-defined and deterministically controlled handedness.

4.6.3 Design and fabrication of the 1/2-VCSEL and the FPE

Fig 4.42 shows schematically the design principle of the azimuthally varying phase function, we azimuthally change the fill factor to introduce the desired phase function $f(\theta)$ given in Eq 4.29.

The design and fabrication steps of the FPE are essentially those presented in Chap 3. However, there are some design considerations specific to this particular example, and that we will point out here in some details. In Chap 3 we have used a metamaterial layer in a resonant configuration, in order to maximize the total phase

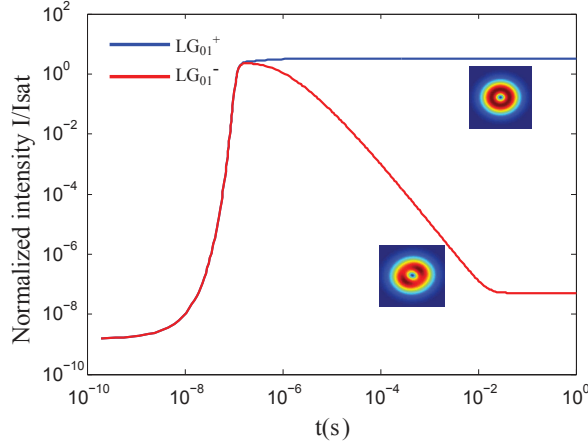


Figure 4.40: Temporal dynamic simulation showing competition between vortex modes of the perturbed cavity, with $\eta = 2$, $\gamma = 2 \times 10^8 \text{ s}^{-1}$. Here the handedness is selected deterministically as the most homogeneous mode 'wins' the competition irrespective to initial conditions.

variations. Here, however, we need a perturbative phase function with a total variation of the order of $2\pi/100$ and using a resonant cavity configuration raises some technological problems. The first one is due to the relatively fast phase variations with the fill-factor (ff), which means that to achieve the desired perturbative phase function, we have to use very thin dielectric layer, and to vary the ff in a very small range. However, it is preferable to work with relatively large layer thicknesses to minimize the relative error between the targeted thickness and achieved one¹. The second problem is the phase discretization step which is inversely proportional to the ff variation range because of the finite resolution of the etching method. Thus to properly discretize the implemented phase function, large ff variation range is preferred². Because of these two problems the anti-resonant configuration (Fig 4.43a) is a better choice to accurately achieve very small phase variation. In Fig 4.43b we show RCWA simulations of phase variation as a function of ff, obtained with the anti-resonant structure, the resulting phase variation is relatively slow. To optimize the metamaterial layer design according to the above mentioned considerations, we set the condition $\delta m = \Delta\phi(\text{ff})_{max}$ in order to use all the usable fill factor range, then we adjust the dielectric layer thickness to make the used ff range correspond to the total phase variations we want. Finally, to calculate the lithography mask we follow the steps presented in Sec 3.4.4.2. Figure 4.44 shows the calculated azimuthal variations of holes diameters required to achieve the perturbative azimuthal phase function $f(\theta)$. These curves are calculated by considering a $\lambda/8$ thick Si_3N_4

¹For example the absolute error when depositing a SiN layer on a 1/2-VCSE chip is of the order of $\sim 5 - 10 \text{ nm}$ which gives a relative error of $5 - 10\%$ for a layer thickness of 100 nm .

²For example, using an e-beam lithography with 4 nm resolution to achieve a phase function with a ff variation $\Delta \text{ff} = 0.05$ results in discretized phase function with 7 levels only, while using $\Delta \text{ff} = 0.3$ gives 42 phase levels.

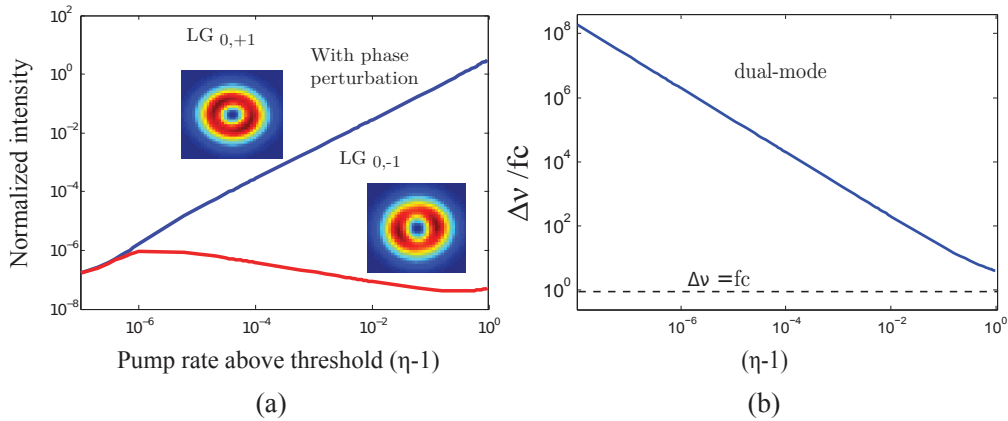


Figure 4.41: (a) Same simulation as in Fig 4.32, but between the modes of the perturbed cavity. Here the handedness is selected deterministically as the most homogeneous mode 'wins' the competition. (b) Phase difference between the two modes.

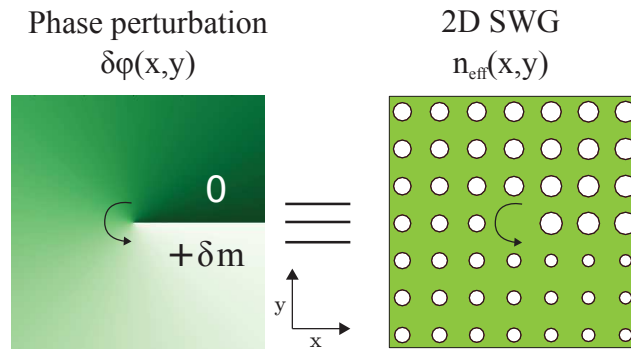


Figure 4.42: Schematic illustration of fill factor profile required to introduce azimuthal phase variation.

layer stacked on the top surface of an anti-resonant 1/2-VCSEL structure. The subwavelength grating lattice equal 280 nm, and the fill-factor $ff \in [0.3 \ 0.6]$.

In order to compensate the decrease of the electric field in the quantum wells due to the anti-resonant configuration, we designed a 1/2-VCSEL structure containing 12 QW distributed in a $13\lambda/2$ active zone, and a Bragg mirror of 27.5 pairs with a reflectivity $R > 99.5\%$

We designed and fabricated two masks-sets, the first one is an all-dielectric mask containing several FPEs consisting of the two parts described above (lossy disk and azimuthally varying artificial refractive index), with different diameters to address modes with different OAM charges. The FPEs dimensions are designed for fundamental mode waists $w_0 \in [20 \ 50 \mu\text{m}]$. Figure 4.45a shows a photograph of the all-dielectric masks-set obtained using an optical microscope. The second masks-set (Fig 4.45b) contains essentially the same items, but fabricated using two stacked layers: a dielectric one to achieve the FPEs, and a sub wavelength metallic

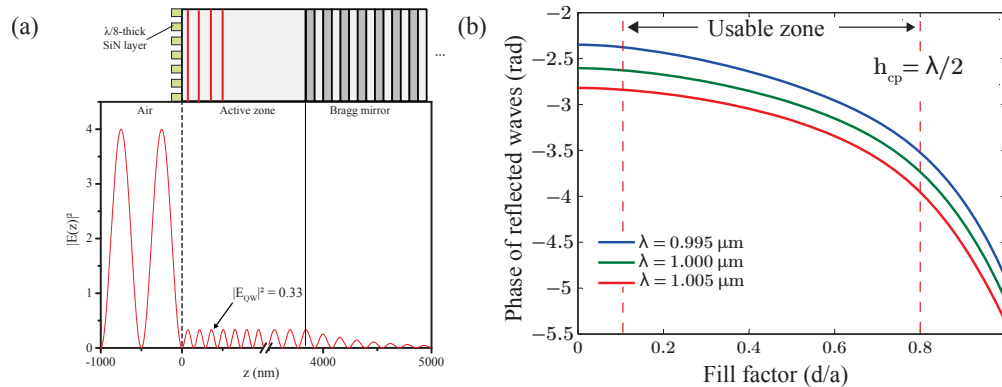


Figure 4.43: (a) Illustration of longitudinal distribution of electric field intensity in an anti-resonant 1/2-VCSEL (gain mirror) incorporating a phase mask. (b) RCWA simulation of the phase shift experienced by waves reflected by the gain mirror in (a).

one to achieve intensity filtering in the outer regions of the modes, (see Fig 4.46). Using this additional amplitude filter allows to release the constraints on the pump spot diameter and shape. Fig 4.47a shows a photograph of this masks-set obtained using a scanning electron microscope, and in Fig 4.47b we show an example of an FPE with a zoom in the center in Fig 4.47c, we can see in this figure the implemented azimuthal variation of the holes diameter.

The optical microscope photograph, was taken using a polarization filter that accentuates the index inhomogeneity, which can reveal surface roughness, presence of impurities ...etc. One can notice the very low density of surface defects. Both metallic and dielectric masks have a very low diffraction loss, and present good thickness uniformity. Furthermore the SEM photographs show the good fabrication quality: holes uniformity and absence of defects. These properties are of a key importance to us, because the low diffraction loss is essential to the spatial coherence of the modes. And low defect density reduces the undesired backscattering effect that tends to lock the modes.

4.7 The article:Vortex Laser with III-V flat photonics: coherent photon state carrying controlled orbital angular momentum

In the following article we present and characterize a VCSEL emitting beams carrying OAM with controlled charge and handedness using the method presented above. The article includes, in a more compact form, some parts that we have already detailed earlier, such as the introduction, the state of the art, and the principle of handedness selection method including vortex modes' dynamics. Thus the reader who has already read the mentioned parts can skip the first three sections and go directly to 'Vortex Laser and physical study' where we show the experimental

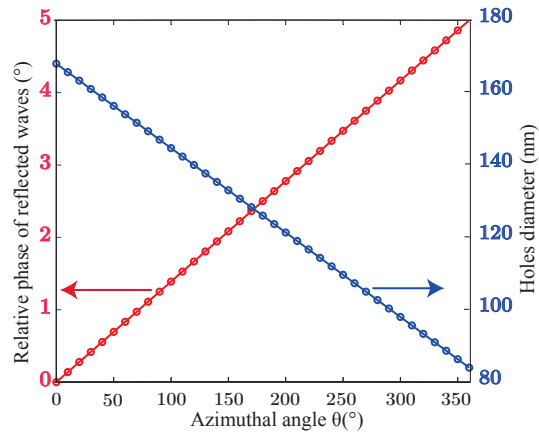


Figure 4.44: Left: wanted azimuthal phase variations. Right: corresponding azimuthal holes diameter. We considered an antiresonant structure and *SiN* layer thickness of 75 nm. The period of the subwavelength grating is $a = 280$ nm and $ff \in [0.3 \text{ } 0.6]$.

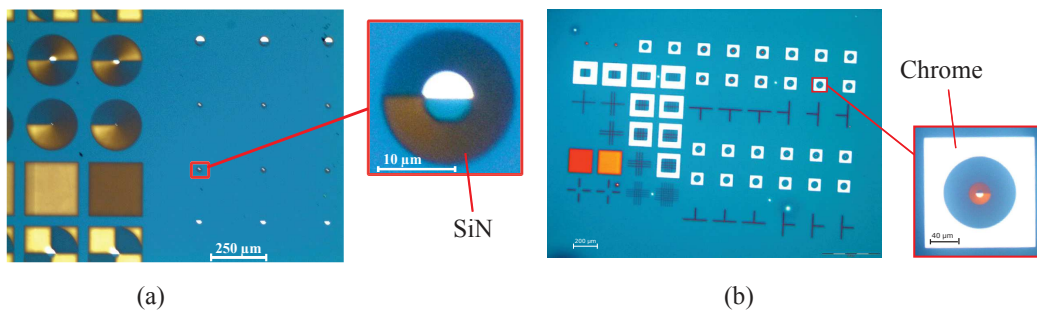


Figure 4.45: Optical microscope photograph of: (a) an all-dielectric set of masks, with a zoom in the handedness control element presented earlier (Fig 4.36). (b) A double layered (chromium +*SiN*) set of masks.

setup, and fully characterize the obtained vortex emission. We also measure the degeneracy lift using the beating between the selected and the residual suppressed mode in the noise spectrum. We compare these values with the ones predicted by our eigenmode calculations, and show that they are in good agreement. Then we conclude and present some prospects.

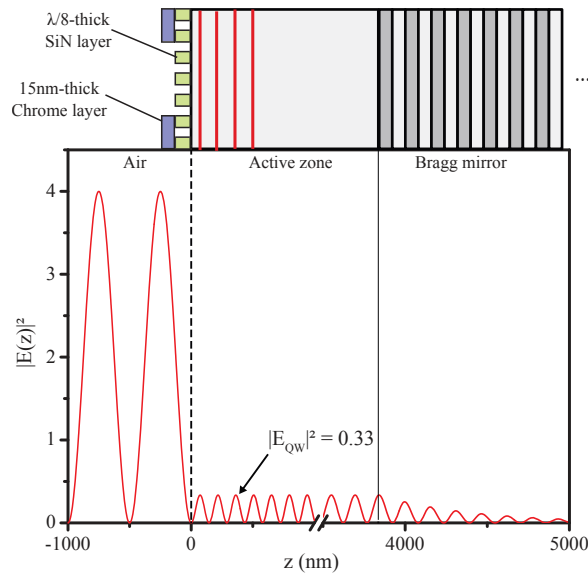


Figure 4.46: (a) Illustration of longitudinal distribution of electric field intensity in an anti-resonant 1/2-VCSEL (gain mirror) incorporating a double layered mask (chromium + SiN).

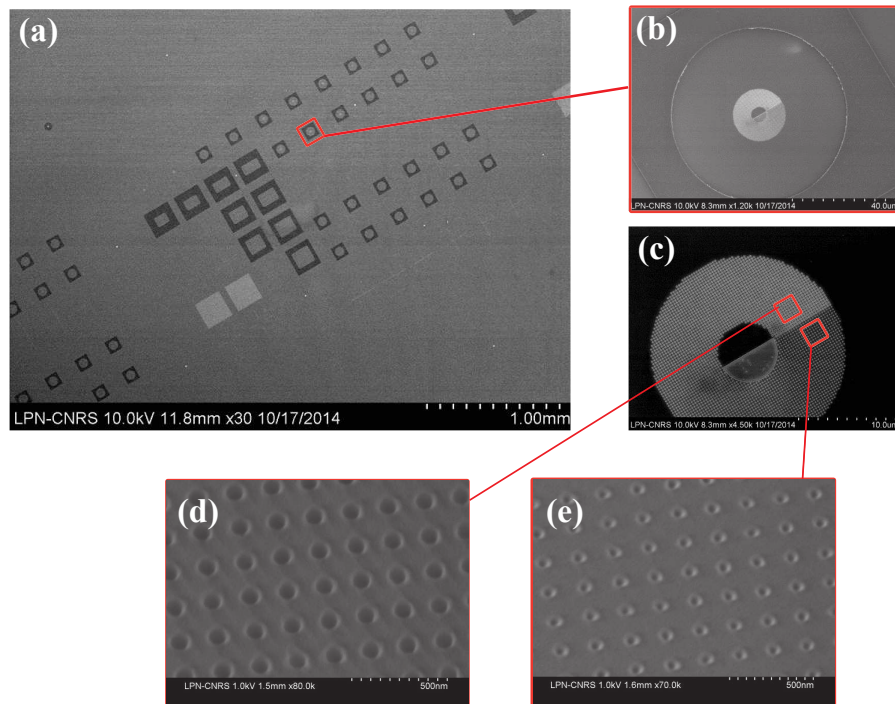


Figure 4.47: Scanning electron microscope photograph of the same masks set shown in Fig 4.45b. In (a) we show the whole set of masks, (b,c) zoom in the handedness control element, (d,e) zoom in two regions of the azimuthally varying refractive index gradient.

Vortex Laser with III-V flat photonics: coherent photon state carrying controlled orbital angular momentum

M.S. Seghilani¹, M. Sellahi¹, M. Myara¹, L. Legratiet², I. Sagnes², G. Beaudoin²,
P. Lalanne³, and A. Garnache¹

Abstract: Generating a large photon number coherent state, with controlled orbital angular momentum $L = \hbar l$ of charge l per photon, is still fundamentally and technologically a challenge: we demonstrate an integrated laser device generating vortex-like coherent light state in the Laguerre-Gauss basis, based on III-V semiconductor flat photonic technology. We use a first order phase perturbation to lift orbital degeneracy of wavefunctions with opposite quantum number $\pm l$, by introducing a weak 'orbital birefringence' based using a meta-material. The induced azimuthal symmetry breakdown allows to select vortex handedness by exploiting a non linear gain saturation dynamical effect called by H. Haken 'Darwin's survival of the fittest'. This photonic device was characterized and studied experimentally and theoretically. It exhibits a low divergence ($< 1^\circ$) diffraction limited circular beam with 49 mW output power, a charge $l = \pm 1, \dots, \pm 4$ with 40 dB opposite vortex intensity extinction, and single frequency operation. Such high performances laser opens the path to widespread new applications of great interest.

Introduction

Vortex optical beams have known a growing interest since the first realization that they carry an Orbital Angular Momentum (OAM) \vec{L} [1]. The study of beams carrying OAM has led to many advanced applications extending from

optical handling of microscopic particles [2–4], atoms manipulation [5, 6] and sub-diffraction limit microscopy [7], to quantum information processing and communication [8–12].

Together with photon energy $\hbar\omega$ and linear momentum $\hbar k$, the angular momentum (AM) $\vec{J} = \vec{L} + \vec{S}$ is one of the most important characteristics of light [1]. For paraxial fields in free space, the eigenmodes of \vec{J} operator are circularly-polarized helically phased beams, where polarization helicity $\sigma = \pm 1$ (or 0 for linear state in anisotropic media) specifies the value of spin AM per photon $S = \sigma\hbar$, whereas the vortex integer topological charge $l = 0, \pm 1, \pm 2, \dots$ yields the OAM per photon $L = \hbar l$. The sign of l gives the direction of rotation of the wave-front (Fig.1(a-d)). A striking difference between L and S momenta is the range of allowed values. Vortex helical wavefronts vary azimuthally with θ in a corkscrew-like manner along direction of propagation z , with a Poynting vector that follows a spiral trajectory around the axis. The wave-function reads as $\propto e^{i(\theta l - kz)}$, with a phase structure containing l intertwined helices. The common transverse field profile looks like a light ring with a dark core and a phase singularity at the center, known as doughnut-shaped modes (Fig.1(a,b)).

Until now, many works have been dedicated to electronic control of photon carrying S for spintronic applications [13,14]. However generating a large photon number N coherent state,

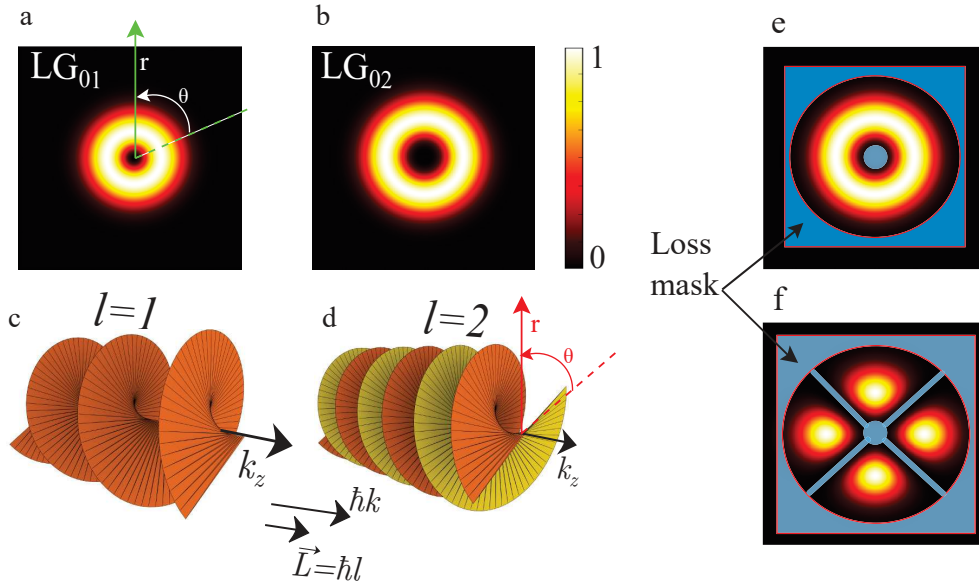


Figure 1: Transverse intensity profile of (a) LG_{01} and (b) LG_{02} modes and their respective helical phase structures (c), (d). Transverse intensity profiles of (e) LG_{02} and (f) degenerate LG_{02}^* along with intracavity loss masks needed for their selection.

of energy $N\hbar\omega$, exhibiting a large OAM NL , with controlled charge and handedness, is still fundamentally and technologically a challenge: in this work we demonstrate for the first time to our knowledge, an integrated laser device generating and controlling such structured coherent light state, based on III-V semiconductor flat photonic technology [15,16]. A fundamental limitation for vortex handedness control arises from the orbital degeneracy and symmetry of wave-functions with opposite orbital quantum number $\pm l$ as in the hydrogen atom: we use a first order phase perturbation to lift degeneracy, by introducing a weak 'orbital birefringence' using a subwavelength-thick meta-material layer. The induced azimuthal symmetry breakdown allows to select the vortex handedness by exploiting non-linear gain saturation dynamical effect, called 'Darwin's survival of the fittest' by H. Haken [17].

Motivated by the potential of emerging applications, several works have been dedicated

to the generation of optical vortices, for example using mode transforming optics in free space such as spiral phase plates [18] or Q-plates [19], spatial light modulators [20], astigmatic mode converter [21]. In these methods the generated beam quality and its power is strongly dependent on the alignment of the transforming optics and their properties such as non-linearities, pixilation, damage threshold and so on. To overcome these limitations, a more promising approach consists in direct laser generation of a coherent vortex beam, by forming the helical wavefront inside an optical cavity (Fig.2(a,c)). This approach has been investigated through numerous experimental works. Various techniques have been studied: locking two Hermite-Gauss modes in a gas laser [22], using ring shaped pump beams [23] and exploiting some spherical aberrations in solid state laser [24]. In most of the reported works the used set-ups are complex and need sophisticated alignment procedures, because of

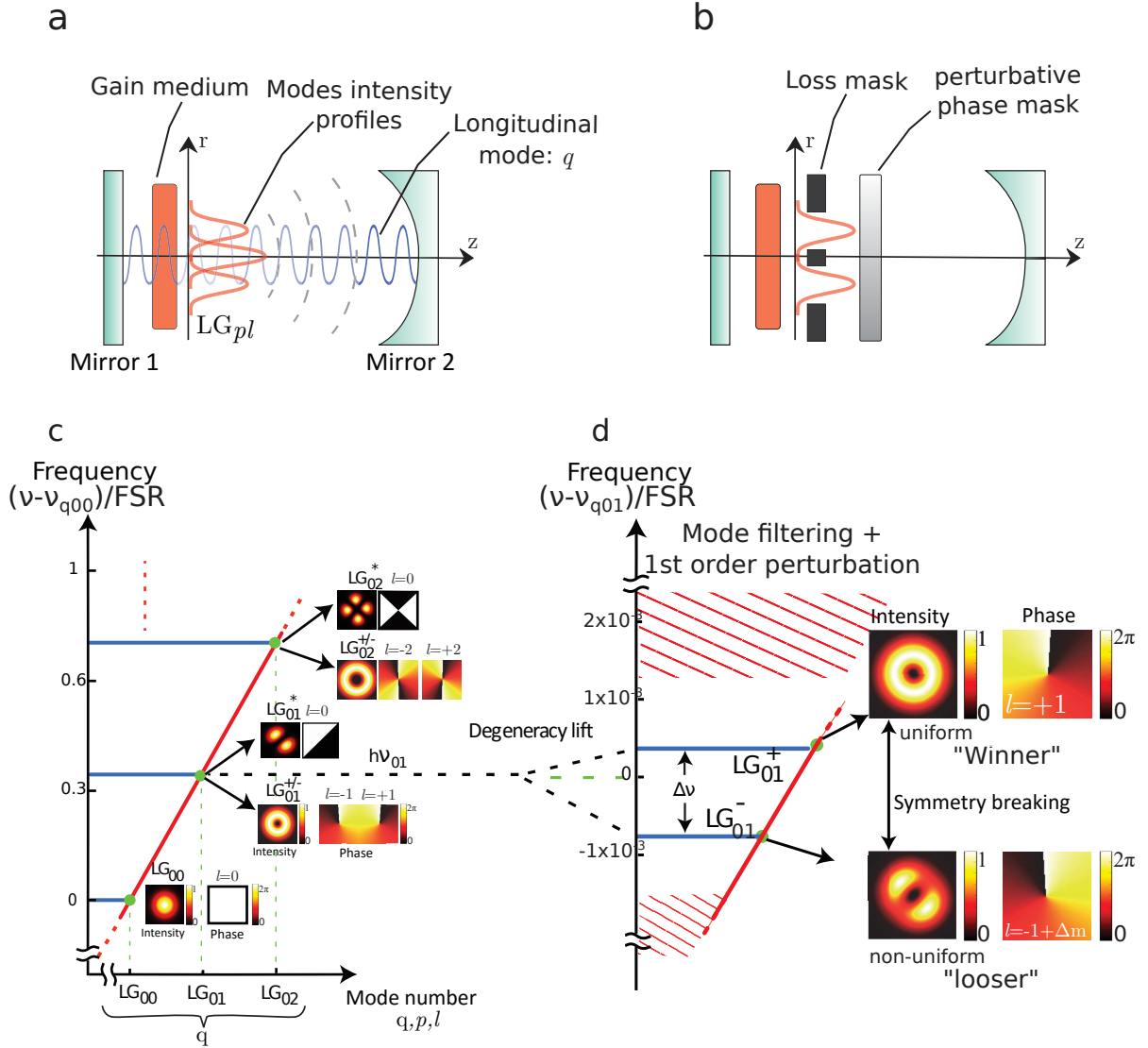


Figure 2: (a) Plano-concave type cavity supporting LG basis, and (b) same cavity perturbed with an azimuthal phase mask. (c) Photon energy (frequency ν) -momentum dispersion diagram for the first three non degenerate LG_{pl} and degenerate LG_{pl}^* transverse modes with longitudinal mode number q ; modes having same OAM charge but opposite handedness have degenerate frequencies and symmetric wave-functions; the momentum difference is normalized to $\hbar\Delta k\varphi$ (see Eq. 2). (d) Introduction of the flat-photonic element lifts orbital frequency degeneracy and breaks orbital wave-function symmetry for LG_{pl} modes with opposite number l .

the required intracavity elements. This leads to low efficiency operation, deteriorates beam coherence and makes the systems cumbersome and unsuitable for integration. More importantly, researchers are faced with the still unsolved important problem of OAM handedness control in a deterministic manner.

Vortices are most commonly assumed to belong to Laguerre-Gaussian LG_{pl} mode basis (or alternatively Bessel-Gaussian). The total intracavity field $\vec{\mathcal{E}}(\vec{r}, t)$ and the transverse LG spatial wave-functions $\Psi_{qpl}(r, \theta, z)$ for a stable plano-concave-type optical cavity (free space, length L_c , radius of curvature R_c), read as [25]:

$$\begin{aligned} \vec{\mathcal{E}}(\vec{r}, t) &= \sum_{qpl} E_{qpl}(t) \Psi_{qpl}(\vec{r}) \frac{\cos(k_q z)}{\sqrt{2L_c}} e^{i\omega_{qpl} t} \vec{x}; \\ \Psi_{qpl} &= \sqrt{\frac{2p!}{\pi w^2(p+|l|)!}} \left(\frac{\sqrt{2}r}{w}\right)^{|l|} L_p^{|l|} \left(\frac{2r^2}{w(z)^2}\right) \\ &\quad \times \exp\left(-\frac{r^2}{w(z)^2} - \frac{ik_q r^2}{2R(z)} + il\theta\right), \end{aligned} \quad (1)$$

where $E_{qpl}(t)$ are slowly varying envelopes and \vec{x} the polarization unit vector. r, θ, z are the radial, azimuthal and longitudinal coordinates. $L_p^{|l|}$ is the generalized Laguerre polynomial; p (q) is the radial (longitudinal) number ($\in \mathbb{N}$); $R(z)$ is the wavefront radius of curvature; $w(z) \gg \lambda$ is the Gaussian beam waist and $z_R = \pi w^2/\lambda$ is the Rayleigh length. λ is the wavelength. $\hbar\omega_{qpl}$ are eigen-energies for q, p, l quantum numbers (Fig. 2(c)), given by the photon energy-momentum dispersion relation, assuming a unique polarization state [25]:

$$\hbar\omega_{qpl} = c\hbar \Delta k \left[q + (1 + 2p + |l|) \frac{\varphi}{\pi} \right], \quad (2)$$

where $\varphi = \cos^{-1}(\sqrt{1 - L_c/R_c})$ is the resonator Gouy phase shift; $\Delta k = 2\pi FSR/c$ is the quantum of momentum; $FSR = c/2L_c$ the cavity free spectral range.

A fundamental advantage of using confined states (with $\varphi \neq 0$) compared to continuum states, is the energy degeneracy lift for different quantum numbers $q, p, |l|$: they are distinguishable spatially and spectrally. However, the orbital degeneracy and symmetry for vortices of opposite quantum number $\pm l$ is clear from Eqs. (1,2): they can not be selected using an intracavity transverse intensity filter, and their linear combination LG^* is still an eigenstate with $L = 0$ and $2l$ intensity lobes (called 'degenerate' modes). It is possible to select a given LG or LG^* mode of quantum number $p, |l|$, by distributing transverse optical losses (gain) in zero (maximum) intensity regions (see Fig. 1(e,f)). For this purpose, an intracavity metallic mask or patterned pump beam can be applied on the axis [22, 23, 26]. But introducing losses in the dark core and periphery region of a LG_{0l} mode results in 50% probability of creating either right-handed or left-handed stable vortex wave, each time the laser builds-up [22, 26]. Thus direct laser generation of vortex beam appears fundamentally challenging.

In this work, we 'break' this fundamental laser light symmetry problem in a deterministic way, thanks to a robust physical and technological concept of great interest for demanding applications. We demonstrate direct laser generation of LG beams thanks to a high finesse compact vertical-external-cavity-surface-emitting-laser (VECSEL) [15] based on III-V semiconductor technology emitting in the Near-IR at $1\mu\text{m}$. The stable laser cavity exhibits a low noise relaxation oscillation free (class-A) dynamics [15, 17, 27] for high coherence. We used a sub-wavelength thick flat photonic element (FPE) integrated onto a quantum-wells (QW)-based gain mirror structure [16] (called '1/2 VCSEL') (see Fig. 3).

This FPE allows to select the right quantum number p, l under non-linear laser phase transition thanks to transverse spatial-hole-burning

(SHB) in the gain medium [17,25]. This source generates a single - transverse (p, l) , longitudinal q , and polarization S - coherent light state at high power.

OAM's charge and sign control in laser cavity

Charge selection, degeneracy lift and symmetry breakdown of cavity eigenmodes

The purpose of this section is to build the cold cavity eigen-basis to create the only-desired LG non-degenerate modes. We used first order perturbation theory like in quantum mechanics as a tool. The FPE acts as a transverse loss filter and weak 'orbital birefringence'.

Figure 3(a1) shows a schematic representation of our two mirror standing wave laser cavity design with integrated FPE on the 1/2 VCSEL. Fig.3.(a1,a2) presents the three building blocks for intra-cavity OAM control. The first one is an axially symmetric free-space stable plano-concave cavity [25], of finesse $F \simeq 625$. It operates far from degeneracy at low Fresnel number, in order to be able to select a transverse mode number $(p, |l|)$ in a discrete LG basis of size $w \gg \lambda$ here (see methods). It consists of a first highly reflective gain mirror containing a distributed Bragg reflector on GaAs substrate, followed by a λ -thick multi-QW-based gain region ended by a window, a millimetre-long L_c air gap, and a dielectric concave mirror as output coupler. The non-degenerate eigen-frequencies $\nu_{qpl} = \omega_{qpl}/2\pi$ (Fig. 2(c)) are given by Eqs. 2. Only azimuthal degeneracy and symmetry for $l = \pm m$ ($m \in \mathbb{N}$) remains in this basis. It is important to note that the FPE being located close to a node of the E-field vertical standing wave and on cavity end mirror, its effect is weak and homogeneous over all q modes within mirror bandwidth.

The second building block is the OAM charge control, i.e. the selection of a 'doughnut' mode numbers $(0, |l| = m)$ thanks to a selective intensity filter. This is achieved by transversally distributing large optical losses in the dark regions of the desired mode, namely the dark core and the peripheral region. This 'kills' the finesse of undesired modes and prevents them from reaching lasing threshold. Here, this is ensured by the central phase step (diffraction losses) of the $\lambda/8$ thick dielectric FPE, processed on the 1/2 VCSEL top surface, and the outer peripheral region is filtered thanks to finite gain - pumping - region diameter. Alternatively, a similar filtering was fabricated using a few nanometres-thick metallic mask located close to field antinode, as shown in Fig.3.(b1,b2) [26], ensuring ultra-low diffraction losses for the vortex beam. This scheme allows to control the charge m , by changing either the cavity length - OAM jumps as the LG mode waist changes -, or the central and peripheral area diameter to fit another vortex charge.

The last function is the control of OAM sign $l = \pm m$. The idea is to weakly perturb the cavity LG eigenbasis by introducing 'orbital birefringence', acting as a first order asymmetric orbital perturbation. It is achieved thanks to the second zone of the FPE surrounding the central lossy region. It consists in a $\lambda/8$ thick dielectric layer, perforated by a 2D array of holes h placed on a square grid, of period a (Fig.3(a2)) [16]. This 2D grating acts as a metamaterial with a refractive index equal to the normalized propagation constant of fundamental Bloch mode, controlled control through the filling factor h/a . We used this feature to implement a weak azimuthal phase difference $\Delta\phi_{SPE} \simeq \pm 2\pi/100$ of amplitude $\ll 2\pi$ for a complete turn (Fig.3(a3)). It is located on dark core side, so radially non-uniform across the doughnut. To calculate the filling factor azimuthal profile we used rigorous coupled-wave

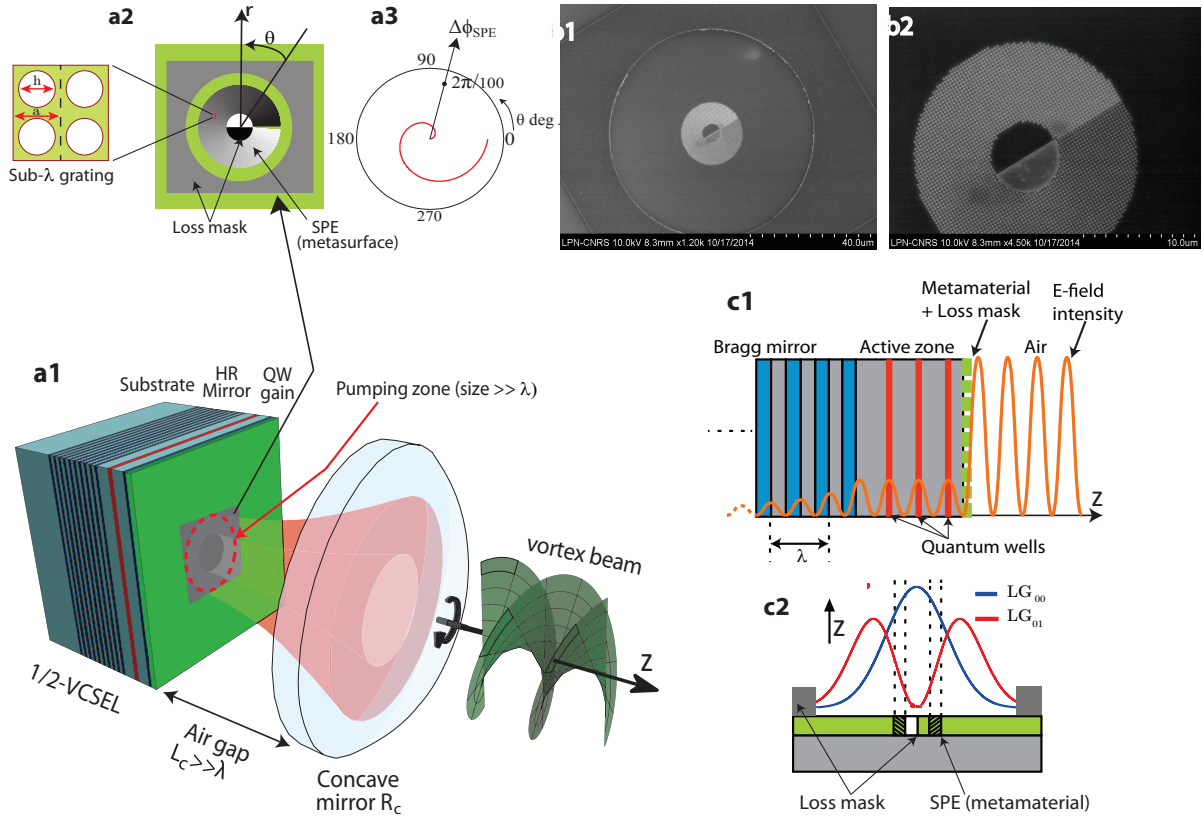


Figure 3: (a1) Schematic description of the vortex semiconductor-laser, based on III-V flat photonics. Stable cavity with a millimetre air gap L_c . Pump diameter $90 \mu\text{m}$. (a2) FPE with the two functions: dielectric spiral phase element SPE and loss mask based filtering. Elementary cell of 2D subwavelength grating. (a3) Perturbative azimuthal phase distribution $\Delta\phi_{SPE}$ induced by FPE. (b1) Scanning electron microscope image of fabricated right-handed FPE surrounded by a Cr metallic mask. (b2) Zoom on SPE ($20 \mu\text{m}$ external diameter). (c1) Longitudinal E-field distribution in the 1/2 VCSEL structure and SPE position. (c2) Cross section of the FPE together with the LG mode distribution.

analysis method [16, 28].

As a result, this spiral phase element (SPE) will lift degeneracy and break orbital symmetry of contra-rotating eigenmodes: they thus become distinguishable. To do this its operation relies on a unique property of vortex : a helical beam of charge $l = -m$ sent through a SPE having a modal phase function $e^{i\Delta m 2\pi}$ with $\Delta m = +m$, will be transformed to a bright central lobe with $l = 0$, whereas a beam having $l = +m$ will diverge further away from centre with $l = 2m$ [1]. This property still work for non-integer values of Δm but with beam distortions. Thus in our cavity a vortex rotating in opposite direction to that of SPE (> 0 for example), experiences slight OAM reduction $l = -m + \Delta m$ every round-trip, which in turns increases overlap and Δm : azimuthal symmetry is broken. This reduction is proportional to round trip modal phase shift $\Delta\phi_{modal}$ brought by perturbation:

$$|\Delta\phi_{modal} = \Gamma\Delta\phi_{SPE}| \ll 2\pi, \quad (3)$$

where Γ is the transverse overlap factor between the beam and the SPE, given by:

$$\Gamma = \iint_{\infty} |\Psi_{0l}(r, \theta)|^2 U_{SPE}(r, \theta) ds, \quad (4)$$

where U_{SPE} is the SPE surface distribution function on the 1/2-VCSEL. This way we end up with two new non-degenerate asymmetric wave-functions given by a linear combination of *LG* eigenmodes: the less perturbed one of charge $l \simeq +m$ (> 0 for example) conserves almost a homogeneous doughnut-like intensity distribution, while the opposite one of non-integer charge $l \simeq -m + \Delta m$ shows significant azimuthal intensity modulation (with $\Delta m/m \simeq 0.1 \ll 1$ in case of Fig. 4.b). As a result the phase of each contra-rotating mode will experience different intracavity Gouy-shift (Eq. 1) [25]. One should then expect a slight

optical frequency degeneracy lift (positive for $\Delta m > 0$) of amplitude $2\pi\Delta\nu = |\omega_{q,0,m} - \omega_{q,0,-m}|$:

$$\Delta\nu \ll FSR. \quad (5)$$

To ensure efficient laser dynamics unlocking of the two contra-rotating waves - even in the presence azimuthal back scattering like in gyro-laser [17, 25] -, one should choose a modal phase perturbation strong enough,

$$2\pi/F < |\Delta\phi_{modal}|, \quad (6)$$

so that $\Delta\nu$ is greater than the cold cavity frequency cutoff f_{cc} ,

$$f_{cc} = FSR/F < \Delta\nu. \quad (7)$$

Thus a high F releases the strain on $\Delta\nu$ value to be in perturbative regime. It is worth noting that the degeneracy lift may result in several sub-states. The frequency splitting is predicted by our numerical calculations of the perturbed eigen-basis (see methods) [31–33]. It is also noteworthy that, under such weak spatial perturbation, the two contra-rotating waves still have negligible diffraction losses. In Fig.3(b2) we show a scanning electron microscope photograph of the fabricated FPE with right-handed SPE, and in Fig.3(b1) we show the complete element surrounded by a metallic mask, as peripheral loss filter. The beam diameter is $\gg \lambda$, typically $100 \mu m$ here for low divergence and high power operation.

To end we want to point out that spin AM is $S = 0$ here, because a III-V 1/2 VCSEL gain mirror exhibits weak linear birefringence, therefore the two non-degenerate polarization eigenstates are linear ones, and oriented along [110] and [1-10] crystal axis [15, 27].

Light-matter interaction in the gain medium and mode competition dynamics

Now comes the role of weak light-matter interaction in the gain medium and semi-classical

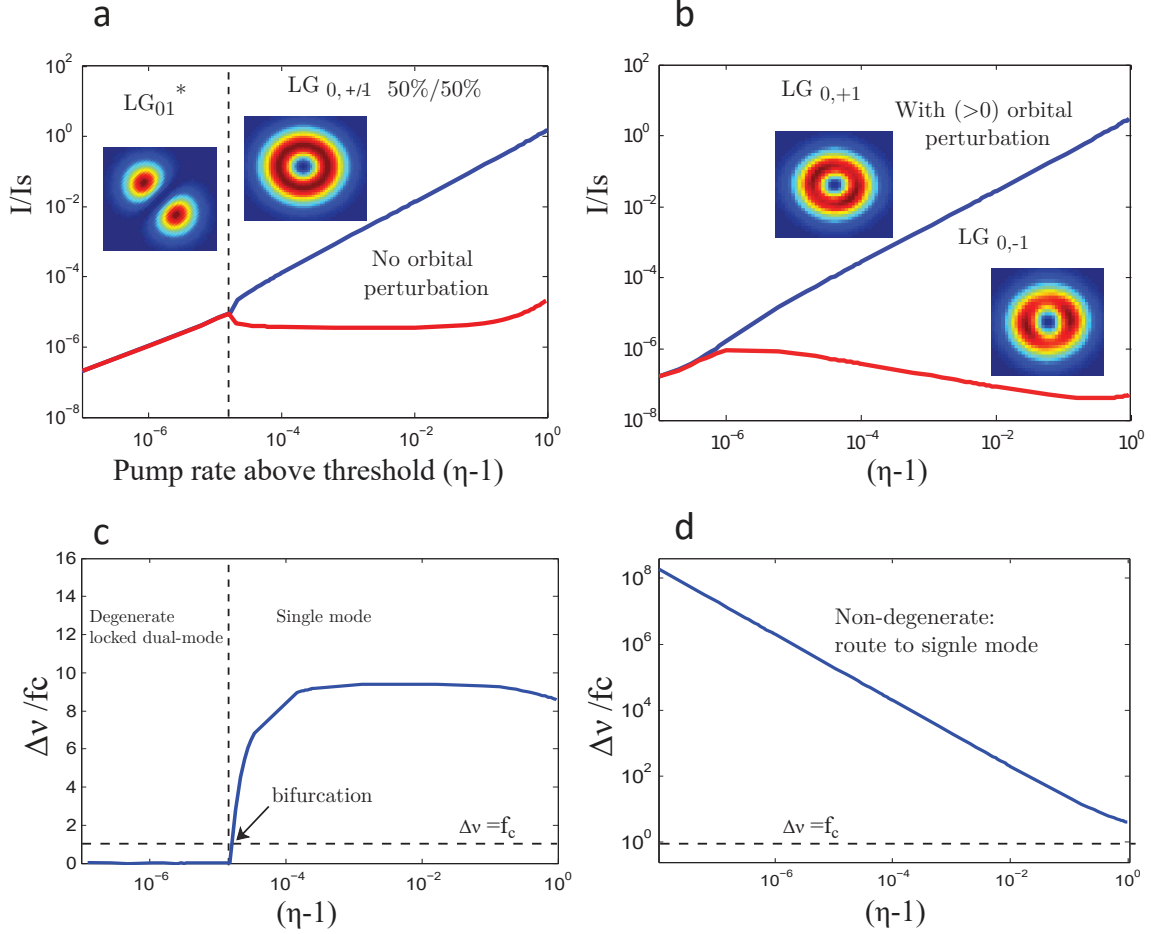


Figure 4: Steady state diagram of the dual-transverse mode laser intensities (normalized to saturation intensity I_s) as a function of pumping rate η of two contra-rotating vortex modes, including spontaneous emission noise and weak linear mode coupling due to back scattering : (a) cavity without phase perturbation, here both handednesses have 50% probability to be generated. (b) With phase perturbation (FPE): the handedness here is deterministically controlled and only the wanted handedness is generated thanks to asymmetric mode competition. In (b) transverse profiles were obtained using an in-house 2D eigenmode solver. (c) and (d) show the laser frequency degeneracy lift for case (a) and (b) respectively, normalized to the laser cavity frequency cut-off $f_c(\eta)$.

laser dynamics to generate a single coherent light state LG_{q0l} at large photon number under phase transition. The intracavity FPE design allows only two non-degenerate transverse modes to oscillate: $LG_{0,+m}$ and $LG_{0,-m}$.

First, thanks to homogeneous and (r, θ) quasi-isotropic QW gain mirror properties, emitting vertically along the quantization axis [001] under interband transition, the energy $\hbar\omega$, the linear momentum $\hbar k$ and also the AM J can be transferred from a 'macroscopic' electronic wave-function to a single photon state wave-function (of volume $\gg \lambda^3$) through stimulated emission. This point has been recently theoretically demonstrated in [29]. Here $S = 0$ and linear gain dichroism will strongly select a single linear polarization state along [110] crystal axis [15, 27]. Moreover, thanks to sub-wavelength thick QW gain localized on longitudinal standing-wave antinode of all q modes (within the gain bandwidth), together with QW homogeneous broadening, a single mode q will be selected [27].

Secondly, one of the two OAM signs will be selected, thanks to non-linear dynamics during laser build-up and the well known transverse SHB effect of the electronic population [25]. This non-linear mode competition, called by H.Haken 'Darwin's survival of the fittest' [17] always favour a laser state with an homogeneous intensity profile, for efficient use of the gain. As shown in figure 4.(a,c), this explains why when one tries to select a vortex laser state without lifting the degeneracy of contra-rotating eigenmodes, at pumping rate far enough above threshold (to prevent mode-locking due back scattering like in gyro-laser [17, 25]), one obtains 50% probability of having either right-handed or left-handed stable vortex mode each time the laser is switched on, due to purely random nature of spontaneous emission assisted seeding [22, 26].

Indeed the superposition of two oppositely rotating degenerate vortex modes will produce

azimuthal standing wave with $L = 0$, leading to significant azimuthal SHB and unstable operation of two locked vortex modes. In the case of asymmetrical degeneracy lift, the unwanted mode exhibits its own azimuthal standing wave pattern, leading to a larger and asymmetric self saturation. The semi-classical non-linear dynamics between these two - degenerate or not - modes are modelled by a bi-mode spatio-temporal Maxwell-Bloch equation set [17, 25], for a class-A laser, by taking into account SPE effect, self-saturation and cross saturation coefficients due to SHB, as well as spontaneous emission noise (Langevin forces) and back scattering (see methods).

Now we move to the laser phase diagram for both intensity and frequency of the E-field. Numerical simulation results of cavity eigenstates and vortex laser states competition are summarized in figure 4. The mode steady state intensities are plotted as a function of the normalized pumping rate above threshold η , for a dual-transverse mode laser ($LG_{0,+1}$ and $LG_{0,-1}$). The laser frequency degeneracy lift $\Delta\nu$ is also plotted, normalized to the laser cavity cut-off $f_c(\eta) = f_{cc}(\eta - 1)/\eta$. Two cases are simulated : a cavity without SPE phase perturbation (Fig.4(a,c)) and a cavity with SPE phase perturbation $\Delta\phi_{modal}$ (Fig.4(b,d)). In the first case the two modes are degenerate and locked up to a certain pumping rate, after which a bifurcation occurs and only one mode can survive. The choice here is purely random and set by quantum noise assisted seeding. In the second case thanks to degeneracy lift the locking is no more possible. The dual mode to single mode second threshold is defined by spontaneous emission, and is very low. More importantly handedness selection is deterministic. These results agree with the experiment addressed in the next section.

Vortex Laser and physical study

Figure 5(a) shows the far field intensity profiles obtained with lasers operating in continuous-wave on vortex modes of different orders LG01 (a1), LG02 (a2), LG03 (a3), LG04 (a4). In the experiment, the charge $|l| = 1, 2, 3\dots$ is changed using a single semiconductor chip by varying L_c . In Fig.5(b) we show corresponding spiral interference patterns of LG01 having right (b1) / left (b2) handedness and LG02 with having (b3) / left (b4) handedness. These patterns were obtained using interference with a reference beam having spherical wavefront in Mach-Zehnder interferometer [30]. It shows a spiral fringe with well-determined integer charge and handedness l .

The generated vortex beams exhibit high spatial coherence, with pure LG_{0l} modes (see Fig 6) close to diffraction limit. We measured a beam propagation parameter M^2 of $(1 + |l|) \times 1.2 (\pm 0.2)$. The theoretical value is $M^2 = (1 + 2p + |l|)$. The highly coherent polarization state is linear here ($S = 0$), along [110] crystal axis [27], with an orthogonal polarization extinction ratio $> 60\text{ dB}$, evaluated by measuring the cross-polarization optical beating on the intensity RF spectrum. Single frequency - longitudinal mode - operation with a side mode suppression ratio of 27 dB was obtained, showing a coherent vortex state. Along with low threshold pump density (0.8 kW/cm^2), differential efficiency of 27% and maximum output power of 49 mW , limited by pump power, were measured.

Spiral fringes show that generated beams possess a well defined single OAM and usually used in the literature as an indicator of its purity. However, this cannot be used to measure quantitatively the purity of the generated OAM. To quantify the optical intensity suppression ratio I_-/I_+ of counter-rotating OAM,

we measured the beating power P_e between the two vortex modes at $\Delta\nu$ in the laser RF power spectral density [25] (see methods).

Figure 6(a) plots the measured Relative-Intensity-Noise (RIN) of the vortex laser. It shows a low noise class-A laser dynamics - free of relaxation oscillations - with a cut-off frequency at $f_c \approx 12\text{ MHz}$, and the expected beat note at $\Delta\nu \simeq 20\text{ MHz}$ for LG_{02} . The measured opposite OAM suppression ratio is thus $I_+/I_- \simeq 40\text{ dB}$ here. Then the RIN stays at the shot noise level until the next longitudinal mode of the cavity at $FSR = 15.8\text{ GHz}$, where we can see the same beat note again. Dashed vertical line in figure 6 corresponds to first other order LG transverse mode beat frequencies. However, in our case we have unique transverse mode with a good suppression ratio ($> 50\text{ dB}$) as the RIN stays at shot noise level.

This degeneracy lift effect is even stronger when the overlap between the SPE and the mode Γ is greater, and comes with a larger degeneracy lift $\Delta\nu$. We calculated $\Delta\nu$ for different overlap values and compared it with measured ones for LG_{01} and LG_{02} modes. Both values are in good agreement with the experiment, as shown in Fig.6.

Discussion

Breaking the bottleneck of OAM's charge and sign selection and control in laser cavities is of crucial importance for many applications: particle manipulation down to nm scale, sensitive long distance rotational speed sensor... The optical method demonstrated here show an effective way to select a pure coherent LG_{0l} vortex mode exhibiting an integer charge value $l = \pm 1, \pm 2, \pm 3\dots$ For this purpose, a new low noise class-A high finesse laser cavity integrating a meta-material based on III-V semiconductor flat-photonics technology has been developed. We use a first order orbital perturbation to

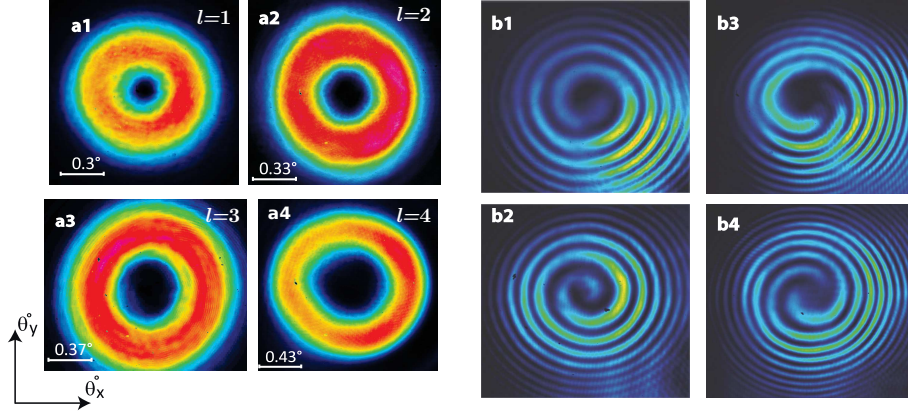


Figure 5: Intensity profiles of obtained LG modes having helical wavefront: (a1) LG_{01} , (a2) LG_{02} , (a3) LG_{03} and (a4) LG_{04} . (b1 (b2)) one-start spiral fringes corresponding to right (left) handed LG_{01} with OAM charge $l = 1$. (b3 (b4)) two-starts spiral fringes corresponding to right handed (left) LG_{02} with OAM charge $l = 2$.

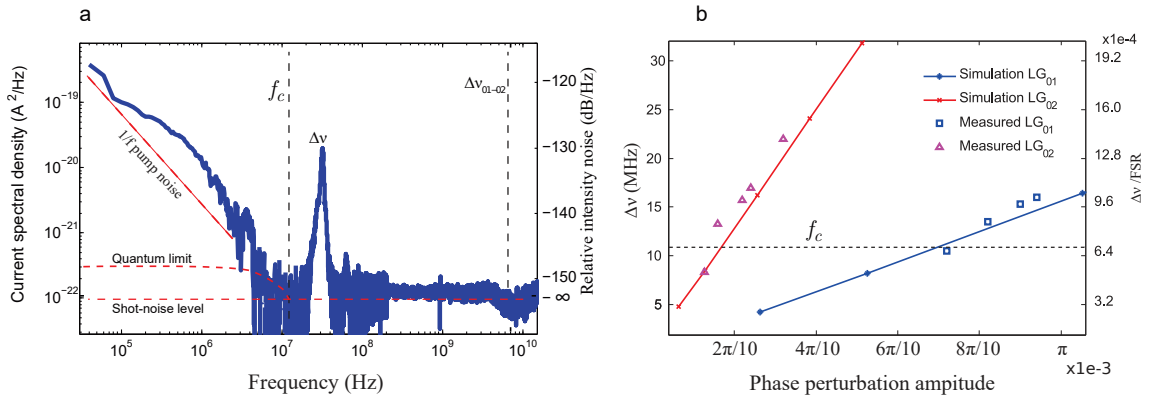


Figure 6: (a) Relative-Intensity-Noise RF spectrum of the vortex laser measured by integrating a fraction of the beam surface, for $\Gamma = 0.024$ (LG_{02}) and $f_c = 12MHz$ (b) Measured and simulated beat frequencies between selected LG_{01} and LG_{02} vortex modes and residual contra-rotating modes, as a function of the overlap factor Γ with SPE. The cavity frequency cut-off $f_c = 12MHz$ ($F = 625$, $\eta \simeq 2$) is represented by dashed horizontal line splitting the figure into two parts: upper and lower with strong and weak control of the OAM sign respectively.

lift azimuthal degeneracy and break spatial symmetry: as a result the non-linear laser phase transition selects the vortex charge and handedness. This generates a single frequency (unique quantum number q, p, l and polarization state, with suppression ratio $> 27\text{ dB}$), highly coherent and high power (49 mW) *LG* vortex beam, exhibiting a diffraction limited low divergence ($\simeq 1^\circ$) circular beam. These performances are of great interest for demanding applications.

This solution overcomes physical and technological limitations of conventional schemes in terms of vortex control, coherence and power. The big advantage of the approach presented here lies in: its physical and technological robustness; cavity design simplicity and symmetry (weak thermal lens, aberrations and astigmatism); no need for extra-intracavity optical elements; the sub-wavelength grating is fabricated using III-V nanotechnology exhibiting ultra low optical roughness and defect density, with a clear interest for the integration (industry-ready)

The purity and coherence of the vortex laser were quantified by measuring the RF spectrum of optical beat note with other cavity eigenstates, close to shot noise above MHz (class-A dynamics); this gives also an upper value of the fundamental Schawlow-Townes laser linewidth (limited by quantum noise in the weak mode here) below 200 kHz . Assuming a fundamental white noise, it gives an estimated fundamental vortex linewidth of about 200 Hz here, leading to a coherence time of about 1 ms . To explain the behaviour of our laser cavity, we used the matrix method and the Fox-Li iterative technique to calculate the transverse eigenmodes, as well as semi-classical Maxwell-Bloch dynamics equations for light-matter interaction to study the laser stability diagram. The vortex laser principle demonstrated here can be extended to high power, to any wavelengths and laser technology, as well to any temporal state,

like ultra short pulse operation. In addition, a spin AM $S = \pm\hbar$ control could be added to the beam OAM, for spintronic applications.

The method demonstrated here is a static one, i.e. one chip can select one OAM sign only: it can not be reversed dynamically; only the OAM charge $|l|$ can be varied. However in the case of the III-V VCSEL technology, this inversion functionality can be fully integrated with a laser matrix for example. Future work would be dedicated to dynamical control of the OAM sign (and charge) in a single device. To replace the static dielectric metamaterial layer used for the SPE here, one could for example integrate μm size liquid crystal pixels on the $100\text{ }\mu\text{m}$ size gain mirror for electro-optic control, a mature VCSEL technology. This would allow to modulate the OAM at very high frequencies in next generation modulators for quantum telecommunications.

Methods and supplementary materials

Design and fabrication of the vortex laser

The 1/2-VCSEL structure was grown by MOCVD. It is composed of an epitaxial high-reflectivity (99.9%) bottom AlAs/GaAs Bragg mirror (27.5 pairs), and a GaAs active layer of $13\lambda/2$ thick containing 12 strain-balanced InGaAs/GaAsP QWs emitting at $\lambda \simeq 1\text{ }\mu\text{m}$. Each group of two QWs is placed at an antinode of the optical standing-wave, following a non-uniform 222020200200 longitudinal distribution (from air to Bragg) ensuring uniform QWs carrier excitation. This ensures a low threshold carrier density and homogeneous gain broadening (with modal gain $\simeq 1\%$ and bandwidth $\sim 10 - 20\text{ nm}$) as needed for single longitudinal mode operation [15, 27]. We optically pumped the gain structure in the QW

barriers close to Brewster incidence angle, allowing compact short millimetre-long cavity. We use 300 mW a low noise single mode 800 nm commercial diode, focused with a pair of aspheric lenses on a $w_p = 45 \mu\text{m}$ spot radius.

Next to fabricate the 2D sub-wavelength grating a $\lambda/8$ thick Si_3N_4 layer was deposited on the gain mirror by ion-beam-assisted electron-beam vacuum evaporation. Then a polymethyl methacrylate (PMMA) resist was spin-coated on the wafer and patterned by electron beam lithography (Vistec EBPG 5000 at 100kV) with 1.25 nm of resolution. After PMMA development in methylisobutylketone (MIBK) solution, the 2D grating holes are transferred to the SiN layer by Reactive Ion Etching (RIE), and at the end the PMMA is removed. Alternatively, a 10 nm thick chromium layer was deposited on the SiN layer to act as a loss mask. The same technological process was used to obtain the desired pattern. Fig 3.(b1,b2) show optical microscope images of the integrated sub-wavelength grating, we can clearly see the realized two phase functions even in the visible spectral range.

We realized various spiral phase elements with internal diameter ranging from 6 microns to 10 microns and external radius of 20 microns for the two handedness. These values are chosen according to intensity profile of targeted LG_{0m} modes into the cavity, this is fully governed by Gaussian beam optics [25].

The passive optical cavity is a high finesse stable plano-concave resonator of $L_c \simeq 9.5 \text{ mm}$. The 1/2 VCSEL integrates a flat HR mirror, and a concave output coupler ($T = 1\%$) of radius of curvature $R_c = 10 \text{ mm}$ is used to close the cavity. The minimum waist for the Gaussian component of the beam occurs at the plan gain mirror and can be determined from the complex beam parameter $\tilde{q} = -iz_R$. In order to lift the degeneracy of modes with different quantum number $q, p, |l|$ the cavity length is chosen to be inside the stability region

$0 < L_c < R_c$, far from stability edge. Once the beam parameter \tilde{q} is calculated, one can write the field distribution of the complete set of LG modes basis using Eq.(1), and choose the suitable mask size to select the wanted mode as in the example shown in Fig.3(c2). The typical fundamental beam waist is $w_0 \sim 25 \mu\text{m}$ here.

Simulation of the cavity eigenstates and mode competition dynamics

To validate the method developed in this work, we used numerical simulation of the perturbed cavity eigenstates, using an approach similar to the first order perturbation theory in quantum mechanics, i.e: first we calculated eigenvalues and the corresponding eigenmodes of the cold cavity, incorporating the loss mask element centred on its axis to select the LG_{0l} doughnut mode. For this we used an in-house 2D cavity eigenmode solver based on matrix method [31, 32]. Then, once the modes calculated, we re-inject the degenerate left-handed and the right-handed helically-phased beams into the same cavity but this time containing the helical SPE and using the Fresnel diffraction based Fox-Li [33] iterative method to study the evolution of each one to the steady-state. one can easily notice the azimuthal symmetry breakdown and degeneracy lift: indeed we see that when the helical wavefront and SPE have the same handedness, the mode conserves its homogeneous intensity distribution with an integer charge l (see $LG_{0,+1}$ in Fig.4(b) inset), whereas when the helical wavefront and the SPE have opposite handedness the mode is perturbed and shows significant azimuthal modulation of the intensity distribution with slightly non-integer OAM charge (see $LG_{0,-1}$ in Fig.4(b) inset).

In a second step, the non-linear laser dynamics of these two - degenerate or not - modes are modelled using the spatio-temporal semi-classical Maxwell-Bloch equations [25], in

the rotating wave approximation, for a class-A laser dynamics free of relaxation oscillations (electron lifetime $A^{-1} \ll \gamma^{-1}$ photon lifetime). Population inversion is at the steady state and can be eliminated adiabatically. The QW gain, of thickness is $L_g \ll \lambda$, is located on one end mirror. We take into account of the SPE effect, self- and cross-saturation due to azimuthal SHB in QWs, as well as spontaneous emission noise (Langevin forces F_E) and weak back scattering $\tilde{\gamma}_b = \gamma_b e^{i\mu}$ ($\gamma_b \ll \gamma \in \mathbb{R}_+$; μ the backscattering phase). The set of dynamical equations for the slowly varying envelopes $E_{1,2}(t)$ of the E-field read:

$$\begin{aligned} \frac{dE_{1,2}}{dt} = & \frac{E_{1,2}}{2} \left(-\gamma + B^* \iint_{S_g} \frac{\frac{\rho}{A} |\Psi_{1,2}|^2 L_g ds}{1 + I_t/I_s} \right) \\ & + \frac{E_{2,1}}{2} e^{\pm i\omega_{21} t} \left(\tilde{\gamma}_b + B^* \iint_{S_g} \frac{\frac{\rho}{A} \Psi_{2,1} \Psi_{1,2}^* L_g ds}{1 + I_t/I_s} \right) \\ & + F_{E_{1,2}} \end{aligned} \quad (8)$$

where $B^* = B(1+i\alpha)$, B is the Einstein coefficient for stimulated emission, α is the phase-amplitude coupling factor in QW (Henri factor), $\rho(r, \theta)$ is the pump distribution in QWs, ω_{21} is the mode angular frequency difference, $I_t(r, \theta, t) = |E_1(t)\Psi_1(\vec{r}) + E_2(t)\Psi_2(\vec{r})e^{i\omega_{21}t}|^2 \times \pi w_0^2/2$ is the total photon number distribution in the QW plane, and $I_s = A/B$ is the saturation photon number for LG_{00} mode. We simulated the laser build up seeded by spontaneous emission noise up to the steady state, after a characteristic time of $\simeq 1 \mu\text{s}$ at twice threshold. The mean values of laser mode intensities and frequencies were extracted. The table 1 below gives the laser parameters.

Table 1: Physical laser parameters for simulation of the vortex VECSEL w/o SPE. η_0 is the normalized pump rate. ξ is the spontaneous emission factor.

Parameters	Value	Units
γ	$2 \cdot 10^8$	s^{-1}
B	0.5	s^{-1}
A	$5 \cdot 10^8$	s^{-1}
α	3	
ω_{21}	0 or $1.25 \cdot 10^8$	s^{-1}
L_g	12×8	nm
γ_b	$5 \cdot 10^{-6} \gamma$	s^{-1}
μ	π	rad
$\rho(r, \theta)$	$\frac{\eta_0 2\gamma A}{B\pi w_p^2 L_g} e^{-2(\frac{r}{w_p})^2}$	$s^{-1} m^{-3}$
$\langle F_{E_i} \rangle$	0	s^{-1}
$\langle F_{E_i} F_{E_j}^* \rangle$	$\xi \gamma \delta(t - t') \delta_{ij}$	s^{-2}
ξ	1.2	

Physical study of the eigenstate purity: optical beating in the RF intensity spectrum

To quantify the optical intensity suppression ratio I_-/I_+ of counter-rotating OAM, we measured the beating power P_e between the two vortex modes at $\Delta\nu$ in the laser RF power spectral density [25]. For this purpose we mixed the modes on a photo-detector and integrate spatially over a fraction $S/3$ of the mode surface (to break orthogonality). The suppression ratio I_-/I_+ reads (I_+ for the strong mode):

$$\left(\frac{I_-}{I_+} \right)^{-1} \simeq \frac{72 \left| \iint_{S/3} \Psi_{0,m} \Psi_{0,-m}^* ds \right|^2}{P_e}, \quad (9)$$

with the assumption $I_+ \gg I_-$. This high resolution and sensitivity RF method is a very sensitive tool to analyse all the spectrum of ex-

isting cavity eigenstates above shot noise (polarization, transverse and longitudinal) [25].

Acknowledgements

This work was supported by the French RENATECH Network, ANR MICPHIR and Labex NUMEV (ANR-10-LABX-20 contract).

References

- [1] Allen, L., Beijersbergen, M. ., Spreeuw, R. J. C. and Woerdman, J. "Orbital angular momentum of light and the transformation of Laguerre-Gaussian laser modes", *Phys. Rev. A* 45, 81858189 (1992).
- [2] Paterson, L., MacDonald, M. P., Arlt, J., Sibbett, W., Bryant, P. E., and Dholakia, K. . "Controlled rotation of optically trapped microscopic particles", *Science*, 292(5518), 912-914 (2001).
- [3] Grier, D. G. "A revolution in optical manipulation", *Nature* 424, 8106 (2003).
- [4] Dholakia, K. and Reece, P. "Optical micromanipulation takes hold", *nanotoday* 1, 1827 (2006).
- [5] J.W.R. Tabosa, and D.V. Petrov, "Optical pumping of orbital angular momentum of light in cold cesium atoms", *Phys.Rev.Lett.*83 (1999) 4967
- [6] K. T. Kapale and J. P. Dowling, Vortex Phase Qubit: Generating arbitrary, counterrotating, coherent superpositions in Bose-Einstein condensates via optical angular momentum beams, *Phys. Rev. Lett.* 95, 173601 (2005)
- [7] Gu, M., Kang, H. and Li, X. "Breaking the diffraction-limited resolution barrier in fiber-optical two-photon fluorescence endoscopy by an azimuthally-polarized beam", *Sci. Rep.* 4, 3627 (2014).
- [8] A. Mair, A. Vaziri, G. Weihs, and A. Zeilinger, Entanglement of the orbital angular momentum states of photons, *Nature* 412, 313 (2001)
- [9] A. Vaziri, G. Weihs, and A. Zeilinger, Experimental two-photon, three-dimensional entanglement for quantum communication, *Phys. Rev. Lett.* 89, 24041 (2002).
- [10] S. Franke-Arnold, S.M. Barnett, M.J. Padgett, L. Allen, "Two-photon entanglement of orbital angular momentum states", *Phys.Rev.A* 65 (2002) 033823.
- [11] G. Gibson, J. Courtial, M.J. Padgett, M. Vasnetsov, S.M. Pasko, V. Barnett, S. Franke-Arnold, "Free-space information transfer using light beams carrying orbital angular momentum," *Opt. Express* 12 (2004) 54485456
- [12] Wang, J. et al. "Terabit free-space data transmission employing orbital angular momentum multiplexing," *Nat. Photonics* 6, 488496 (2012).
- [13] M. Holub and P. Bhattacharya, "Spin-polarized light-emitting diodes and lasers", *J. Phys. D: Appl. Phys.* 40 (2007), pp. 179
- [14] J. Frougier, G. Baili, M. Alouini, I. Sagnes, H. Jaffres, A. Garnache, C. Deranlot, D. Dolfi, and J-M.George , "Control of light polarization using optially spin-injected Vertical External Cavity Surface Emitting Lasers", *Appl. Phys. Lett.*, 103 (2013), pp. 252402
- [15] A. Laurain, M. Myara, G. Beaudoin, I. Sagnes, and A. Garnache, "Multi-wattpower highlycoherent compact

- singlefrequency tunable vertical-external-cavity-surface-emitting-semiconductor-laser." *Opt. Express* **18**, 14627–14636 (2010).
- [16] M. S. Seghilani, M. Sellahi, M. Devautour, P. Lalanne, I. Sagnes, G. Beaudoin, M. Myara, X. Lafosse, L. Legratiet, J. Yang, and A. Garnache, "Photonic crystal-based flat lens integrated on a Bragg mirror for high-Q external cavity low noise laser," *Opt. Express* **22**, 5962 (2014).
- [17] H. Haken, "Laser Light Dynamics", North Holland Physics publishing, 1985.
- [18] M. W. Beijersbergen, R. Coerwinkel, M. Kristensen, and J. P. Woerdman, Helical-wavefront laser beams produced with a spiral phase plate, *Opt. Commun.* **112**(5-6), 321327 (1994).
- [19] Marrucci, L., Manzo, C. Paparo, D. "Optical Spin-to-Orbital Angular Momentum Conversion in Inhomogeneous Anisotropic Media," *Phys. Rev. Lett.* **96**, 163905 (2006).
- [20] V.Y. Bazhenov, M.V. Vashnetsov, M.S. Soskin, "Laser beams with screw dislocations in their wave-fronts", *JETP Lett.* **52** (1990) 429431
- [21] M.W. Beijersbergen, L. Allen, H. Venderveen, J.P. Woerdman, "Astigmatic laser mode converters and transfer of orbital angular momentum", *Opt. Commun.* **96** (1993) 123132
- [22] M. Harris, C. Hill, P. Tapster, and J. Vaughan, "Laser modes with helical wave fronts," *Phys. Rev. A* **49**, 31193122 (1994).
- [23] D. J. Kim, J. W. Kim, and W. A. Clarkson, "Q-switched Nd : YAG optical vortex lasers," *Opt. Express* **21**, 275280 (2013).
- [24] S. P. Chard, P. C. Shardlow, and M. J. Damzen, "High-power non-astigmatic TEM00 and vortex mode generation in a compact bounce laser design," *Appl. Phys. B* **97**, 275280 (2009).
- [25] A. E. Siegman, "Lasers," University Science Books, 1986.
- [26] M. Sellahi, M. S. Seghilani, I. Sagnes, G. Beaudoin, X. Lafosse, L. Legratiet, P. Lalanne, M. Myara, and A. Garnache, "Generation of new spatial and temporal coherent states using VECSEL technology: VORTEX, high order Laguerre-Gauss mode, continuum source," *Proc. SPIE* **8966**, 89660U-89660U-7 (2014).
- [27] A. Garnache, A. Ouyard, and D. Romanini, Singlefrequency operation of external-cavity VCSELs: Non-linear multimode temporal dynamics and quantum limit, *Opt. Express* **15**, 94039417 (2007).
- [28] P. Lalanne and G. M. Morris, "Highly improved convergence of the coupled-wave method for TM polarization," *J. Opt. Soc. Am. A* **13**, **779** (1996).
- [29] G. F. Quinteiro and P. I. Tamborenea, "Twisted-light-induced optical transitions in semiconductors: Free-carrier quantum kinetics", *Phys. Rev. B*, **82**, 125207 (2010).
- [30] L. Allen, M. J. Padgett, and M. Babiker, The orbital angular momentum of Light, *Prog. Opt.* **39**, 291372 (1999).
- [31] W. P. Latham and G. C. Dente, "Matrix methods for bare resonator eigenvalue analysis," *Appl. Opt.* **19**, 161821 (1980).
- [32] F. X. Morrissey and H. P. Chou, "Mode calculations in asymmetrically aberrated

laser resonators using the Huygens-Fresnel kernel formulation,” Opt. Express 19, 197027 (2011).

- [33] A. G. FOX and T. Li, ”Resonant Modes in a Maser Interferometer,” Bell Sys Tech. j 40, 453488 (1961).

4.8 conclusion

We started this chapter by presenting phase- and amplitude-structured light. We have seen that high order beams of several transverse mode families fall under this category. These modes can exist in the continuum state of free-space, and also inside a free-space or mode-guided optical cavity. Free-space optical cavities are the most suitable for efficient selection of a desired mode with high purity, because:

- Unlike in the continuum of state of free-space, the modes form a discrete spectrum with different resonance frequencies and can be discriminated efficiently.
- Unlike in mode-guided cavities, in free-space cavities, the modes have wave-functions with different spatial spread, which enables to introduce strong discrimination using adequate transverse phase and amplitude masks.

Mode selection is also governed by the competition process in the gain medium, which we described using the semi-classical Maxwell-Bloch equations. We can select a given mode by modifying the cavity in such a way that all the modes except the desired one undergo high loss, which prevents them from reaching the threshold. We can also modify the cavity to change the dynamic properties (self- and cross-saturation) in a way that favors the desired mode.

When possible, the first method is preferred because it is robust, easy to understand and to implement, and works regardless of the intracavity intensity as it relies on passive terms. This is what we did to generate HG and degenerate LG beams. But, unfortunately this method is not sufficient to generate vortex modes with controlled handedness, because contra-rotating vortices have identical intensity distributions. Therefore, in this case we used both methods: we used loss to suppress all the modes except vortices with the wanted charge (absolute value). And modified the cavity by introducing a perturbative flat-photonics element. The latter changes the intensity pattern and thus, the dynamic self-saturation coefficient of the unwanted mode in a way that disfavors it.

Equipped, with powerful theoretical tools (eigenmode solver, and mode competition equations) and an accurate transverse phase and intensity modulation technology, we designed and implemented several sets of masks to select modes with OAM=0 and also modes carrying OAM with controlled charge and handedness. The experimental results we obtained demonstrate the effectiveness of the developed approach. Even if we focused on generation of LG and HG modes, this method is a general one and can be used in principle to generate any kind of beams providing that they belong to a well-defined Eigenbasis, such as Bessel-Gauss beams and Ince-Gauss beams.

Generation and control of coherent polarization states in VECSELs

5.1 Introduction

The control of the polarization state in a laser involves studying the polarization properties which depend on the complex electric susceptibility χ in the cavity and the gain medium. The susceptibility can present different types of anisotropies that can be classified among phase and amplitude anisotropies and linear and circular anisotropies [Van Haeringen 1967].

Linear and circular anisotropies of the real part of χ , give rise to linear and circular birefringences, respectively. Similarly, the imaginary part can present linear and circular anisotropies that give rise to linear and circular gain or loss dichroisms. The linear birefringence may occur naturally in gain media with asymmetric crystalline structures including semiconductors. The circular one can also occur in some chiral media, the simplest example of circular birefringence being a Faraday rotator.

In chapter 1 we discussed briefly the effect of the birefringence and the gain dichroism on the polarization state. We have seen that the presence of linear birefringence in a cavity gives rise to two polarization eigenstates parallel to the ordinary and the extraordinary crystal axis. The linear dichroism allows to select one of these modes thanks to mode competition in the gain medium. These physical effects are common to all the laser systems, although they have different origins. Thus, the simple theoretical approach we presented allows us to discuss the general polarization properties of most laser families. For example, in gas lasers the gain medium and mirrors are isotropic, the polarization eigenstate is then not defined. For this reason gas lasers are usually not polarized, and to resolve this problem a Brewster plate is introduced inside the cavity to fix a linear polarization state as shown in Sec 1.15. In solid state lasers, two cases are possible depending on the nature of the used solid state gain medium. Because gain media with crystalline structure have usually a natural birefringence between the crystal axis, this implies that the polarization eigenstates are linear oriented along the two crystal axis. However, we still need the dichroism to make the laser select one of them efficiently. On the other hand, when the gain medium is amorphous as for doped glasses, and fibers, we obtain a situation similar to the one of gas lasers.

In edge emitting semiconductor diode lasers the polarization state is defined by the waveguide geometry, because the TE mode which is polarized in the plane of the active region, has a better confinement and thus experiences a stronger modal gain, furthermore compressively strained QWs provide a larger gain for TE polarization [Coldren 2012, Zory 1993].

In the case of VECSELs, the vertical cavity configuration results in a good isotropic emission, and thanks to the free space propagation the polarization state and the transverse mode are independent. However, since the early days of VCSELs, experiments shown that in most cases the emitted light is polarized along the $[110]$ and $[1\bar{1}0]$ crystal axis [Shimizu 1988], this is explained by the presence of residual birefringence and dichroism in these lasers.

In this chapter, we will study polarization properties of optically pumped VECSELs, we will show how to measure the intrinsic linear birefringence and linear dichroism in the 1/2-VCSEL gain structure. These measurements allow to determine the polarization eigenstate of our passive cavity. Then, to describe the effect of non-linear light-matter interaction on polarization mode dynamics and selection, we use an accurate theoretical model based on Maxwell-Bloch equations, called the spin-flip model. This dual mode model considers the light polarization as a degree of freedom in order to study the temporal dynamics and the noise properties of polarization states. Furthermore, comparison of theoretical and experimental results will allow us to understand some important properties of polarization modes dynamics and to estimate the spin-flip rate of the quantum wells in our gain structures. Next we will address generation of circularly polarized eigenstates. For this purpose we compensate linear dichroism and linear birefringence in the cavity, and introduce circular birefringence using a Faraday rotator. We pump the cavity with polarized pump beam. The goal is to control spin of photons via spin of electrons.

5.2 Polarization properties of 1/2-VCSEL structure

5.2.1 Linear dichroism in $[001]$ Quantum wells structures

One would expect the 1/2-VCSEL gain structures to provide an isotropic gain due to their symmetry with respect to the $[110]$ and $[1\bar{1}0]$ growth crystal axis¹. However, the QWs are known to provide an optical gain that varies with the polarization angle, this variation is due to the anisotropy of zinc-blende crystal structures [Schroeder 1995, Krebs 1996, Krebs 1997] which means that the effective mass m^* varies according to the considered axis, resulting in an anisotropic density of state.

The transition dipole moment is also affected and becomes anisotropic. These effects are due to valence band mixing in QWs [Krebs 1996, Krebs 1997] arising from QW asymmetrical interfaces. These effects are affected by anisotropic strain in the QW structures, because it breaks the symmetry of the crystal.

In this section we propose a simple experimental setup to measure the gain

¹for $[100]$ oriented substrate, see Fig 2.12 in Chap 2.

dichroism between the crystal axis $[110]$ and $[1\bar{1}0]$ of our 1/2-VCSEL structures.

The basic idea behind this method is that, at laser threshold the modal gain equals the total loss in the cavity. Thus, if one knows what are the loss inside the laser cavity he can deduce the modal gain provided by the multi quantum wells structure. For this purpose, we use the cavity scheme depicted in Fig 5.1. which

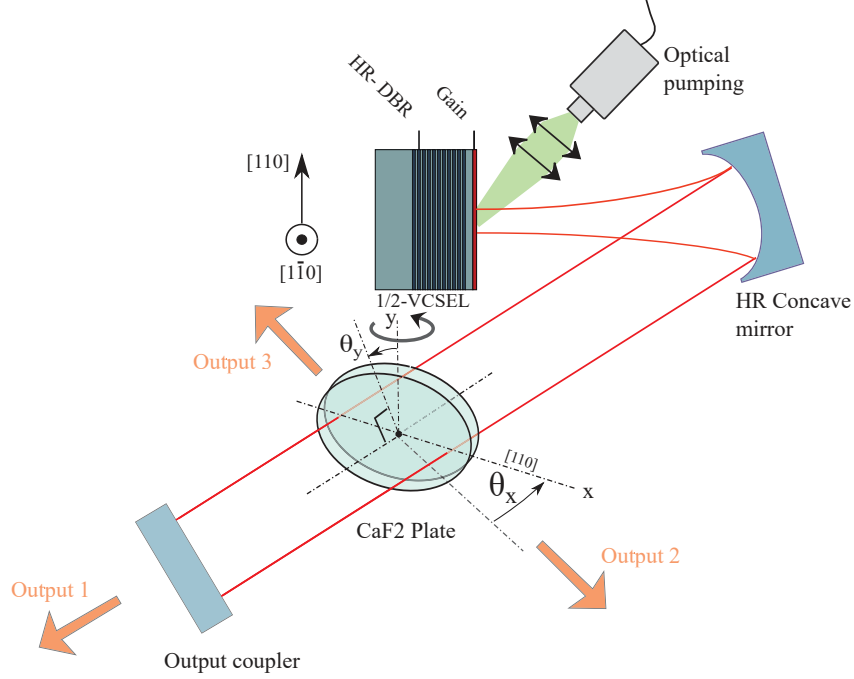


Figure 5.1: Schematic illustration of gain measurement setup.

consists in an optically pumped 1/2-VCSEL structure in a V-shaped geometry, incorporating a glass window. This latter is intended to be used as a Brewster plate to force the laser to oscillate in the wanted linear polarization mode, say the one oriented along $[110]$ that we call the Lp_{-x} , the orthogonal one will be then the Lp_{-y} . The operation principle of this resonator is explained in Sec 1.4.4.1 on page 24. We vary the plate angle around the Brewster one ($\theta_x = \theta_B + \Delta\theta$) in order to vary the loss inside the cavity, because when θ depart from Brewster value the reflections on the facets are not null (output 2,3 $\neq 0$). We record the variations of the pump density at the threshold as a function of θ , each angle corresponds to different intracavity loss that we evaluate using Fresnel reflection on the window facets. By doing so, we obtain the gain of the structure for Lp_{-x} mode as a function of the pump density. Then we set $\theta_x = 0$ and $\theta_y = \theta_B$ to force the Lp_{-y} polarization, then we vary θ_y around θ_B and repeat the previous measurements. The dichroism is obtained by comparing the Lp_{-x} and Lp_{-y} gain curves.

It is important to note that in order to accurately measure the gain, one must carefully measure all the losses inside the cavity including losses due to the mirrors transmissions, absorption and defects, prior to the gain measurement. We achieved this by measuring the slope efficiency as a function of the window angle θ to deduce

the internal losses.

We performed the gain measurement experiment with two 1/2-VCSEL structures. The first one contains containing 6 strain balanced QWs, and its top surface is antireflection treated to cancel the micro-cavity effect. The second structure is based on the same active zone but incorporates an additional moderately reflective Bragg mirror (4 pairs) to enhance the micro cavity resonance factor (see Fig 5.2), these are the *Gas680* and *Gas656* structures, presented in Chap 2.

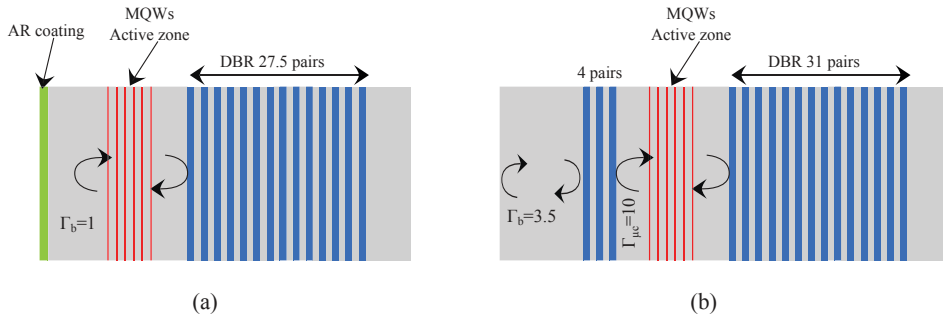


Figure 5.2: Schematic of the two 1/2-VCSELs configurations used in the studies. (a) *Gas680*: A structure with an anti-reflection coating. (b) *Gas656*: a structure without coating, plus an second moderately reflective Bragg mirror.

The obtained results are summarized in Fig 5.3 where we superimposed the gain curves of the Lp_x and Lp_y modes: parallel to $[110]$ and to $[1\bar{1}0]$, measured in the *Gas680* (Fig 5.3a) and the *Gas656* (Fig 5.3b). The curves have a logarithmic shape as predicted by theory [Coldren 2012]. We can also clearly see a gain difference between the $[110]$ and $[1\bar{1}0]$ axis in each structure. In our experiments this difference is around $\Delta G/G \simeq 20\%$. We note that the larger modal gain values measured with the *Gas656* are due to its higher micro cavity resonance factor $\Gamma_{\mu c} \simeq 10$.

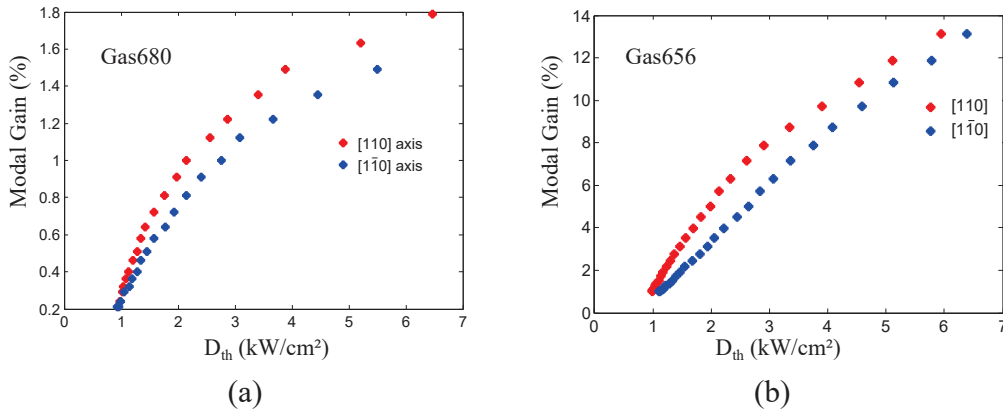


Figure 5.3: Measured gain curves of: (a) the *Gas680* 1/2-VCSEL, (b) the *Gas656*.

5.2.2 Dichroism control

Knowing that the dichroism is due to the crystal anisotropy [Biermann 2003], one can alter it by introducing thermally induced strain. In optically pumped VCSELs this can be achieved by using asymmetric pump-spot, which creates an anisotropic heat profile and thus a strain profile that can compensate the crystal anisotropy. To show this effect we used an elliptically shaped pump spot to pump the *Gas680* structure, the spot has an ellipticity of 7%, the ellipse is oriented along the $[1\bar{1}0]$ axis. The measured gain curves are shown in Fig 5.4. We notice that the $[110]$ and $[1\bar{1}0]$ axis have nearly the same gain now, which implies that the gain dichroism is significantly reduced.

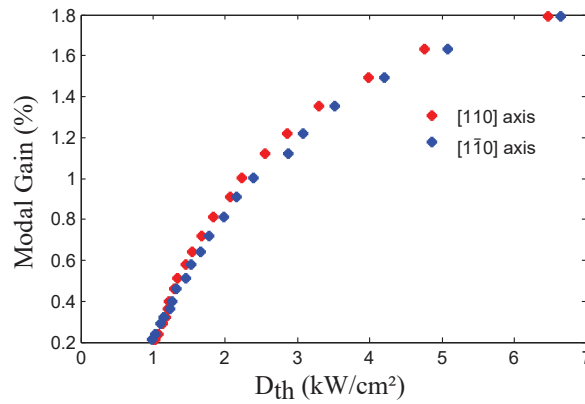


Figure 5.4: Gain curves measured with the *Gas680* 1/2-VCSEL, using an elliptically(7%) shaped spot pump to reduce the dichroism by introducing anisotropic strain.

5.2.3 Linear birefringence in 1/2 VCSEL structure

The birefringence can be deduced by measuring the induced frequency splitting of polarization modes emission wavelengths, this splitting is due to the difference of their optical paths. However, unlike in microcavity VCSEL, for mm-long VCSEL, the expected frequency splitting¹ is too small to be observed with a commercial optical spectrum analyzer limited to GHz resolution. Alternatively a HR confocal FP interferometer could be used. In addition, the noise floor is usually too high with optical spectrometers, thus the suppression ratio could be limited by the apparatus function. Therefore, we propose to use the same method we used to measure the extinction ratio of transverse modes, which is to mix the two orthogonal modes and observe the beat note in the RF domain. In concrete terms this means to measure the RIN spectrum of the laser, detected with a fast photodiode and a low noise amplifier. This allows to achieve high spectral resolution and high dynamics in terms of amplitude (>80 dB).

¹According to birefringence values reported in the literature.

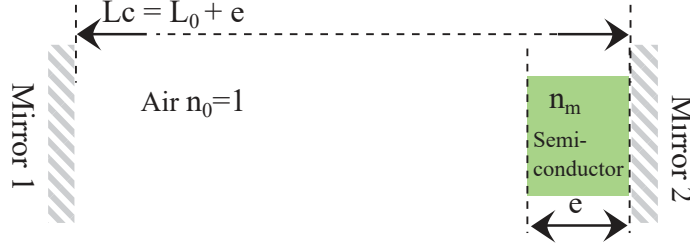


Figure 5.5: Schematic illustration of a laser cavity incorporating birefringent medium.

But before starting the description of the experiments, let us see how to relate the beating frequency to the birefringence and what are the involved laser parameters. The general case of a laser cavity containing a birefringent gain medium is represented in Fig 5.5. The round-trip phase difference between Lp_{-x} and Lp_{-y} (parallel to $[110]$, $[1\bar{1}0]$ respectively) can be calculated by taking account of the non-homogeneous index distribution inside the cavity. Mode spacing in such a resonator has been treated by [Coldren 2012] as the three mirror cavity problem. The cavity shown in Fig 5.5 is equivalent to a two-mirror cavity with one mirror having complex effective reflectivity $r_{eff} = |r_{eff}|\exp(-j\phi_{eff})$. Mode frequencies for Lp_{-x} and Lp_{-y} polarizations are given by:

$$\begin{aligned} \nu_{Lp_{-x}}^q &= q \frac{c}{2[n_0 L_0 + (n_m^e - 1)L_{eff}]} \\ \nu_{Lp_{-y}}^q &= q \frac{c}{2[n_0 L_0 + (n_m^o - 1)L_{eff}]} \end{aligned} \quad (5.1)$$

where q is the longitudinal mode order, c is the speed of light, n_m^o, n_m^e are the refractive indices of the ordinary and the extraordinary axis of the birefringent medium (semiconductor), and n_0 is the one of vacuum. L_{eff} is an effective length equivalent to ϕ_{eff} . If no reflection exists at the semiconductor-air interface then $L_{eff} = e$ and $\phi_{eff} = -2k_0 e$, where e is the thickness of the birefringent medium. For the more general Fabry-Perot etalon, the slope of the phase will be dependent on whether we are near a resonance or an antiresonance of the microcavity, and thus on the resonance factor Γ_b^1 (see Fig 5.2). Consequently L_{eff} can be larger or smaller than e . From these equations it can be shown that the modal phase shift due to the birefringence reads as:

$$\Delta\varphi_p = 2k_0 e \Delta n \Gamma_b, \quad (5.2)$$

where $k_0 = 2\pi/\lambda$, $\Delta n = n_m^o - n_m^e$. The frequency splitting can be expressed in terms of the linear birefringence γ_p as:

$$\Delta\nu_p = -\Delta\varphi_p FSR = 2\gamma_p \quad (5.3)$$

¹This derivation assumes that ϕ_{eff} varies linearly, it is thus accurate for moderate reflectivity of semiconductor air interface (~ 0.3).

Eq 5.3 would be sufficient in the case of a passive cavity, however, when the cavity contains an active region, the QW's gain anisotropy gives rise to an additional frequency difference $\Delta\nu_G$ because of the phase-amplitude coupling effect in the QWs (frequency pulling) [Siegman 1986, Coldren 2012]. The induced $\Delta\nu_G$ can be written as follows:

$$\Delta\nu_G = \frac{1}{2\pi} \frac{\alpha_h}{2} \gamma_c \frac{\Delta G}{G} \quad (5.4)$$

where γ_c is the decay rate of the laser cavity, and $\Delta G/G$ is the relative linear dichroism of the modal gain. The total frequency difference will be then given by:

$$\Delta\nu_b = \Delta\nu_p + \Delta\nu_G + \Delta\nu_s \quad (5.5)$$

Where $\Delta\nu_s$ is an additional frequency shift caused by dynamics effects as we will see next (Sec 5.3.4.3). This effect can be neglected when the laser operates close to the threshold. In the following measurements we will measure the beating in this condition and neglect $\Delta\nu_s$.

5.2.3.1 Experiments

The birefringence measurement principle is described in Fig 5.6a, we use a linear polarizer oriented at 45° with respect to the polarization axis. This way the Lp_{-x} and Lp_{-y} modes are projected equally on the bisecting axis. Then, the beam is merely focused on a low noise detector and the noise spectrum of the laser is measured using an RF spectrum analyzer. Fig 5.6b shows an example of the obtained spectra, in this measurement we used a VCSEL based on the Gas680 1/2-VCSEL, a concave mirror ($Rc = 10$ mm), with a cavity length $L_c = 8$ mm. The RIN curve is superimposed with another one measured with the same setup with a polarizer oriented along the dominant polarization axis ([110]). The absence of the peak in the second curve, confirms that the observed beat note is due the orthogonal polarization mode. We repeated this measurement by changing the output coupler (to reduce the cavity loss), and then by using the second 1/2-VCSEL (Gas656). The goal of these measurements is to study the birefringence by varying some of the relevant parameters of the gain structures, mainly the dichroism and the micro-cavity confinement γ_b . We summarized the measurement results in table 5.1.

Let us stop for a moment to consider the experimental results of this table, to see what information can be deduced from it. When we look at the measured frequency splitting values, it is indeed quite difficult to establish the link with the birefringence. For example, in row 2, although we used the same gain structure as in row 1, changing the output coupler transmission changed the measured frequency splitting because of the phase-amplitude coupling effect ($\Delta\nu_G$ in Eq 5.5). We think that omitting this term is one of the reasons of the disparity of the values reported in the literature. But when we take it into account, we notice that the frequency splitting values due to the pure birefringence are the same (see the last column), which is logical given that we haven't changed the 1/2-VCSEL. By comparing the

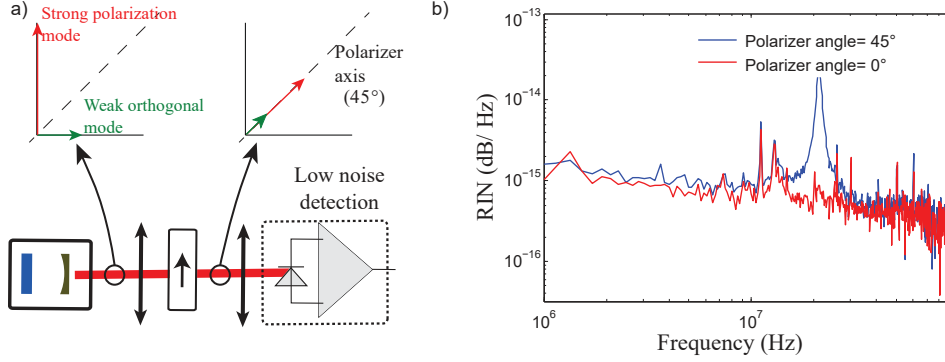


Figure 5.6: (a) Experimental setup for birefringence measurement, via polarization mode beating. (b) An example of measured spectrum, obtained with Gas680 in 8 mm long cavity, a beam waist $w_0 = 37 \mu\text{m}$, and a concave output coupler of 0.7% transmission.

Structure	$\Delta\nu_b$	$\Delta\nu_G$	$\Delta\nu_p$	$2\gamma_p(< 0)$	$2\gamma_p/\Gamma_b$
Gas680 with OC (0.7%)	-16.4 MHz	7.6 MHz	- 24 MHz	$-151 \times 10^6 \text{ s}^{-1}$	$-151 \times 10^6 \text{ s}^{-1}$
Gas680 with HR (0.2%)	-23 MHz	1.5 MHz	-24.5 MHz	$-154 \times 10^6 \text{ s}^{-1}$	$-154 \times 10^6 \text{ s}^{-1}$
Gas656 with OC (10%)	-69 MHz	13.4 MHz	-82.4 MHz	$-518 \times 10^6 \text{ s}^{-1}$	$-149 \times 10^6 \text{ s}^{-1}$

Table 5.1: Measured polarization modes' beat frequency and deduced birefringence values for 3 VeCSEL configurations based on Gas680 and Gas656 structures in a 7.5 mm long cavity.

first two rows we can deduce an important information which is the sign of the birefringence. In fact, the beating in the RIN spectrum gives only the absolute value of the birefringence. From the table, when we decreased γ_c (by using a HR mirror) the measured beating increased, this implies that γ_p is negative according to Eq 5.5: $n_{[110]} > n_{[1\bar{1}0]}$.

Let us consider now the third row of the table, here we used the second structure (Gas656), whose gain curves and its configuration are shown in Fig 5.3b and Fig 5.2 respectively. This structure has two confinement factors, $\Gamma_b = 3.46$ is due to the air-semiconductor interface (first GaAs lambda/4 layer), and $\Gamma_{\mu c} = 3\Gamma_b \simeq 10$ due to the moderately reflective second Bragg reflector. When we look at the birefringence values of the Gas656 we see that the $\gamma_p(\text{Gas656}) \simeq 3.5\gamma_p(\text{Gas680})$. This means that the birefringence is only affected by the air/semiconductor interface, and totally independent from the micro-cavity confinement factor $\Gamma_{\mu c}$, which reinforces the idea that the birefringence originates from an elasto-optic effect [Lastras-Martínez 2001, Park 2000] that happens very close the 1/2-VCSEL top surface, on a distance of the order of $e \sim \lambda/(4n)$ ($\sim 50 \text{ nm} - 100 \text{ nm}$). Knowing this, we estimated the refractive index difference between the crystal axis of our 1/2-VCSEL structures: $\Delta n = n_{[110]} - n_{[1\bar{1}0]} \in [8 \cdot 10^{-3} - 16 \cdot 10^{-3}]$. Note that this value is about an order of

magnitude stronger than what one would obtain by taking into account only the electro-optic effect at the air/semiconductor surface [Park 2000].

5.2.3.2 Birefringence control

To accurately control the birefringence in 1/2-VCSELs structures we propose two methods, the first one is based on the integrated metamaterial technology developed in Chap 3. We have seen that it is possible to achieve birefringent artificial dielectric layers by using a sub-wavelength grating with an asymmetric pattern. For example, Fig 5.7 shows simulation result of the phase shift induced by rectangular holes in 131 nm thick SiN layer, integrated on the Gas680 structure. These curves show a phase difference between TE/TM-polarized electric field. We implemented this pattern on the top surface of the *Gas680*, we set $ff_x = 1$ to obtain the maximum birefringence value ($\Delta\varphi = 0.29$ rad) with the rectangular holes oriented parallel to the [110] crystal axis, in order to reinforce the intrinsic birefringence. Fig 5.8a,b show a SEM and an optical microscope photographs of the fabricated mask.

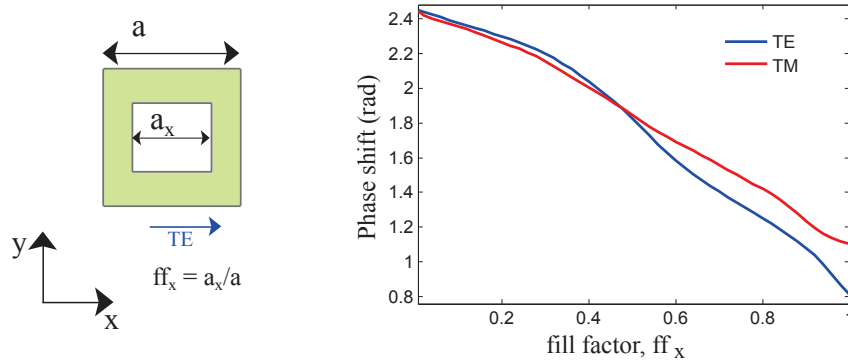


Figure 5.7: RCWA simulation results of the phase shift induced by rectangular holes in 131 nm thick SiN layer, integrated on the Gas680 structure. In the simulations $ff_y = 0.2$ and only ff_x varies.

In order to illustrate the polarization effect, we placed a second mask with the same pattern but oriented perpendicularly and observe the two using an optical microscope with a polarization filter in order to accent the index inhomogeneities and /or variations. We can see that although the masks are designed to work at $\lambda = 1 \mu\text{m}$, the effect of the birefringence can be observed in the visible range. One can clearly notice the effect of the refractive index difference, between the mask and the surrounding SiN area in the first place, and then the difference between the two masks oriented perpendicularly to each other¹.

We used this gain structure integrating a birefringent metasurface with the fast axis oriented parallel to the [110] crystal one, to build a 8 mm length optically pumped VCSEL similar to the one we used in previous birefringence measurements.

¹Note that thanks to the polarizing filters of the microscope, the refractive index variations are transformed to a color variations.

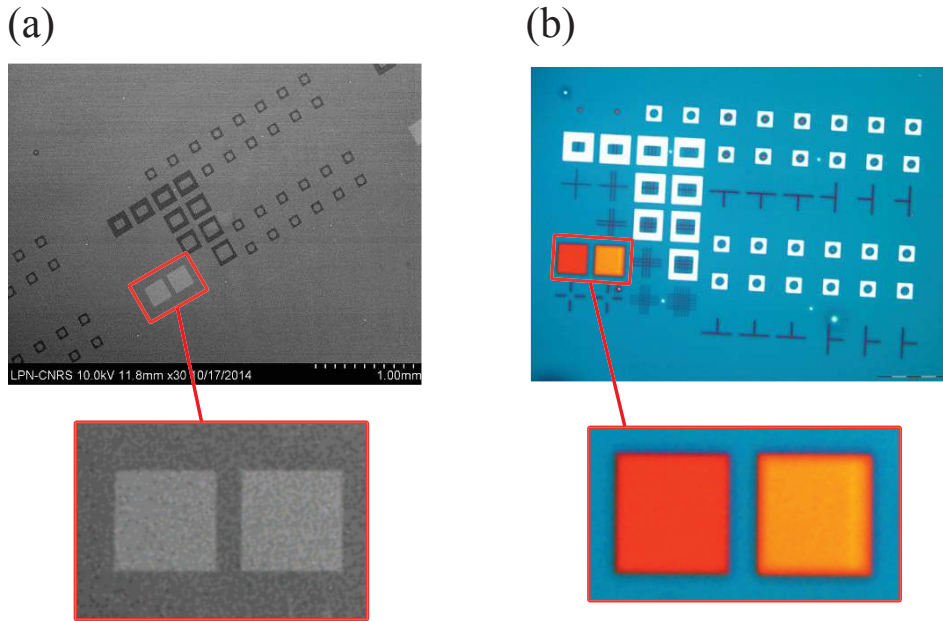


Figure 5.8: Scanning electron microscope (a), and optical microscope (b) photographs of the fabricated birefringent masks on the Gas680 1/2-VCSEL structure.

Then we performed the same experiments to observe the polarization beat-note. Fig 5.9 shows the measured RIN spectrum. For comparison, we superimposed the RIN obtained with the same structure but operating without the birefringent mask.

These curves show that the birefringent filter increased the birefringence of the 1/2-VCSEL structure by a factor $\simeq \times 6$. This value is in good agreement with theoretical prediction: from Fig 5.7, if we compare the calculated birefringence (between TE and TM curves) at $ff_x = 0$ and $ff_x = 1$, and by considering the layer thickness precision of ± 10 nm, one obtains a theoretical birefringent increase by a factor $\simeq \times 6 - \times 8$.

The method shown here, can be used to solve the problem of polarization instability in VECSELs with weak birefringence. For example, 1/2-VCSEL structures processed for high power (thermal management) usually require heavy technological steps such as substrate removal and bounding, which alter the natural anisotropy of the gain structures. This results in unstable polarization state without preferential axis. Thus, introducing strong birefringence and dichroism by means of metamaterials would force the polarization modes along the crystal axis again. Next we will show a second method, intended primarily to compensate the birefringence inside the VECSEL cavity, this method is described in Sec 5.4.1.

5.2.4 Circular dichroism and circular birefringence

The linear birefringence and dichroism allowed us to explain the linear polarization mode selection using a simple theoretical approach. In this section we introduce the circular birefringence and dichroism. These two anisotropies will enable us to

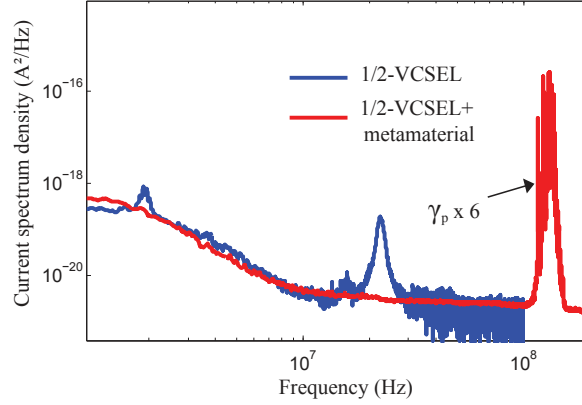


Figure 5.9: RIN spectrum of a laser incorporating a birefringent metamaterial-based mask, for comparison we superimposed the curve obtained with the same laser without the mask. The curves are obtained with Gas680 in 8 mm long cavity, a beam waist $w_0 = 37 \mu\text{m}$, and a concave output coupler of 0.7% transmission.

treat the circular polarization states.

The circular birefringence can naturally occur in some chiral media, and can be introduced in a laser cavity simply using a Faraday rotator. The rotator lifts the degeneracy of left and right circularly polarized modes of the cavity and introduces a frequency difference of $FSR/2$ between them for a rotation angle $=45^\circ$. Unlike in the linear case, this frequency shift can be measured with a high resolution Optical spectrum analyzer if the cavity is short enough, or with a confocal Fabry-Perot interferometer.

Circular dichroism means that one circular polarization mode experiences higher loss than the other one. This can occur in presence of chirality in the resonator, but a similar effect can also be obtained by means of spin-polarized pumping of one circular mode by generating carriers with $\sigma+/-$ using for example right/left handed circularly polarized pump beam. We note that in this case one obtains a circular gain-dichroism rather than loss. This implies that there are two spin reservoirs and that the spin imbalance due to pumping is conserved. However, it has been shown that the carrier populations with opposite spins are mixed in the gain medium by several processes modeled by the spin flip rate γ_s ($= 1/\tau_s$) [San-Miguel 1995]. Based on experimental measurements of the spin relaxation rate, it has been estimated that [Damen 1991, Bar-Ad 1992]:

$$\gamma_e \leq \gamma_s \leq 10^2 \times \gamma_e \quad \text{or, } \tau_e \times 10^{-2} \leq \tau_s \leq \tau_e \quad (5.6)$$

In VCSELs the carrier lifetime τ_e is $\simeq 2 - 3$ ns typically, the spin flip time is then $\tau_s \in [10 \text{ ps} - 1 \text{ ns}]$. This phenomenon has been introduced within the spin-flip model that we describe in Sec 5.3.3.

5.3 Generation of pure linear polarization

5.3.1 Inherent selection of linear polarization in VECSELS

By studying the polarization properties of VECSELS pumped with unpolarized electrons we have seen that they naturally emit linearly polarized light thanks to their intrinsic linear birefringence and linear dichroism. However, this is true only for VECSELS with good crystal quality. For example VECSELS emitting at telecoms wavelengths and electrically pumped VECSELS require heavy technological steps that alter the intrinsic crystal anisotropy. In this case one must introduce the required linear anisotropies to ensure stable linear polarization state.

The polarization mode beat can be used to measure the purity of the state characterized by the polarization extinction ratio (PER) given by:

$$PER = \frac{P_w}{P_d} \quad (5.7)$$

where P_w , P_d are the power of weak mode and of dominant mode, respectively. The PER can be deduced from the power in the beat peak P_{beat} as:

$$PER \simeq \frac{P_{beat}}{\bar{P}} \simeq \Delta f \times RIN \quad (5.8)$$

where Δf is the FWHM of the peak and \bar{P} is the average output power. In our measurements $\Delta f \simeq 2$ MHz (see Fig 5.6b) which results in a $PER \simeq 80$ dB. This value agrees well (at 3 dB precision) with the theoretical quantum limit given by [Laurain 2010b]:

$$PER = 10 \log \left(\frac{P_{out} \lambda}{hc \gamma_c \varepsilon} \times \frac{\Delta G}{G} \right) \quad (5.9)$$

By assuming a dichroism value $\Delta G/G = 10\%$, optical losses of 1.5% and setting $L_c = 8$ mm, $P_{out} = 38$ mW we obtain $PER = 77$ dB according to Eq 5.9.

5.3.2 The problem of the suppressed mode linewidth

This problem stems from the measured typical values of the PER, for example, we found a $PER \simeq 80$ dB with a total output power $P_{out} = 38$ mW and a total optical losses of 1.5%. This implies that the residual polarization mode contains only few intracavity photons, this is not a problem itself, but the mode linewidth and thus the beat peak linewidth, should not be smaller than a few tens of MHz according to the passive cavity linewidth (Eq 1.77). However, in our experiments the beat peak has a typical linewidth of 2 MHz, so how could this be possible?

To find an answer to this problem we have to study the dynamics of polarization modes. Our goal will be to determine the theoretical noise spectrum of the laser. However, it is easy to see that the Lamb equations we used so far fail to give an answer, thus, as we did in the transverse modes case we will use a more accurate model based on the semi-classical Maxwell-Bloch equations (Sec 4.5.3.1)

and written in a fashion that takes account of all the polarization properties of the laser presented earlier in this chapter: linear and circular, phase and amplitude anisotropies of the electric susceptibility, in addition to the coupling process between carrier in the spin reservoirs (circular gain dichroism, and the fundamental Langevin noise sources). This model is called the Spin-Flip Model (SFM), that we present it in the following section. Next, to study the noise spectrum we linearize the SFM equations and calculate the spectral density of power fluctuations using a semi-analytical approach. At the end, we compare the theoretical spectra with experimental ones which shall allow us to validate our measurements and to estimate the spin-flip rate of our QW-based gain structures.

5.3.3 Dynamics of polarization modes: the SFM model

The spin-flip model (SFM) has been first introduced for VCSELs by [San-Miguel 1995]. This model is based on Maxwell-Bloch equations in a four-level system, by including the conduction band (CB) and the Valence band spin-sub-levels of the semiconductor quantum wells.

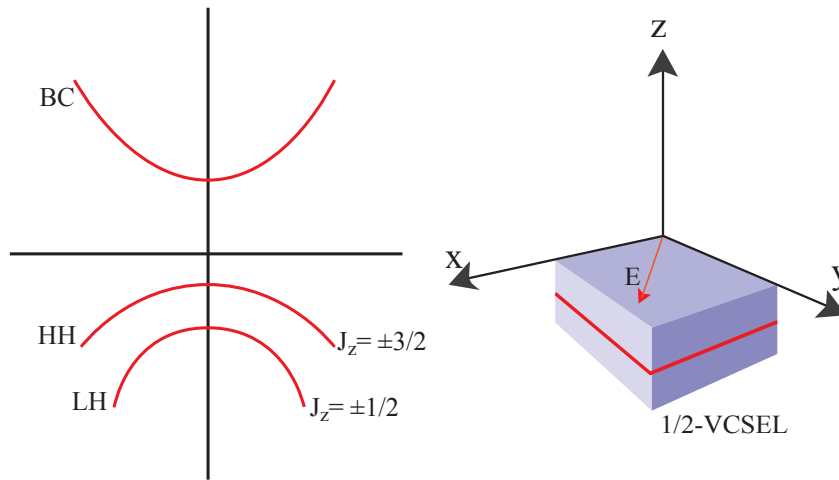


Figure 5.10: (a) Band structure of a QW. (b) Geometry of a surface emitting laser.

In the case of QW-based surface emitting lasers, the electric field is in the x-y plane (see Fig 5.10), the allowed dipole transitions are those having an angular momentum $\Delta J_z = \pm 1$: $CB(-1/2) \rightarrow HH(-3/2)$ ($\sigma+$) and $CB(1/2) \rightarrow HH(3/2)$ ($\sigma-$), which results into right and left circular polarization of the electric field, respectively. Consequently, this model considers light polarization as a degree of freedom. The SFM equations under basic assumptions of slowly varying amplitude ap-

proximation, and single transverse and longitudinal modes, read [San-Miguel 1995]:

$$\begin{aligned} \dot{E}_{\pm} &= \left[\frac{B}{2}(1 + i\alpha_h)(D + d) - \frac{\gamma_c}{2} \pm i\gamma_c \right] E_{\pm} - (\gamma_a + i\gamma_p) E_{\mp} + F_{\pm} \\ \dot{D} &= \frac{P_+ + P_-}{2} - AD - B(D + d)|E_+|^2 - B(D - d)|E_-|^2 - F_D \\ \dot{d} &= \frac{P_+ - P_-}{2} - \gamma_s d - B(D + d)|E_+|^2 + B(D - d)|E_-|^2 - F_d \end{aligned} \quad (5.10)$$

where E_{\pm} are the two circular polarization components of the electric field which are related to the linear components by $E_{\pm} = (E_x \pm iE_y)/\sqrt{2}$. The carrier numbers in the two spin reservoirs i.e., N_{\pm} , are written in terms of the total carrier population $D = (N_+ + N_-)/2$ and the carrier difference $d = (N_+ - N_-)/2$. P is the total pumping rate is written in terms of the two pumping rates of N_{\pm} carrier's reservoirs. $P = P_+ + P_-$. We note that in our case as we pump in the barriers, the effective pumping rate in QW is calculated through the real degree of polarization of carrier in GaAs bulk barriers (3/4 - 1/4 of $\sigma+$ and $\sigma-$ polarized electrons for a 100% polarized pump), plus the depolarization rate due the spin-flip rate in the barriers and the finite capture time in the QWs (~ 10 ps). In our case one finds a ratio $P_+/P_- \sim 2$, for P_+ pumping.

The cavity decay rate is γ_c , α_h is the Henry factor, A , B are Einstein coefficients related to spontaneous and stimulated emission, respectively, and γ_s is the spin-flip rate. γ_a (loss dichroism) and γ_p (birefringence) are the linear passive anisotropies of the cavity, and γ_c is the circular birefringence. The terms F_{\pm} , $F_{\left(\frac{D}{d}\right)}$ are the Langevin sources for the electric field and the population inversion, respectively. These terms are introduced to take into account all the noise sources that arise from the spontaneous emission processes, they read:

$$F_{\pm} = \sqrt{\zeta B (D \pm d)} X_{\pm}(t) \quad (5.11a)$$

$$F_{\left(\frac{D}{d}\right)} = \sqrt{2\zeta B (D + d)} E_+ X_+(t) \pm \sqrt{2\zeta B (D - d)} E_- X_-(t) + c.c \quad (5.11b)$$

where $\zeta \simeq 1.1$ is the spontaneous emission factor, and $X_{\pm}(t)$ are two independent complex noise sources with zero means and correlation $\langle X_{\pm}(t) X_{pm}(t') \rangle = \delta(t - t')$.

When we use an unpolarized pumping, carriers with two opposite spins (σ^+ , σ^-) are generated equally, they give rise to two circular component E_+ , E^- respectively. The linear anisotropies always tend to couple them and generated linear components Lp_{-x} , Lp_{-y} .

We would like to point out here that we introduce phenomenologically as a perturbation the measured linear gain dichroism (see sec 5.2.1) as a loss dichroism term ($\gamma_a \ll \gamma_c$). Indeed, the circular eigen basis was used in the SFM to model the electromagnetic dipole in the matter, which prevents from injecting linear transition dipole moment in a simple way.

In Fig 5.11 we show an example of polarization mode dynamics, we obtained using the spin-flip equations in a typical 8 mm length VECSEL, with a mode waist

Parameter	Value
γ_c	$175 \times 10^6 \text{ s}^{-1}$
$\tau_e = 1/\gamma_e$	$\simeq 2 \text{ ns}$
$2\gamma_p$	$-2\pi \times 20 \text{ MHz}$
γ_c	0 s^{-1}
$2\gamma_a$	$0.1 \gamma_c$
τ_s	100 ps
ξ	~ 1.1
B	1 s^{-1}

Table 5.2: Laser parameters used in linear polarization modes dynamics simulation.

$w_0 = 37 \mu\text{m}$, the used parameters are summarized in table 5.2. At the steady state the stable polarization mode is a single linear one, whose orientation is determined by the birefringence and the linear dichroism. The other mode is at the spontaneous emission level. When the polarization components are slightly elliptical (due to

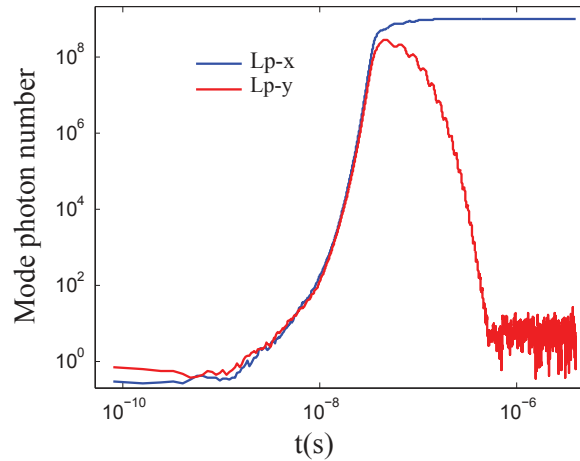


Figure 5.11: Temporal dynamics simulation at start-up, seeded by spontaneous emission, of linear lp_{-x} , lp_{-y} polarization modes, the used parameter are summarized in table 5.2. The pump rate $\eta = 2$.

coherent coupling of the linear light states thanks to circular dichroism in the gain), we obtain an additional weak polarization mode, orthogonal to the dominant one. This may seem obvious, but implies a key point for our analysis, which is that the noise sources, mainly due to fluctuations of the atomic polarization, are added to the circular components and not on the linear ones. As the passive cavity eigenstates are linear (dominant mode + weak orthogonal mode) the dipole radiates on a linear combination $\frac{E_+ + E_-}{\sqrt{2}}$. Therefore, it becomes obvious that the width of the weak mode cannot be estimated using directly the Schawlow-Townes expression as we did in Sec 5.3.2. Instead, one has to use the SFM to introduce the noise sources on the circular components, and then study the dynamics and the noise impact on

each linear component by taking account of all the dynamical processes involved. To this end, in the following section we derive the noise spectrum by linearizing the SFM equations, the theoretical spectrum will allow us to study the beating between the linear modes and understand the role of the spin-flip rate in the purity of polarization modes.

5.3.4 Theoretical noise spectrum and polarization modes beating

5.3.4.1 Normalized dimensionless SFM equations

The system of equations 5.10 can be written in terms of N_{\pm} dimensionless equations. To this end we normalize all the rates (except γ_s) to κ , where $\kappa = \gamma_c/2$ is the loss rate for the E-field. The normalized time is then $\tau = t\kappa$. The total linear loss dichroism is defined for the E-field and given by $2\gamma_a = \Delta G/G \times \gamma_c/2$. And the total E-field birefringence is $2\gamma_p$. We also normalize the photon number P to saturation photon number $P_s = \gamma_e/B$ so $E = E/\sqrt{(P_s)}$ where $B \simeq 1 \text{ s}^{-1}$ (for a typical 8 mm long cavity design with a beam waist of 30 μm) and $\gamma_e \simeq 2\pi \times 80 \text{ MHz}$ is the spontaneous carrier decay rate. The population inversion N is normalized to its steady state value γ_c/B . The E-field Langevin force has a variance of $\langle F_{\pm} F_{\pm}^* \rangle = \gamma \zeta \delta(t)$. After normalization, one gets $\langle \xi_{\pm} \xi_{\pm}^* \rangle = 2\varepsilon \delta(\tau) = 2\zeta/\gamma P_s \times \delta(\tau) \text{ Hz} = \zeta/\kappa P_s \times \delta(\tau) \text{ Hz}$, where ε denotes the rate of spontaneous emission into the mode. The system of equations 5.10 now reads:

$$d_t E_{\pm} = (1 + i\alpha)(N_{\pm} - 1)E_{\pm} + (\gamma_a + i\gamma_p)E_{\mp} + \xi_{\pm}, \quad (5.12)$$

$$\frac{1}{\gamma_e} d_t N_{\pm} = \mu - N_{\pm} \mp \gamma_s(N_{+} - N_{-}) - N_{\pm} |E_{\pm}|^2 - \frac{E_{\pm}^* \xi_{\pm} + c.c.}{2} + \chi_{\pm} \quad (5.13)$$

where μ is the normalized pump rate. The Langevin forces are uncorrelated to each other, and verify the usual zero-mean and delta-correlated variance properties:

$$\langle \xi_{\pm} \xi_{\pm} \rangle = 0, \quad \langle \xi_{\pm} \xi_{\pm}^* \rangle = 2\varepsilon \delta(\tau), \quad (5.14)$$

$$\langle \chi_i \chi_j \rangle = \mu_p \delta_{ij} \quad i, j = \pm, \quad (5.15)$$

where μ_p is the rate of fluctuations in the pump, which is assumed to be the same for both spin reservoirs. There is no correlation between pump noise and Langevin forces.

5.3.4.2 Linearization and noise spectrum calculation

One must solve for the deterministic steady state, which we assume to be $Lp-x$, i.e., we have $\gamma_a > 0$. In this state, $E_{\pm} = A_x e^{i\omega_x t} = e^{i\phi} e^{i\omega_x t} \sqrt{\mu/(1 - \gamma_a) - 1}$, $\omega_x = \gamma_p - \alpha\gamma_a$, and $N_{\pm} = N_x = 1 - \gamma_a$. Now, we perturb this state: $E_{\pm} = (A_x + a_{\pm}) e^{i\omega_x t}$,

$N_{\pm} = N_x + n_{\pm}$. The linearized evolution equations read:

$$d_t a_{\pm} = (1 + i\alpha)A_x n_{\pm} - i\omega_x a_{\pm} + (\gamma_a + i\gamma_p)a_{\mp} + \xi_{\pm}, \quad (5.16)$$

$$\begin{aligned} \frac{1}{\gamma_e} d_t n_{\pm} &= -\left(1 + |A_x|^2\right) n_{\pm} \mp \gamma_s (n_+ - n_-) - n_{\pm} |A_x|^2 - N_x (A_x^* a_{\pm} + A_x a_{\pm}^*) \\ &\quad - \frac{A_x^* \xi_{\pm} + cc}{2} + \chi_{\pm}, \end{aligned} \quad (5.17)$$

Due to the a_{\pm}^* terms in the equations for n_{\pm} , the former equations must be supplemented with the evolution equations for a_{\pm}^* . Remark that, in this context, a_{\pm} and a_{\pm}^* must be treated as independent variables (as indeed they are if the real and imaginary parts of a_{\pm} are independent).

The solution can be found by Fourier Transform. In this case, it is better to work with $c_{\pm} = A_x^* a_{\pm}$. The system can then be written as

$$\mathbf{M}^{-1} \cdot \vec{x} = \vec{v} \quad (5.18)$$

where the vectors of Fourier component are:

$$\vec{x}^T = (c_+, c_-, c_+^*, c_-^*, n_+, n_-), \quad (5.19)$$

and

$$\vec{v}^T = (\hat{\xi}_+, \hat{\xi}_-, \hat{\xi}_+^*, \hat{\xi}_-^*, -(\hat{\xi}_+ + cc)/2 + \chi_+, -(\hat{\xi}_- + cc)/2 + \chi_-), \quad (5.20)$$

with $\hat{\xi}_{\pm} = A_x^* \xi_{\pm}$, and we have defined:

$$\mathbf{M}^{-1} = \begin{pmatrix} i(\omega + \omega_x) & -\gamma_a - i\gamma_p & 0 & 0 & (-1 - i\alpha)P_x & 0 \\ -\gamma_a - i\gamma_p & i(\omega + \omega_x) & 0 & 0 & 0 & (-1 - i\alpha)P_x \\ 0 & 0 & i(\omega - \omega_x) & -\gamma_a + i\gamma_p & (-1 + i\alpha)P_x & 0 \\ 0 & 0 & -\gamma_a + i\gamma_p & i(\omega - \omega_x) & 0 & (-1 + i\alpha)P_x \\ N_x & 0 & N_x & 0 & \frac{i\omega}{\gamma_e} + \gamma_s + P_x + 1 & -\gamma_s \\ 0 & N_x & 0 & N_x & -\gamma_s & \frac{i\omega}{\gamma_e} + \gamma_s + P_x + 1 \end{pmatrix}. \quad (5.21)$$

Thus, the solution to the system is given by $\vec{x} = \mathbf{M} \cdot \vec{v}$. Unfortunately, we can not obtain a simple and amenable analytical expression for \mathbf{M} , it can be however, straightforwardly computed numerically.

From the correlation properties of the noise sources, we can compute the correlation matrix for \vec{v} , $C_v^{ij} = \langle v_i^* v_j \rangle$. We find that:

$$\mathbf{C}_v = \begin{pmatrix} 2\epsilon' & 0 & 0 & 0 & -\epsilon' & 0 \\ 0 & 2\epsilon' & 0 & 0 & 0 & -\epsilon' \\ 0 & 0 & 2\epsilon' & 0 & -\epsilon' & 0 \\ 0 & 0 & 0 & 2\epsilon' & 0 & -\epsilon' \\ -\epsilon' & 0 & -\epsilon' & 0 & \epsilon' + \mu & 0 \\ 0 & -\epsilon' & 0 & -\epsilon' & 0 & \epsilon' + \mu \end{pmatrix}, \quad (5.22)$$

where $\epsilon' = \varepsilon P_x$, and now we can compute the spectrum of any quantity related to \vec{x} . The corresponding correlation matrix for \vec{x} is

$$\mathbf{C}_x = \mathbf{M}^* \cdot \mathbf{C}_v \cdot \mathbf{M}^T$$

5.3.4.3 Comparison with experiments

In the experiment, a linear polarizer at 45 deg from the $Lp-x$ direction mixes the two polarization components. The field at the output of the polarizer is then:

$$F = \frac{E_x + E_y}{\sqrt{2}} = \frac{1-i}{2}E_+ + \frac{1+i}{2}E_- . \quad (5.23)$$

and around steady-state, then:

$$F = e^{i\omega_x t} \left(A_x + \frac{1-i}{2}a_+ + \frac{1+i}{2}a_- \right) . \quad (5.24)$$

This is sent to a photodiode, that generates a current I given by:

$$I \sim |F|^2 = |A_x|^2 + \left[A_x^* \left(\frac{1-i}{2}a_+ + \frac{1+i}{2}a_- \right) + cc \right] + \dots \quad (5.25)$$

$$= |A_x|^2 + \left(\frac{1-i}{2}c_+ + \frac{1+i}{2}c_- + cc \right) + \dots \quad (5.26)$$

where we neglect second order terms in the sum (denoted by "...” in equation). Defining $y = (1-i)/2c_+ + (1+i)/2c_- + cc \equiv \vec{\lambda} \cdot \vec{x}$, the spectral density associated with I is then going to be:

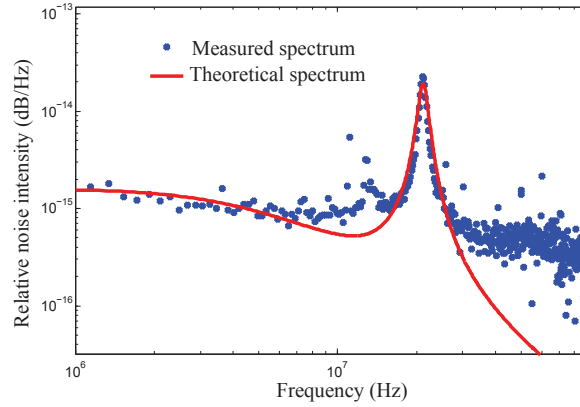
$$|I(\omega)|^2 \sim (|A_x|^2 2\pi)^2 \delta(\omega) + \lambda^* \cdot \mathbf{C}_x \cdot \lambda + \dots \quad (5.27)$$

We calculated the relative power spectra using Eq 5.27 and the first thing we note is that the calculated spectrum shows a beating peak with a shape, amplitude and a width that are in very good agreement with the measured ones. For example, in in Fig 5.12 we show measured spectrum superimposed with theoretical one calculated by injecting the parameters of VeCSEL with a 8 mm long cavity based on the Gas680 gain structure. In what follows we will be using the Gas680 structure in two configurations: with an output coupler and with a HR mirror. For the sake of clarity the used parameters in each case are summarized in table 5.3. The measured spectrum shown in Fig 5.12 corresponds to the experimental conditions of configuration (2) in the table, thus, we naturally used the corresponding parameter to obtain the theoretical spectrum.

The theoretical spectra also show that the frequency and the width of the beating peak depend on the pumping rate and more importantly on the spin flip rate. To illustrate this, we plot the evolution of the peak frequency in Fig 5.13a and the peak width in Fig 5.13b both as a function of the pump rate, and for several γ_s values. The first figure shows that the peak frequency decreases with the pump rate increase. This is due to the phase-amplitude coupling effect, because higher pumping rate implies higher laser intensity, and thus larger induced phase shift (frequency pulling). However, the intensity increase alone cannot explain this effect, because the beat represents the frequency difference between the two $Lp-x, Lp-y$ modes, thus if the intensity of each mode grows at the same rate with the pumping, the frequency difference should stay constant. In fact, the variations of Δf_b we

Parameter	Config 1 (HR)	Config 2 (OC)
$\gamma_c (10^6 \text{ s}^{-1})$	35	130
α	3	3
$\gamma_a > 0$	0.05/2	0.17/2
$\gamma_p < 0$	-4.4	-1.18
γ_e	28.7	7.7
γ_s	$\in [5 - 25]$	$\in [5 - 25]$
ε	8.6×10^{-17}	2.3×10^{-17}
$\mu_p < 2 \varepsilon$	~ 0	~ 0

Table 5.3: VECSEL parameters used in the SFM dynamics simulations.

Figure 5.12: Theoretical noise spectrum, showing polarization modes beating and superimposed with experimental one. The used parameters correspond to 'Config 1' in table 5.3, the pump rate $\eta = 4$.

observe here are due to the dynamical phase shift ($\Delta\nu_s$), caused by the imbalance between the spin reservoirs. As can be seen from the curves, when γ_s is low this dependence is more pronounced. This is explained by the fact that the mixing of the populations with opposite spins is slow, which implies that the imbalance between the reservoirs is maintained. On the other hand, when γ_s is high the mixing is fast, the imbalance decreases and Δf_b variation with η is slower. We note that all the curves in Fig 5.13 coincide at the $\eta = 1$, because this dynamical effect is null at the threshold, and can be neglected close to it as we did by neglecting ν_s in Eq 5.5.

The second figure (5.13b) shows us that the peak width is also dependent on the spin-flip rate. This effect results from fluctuation due to the mixing (γ_s), and the Langevin forces on each reservoir (χ_+ , χ_-). From the figure we notice that peak width is larger for large values of γ_s . This can be understood as follows: for small values of γ_s the mixing of the spin reservoirs is slow, thus each circular component 'burns' carrier from its own reservoir separately, the extreme case when $\gamma_s \rightarrow 0$ would be equivalent to having two separate lasers, each one with its own noise source.

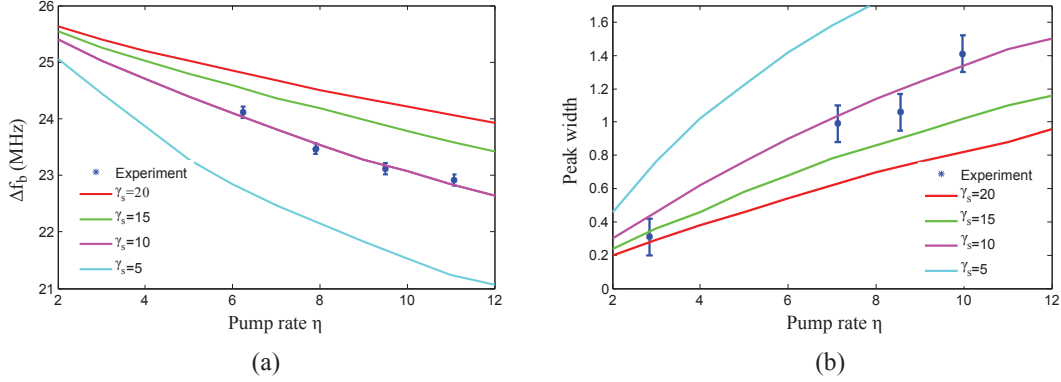


Figure 5.13: Variations of the polarization beating peak’s frequency (a) and width (b) as a function of the pump rate for several spin-flip rate γ_s values, the curves in both figures are superimposed with experimental ones in order to extract γ_s value of our quantum wells.

Pump rate η	PER (measured)	PER (simulated)	PER from Eq 5.9
2	-68.8 ± 5.1	-71.7	-71
6	-85.7 ± 5.9	-84.8	-82

Table 5.4: Comparison of theoretical and measured polarization extinction ratios PER.

On the other hand, for large values of γ_s due to fast mixing, the two circular components has almost to share the same carrier reservoir ($N^+ \simeq N^-$), the coupling via γ_s gives rise to a correlation between E_+ and E_- noises, which results in a smaller peak width.

The experimental results that we have superimposed with theoretical curves in these two figures, allow to support these explanations. Furthermore, they enable us to estimate γ_s in our QW-based structures. From Fig 1.15a,b and by taking $\alpha_h = 3$ one obtains $\gamma_s \simeq 10$ which means that the spin flip time is:

$$\tau_s = 1/(\gamma_s \gamma_e) \simeq 190 \text{ ps} \pm 40 \text{ ps} \quad (5.28)$$

We can also estimate the polarization extinction ratio PER from the theoretical spectra, in table 5.4 we show calculated values compared with measured ones and also with PERs obtained using the analytical expression given in Eq 5.9. The three values are in good agreement.

5.4 Generation of controlled circular polarization with electronic spin transfer

5.4.1 Preparing the cavity eigenstate

To prepare the laser cavity for circular polarization generation, the basic idea is to eliminate the linear anisotropies and introduce circular ones. For this purpose, we build a laser cavity in which we compensate the linear birefringence and dichroism, and introduce a circular birefringence using a Faraday rotator, and a circular dichroism using preferential pumping of one spin reservoir.

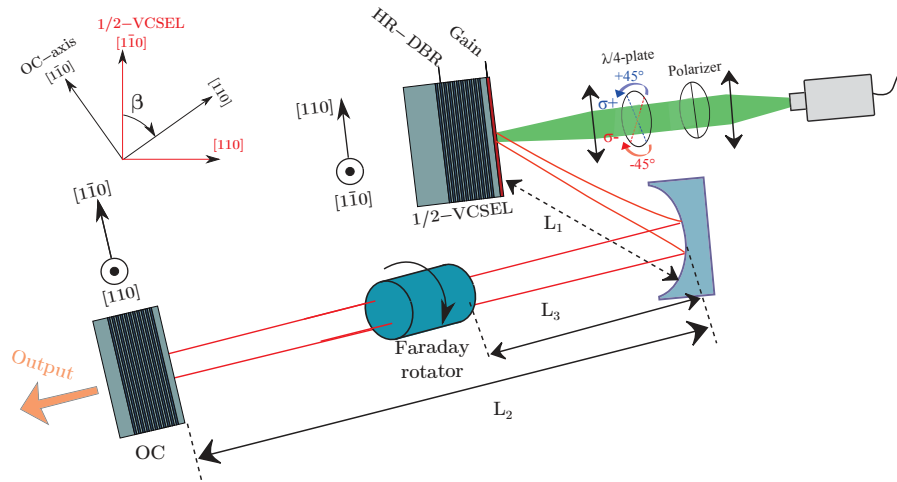


Figure 5.14: Schematic of V-shaped Spin-laser cavity.

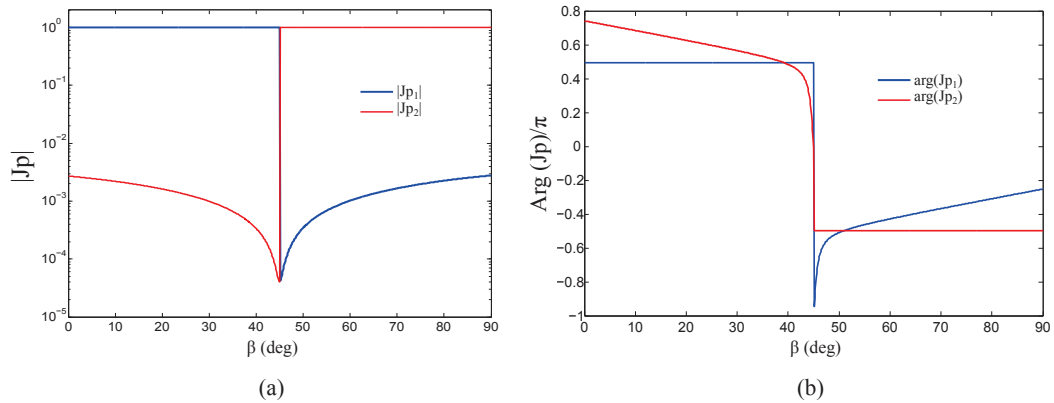


Figure 5.15: Polarization eigenstates of the Spin-laser cavity (a) the absolute value of the complex eigenvector components, and in (b) their argument.

We use the VCSEL cavity scheme depicted in Fig 5.14, the laser is based on the 1/2-VCSEL structure described previously (Gas680) with an anti-reflective coating in a V-shaped cavity with a total length $L_c = 40$ cm. The folding concave mirror is put at a distance L_1 close to its focal length, by doing so we obtain a collimated

beam in the second cavity arm, where we put a Faraday rotator to introduce circular birefringence. However, one must carefully chose the focal length of the mirror in order to ensure that the size of collimated beam is smaller than the aperture of the Faraday rotator. We used a folding mirror with a radius of curvature $R_c = 10$ cm, put at $L_1 = 54$ mm with a folding angle of ~ 5 deg. This results in a mode waist on the 1/2-VCSEL surface of $36 \mu\text{m}$ and a beam waist at the Faraday rotator $w_f = 0.75$ mm.

In order to compensate the birefringence effect inside the cavity, we designed and fabricated a semiconductor structure similar to the 1/2-VCSEL but without the active zone, and with less Bragg pairs (20 instead of 27). It is Gas620 shown in Chap 2 (Fig 2.21 on page 65). We used this structure as an output coupler that we placed in the cavity by orienting its $[110]$ ($[1\bar{1}0]$) crystal axis with an angle β with respect to the $[\bar{1}10]$ ($[110]$) axis of the 1/2-VCSEL.

If we assume that the 1/2-VCSEL and the Bragg mirror have similar birefringence values, the two linear polarizations Lp_{-x} and Lp_{-y} will experience the same optical path in this cavity when $\beta = 0$. We reduced the gain dichroism by using an elliptically shaped spot pump (see Sec 5.2.2) and by operating at low carrier density (low optical loss, see Fig 5.3). The 1/2-VCSEL is pumped optically using a pump diode followed by a polarizer and quarter-wave plate to obtain circular polarization, the handedness of the circular polarization can be changed by rotating the plate axis. The goal of using circularly polarized pump is to achieve preferential pumping of one spin reservoir (σ^+ or σ^-), thus for maximum photon-carrier spin transfer one has to set the beam pump at normal incidence with respect to the 1/2-VCSEL surface.

The eigenstates of this cavity depends on the orientation angle β of the Bragg mirror. We used Jones matrices to calculate them as a function of β . We plot the obtained result in Fig 5.15a,b. In the first one (a) we represented the absolute value of the eigenvector components, and its argument in the second figure (b). We note that we plotted the eigenvector of one circular polarization only, as the other one shows symmetric curves. When $\beta = 45$ deg, the curves show that the eigenstates are two circular components. But when β departs from 45 deg the eigenstates are slightly elliptical, as we notice the appearance of a small second component in the eigenvector module.

5.4.2 Experimental results and analysis

5.4.2.1 First observations

In the first step we set $\beta \simeq 45$ deg. Fig 5.16a shows the angular diagram of the VECSEL output power, we recorded this diagram by varying the angle of a polarizer placed between the VECSEL and a power-meter. The obtained curve is isotropic, which implies that the laser is either circularly polarized or totally unpolarized, to fully characterize the polarization state we used the scheme shown in Fig 5.17 to transform the right (left) circular polarization E_+ and E_- , respectively, using

5.4. Generation of controlled circular polarization with electronic spin transfer 183

a quarter-wave plate to Lp_{-x} (Lp_{-y}) linear polarization, and use a beam splitter to analyze both of them simultaneously. In the left axis of Fig 5.16b we plot the polarization-resolved output power as a function of the pump power of our VECSEL, and the right axis represents the Stokes parameter S_3 describing the degree of circular polarization. We notice a difference in the thresholds of E_+ and E_- , the first mode that start lasing is the one favored by the pump. When we change the handedness of the pump polarization, we observe a change of the handedness of the first mode to lase. Thus, near the threshold we can consider that a laser emit relatively pure circular polarization with a handedness controlled by the spin of the pump.

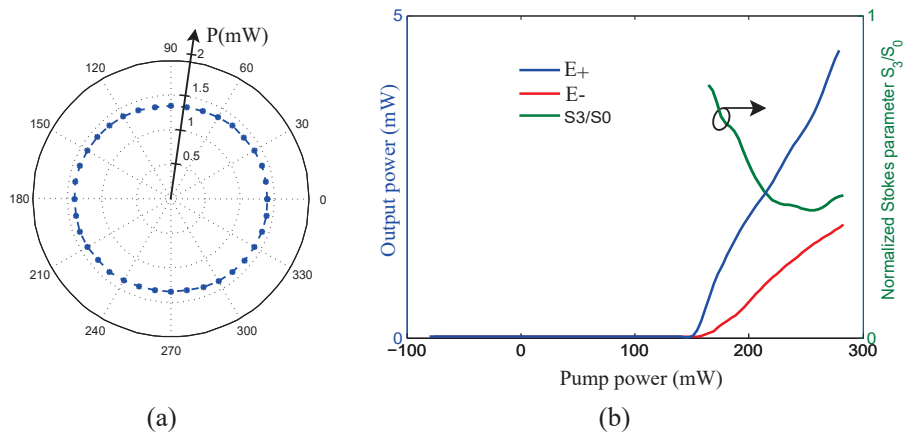


Figure 5.16: (a) Angular power diagram of the spin-laser output. (b) Polar resolved output power as a function of the pump power.

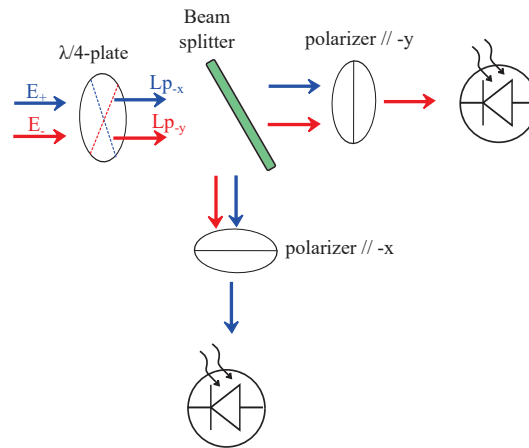


Figure 5.17: Experimental setup used to characterize circular polarization states emitted by the laser.

This observation is important, because it shows that even if the spin-flip mixing is relatively fast compared to the carrier relaxation rate ($\gamma_s/\gamma_e \simeq 10$, obtained in Sec 5.3.4.3), there is a residual imbalance between the two spin reservoirs that

creates a difference in the threshold. But the threshold difference is quite small which gives the desired spin-laser operation in a narrow region close to the threshold with a limited output power, and out of this region the two circular polarizations are lasing simultaneously which reduces the S3 parameter.

5.4.2.2 Perturbing the circular eigenstates to enable mode competition

The problem here comes from the fact that the two polarization modes are orthogonal in the laser cavity, in addition, each one has almost its own carrier reservoir, this is a typical case where two modes can coexist without competing as there is no cross coupling between them (see Sec 1.6). In order to address this problem we propose to slightly perturb the circular eigenstates so that the modes will be slightly coupled and would compete with each other. This can be achieved by re-introducing a small linear birefringence in the cavity, the modes will be slightly elliptical. This will force the two polarization components E_+ and E_- to share carrier from both reservoirs, and therefore, induce a competition between them.

We perform this by changing the orientation of the semiconductor output coupler to have a slightly elliptical eigenstates (see Fig 5.15), then we re-performed the measurements. The new polarization-resolved output power curves are shown in Fig 5.18. We notice the same behavior near the threshold, however, a little further we observe a sharp fall of the weak mode power that lasts to relatively high pump power. This is a typical behavior of a nonlinear coupling effect that requires high intensity to operate, the modes are now coupled and thus compete for the available gain, which results in an efficient mode selection with $PER > 24$ dB. We note that the selected mode still follows the spin of the pump.

We pushed the characterization of the generated light-state further to ensure that there are no other transverse or longitudinal effects disturbing the mode selection. First, we note that in all the measurements the laser operates in a single transverse mode, this is ensured by a careful pump-mode matching and a stable highly filtering cavity (due to the low Fresnel - number).

In Fig 5.19a we show the optical spectrum of the laser emission at high output power, we measured this spectrum using a Fabry-Pérot confocal spectrometer having a $FSR_c = 7.5$ GHz and a resolution of 60 MHz. We intentionally choose a region where the two modes coexist, in order simultaneously measure their spectra and the frequency splitting between them. The obtained spectrum shows that E_+ and E_- are separated by q times the laser cavity FSR : $q \frac{FSR}{2}$, with $q = 7$ in this measure. The $FSR/2$ is due to degeneracy lift introduced by the Faraday rotator and the integer q means that the two modes operate at longitudinal modes with different orders. We also measured the spectrum in the case of single polarization mode operation, as shown in Fig 5.19b the laser shows a single longitudinal mode operation with a $SMSR > 30$ dB.

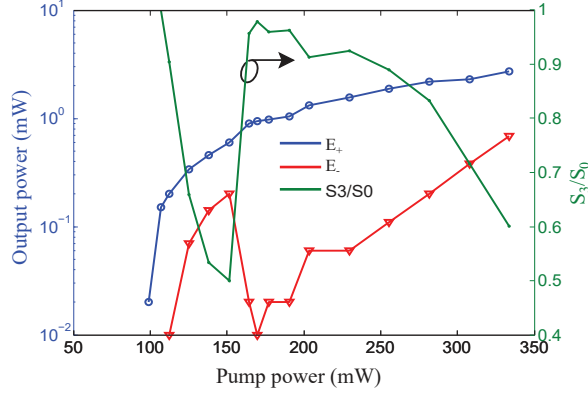


Figure 5.18: Left axis: measured polarization resolved output power of the spin laser with a perturbed cavity. Right axis: normalized S_3 Stokes parameter characterizing the degree of circular polarization.

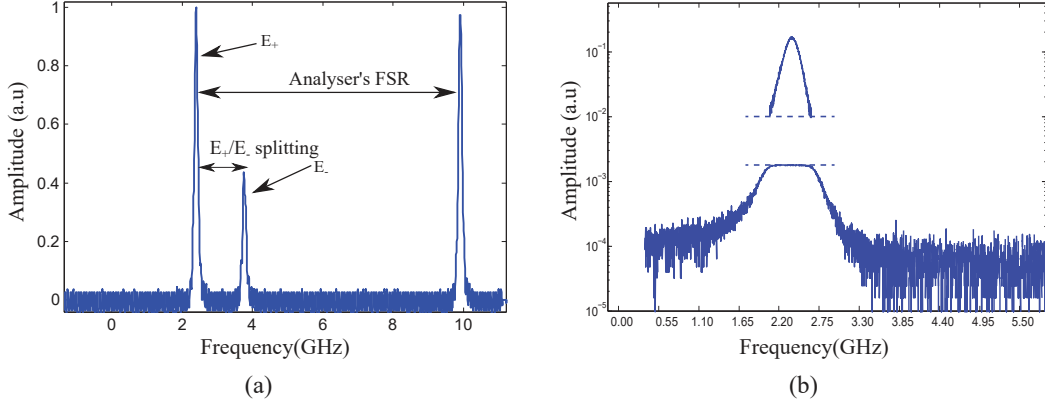


Figure 5.19: (a) Optical spectrum of the spin laser: (a) emitting two components E_+ , E_- having separate frequencies, (b) one component.

5.4.2.3 Mode dynamics: numerical results

We used the SFM equations to simulate the case of perturbed cavity, we choose the parameters to be the closest possible to the experimental conditions:

In the first step, to estimate the pumping rate of each spin reservoir, we take account of the carrier capture times in the quantum wells τ_{cap} (see Sec 2.4.2.2 and the spin flip rate in the quantum wells γ_s measured earlier in this chapter (Sec 5.3.4.3), and also $\gamma_{sb} \sim 50$ ps in the barriers, for $\tau_e \simeq 2$ ns. By doing so, one obtains a ratio of spin reservoirs' pumping rates $\eta_+/\eta_- \in [2.1 - 2.4]$. The total pumping rate being $\eta = \eta_+ + \eta_-$.

The linear dichroism is negligible (compensated), and we take the linear birefringence $\gamma_p = \pi \frac{FSR}{100}$ for a cavity length $L_c = 40$ cm, and the circular birefringence $\gamma_c = 2\pi FSR/2$ with $FSR = 380$ MHz.

We also take account of the multi-longitudinal mode behavior of the laser at startup, the spontaneous emission factor is then $\zeta = 1.5 \times \pi Q$ where $2Q$ is the number of

longitudinal modes in the gain curve, in our case $Q \simeq 37000$. We added this in order to check whether the irregularities in the measured power curve correspond to the multi-mode regime when the laser intensity builds up, and near the threshold. In Fig 5.20a we plot an example of E_+ , E_- temporal dynamics we obtained for a

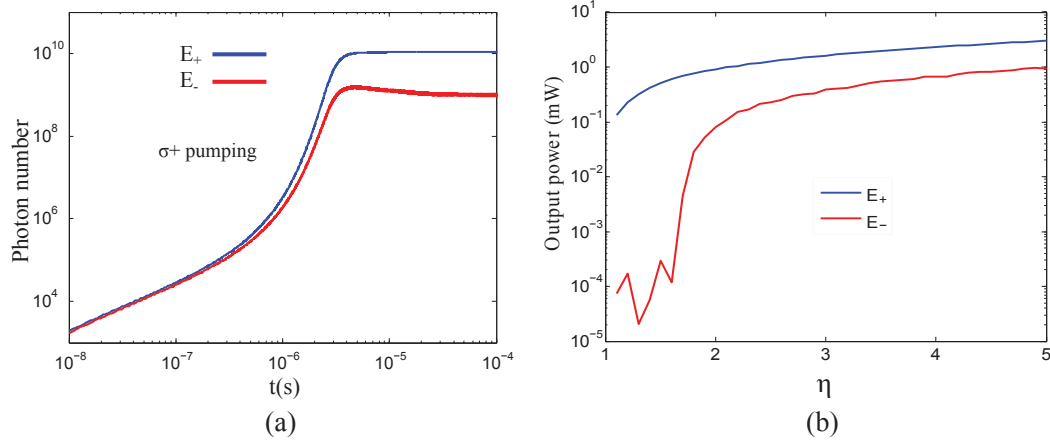


Figure 5.20: (a) Temporal dynamics simulation of circular E_+ , E_- polarization modes, obtained using the SFM at a pump rate $\eta = 2$. (b) Simulation of polarization resolved output power as a function of the pumping rate η for $\sigma+$ pumping.

pumping rate $\eta = 2$. In (b) we show a simulated evolution the polarization-resolved output power as a function of the pumping rate. The curve shows a difference in threshold between E_+ and E_- as expected, due to the preferential pumping and the imbalance maintaining thanks to a non-null spin-flip time. The weak component experiences some instabilities at the startup because of the multi longitudinal-modes regime. However, unfortunately the curves does no explain the non-linearity we observe in experiments.

5.5 Conclusion

The polarization state in lasers is determined by the anisotropies of the complex electric susceptibility, which are linear birefringence and linear dichroism, and /or circular birefringence and circular dichroism. The goal of this chapter was to study the effects of these parameters on polarization mode selection in VeCSELS.

We have shown how to measure the linear birefringence and the linear gain dichroism of QW-based 1/2-VCSEL structures. Then we have shown how to control both of them. We reduced the dichroism by using an elliptically shaped pump spot, this creates a strain anisotropy in the crystal that affects the carrier effective mass and thus the density of states. We have also presented two techniques to control the birefringence: the first one consists in using a birefringent integrated phase-mask based on a metasurface. The second technique is suited for the birefringence compensation, it consists in introducing a semiconductor mirror having a birefringence equivalent the 1/2-VCSEL one, and to use it as an output coupler.

The key point here was to orientate its fast axis parallel the slow 1/2-VCSEL one and vice-versa, by doing so, we compensates the optical paths of linear polarization components in the cavity.

In the second part we studied the polarization dynamics using the so-called spin-flip model. This model considers two carrier reservoirs coupled via the spin-flip rate. And each reservoir feeds one circular component of the cavity eigenstates $E_{+/-}$, and linear ones are obtained as a combination of them. This model allowed us to study the purity of linear polarization eigenstates that occur naturally in VCSELs thanks to the intrinsic linear birefringence and dichroism of the gain mirror. Because the laser emission contains two linear components: a dominant one (favored by the gain dichroism) and a residual one, when we mix the two using a polarizer oriented at 45° we observe a beating peak close to quantum noise level. By linearizing the SFM equations and computing the spectrum of the output power, we obtained theoretical noise spectra that are in good qualitative and quantitative agreements with the measured ones. And by comparing them, we deduced the spin-flip rate in our QW's.

In the last part, we experimentally investigated the generation of circular polarization with a handedness controlled by the spin of electrons. For this purpose, we used a cavity where we compensated the linear anisotropies and introduced circular ones. The circular birefringence was introduced by means of a Faraday rotator, whereas the circular dichroism was introduced by asymmetrically pumping of spin reservoirs. But the problem here is that each reservoir feeds one polarization component. This corresponds to a situation when two modes can coexist, and the only effect we observed is a difference in threshold as if they were two separate lasers. To overcome this problem we modified the cavity eigenstates to become slightly elliptical, which means that it is a linear combination of (E_+ and E_-), by doing so each component burns carriers from its own reservoir principally but also from the other one with opposite spin. And as they share carriers now, they are expected to compete with each other for the available gain. Our experimental results have confirmed this effect, but theoretical results were not in good agreements. This will be one of the open questions to address in future work.

Structured laser light for self-mixing sensing

6.1 Introduction

The main goal of this chapter is to show novel sensing application capabilities, enabled by the unique properties of some of the exotic lasers developed in the previous chapters. For this purpose, we will demonstrate a self-mixing laser sensor that takes advantage of the helically phased beams to measure the rotational velocity in the transverse plane of the light axis, using the rotational Doppler effect . Furthermore, the high spatial coherence and low divergence ($< 1^\circ$) of the generated beams make them easy to manipulate and to be focused to spots $< 1\mu\text{m}$ using a standard commercial lens. And the high spatial coherence allows to do long-distance interferometric measurements .

The rotational Doppler effect has first been suggested by Poynting in 1909 [Poynting 1909] for circularly polarized light, then demonstrated experimentally for the first time in beams carrying SAM in 1936 by Beth et al [Beth 1936], then in beams carrying OAM in the microwave domain [Courtial 1998]. And very recently Lavery et al [Lavery 2013] experimentally measured this effect in petal-like LG laser beams when reflected by spinning objects. It is still a field of active research because of the growing interest in light carrying OAM, and momentum transfer to matter. In these reported works, this effect has been used in conventional velocimetry setup, which is particularly cumbersome in the rotational case because it requires beam transforming setup in addition to the interferometric one. The transforming devices also limits the power and the spatial coherence of the beam. One of the aims of the present work is to overcome these limitations, the key points of this chapter can be summarized as follows:

- Show that the rotational Doppler effect due to the AM of light can be detected using laser-feedback interferometry, which has never been done before.
- As the interference takes place inside the laser cavity, describe the relevant laser features required to successfully implement this new sensor, and analyze their impact on its performances.

In the first part of the chapter we briefly introduce the self-mixing technique and discuss its main advantages over conventional interferometric setups. Then we provide the simple coupled cavities approach, used in the literature to analyze

the laser behavior under feedback. We will use it to identify the parameters one should take into account when designing a self-mixing sensor. Then, we present our experimental demonstration of rotational Doppler effect using self-mixing in a vortex laser. We end this chapter by proposing another self-mixing sensor design for particle sizing. For this purpose we take advantage of the multi-lobe spatial structure of Hermite Gaussian beams, which, when is reinjected inside the laser cavity produces a temporal signal that contains a signature of the particle size.

6.2 Presentation and theoretical elements of Laser-self-mixing

6.2.1 Presentation of the method

Laser self-mixing, or laser feedback interferometry (LFI) is a phenomenon that occurs when a fraction of the emitted laser light is coupled back into the cavity and interferes with the lasing field. This effect is usually considered as a nuisance for the stability of the laser emission. It was identified, however, as a simple system to study nonlinear effects in laser dynamics [Kane 2005]. Depending on the relative amount of the reinjected power into the laser, the system undergoes different dynamic regimes. This effect can be studied using the Lang and Kobayashi equations [Lang 1980] which consist in laser rate equations with an additional delayed source term representing the feedback. This model is based on the assumption that the emitted laser light reenters the cavity after one round trip forth and back from a partially reflective target, and neglect additional reflections because of the strong attenuation.

The self-mixing interferometry is a well-established method for remote sensing applications [Giuliani 2002], it offers significant advantages compared to conventional schemes: First, the intensity modulation induced by the coherent interaction between the laser field and the reinjected one, can be several orders of magnitude higher. Second, the measurement scheme is much simpler and requires less optical elements, because the sensor is self-aligned, and the interference takes place and is amplified, inside the laser cavity. Third, the remote sensing information is carried by the laser emission and thus, can be picked-up anywhere in the optical setup including light emitted from the back facet of laser diodes.

This method has been used in several applications, such as the detection of small particles flow in fluids [Sudo 2007], real-time high resolution vibrometry [Sudo 2006], non-invasive cardiovascular pulse detection [Hast 2003] and highly sensitive profiling and imaging methods, such as the so-called laser optical feedback imaging (LOFI) [Lacot 2001]. More recent research works focus on adapting the source properties to enhance the sensor performances, for example [Columbo 2012] investigated theoretically the potential of self-mixing in a multi-transverse mode laser, and in [Zeng 2013] a dual frequency laser has been used to achieve nano-scale resolution displacement measurement.

After this brief presentation of the self-mixing method, it becomes clear that using it in laser source emitting structured light would allow to combine the advantages of the self-mixing and those of structured light presented in Chap 4. In the following we will briefly study the different feedback regimes. Our goal is to show how to identify them, the involved laser parameters and which regimes are the most suited for sensing applications.

6.2.2 Equivalent cavity model

To study the feedback regimes we will consider the backscattering target as a third mirror and analyze the resulting three mirrors Fabry-Perot cavity [Coldren 2012] (see Fig 6.1). This three mirror cavity is represented by an equivalent one, by

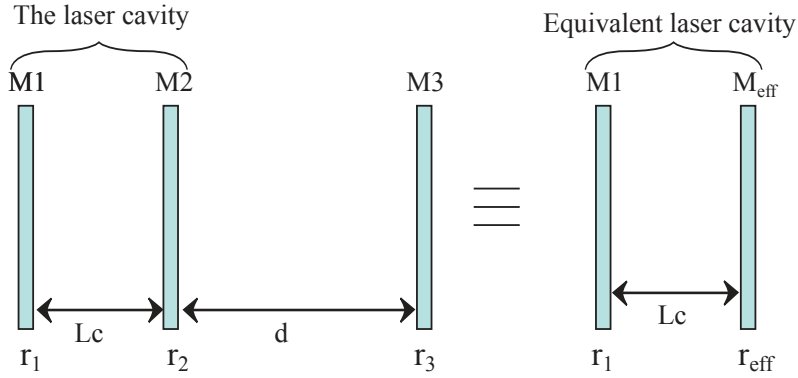


Figure 6.1: Equivalent effective cavity to model feedback in a laser cavity.

replacing the mirror M2 by an effective mirror having a complex reflectivity given by:

$$r_{eff} = r_2 + \frac{t_2^2 r_3 \exp(-2jkd)}{1 + r_2 r_3 \exp(-2jkd)} \quad (6.1)$$

where k is the wave-vector and d is the target distance, their product represents the feedback phase, which can be expressed as $\omega_c \tau$. Where ω is the pulsation of the laser field, and τ is the photon's roundtrip time between the two mirrors M2 and M3 (the target), r_i is the reflectivity of the mirror M_i , and $t_i = \sqrt{1 - r_i^2}$ its transmission. If we assume that ($r_3 \ll r_2$) we can neglect the multiple reflections effect and can get rid of the resonance term in Eq 6.1. One obtains the following reflectivity variation:

$$\Delta r_{eff} = t_2^2 \sqrt{\gamma_{ext}} \cos(2kd) \quad (6.2)$$

where γ_{ext} is the feedback reinjection rate, it is given in terms of the cavity decay rate γ_c and the effective parameter R_{eff} that represents the amount of the reinjected photons into the laser mode:

$$\gamma_{ext} = \gamma_c \sqrt{R_{eff}} \quad (6.3)$$

Because of the feedback, the phase angle of the net reflection at mirror M2 is different from zero, this changes the resonance condition of the cavity and thus, induces a frequency shift $\Delta\omega_\phi$. To this shift, one must add an additional one $\Delta\omega_N$ caused by the change in the laser threshold and phase-amplitude coupling in the gain medium. The total frequency shift is $\Delta\omega = \Delta\omega_N + \Delta\omega_\phi$, with:

$$\Delta\omega_\phi = -\gamma_{ext} \sin(\Delta\omega\tau + \omega_c\tau) \quad (6.4)$$

and

$$\Delta\omega_N = -\alpha\gamma_{ext} \sin(\Delta\omega\tau + \omega_c\tau) \quad (6.5)$$

After simplification The total frequency shift reads [Coldren 2012]:

$$\Delta\omega = \Delta\omega_N + \Delta\omega_\phi = -\gamma_{ext} \sqrt{1 + \alpha^2} \sin(\Delta\omega\tau + \omega_c\tau + \arctan(\alpha)) \quad (6.6)$$

Equation 6.6 cannot be solved for $\Delta\omega$ analytically, however one can solve it graphically in order to get approximate solutions, as we will do in the following section.

6.2.3 Feedback regimes

The feedback regimes are established according to the possible solutions of the phase-condition of Eq 6.6 as a function of the so-called feedback parameter C given by:

$$C = \gamma_{ext} \sqrt{1 + \alpha^2} = T \frac{d}{L_c} \sqrt{R_{eff}} \sqrt{1 + \alpha^2} \quad (6.7)$$

The solutions of Eq 6.6 represent the possible operation frequencies that satisfy the new phase condition. As illustrated in Fig 6.2 three different cases are possible:

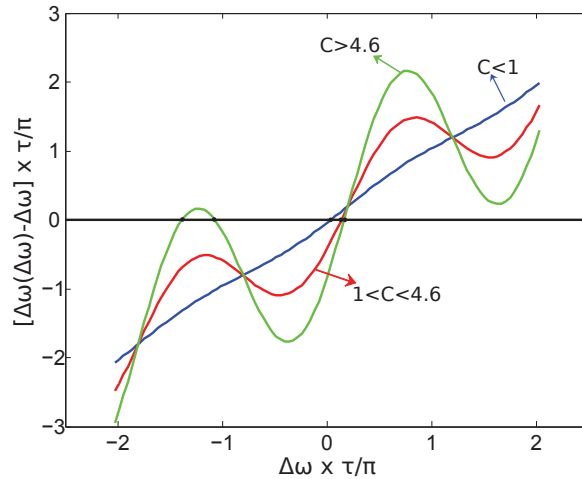


Figure 6.2: Graphical resolution of the transcendental frequency shift equation (Eq 6.6), the number of solutions determines the feedback regime.

- $C < 1$: This is the case of weak feedback regime, there is only a single possible frequency that satisfies the phase condition. The laser is stable and operates in a single longitudinal mode. It is the most suitable regime for sensing applications, because the spectral stability of the laser is very important in such applications. Furthermore, the laser response (modulation index) is linearly proportional to the amount of the backscattered power.
- $1 < C < 4.6$:¹ We are in the moderate feedback regime, the laser response starts to be distorted, but as there is always one possible solution. It is still possible to use the laser in sensing applications.
- $C > 4.6$: This is the strong feedback regime, in this case the laser loses its stability and enters in frequency-hopping regime, therefore, the feedback cannot be used for sensing applications. For higher C values the laser enters in a chaotic regime where the behavior becomes very hard to describe theoretically.

In our experiments we assume that we work in the weak feedback regime, this assumption is largely justified because we will be working with no cooperative targets².

6.2.4 Self-mixing for sensing applications

Laser self-mixing is mainly used in two sensing applications: displacement measurement and velocity measurement. These applications rely on different effects which we describe below.

6.2.4.1 Displacement measurement

Displacement measurement is achieved using the dependence of the effective reflectivity or the laser frequency on the target distance. According to Eq 6.2 and Eq 6.6, when the target moves toward or away from the laser, both the effective reflectivity r_{eff} and the laser frequency undergo a periodic modulation with a period of $\lambda/2$. Hence, by counting the number of periods, say N_{per} , one obtains the displacement $\lambda/2 N_{per}$ the target has made toward or away from the laser. For illustrative purpose, we carried out the experiment described schematically in Fig 6.3. We used a metallic mirror to reflect the laser light back into the cavity. The mirror is mounted on a piezoelectric actuator to make micro displacements. To analyze the laser frequency, we picked up a fraction of the laser beam using a beam splitter and analyzed it using a Fabry-Perot confocal, high resolution (60 MHz) spectrum analyzer.

The laser frequency behavior we observed is depicted in Fig 6.4: when we displace the mirror, the laser frequency is detuned continuously until the displacement

¹This value of C is determined graphically, it is the value for which Eq 6.6 admit more than one solution (3 for $C \simeq 4.6$).

²Also called Lambertian targets, which are targets that have a diffusely reflecting surface.

reaches $\lambda/2$, then it returns back to its initial position and redo the same movement periodically as predicted by Eq 6.6.

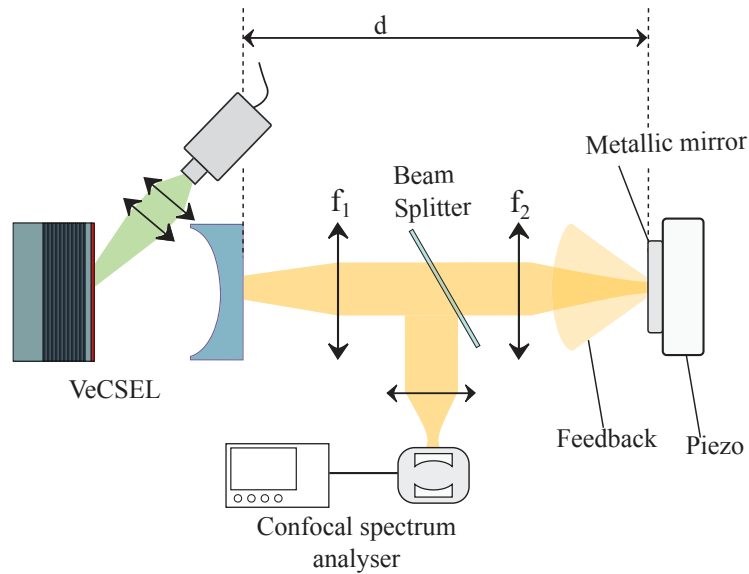


Figure 6.3: Schematic illustration of self-mixing displacement measurement setup.

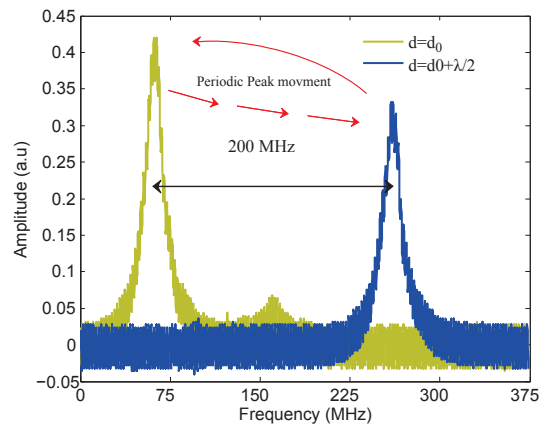


Figure 6.4: Measure of the laser frequency periodic variation under feedback from a moving target.

6.2.4.2 Velocity measurement

Velocity measurement using self-mixing, relies on the Doppler effect. Because the light backscattered by a moving target at a speed \vec{v} undergoes a Doppler frequency

shift Δf_l given in the case of self-mixing by¹:

$$\Delta f_l = \frac{\vec{v} \cdot \vec{p}}{\pi \hbar}, \tag{6.8}$$

where \hbar is the reduced Planck constant and $\vec{p} = \hbar \vec{k}$, is the momentum of photons, with $k = 2\pi/\lambda$. When the frequency-shifted feedback re-enters the laser cavity it causes a beating between the lasing field and the reinjected one at the frequency difference Δf_l . The laser output intensity is then modulated at Δf_l around its steady state value.

This measurement is achieved in the very weak feedback regime ($C \ll 1$). In this case the output intensity variation and laser frequency shift due to feedback ($\Delta\omega$) are assumed to be negligible. Thus the laser intensity is only modulated by the Doppler beating.

Again, for illustration, we took the previous setup and replaced the mirror by a rotating disk at an angular speed $\omega = 400$ rad/s, tilted by an angle $\alpha = 45$ deg with respect to the beam axis. This gives rise to a linear velocity component parallel to the beam axis of 0.6 m/s (see Fig 6.5). This linear velocity component causes a beating that modulates the laser intensity at $\Delta f_l = 1.2$ MHz as shown in Fig 6.6 where we represent the temporal signal in (a) and its spectrum in (b).

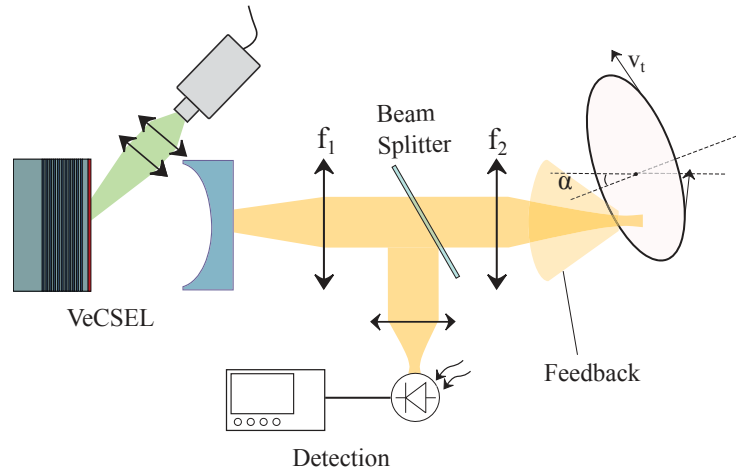


Figure 6.5: Linear velocity self-mixing measurement scheme.

6.2.5 How to choose a laser source for self-mixing

Now that we have introduced the self-mixing effect and defined some of the parameters involved in it. One can discuss the self-mixing sensing potential of some existing laser systems. We will consider three properties: (1) the robustness under feedback; (2) the frequency transfer function; (3) the intensity noise. The importance of the

¹In the case of self-mixing as in radars, because the Doppler shift affects the wave incident upon the target as well as the wave reflected back to the source, the change in frequency observed by the source is twice that from the same target emitting a wave.

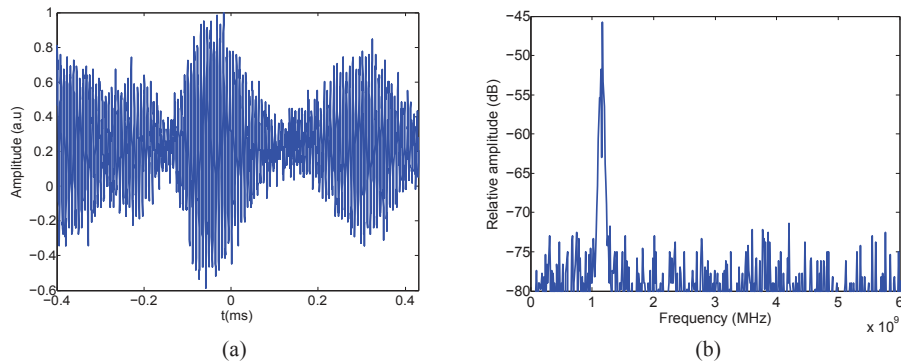


Figure 6.6: (a) Temporal Doppler beating of the laser intensity. (b) Spectrum of the laser intensity showing the Doppler beating peak.

robustness is obvious, if the laser enters in a chaotic regime under feedback it becomes unusable for sensing applications. The frequency transfer function is the second important parameter, because it indicates how the laser will respond to a modulation at a given frequency. Due to the decay rate of the cavity, this response takes the form of a low pass filter, the cutoff frequency will set then, a maximum allowed beat frequency. Last and not least, the intensity noise level determines the minimum detectable beat amplitude.

According to Eq 1.15 the C parameter depends upon the laser cavity decay rate, the target distance and effective reflectivity. This means that for the same target and at fixed distance, different lasers may behave differently. Laser diodes are the most affected by the feedback, because of the high decay rate of their cavities, sometimes using laser diodes requires variable attenuators to ensure that the reinjected power is always in the supported range. Attenuators usually consist of LCDs with an electronic control circuit. Monolithic VCSELs are slightly less affected, followed by DFBs, however, in the latter the C parameter depends strongly on the coupling factor of their Bragg reflector. These three laser families have a cutoff frequency of the order of ~ 1 GHz which allows to measure relatively high velocities, but the transfer function is not flat because of the oscillation relaxations (class-B). Lasers with higher finesse cavities such as DPSSLs and VECSELs are more robust under feedback. These sources present a better stability under relatively high levels of back-reflected power, which permits to get rid of variable attenuators. VECSELs present a relaxation-oscillation free dynamics, with a flat transfer function and a cutoff frequency that can go from <1 MHz to more than 100 MHz. DPSSLs however, present a class-B dynamic behavior and a relatively low cutoff frequency because of the low carrier decay rate in the gain medium.

However, in the case of displacement measurement lasers that show high robustness under feedback are not the best choice. Instead, laser sources that are highly sensitive to feedback such as laser-diodes and monolithic VCSELs are ideal candidates because they allow lower detection threshold. But in the case of velocity measurement, the ultimate sensitivity is determined by the noise properties of the

laser, therefore robust sources with low intensity noise are candidates of choice.

6.3 Article :Self-mixing in low noise semiconductor vortex laser: detection of rotational Doppler shift in backscattered light

In the following section we present a paper dedicated to rotational velocity measurement using self-mixing in a vortex laser. The paper introduces the rotational Doppler effect, and gives the state of the art of experimental and theoretical studies related to this effect. Exploiting beams carrying OAM in sensing applications is still in its infancy and clearly arouse a growing interest, indeed, at the time of this writing several working papers are released by researchers such as [Rosales-Guzmán 2015, Berg-Johansen 2015]. Then, the second part presents very briefly the self-mixing method and its characteristic quantities.

In the experimental part we use a VECSEL integrating a flat-photonics element to select a vortex beam as shown in Chap 4. The beam is focused onto a rotating target, the back-scattered light undergoes then a frequency shift and causes a beating that we measure in the relative intensity noise of the laser. This measurement can be achieved with both small ($\sim \lambda$) and large ($\gg \lambda$) targets. At the end we discuss the sensitivity of the sensor and present some prospects.

This demonstration is of special interest in advanced sensing applications such as turbulence analysis. And open the path to other new applications, for example when using the vortex laser as an optical tweezer that applies a torque on a particle in order to rotate it, the angular speed of the particle depends on the beam energy, and also on the characteristics of the surrounding medium such as its viscosity. Thus as the beam energy is usually well known, one can instantly obtain the characteristics of the surrounding medium by simultaneously measuring the particle velocity while tweezing it.

Self-mixing in low noise semiconductor vortex laser: detection of rotational Doppler shift in backscattered light

Mohamed Seghilani¹, Mikhal Myara¹, Isabelle Sagnes², Baptiste Chomet¹, Ryad Bendoula³,
and Arnaud Garnache^{1,*}

¹*IES, CNRS UMR 5214, Univ. Montpellier, 34000, Montpellier, France*

²*Laboratoire de Photonique et Nanostructures, CNRS-UPR 20, Marcoussis, France*

³*Irstea UMR ITAP, 361 rue J-F Breton BP 5095, 34196 Montpellier Cedex 5, France*

**Corresponding author: arnaud.garnache@ies.univ-montp2.fr*

Author manuscript. Accepted for publication in Optics letters, doc. ID 249927

Abstract

Light carrying orbital angular momentum \vec{L} , scattered by a rotating object at angular velocity $\vec{\Omega}$, experiences a rotational Doppler shift $\vec{\Omega} \cdot \vec{L}$. We show that this fundamental light-matter interaction can be detected exploiting self-mixing in a vortex laser under Doppler shifted optical feedback, with quantum noise limited light detection. We used a low noise relaxation oscillation free (class-A) vortex laser, based on III-V semiconductor vertical-external-cavity-surface-emitting-laser technology, to generate coherent Laguerre-Gauss beams carrying $L = \hbar l$ ($l = \pm 1, \dots, \pm 4$). Linear and rotational Doppler effects were studied experimentally and theoretically. This will allow to combine a velocity sensor with an optical tweezer for micro-manipulation applications, with high performances : compact, powerful $\gg 10$ mW, high quality beam, auto-aligned, linear response up to $> 10^8$ rad/s or > 300 km/h, low back-scattered light detection limit $< 10^{-16}$ /Hz.

The main text

In addition to carrying linear momentum ($p = \hbar k$), light carries two kinds of angular momenta (AM) : spin AM (SAM) $S = \hbar \sigma$ associated with circular polarization ($\sigma = \pm 1$), and orbital AM (OAM) $L = \hbar l$ of charge l . OAM is carried by vortex beams with helical wavefront and a doughnut-like shape intensity profile, with a dark core and phase singularity at the beam center[1]. Light carrying OAM has been extensively studied during the last two decades leading to a widespread new applications in different fields: telecommunications [2], micro-manipulation [3], microscopy [4] and astronomy[5].

Among new effects related to AM, the fundamental light-matter interaction leading to rotational Doppler shift has been first studied decades ago in beams carrying SAM [6], then OAM in microwave domain [7]. When light carrying AM is scattered by rotating objects at angular speed $\vec{\Omega}$, it experiences a rotational Doppler shift Δf_r given for back-scattered wave by [7]

$$\Delta f_r = \vec{L} \cdot \frac{\vec{\Omega}}{2\pi}. \quad (1)$$

in analogous way as linear Doppler shift given by scalar product of linear velocity \vec{v} and \vec{p} by [7]

$$\Delta f_l = \frac{\vec{v} \cdot \vec{p}}{\pi \hbar}. \quad (2)$$

Recently, light OAM properties in a "petal"-shaped beam carrying no OAM, has been exploited to measure the angular velocity of a spinning disk [8], and of a micron-sized particle [9] at low light sensitivity, in a traditional complex, low power, and bulky free space scheme with reduced spatial coherence. Usually, OAM beam is generated externally using transforming optics like spatial light modulators. However, using coherent vortex beams directly generated from a laser source [10], overcomes the previous limitations and allows to develop compact combined auto-aligned sensitive speed sensor and powerful optical tweezers/trap. It is the goal of this work.

We demonstrate for the first time to our knowledge, that the rotational Doppler shift in light backscattered from spinning particles can be detected, together with linear one, using self-mixing in a vortex laser carrying $L = \hbar l$, with quantum noise limited light amplitude detection. To reach this goal, we take advantage of a patented [11] low noise vortex laser design generating highly coherent diffraction limited Laguerre–Gauss (LG) beams, and exhibiting relaxation oscillations-free dynamics (class-A) [12]. It is based on compact and powerful III-V semiconductor Vertical-External-Cavity-Surface-Emitting-Laser (VECSEL) technology, integrating flat photonics [13, 14]. Thanks to band-gap engineering and wafer bonding technology, VECSELs allow wide wavelength coverage and power scaling to multi-Watt level [13]. The efficiency is as high as for solid-state-lasers, with a design free of thick intracavity element. A vortex solid-state-laser has been demonstrated [10] in pulse regime only, unsuitable for self-mixing application.

In self-mixing, the laser source acts as a sensitive sensor: a fraction of the emitted light is backscattered by a moving target and re-enters the cavity (Fig. 1(a)). The resultant laser dynamics can be analyzed using compound cavities model, where the remote target is considered as a third mirror with an effective reflectivity $R_{\text{eff}} \ll 1$ that represents the amount of back-coupled ballistic photons into the laser mode. The level of feedback is characterized by the so-called feedback coefficient C given by the well established Lang-Kobayashi model [15, 16]

$$C = \gamma_{\text{ext}} \tau \sqrt{1 + \alpha^2} = T \frac{d}{L_c} \sqrt{R_{\text{eff}}} \sqrt{1 + \alpha^2}, \quad (3)$$

where $\alpha \simeq 3$ is the linewidth enhancement factor, which characterizes the phase-amplitude coupling in semiconductor gain media [16], $\tau = 2d/c$ is the photon round-trip time between

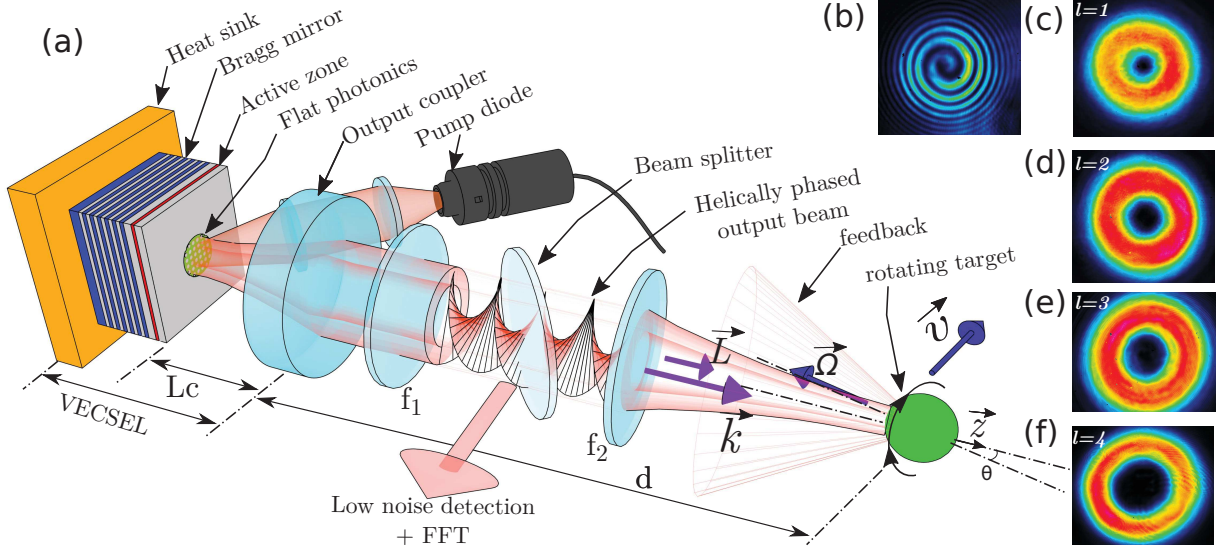


Figure 1: (a) Self-mixing rotational Doppler shift measurement scheme, using a coherent optically pumped VECSEL. $L_c=1$ mm, $d=50$ cm, $f_1 = f_2 = 50$ mm achromatic lenses. (b) Spiral interference fringes of the output VORTEX beam with a reference plane wave (Mach-Zehnder interferometer), showing the presence of OAM. (c-e) Spatial intensity profiles of beams with $l = 1, 2, 3, 4$.

the laser and the target, and $\gamma_{ext} = \gamma_c \sqrt{R_{eff}}$ is the feedback re-injection rate. It depends on the cavity decay rate $\gamma_c = cT/2L_c$. T represents the transmission losses, L_c and d are the cavity length and the target distance respectively.

Remote sensing applications rely on very weak feedback regime ($C \ll 1$), obtained when working with non-cooperative targets as in our experiments ($C \sim 10^{-5}$). In this linear regime the laser output power P is modulated at the heterodyne RF frequency $f = \Delta f$ as follows [17]

$$P = P_0[1 + m(f) \cos(2\pi ft + \phi)], \quad (4)$$

where P_0 is the average output power, and ϕ an additional phase term related to the target distance. In class-A lasers ($\gamma_c^{-1} \gg \tau_e$ the carrier lifetime) the modulation index m [17] is proportional to $\sqrt{R_{eff}}$ and reads as

$$m(f) = 2\sqrt{\frac{R_{eff}}{1 + (f/f_c)^2}} \left(\frac{\eta}{\eta - 1} \right), \quad (5)$$

$m(f)$ defines the sensor frequency response (1st order low pass filter), where η is the pump rate, and $f_c = \gamma_c/2\pi \times (\eta - 1)/\eta$ denotes the cutoff frequency [13], it defines the maximum range of measurable frequencies, thus velocities Ω and/or v . Self-mixing interferometry is possible for $2d$ shorter than the laser coherence length, and being a homodyne detection, speed resolution is not limited by the laser coherence as in conventional Doppler velocimetry.

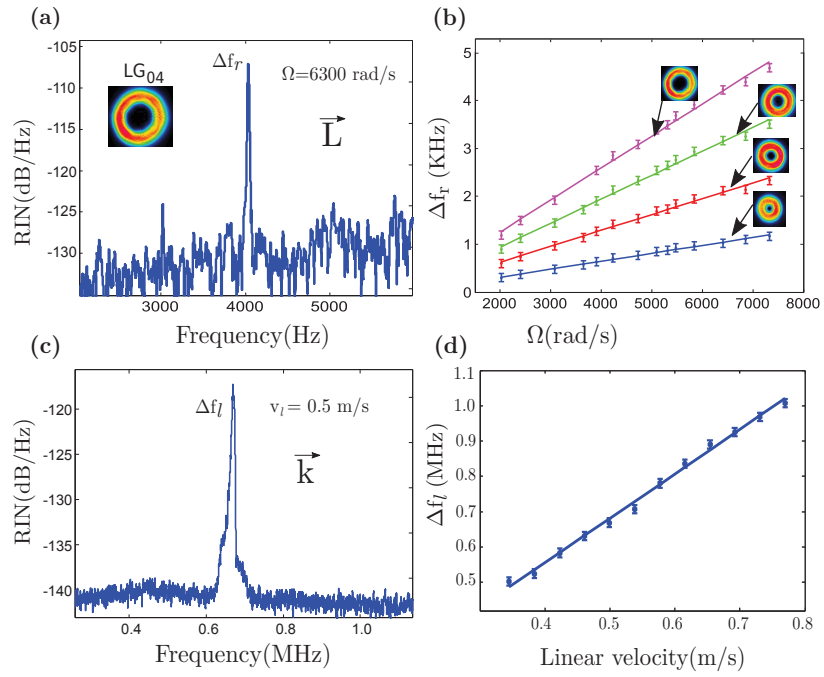


Figure 2: (a) Measured Relative-Intensity-Noise RF spectrum of the vortex laser output power under feedback, backscattered from a rotating target; resolution bandwidth $\delta f = 10$ Hz. The beam OAM charge is $l = 4$. (b) Doppler shift frequency Δf_r as a function of angular velocity, using OAM beams with charges $l = 1, 2, 3, 4$ (bottom to top). (c, d) Measurement of translational Doppler shift using the same sensor set-up. The linear velocity is obtained with a tilted rotating disc at $\vec{\Omega}'$ and given by $v_z = \Omega' . r . \sin(\theta)$. Solid lines in (b, d) represent theoretical curves according to Eq. (1) and Eq. (2), respectively.

Fig. 1(a) shows the experimental set-up. We built an optically pumped VECSEL generating a coherent controlled vortex beam [11], emitting in cw at $1\ \mu\text{m}$ at 300 K. It is formed by a few λ thick GaAs-based gain mirror and a concave dielectric output coupler ($T = 1\%$) separated by mm-length air gap ($L_c = 1\ \text{mm}$). It defines a stable cavity of high axial symmetry, supporting the LG_{pl} mode basis [12]. The 1/2-VCSEL gain mirror structure contains a high reflectivity (99.95 %) AlAs/GaAs Bragg mirror epitaxially grown on [001] GaAs substrate, and 6 strain-balanced InGaAs/GaAsP/GaAs quantum wells, ensuring a homogeneous gain. A low noise 808 nm single mode GaAs commercial diode laser is used for pumping, on a $90\ \mu\text{m}$ spot diameter, with an incidence angle of 70 deg. The gain mirror integrates a sub-wavelength absorbing metallic mask, that introduces high loss in the dark-core and periphery of the LG_{0l} vortex mode, to control its charge $|l|$. Then a 2D sub-wavelength grating introduces an asymmetric perturbative spiral phase element in the donut mode (total phase shift $\sim 2\pi/4000$) to select its handedness $\pm l$ (see Ref [11, 14] for more details). $|l|$ is varied by changing the cavity beam waist with L_c [12]. The obtained modes intensity profiles are shown in Fig. 1(b-e) with typical output power of 20 mW, limited by pump power, and a typical efficiency of 25% – 20% for $|l| = 1 - 4$, respectively.

This laser demonstrates important features for self-mixing operation together for optical trapping : it generates a powerful highly temporally and spatially coherent LG_{0l} beam, with a quality factor $M^2 < 1.2(l + 1)$ and a low divergence $\theta < 2$ deg. These diffraction limited beams are easy to manipulate and focused to spots $< 500\ \text{nm}$ using a standard commercial high NA microscope objective. Here, light polarization is linear along [110] crystal axis ($\sigma = 0$) [13], with measured orthogonal-axis suppression ratio $> 60\ \text{dB}$. The vortex laser is illuminating a 2 mm width target at distance $d = 50\ \text{cm}$ using an achromatic lens f_2 . The target consists of quasi-hemispherical unpolished metallic rotor head, of high speed motor rotating at $\Omega = 6300\ \text{rad/s}$. A beam splitter takes a fraction of the emitted light (20%), which is focused on a low noise detector. The photocurrent is analyzed using an FFT analyzer (resolution bandwidth $\delta f = 10\ \text{Hz}$). Figure. 2(a) shows the power spectrum for a laser emitting an OAM charge $l = 4$ under feedback. One sees a clear beat note at the rotational Doppler shift frequency $\Delta f_r = 4.03\ \text{kHz}$ (FWHM=10 Hz) given by Eq. (1) ($\pm 40\ \text{rad/s}$ motor stability limited). The typical measured relative backscattered power is $R_{\text{eff}} \simeq 1.5 \times 10^{-12}$.

We varied the rotation speed Ω , and repeated the experiments using vortex lasers with different OAM charges ($l = 1, 2, 3, 4$). Figure. 2(b) plots the obtained laser sensor response. All the curves verify the relationship given by Eq. (1) (solid lines in the figure), and self-mixing equation Eq. (4). The same scheme is used to measure the linear Doppler shift. This is of great interest for applications where simultaneous measurement of rotational and linear Doppler shifts is needed, such as turbulence analysis. We used a target having linear velocity component along the laser axis, that causes a Doppler shift as shown in Fig. 2(c,d). The curve satisfies the linear Doppler shift relation (Eq. (2)).

This measurement system is dynamically stable and exhibits a linear and flat frequency response up to the cut-off frequency f_c , as predicted by Eq. (5) : these properties stem from Class-A dynamic regime of VECSEL. Furthermore, the low-intensity noise operation of the laser confers to the sensor a close to quantum-limit noise capability (+3 dB) in terms

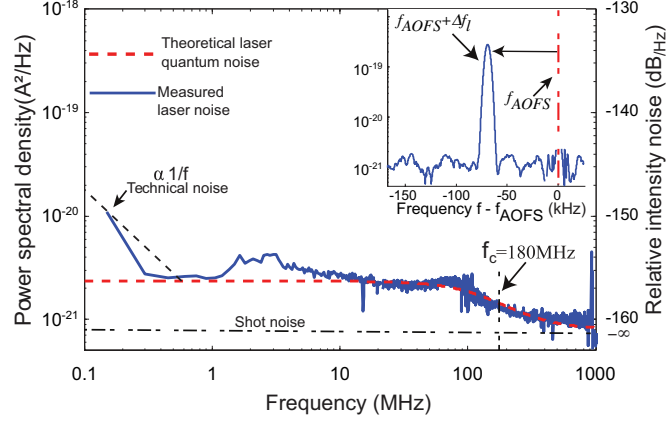


Figure 3: Measured relative intensity noise RF spectrum at laser output. Average photocurrent $\langle I_{ph} \rangle = 3$ mA; resolution bandwidth $\delta f = 150$ kHz (6 kHz for inset). Laser frequency cutoff f_c , theoretical quantum noise [16, 13], and $1/f$ technical noise are depicted. The inset shows linear velocity measurement of a Lambertian target (albedo $\simeq 0.6$) at a distance $d = 10$ m moving off the laser at a speed of $v = 3.5$ cm/s, where the laser frequency is shifted by $f_{AOFS} = 220$ MHz using an AOFS.

of back-coupled light amplitude detection. Indeed, the intensity noise is a key parameter, because it defines the limits of sensitivity and measurable frequency range. Both of these limits can be obtained straightforwardly by measuring the relative intensity noise spectrum of the laser (RIN), which characterizes the noise power spectral density of the laser output power normalized to P_0^2 [16]. We measured the RIN using a RF spectrum analyzer. The experimental RIN is shown in Fig. 3 superimposed with theoretical one calculated from references [16, 13]. The laser RIN exhibits a cut-off frequency $f_c \simeq 180$ MHz (dot-dashed vertical line) which allows to measure angular speeds up to $\Omega = 180 \times 10^6$ rad/s and translational velocities up to $v = 320$ km/h (at $\lambda = 1 \mu\text{m}$). The light sensitivity limit is given by the ratio of RF power spectral density $\langle S^2 \rangle$ of Doppler beating signal to laser noise spectral density $\langle N^2 \rangle$. By writing $\langle S^2 \rangle$ from Eq. (4) and $\langle N^2 \rangle$ in terms of RIN [13] one obtains

$$S^2/N^2 = \frac{4 R_{\text{eff}} P_0^2 \left(\frac{\eta}{\eta-1} \right)^2}{\pi \delta f (RIN P_0^2 + 2h\nu P_0) \varepsilon}, \quad (6)$$

where ν is the laser light frequency, δf the detection bandwidth, and $\varepsilon = 1 \pm 1/\sqrt{2N_{\text{acq}}}$ is the power density estimation error when averaging over N_{acq} averages.

In the kHz domain, the RIN is dominated by pump induced $1/f$ technical noise [13] (Fig. 3), which defines a minimum detectable effective reflectivity in our experiments $R_{\text{eff}}/\delta f \sim 10^{-15} \text{ Hz}^{-1}$. The laser RIN can be reduced by using a closed-loop control system on the pump-diode. The sensitivity will then be asymptotically limited by quantum noise N_Q due

to spontaneous emission. The S/N_Q [13, 16, 17] can be written for $\eta \gg 1$ as

$$S^2/N_Q^2 \simeq \frac{2 R_{\text{eff}} P_0}{\delta f h\nu(\xi + \pi)\varepsilon}, \quad (7)$$

where $\xi \simeq 1.4$ is the ratio of the spontaneous-emission rate into the laser mode to the stimulated-emission rate per photon. In this case, $R_{\text{eff}}/\delta f$ could be as low as $4 \times 10^{-17} \text{ Hz}^{-1}$ for 10 mW. Alternatively, one can use a low noise frequency shifter to move the Doppler peaks to higher frequency region in the MHz range [17] in order to get rid of $1/f$ noise and reach the quantum limit, this way one can also determine the sign of velocity vector. We tested this configuration using a commercial acousto-optic-frequency-shifter (AOFS) of high spectral purity ($< 1 \text{ Hz}$) operating in the MHz range, which allowed us to reach the quantum limit specified above. The AOFS is placed after the first lens f_1 , and f_2 is removed. We used a collimated beam (Rayleigh length $\simeq 20 \text{ m}$) and a lambertian target (albedo $\simeq 0.6$), at a distance $d = 10 \text{ m}$ and moving off the laser at low speed ($v = 3.5 \text{ cm/s}$). As shown in the inset of Fig 3, this gives a Doppler beat note that departs from the AOFS frequency (here $f_{\text{AOFS}} = 220 \text{ MHz}$) by $\Delta f_l = -70 \text{ kHz}$.

This sensitivity limit is valid below the laser coherence length. Unlike laser diodes, where this length is limited by quantum noise at short distance of few meters, here the coherence length is of the order of 10 km limited by technical noise [13], whereas the fundamental quantum limit is larger than 90 000 km, which is of great interest for long distance telemetry.

The work presented here is a generalization of Doppler-feedback interferometry to rotational case. We demonstrated that both rotational and linear Doppler shifts present in light backscattered from spinning objects, can be measured using self-mixing in a vortex laser. We used highly coherent diffraction limited LG beams carrying OAM with controlled charges $l = \pm 1, \pm 2, \pm 3, \pm 4, \dots$. These beams were generated using a class-A III-V semiconductor VECSEL source: this technology is clearly interesting for integration (industry ready). This confers to the sensor a linear response and broad measurable angular velocity range up to $\Omega = 10^8 \text{ rad/s}$ and linear speed up to 300 km/h, with a sensitivity limited by spontaneous emission quantum noise in terms of effective power reflectivity.

Such high performances compact laser system opens the path to a new family of laser sensors of great interest for demanding photonic applications, such as optical micro manipulation, atom guiding and acceleration, and manipulation of Bose-Einstein condensates. This would enable to achieve compact, high performances and cost-effective systems, as the vortex laser can be used at the same time as an optical tweezer and an auto-aligned, highly sensitive speed sensor.

Acknowledgments

This work was supported by the French RENATECH Network, ANR MICPHIR and Labex NUMEV (ANR10LABX20 contract).

References

- [1] L. Allen, M. W. W. Beijersbergen, R. J. C. Spreeuw, and J. P. P. Woerdman, *Phys. Rev. A* pp. **45**, 8185–8189 (1992).
- [2] G. Gibson, J. Courtial, M. Padgett, M. Vasnetsov, V. Pas’ko, S. Barnett, and S. Franke-Arnold, *Opt. Express*. **12** , pp. 5448–5456 (2004).
- [3] L. Paterson, M. P. MacDonald, J. Arlt, W. Sibbett, P. E. Bryant, and K. Dholakia, *Science*. **292**, 912–914 (2001).
- [4] Y. Xue, C. Kuang, S. Li, Z. Gu, and X. Liu, *Opt. Express* **20**, 17653 (2012).
- [5] M. Harwit, *Astrophys. J.* **597**, pp. 1266–1270 (2003).
- [6] B. A. Garetz and S. Arnold, *Opt. Commun.* **31**, pp. 1–3 (1979).
- [7] J. Courtial, D. A. Robertson, K. Dholakia, L. Allen, and M. J. Padgett, *Phys. Rev. Lett.* **81**, pp. 4828–4830 (1998).
- [8] M. P. J. Lavery, F. C. Speirits, S. M. Barnett, and M. J. Padgett, *Science*. **431**, pp. 537–541 (2013).
- [9] D. B. Phillips, M. P. Lee, F. C. Speirits, S. M. Barnett, S. H. Simpson, M. P. J. Lavery, M. J. Padgett, and G. M. Gibson, *Phys. Rev. A* **90**, pp. 1–5 (2014).
- [10] D. J. Kim, J. W. Kim, and W. A. Clarkson, *Opt. Express*. **21**, pp. 275–280 (2013).
- [11] A. Garnache, M. Seghilani, M. Myara, M. Sellahi, I. Sagnes, L. Legratiet, and P. Lalanne. European Patent 14307037.3, December 15, (2014).
- [12] A. E. Siegman, *lasers* (University Science Books, 1986).
- [13] A. Laurain, M. Myara, G. Beaudoin, I. Sagnes, and A. Garnache, *Opt. Express*. **18**, pp. 14627–14636 (2010).
- [14] M. S. Seghilani, M. Sellahi, M. Devautour, P. Lalanne, I. Sagnes, G. Beaudoin, M. Myara, X. Lafosse, L. Legratiet, J. Yang, and a. Garnache, *Opt. Express* **22**, pp. 5962 (2014).
- [15] R. Lang and K. Kobayashi, *IEEE J. Quantum Electron.* **16**, pp. 347–355 (1980).
- [16] L. a. Coldren, S. W. Corzine, and M. L. Mašanović (John Wiley & Sons (2012), Inc., Hoboken, NJ, USA).
- [17] E. Lacot, R. Day, and F. Stoeckel, *Phys. Rev. A.* **64**, pp. 1–11 (2001).

6.4 Feedback in a Hermite-Gaussian laser for particle sizing

Our aim here is to propose a particle sizing sensor design, for particle sizes $> \lambda$ typically $\sim 10 \mu\text{m} - 100 \mu\text{m}$. This would be another example of an advanced sensing application enabled by a direct generation of structured light from a laser source.

This time, laser modes of interest to us are high order HG modes. The sensor setup we will propose is quite similar to the one presented in Sec 6.3, because we still use the self-mixing technique. However, the key difference with the previous sensor, is that the measurement method we present here is based on the spatial variation of the optical feedback rather than the temporal ones used in frequency shifted feedback.

Before going into the details, in the following section we very briefly present some of the conventional particle sizing methods. Our goal is clearly not to conduct an exhaustive state of the art study, but to describe some of the most widely used techniques to help the reader easily understand the design we propose, and visualize its main advantages in comparison with the conventional approaches. The reader interested in particle sizing and speed measurement techniques can find detailed studies and systems design in [Albrecht 2003].

6.4.1 Brief overview of conventional particle sizing techniques

6.4.1.1 Phase Doppler Anemometry

This technique is a well-established one and implemented in commercially available particle sizing systems, its principle is illustrated in Fig 6.7 [Durst 1976, Bachalo 1984]. A CW-laser beam is split, then recombined to create interference fringes in a volume called the measurement volume. A spherical particle, can be considered as a ball-lens whose focal length f_p depends on its diameter D and its refractive index. Two detectors are placed out of the particle passage plane and separated by a given distance. When the particle moves in the measurement volume it images the fringe pattern with a magnification that depends on its focal length, and because the detectors are separated, they generate basically the same signal but with a certain time delay that depends on the magnification of the equivalent ball lens. Therefore, the measurement of this delay is a measurement of f_p and thus the particle diameter. To make this time delay independent of the particle speed it is usually divided by the period of the signal, the obtained quantity is then a phase difference, hence the name 'Phase Doppler technique'. In order to predict the phase-difference as a function of the particle diameter, we usually use ray tracing methods. However, due to possible multiple reflections inside the particle, this latter can have several scattered orders as can be shown by the Lorentz-Mie theory [Mie 1908, Bohren 2008]. Thus, to simplify the predictions, the detectors are placed in a region where there is only one dominant order, this region is determined by

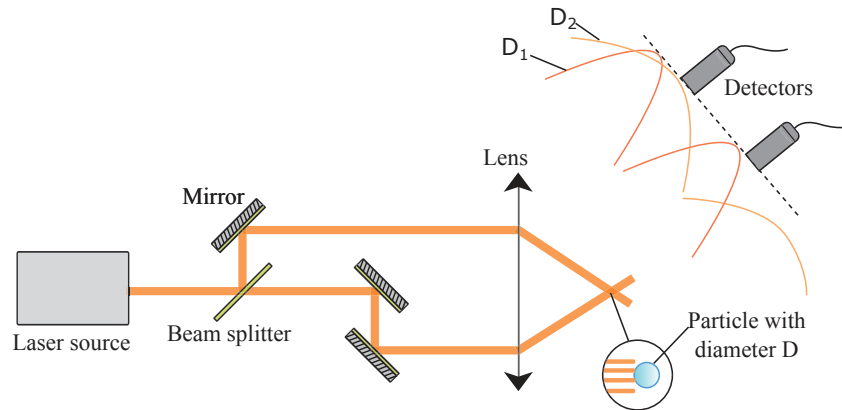


Figure 6.7: Phase Doppler Anemometry scheme illustration.

calculating the Mie scattering diagram of the particle. The main disadvantage of this technique is the cumbersomeness, because the detectors have to be placed at specific locations, with specific elevation angle. Otherwise the characteristic curves that connect the measured phase to the particle size has to be recalculated. Thus, although this system is commercially available, it is more akin to a laboratory measurement system rather than a sensor.

6.4.1.2 Interferometric particle imaging

The principle of this technique is illustrated in Fig 6.8, it is based on scattering and imaging of light from a single laser beam. An in-focus image of the particle will consist of only two glare points, whose projected separation will be directly related to the particle size [Van de Hulst 1991]. In principle, this can be used as a direct measurement, however this will require a very high resolution image. Out of focus however, the image contains an interference pattern where the fringes spacing depends on the glare points spacing and thus the size of the particle. This technique

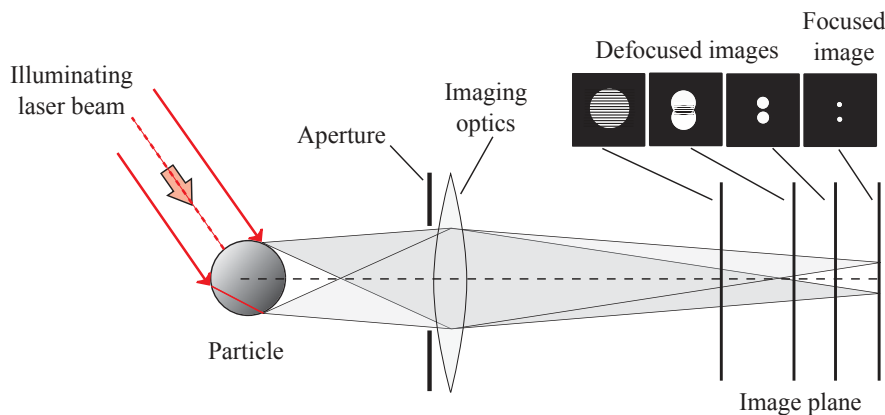


Figure 6.8: Interferometric particle imaging principle.

was first demonstrated by [König 1986], who focused a single beam onto a droplet

and measured the resulting fringe pattern in the far field. They recognized the potential of the technique for particle sizing and applied it to measure the droplet evaporation. Since then this technique is a field of active research in order to achieve compact and on-board particle sizing sensors [Shen 2014, Brunel 2014]

However, this approach can only be used with transparent particles such as droplets and bubbles, and it suffers from the same cumbersomeness problem as the phase Doppler technique, because the measurement volume has to be between the laser and the camera. Furthermore, unlike the phase Doppler technique, the interferometric imaging doesn't allow to simultaneously measure the speed of particles.

6.4.2 The proposed design: Spatially-resolved feedback for particle sizing

The design we propose in this section relies on an approach close to the one of the phase Doppler technique. Its principle is illustrated in Fig 6.9. A high order HG beam is focused in the measurement volume, when a spherical particle with a radius $R_p \gg \lambda$ goes through this volume it reflects back the beam with a magnification that depends on its radius of curvature. For simplicity we consider a metallic-like particle without multiple internal reflections (scattering orders). Here the beam spatial structure replaces the interference pattern, and the lens system we use to focus the beam plays also the role of the collection system. In phase Doppler technique more than one detector is required to measure the inter-fringe spacing and deduce the magnification. In our approach, the magnification is deduced thanks to the finite aperture of the collection lens (f2). Because it allows to only a part of the back-reflected beam to be re-injected in the laser cavity, and obviously the induced laser intensity increase depends on which part is re-injected, for example it is maximal when we re-inject a lobe of the beam, and minimal between two lobes. Therefore, when the particle moves in the measurement volume the backscattered image sweeps the collection lens, accordingly, when we look at the time variations of the laser intensity, we should observe a particular signature due to the beam spatial structure. This signature depends on the target diameter and the collection lens aperture.

To illustrate this approach, let us take a practical example. The first thing we need is a laser source emitting a high order Hermit-Gauss beam. We choose one of the lasers we developed in Chap 4. These sources use an integrated amplitude masks that impose the rectangular symmetry required for the HG basis as we have seen in Sec 4.4.2.4. By using a stable plano-concave VECSEL cavity, with a length $L_c = 9\text{mm}$ we obtain HG beams having a fundamental mode waist $w_{00} = 30\ \mu\text{m}$. Higher order beams have two waists given by¹: $w_x = w_{00}\sqrt{1+n}$, and $w_y = w_{00}\sqrt{1+m}$. In Fig 6.10 we show typical measured HG beams and their dimensions on the 1/2-VECSEL surface, and also a schematic of the loss mask used to obtain the HG_{02} mode. For the following simulations, we will consider a VECSEL emitting a HG_{02} mode with the dimensions shown in Fig 6.10. We will discuss later the implications

¹By assuming that $n+1$, $m+1$ represent the number of lobes along x - and y - axis respectively.

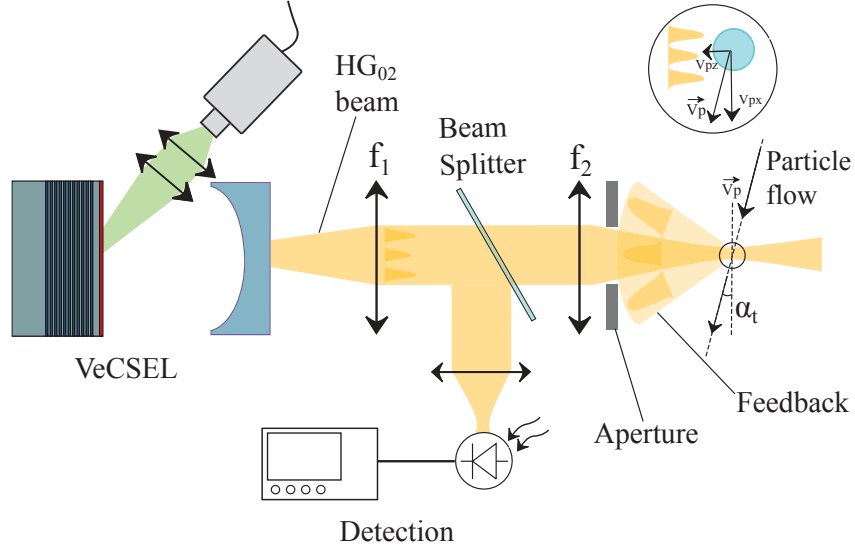


Figure 6.9: Self-mixing granulometer design based on a VECSEL emitting high order HG beam.

of using a higher order mode. But for the time being, we describe the simulation procedure we used to calculate the self-mixing signal, and show how to extract the particle size information from it.

6.4.3 Self-mixing signal simulation

To simulate the self-mixing signal, we use the Fresnel propagation integral through an ABCD system given by:

$$E^{(1)} = \iint K(x_1, y_1, x_0, y_0) E^{(0)}(x_0, y_0) dx_0 dy_0 \quad (6.9)$$

Where $E^{(i)}$ is the E-field pattern of the considered mode (HG_{02} in our case), and $i = 0, 1$ denotes the starting and the final planes having a coordinates x_0, y_0 and x_1, y_1 respectively. And $K(x_1, y_1, x_0, y_0)$ is the propagation Kernel already presented in Chap 1 (Eq 1.29). We propagate the beam through the optical system, from the 1/2-VECSEL surface to the plane of the particle, then multiply the E-field by the transfer function of the particle which is represented by a spherical reflector (reflectivity of 4%) plus an aperture corresponding to its diameter. Then we propagate back the beam to the 1/2-VECSEL surface by taking into account the apertures of the optical elements. Then to calculate the increase of the laser intensity, we compute the overlap integral between the back-reflected E-field E_{br} and the laser mode given by:

$$I_{sm} = \iint E^0(x, y) E_{br}(x, y) dx dy \quad (6.10)$$

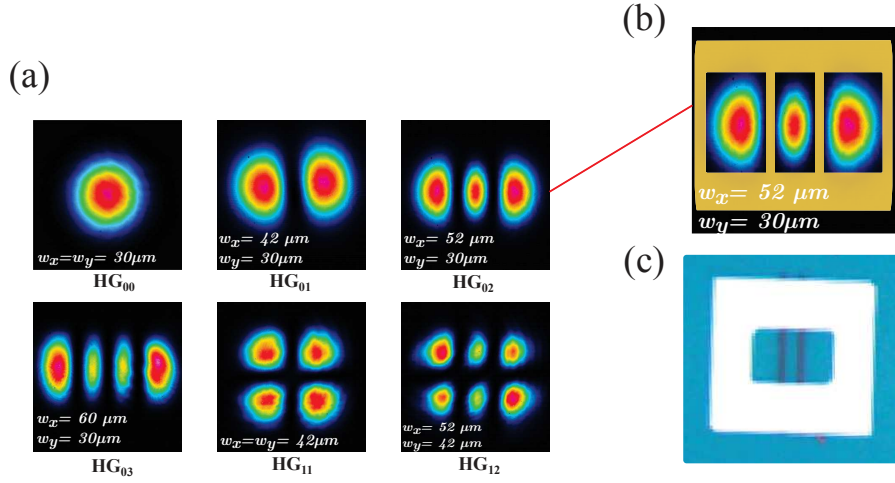


Figure 6.10: (a) Hermite Gauss laser beams generated in a 8mm length VECSEL cavity. (b) HG₀₂ mode, and schematic of the used loss mask. (c) Optical microscope photograph of the integrated mask used to select the HG₀₂ mode.

At this stage we have calculated the self-mixing signal at a single time-step, and a single particle location. Next, we use a time discretization, with a time step Δt . By assuming a particle's speed \vec{V}_p , the time discretization results in a spatial one Δ_s given by:

$$\vec{\Delta}_s = \vec{V}_p \Delta_t \quad (6.11)$$

In the interest of simplicity, we assume that the particle speed has only two components, V_{px}, V_{pz} (see Fig 6.9).

To simulate the self-mixing signal, we redo the same propagation procedure from the beginning by increasing the time step and record the obtained intensity I_{sm} . In Fig 6.11 we show an example of simulated time variations of the self-mixing signal intensity for the setup illustrated in Fig 6.9, with $f1 = f2 = 50$ mm, $L1 = 50$ mm, $L3 = 40$ mm and aperture diameter $D = 25.4/3$ mm, a laser emitting HG₀₂ having a fundamental waist $w_0 = 30$ μm (beam size of $2 \times w_{02} = 104$ μm). The signal is calculated for a particle moving through the measurement volume at a speed of $V_p = 2$ m/s. We considered three particle's radii: 20, 60 and 100 μm . To generalize the curves, we multiplied the time axis by the speed of particles and normalized the obtained effective distance to the beam size, by doing so, when we measure the width of the pattern we obtain a normalized effective image width (EIW/ w_0) independent of the particle speed and the fundamental beam waist w_0 . From this figure we can see that the curves take a form close to the beam intensity pattern (see Fig 6.12). When the particle size changes, we notice a change in the pattern width (signal duration) that we called the EIW, and also in the modulation depth. The EIW increases with the particle size, is simply explained by the fact that a bigger particle stays longer in the measurement volume (see illustration in fig 6.13). And the increase in the modulation depth with the decrease in the particle size,

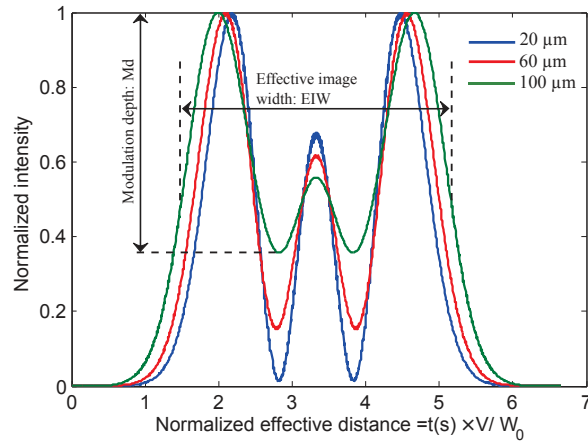


Figure 6.11: Simulated time variation of the self-mixing signal for three particle radii, the time axis (x) is multiplied by the particle speed to obtain an equivalent distance, this latter is then normalized to the fundamental waist of the HG_{02} beam. The double arrow show the FWHM of the obtained pattern with particle radius = 100 μm .

is due to the fact that a big particle has a small magnification, which means that a bigger part of the beam is reinjected, and thus the beam intensity structure is averaged. The worst case would be to have a flat particle, then all the beam can be reinjected inside the cavity. The self-mixing signal will take then, the form of monotonic increasing function that starts when the particle enters the measurement volume, then decreases monotonically when the particle starts leaving the volume.

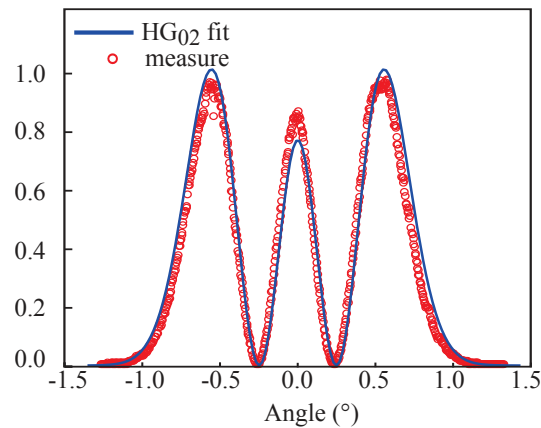


Figure 6.12: Cross section of the HG_{02} beam pattern.

The idea we propose, is to use these two properties (the pattern width and the modulation depth) as signature to measure the radius of spherical particles. For this purpose we simulated the variations of both of them as a function of the particle size. The obtained results are shown in Fig 6.14, we considered the FWHM

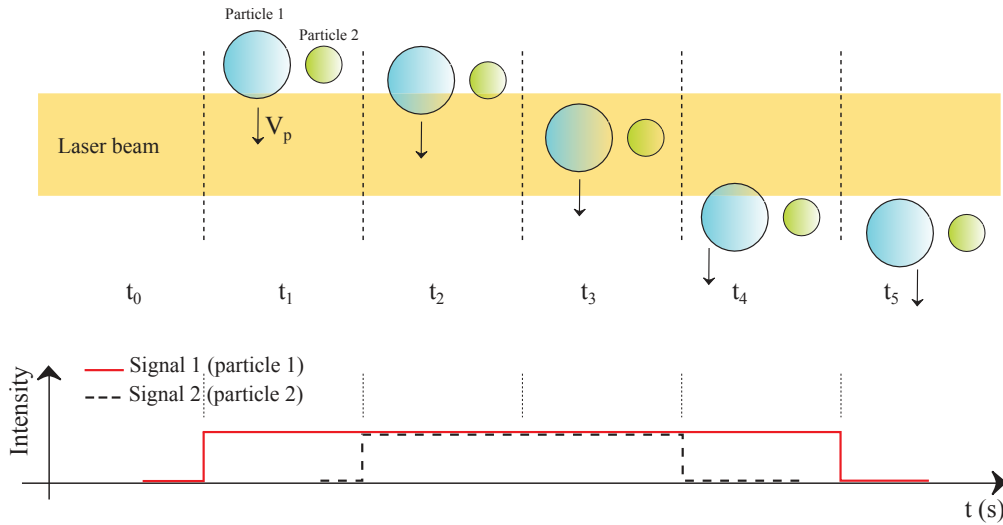


Figure 6.13: Illustration of the particle size effect on the signal duration.

for the EIW width and peak-to-valley for the modulation depth. We notice that the two functions are monotonic which is ideal for the measurement application. However, the modulation depth reaches its minimal value ($\sim 60\%$) for particle radius larger than $120\ \mu\text{m}$. The simulations we performed shows that after this value additional lobes occur in the signal pattern that departs from the beam one. From this value we consider that the signal cannot be used unambiguously to determine the particles size, because one has no mean to be sure that what he sees is the reflected image of the beam. A remedy is to reduce the aperture size to measure larger particles, however, this will be at the expense of the signal level and the measurement accuracy. Because reducing the aperture size will reduce the slope of the second curve (modulation depth) until it becomes completely flat for very small aperture¹. In this case we lose the information about the spatial spread of the beam image. The optimal design is thus a compromise between the measurable range of particle size and the measurement accuracy. However, it is possible to change the range of the measurable particle size simply by changing the beam size in the measurement volume, but in order to use the same curves one must conserve the same focal ratio² of the optical system (i.e. f/D). This example shows that it is possible to use this scheme as a particle sizing self-mixing sensor.

So far we have used normalized intensities of the self-mixing signal to simplify the analysis. But as one may expect, there is an intensity decrease related to the reflection of the particle and the aperture effect. To give an idea about the amplitude of the signal, without normalization, the curves of Fig 6.11 will show a maximum relative intensities ($I_{\text{signal}}/I_{\text{output}}$) of 1.4×10^{-5} , 3.6×10^{-5} , 5.1×10^{-5} for particle radii of $20\ \mu\text{m}$, $60\ \mu\text{m}$ and $100\ \mu\text{m}$, respectively. For example, in this case the self-mixing signal can be detected in a laser having a relative intensity noise,

¹Very small aperture can be assimilated to one pixel detector.

²Also called the f-number.

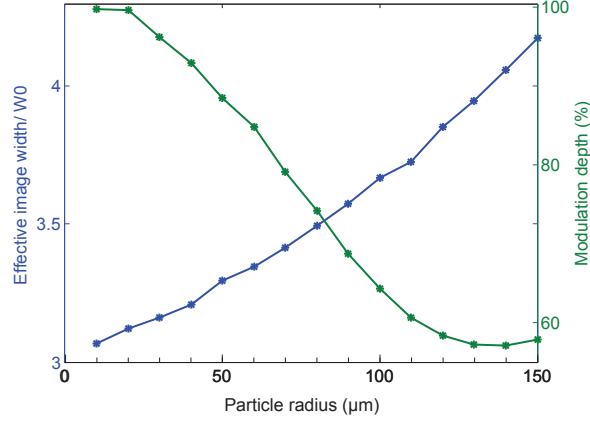


Figure 6.14: Plot of the effective image width (left) and the modulation depth (right) of the self-mixing signal (see Fig 6.11) as a function of the particle radius.

up to $RIN \sim 10^{-13} \text{ Hz}^{-1}$, with detection bandwidth of 1 kHz.

Using higher order beams will modulate the laser intensity at a higher frequency, which allows to enhance the signal to noise ratio, because the noise level decreases when the frequency increases (due to the $1/f$ noise).

6.4.3.1 Simultaneous size and velocity measurement

To measure the particle radius using the curves of Fig 6.14 one must know the speed of the particle. This latter can be measured separately, or simultaneously by slightly tilting the particle trajectory with an angle α_t in such a way as to have a longitudinal speed component in the optical axis. This will create a beat note thanks to the Doppler effect. But one must ensure that the beat period T_l is much smaller than the duration required to record the effective image, otherwise it would be difficult to separate the two modulations. This condition can be expressed as: $T_l \gg \text{EIW}/V_p$. The two periods are related, but thankfully the Doppler frequency can be controlled by changing the tilt angle:

$$\Delta f_l = \frac{2V_p \sin(\alpha_t)}{\lambda} \quad (6.12)$$

according to this equation, the beat period condition can be written as follows:

$$\frac{\alpha_t}{\arcsin\left(\frac{1}{2} \frac{\lambda}{\text{EIW}}\right)} \gg 1 \quad (6.13)$$

For example, for $\text{EIW} = 50 \text{ μm}$ and $\alpha_t = 20 \text{ deg}$ the ratio of Eq 6.13 $\simeq 70$ which means that this angle is sufficient to distinguish the beat frequency, and also the two particle sizing parameters (modulation depth and EIW) from the envelope. This is illustrated in Fig 6.15 where we plot the simulated self-mixing signal plus the Doppler beating with $\alpha_t = 20 \text{ deg}$.

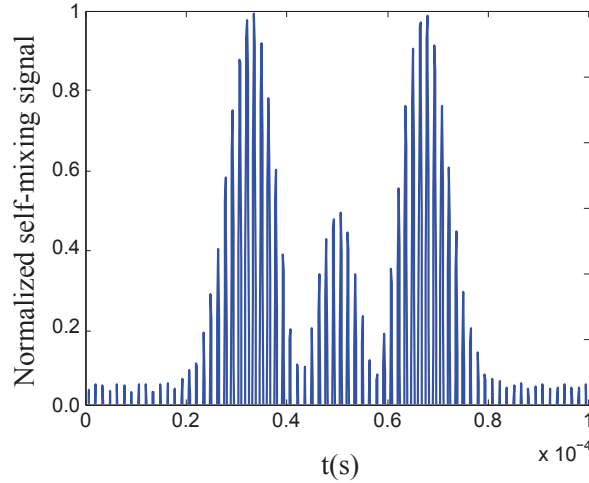


Figure 6.15: Simulated temporal record of the self-mixing signal obtained with a particle radius of $50 \mu\text{m}$ crossing the measurement volume at a speed $V_p = 2 \text{ m/s}$ with a tilt angle $\alpha_t = 20 \text{ deg}$.

6.5 Conclusion

The scheme illustrated here can be used as a velocimetry/ granulometry in situ self-mixing sensor. We related the width and the modulation depth of the temporal self-mixing signal to particle size in the measurement volume (Fig 6.14). We expressed, the y-axis in a unitless normalized form, thus this curve can be used independently from the speed of the particle and the beam size. However, if one of the optical system parameters (lens system magnification and the apertures) changes one has to recalculate the curves of Fig 6.14. This measurement scheme transposes all the previously discussed advantages of the self-mixing configuration to the particle sizing application. This is possible thanks to the direct generation of a high order HG beam. By presenting this design our purpose is to give another example of how a laser source emitting structured light may enable novel applications that present several advantages over traditional techniques. For example the two sensor designs shown in this chapter are very compact, and don't require complex positioning of additional optical elements as in Phase Doppler technique for instance. The theoretical study we conducted, is based on a laser generating a HG_{02} beam, however, other high order beams can be used. As noted previously, beams with faster spatial modulations will modulate the laser intensity at higher frequencies which would enhance the signal to noise ratio. Furthermore, HG beams have anisotropic transverse pattern, this can be used to determine the orientation of the particle movement. On the other hand, using modes with isotropic transverse profile such as LG ones, will enable to obtain the same self-mixing signal regardless of the particle movement orientation as illustrated in Fig 6.16. In order to completely validate this design, we need of course, further investigations accompanied by an experimental study.

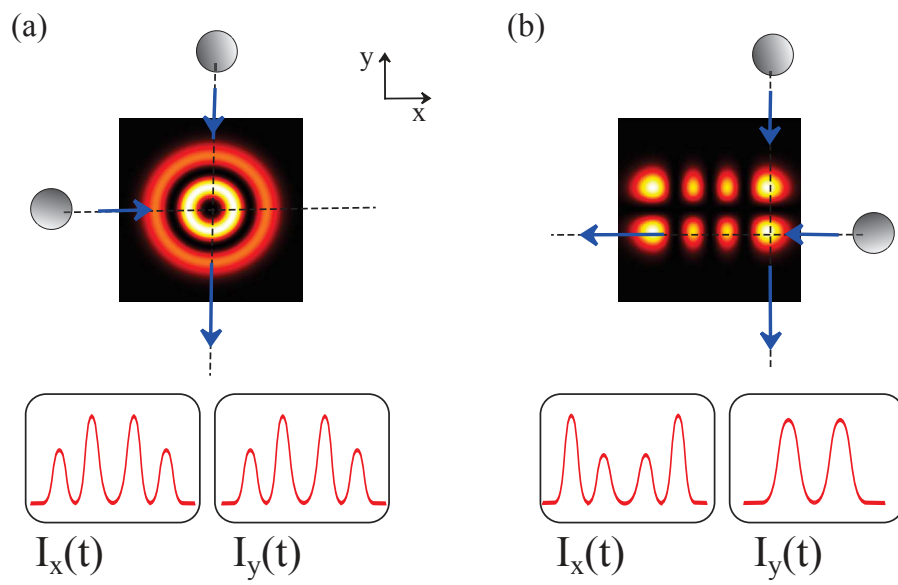


Figure 6.16: Illustration temporal self-mixing signal obtained with a particle crossing a beam with an (a) isotropic, (b) an anisotropic pattern.

Conclusion

The goal of this thesis was to generate phase-,amplitude-, and polarization structured coherent states of light in a laser cavity, and to show the potential of these exotic laser sources for sensing applications. To do this we have followed three main lines of work:

In a first step we provided the theoretical framework required to tackle the issue of mode selection in a laser cavity. We used the matrix method with Huygens-Kernel formulation to calculate the transverse eigenmodes of a passive cavity¹, including unconventional ones (with phase and intensity masks). To determine the polarization eigenstates, we presented Jones matrices and vectors.

Next, we studied light matter interaction in the gain medium in order to understand mode competition in the active cavity. For this purpose, we used dual-mode dynamics, which we introduced in chapter 1 using the Lamb model. This model is general and easy to understand. It helped us to have an intuitive feel of the physical ingredients involved in mode competition that can be summarized as follows:

- Gain and loss of the modes: mode with lower loss has a lower threshold and is the most likely to be selected.
- Self- and cross-saturation coefficients: they describe the gain saturation of each mode by its own intensity, and the gain saturation of each mode by the intensity of the other one. We have seen that the laser always favors the mode with the most homogeneous intensity distribution, because it is the one that makes the most efficient use of the gain as described H. Haken's principle of laser mode competition "Darwin's survival of the fittest".

However this all intensity model is not suited to study phase-effects, such as locking of modes by backscattering effect and coherent superposition of eigenstates. Thus, we have adopted the more accurate semi-classical approach by writing Maxwell-Bloch equations for our lasers. To treat polarization dynamics, we used the spin-flip model, which is based on the same Maxwell-Bloch equations in a four-level system, by including the conduction band (CB) and the Valence band spin-sublevels of the semiconductor quantum wells. This semi-classical approach helped us to understand several points, mainly:

- The locking of contra-rotating vortex modes observed close to threshold. This effect is caused by the backscattering due to defects in the cavity mirrors.
- The random handedness selection of vortex modes. This effect observed in laser cavities since the early days of vortex generation [Harris 1994a] and was still not understood when we started this work [Kim 2013].

¹ A the time of this writing the eigenmode-solver developed within the framework of this thesis is being prepared to be provided as an open source Python package (<http://seghil.github.io/OpenCavity/index.html>).

- The effect of spin-flip time in polarization mode dynamics. By comparing theoretical noise spectra (induced by Langevin noise sources) and measured ones, we extracted a microscopic property of electron in QW: the spin-flip time with more than 50% accuracy, which shows that the laser is a powerful tools to study physical systems.

The second line of work deals with the development of mode control technology based on multi-layered subwavelength phase/intensity masks. The phase masks achieved are using all-dielectric metamaterials. Intensity masks for their part are made of subwavelength-chromium layer designed to introduce highly selective 2D loss patterns.

We integrated these masks in highly coherent III-V semiconductor laser sources based on multi-quantum wells (InGaAs/GaAs/AlGaAs) Vertical-External-Cavity-Surface-Emitting-Laser technology (VECSEL), operating in the near infra-red (IR). These masks enabled us to select the desire cavity eigenstates.

We have also seen that VECSELs present many features that make them ideal candidates for structured light generation: The band-gap-engineered compound semiconductor materials confer to VECSELs wide wavelength coverage at watt power level. They exhibit compactness, pump flexibility and versatility thanks to the extended cavity space. The low thickness of the QW-based active medium ensure high homogeneity, weak non linearity and prevents distortion effects induced by thermal lensing in thick gain media.

The developed mode control technology, overcome in several respects the shortcomings of existing methods: first, subwavelength dimension of the periodic structure means that there are no diffraction losses as is SLMs (pixel pitch $\sim 10 \mu\text{m}$ and fill factor $\sim 80\%$) and other diffractive elements. Then, the metamaterials are fabricated using micro-lithography and associated semiconductor technologies, which enables to achieve compact, auto-aligned, cost-effective and high quality elements. Moreover, The effective refractive index can be controlled locally by changing the structural geometry which enables us to create two dimensional refractive index profiles with high accuracy, in order to modulate the phase and the intensity of the intracavity waves.

The third line of work, consists in using the developed theoretical tools and the integrated mode control technology to design, fabricate and characterize laser sources emitting the desired phase-, amplitude, and polarization structured eigenstates of light.

We designed and implemented several sets of masks to select degenerate LG modes and HG modes . Then, we characterized the obtained eigenstates by measuring the optical spectrum (SMSR $\sim 50 \text{ dB}$), the output power ($\sim 40 \text{ mW}$ pump limited) and analyzing the noise spectrum in the RF domain.

Next, we addressed the problem of controlling the sign of OAM in a laser cavity. To do this we used loss masks to suppress all the modes except vortices with the wanted OAM charge (absolute value), and introduced a weak 'orbital birefringence' to slightly perturb at first order the cavity eigenbasis in an asymmetric way. This breaks the symmetry of mode wavefunctions, resulting in inhomogeneous intensity pattern and thus larger self-saturation for the unwanted mode.

By doing so, we successfully generated vortex modes with charges $l = \pm 1, \pm 2, \pm 3, \pm 4$. with single frequency operation ($SMSR \simeq 30$ dB), and single linear polarization state ($PER \simeq 70$ dB). Because of the degeneracy lift, when we mixed the modes on a photodiode, we measured a beat note at the frequency difference, which allowed us to measure the degeneracy lift and also the suppression ratio down to 80 dB.

Although we focused in this work on generation of LG and HG modes, the technology we presented is a general one, and can be used in principle to generate any kind of eigenmode families, such as Bessel-Gauss and Ince-Gauss beams.

We also addressed the control of polarization state. We have seen that this latter is determined by the anisotropies of the complex electric susceptibility, which are linear birefringence and linear dichroism, and circular birefringence and circular dichroism. Here we have shown how to measure and control the linear birefringence and dichroism in III-V semiconductor QW-based 1/2-VCSEL structures. The linear birefringence lifts the degeneracy between linear polarization states, and the QWs dichroism favors the one parallel to [110] crystal axis. Thanks to the large intrinsic gain dichroism in III-V-semiconductor QWs $\Delta G/G \simeq 10\%$, polarization extinction ratios of the order of ~ 80 dB were obtained.

In the last part, we investigated the generation of circular polarization with a handedness controlled by the spin of electrons. For this purpose, we used a cavity where we compensated the linear anisotropies and introduced circular ones. The circular birefringence was introduced by means of a Faraday rotator, whereas the circular dichroism was introduced by asymmetrically pumping of spin reservoirs. But due to fast spin flip time compared to radiative lifetime, the resultant circular dichroism is weak (below 10% under spontaneous emission). Furthermore each reservoir feeds one circular polarization component, which implies that they can coexist. In an attempt to address this problem we coupled the components in the gain medium by perturbing the cavity eigenstates. This way we obtained circular polarization controlled by pump spin with an extinction ration $PER \simeq 24$ dB.

In the last part of this work, we demonstrated new integrated sensor concepts exhibiting high sensitivity and high resolution. The idea was to show new sensing capabilities enabled by some of the developed exotic laser sources. To do this, we demonstrated angular velocity measurement using self-mixing in a vortex laser. This measurement is based on the rotational Doppler shift that occurs in beams carrying angular momentum. Then we presented another design that uses the spatial structure of the feedback in a HG laser to measure the size of backscattering targets. These new sensor concepts show examples of a measurements, inaccessible using conventional laser sources

Prospects

The exotic lasers demonstrated in this work can be used to show new sensing capabilities. For example the vortex laser can be used as an optical tweezer that applies a torque on a particle in order to rotate it; the angular speed of the particle depends on the beam energy [Padgett 2004], and also on the characteristics of the surrounding medium such as its viscosity. Thus, as the beam energy is usually well known, the characteristics of the surrounding medium can be probed by using feedback to simultaneously measure the particle velocity while tweezing it.

The OAM spectroscopy is a new emerging field [Noyan 2015]. By observing the OAM spectrum of light backscattered by a given target, one can obtain information about the target spatial structure. This is another application where a vortex laser can be used as an emitter and OAM spectrum analyzer at the same time. Indeed, the OAM states in the backscattered light will be projected on the cavity ones [Bekshaev 2008].

The particle sizing design we proposed in Chap 6 is very promising for in situ and on board particle sizing sensors. The following steps will be to demonstrate the concept experimentally, characterize and optimize its sensitivity limit and size selectivity, achieve long distance measurement (>10 m) thanks to the laser coherence, and study the possibility of using other kind of beams such as non-diffracting Bessel beams.

The integrated mode control technology allows to generate other kind of beams of interest for several applications. For example to generate Bessel-Gauss beams one has to implement a metamaterial with a conical phase function on the 1/2-VCSEL structure, as shown by calculated eigenmodes of such a cavity in Fig 4.3. This should be soon addressable with the technology demonstrated here.

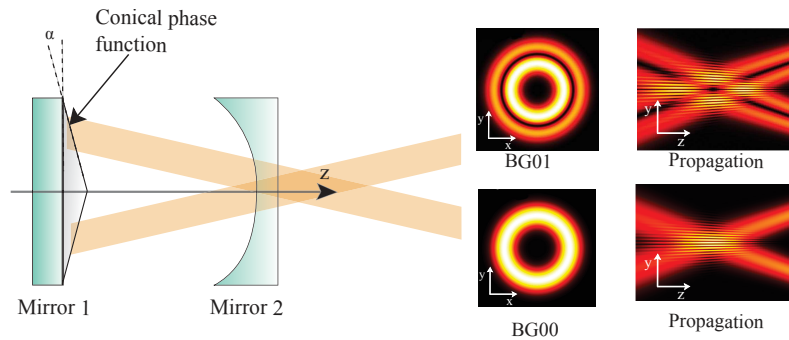


Figure 6.17: Bessel-Gauss modes of a cavity with a conical phase mask.

With the material choice we have made in this work the maximum achievable phase difference is $\simeq \pi/2$. Increasing this limit to 2π will allow to achieve any phase function, and release the cavity design constrains (length, mode size ...). Several solutions can be considered, like increasing the metamaterial layer thickness four times ($\sim 1 \mu\text{m}$ thick SiN layer), but the challenge here is to make very deep holes while keeping a good homogeneity, which is quite difficult with current-etching tech-

niques. Another option would be to choose other materials with higher refractive index, however these materials must enable selective etching as well, like GaAs on AlAs.

In the method we demonstrated, the handedness is controlled via passive static masks (one mask for one handedness). It would be very interesting to investigate other active control possibilities using for example, electrically controlled metamaterials [Jun 2012], or intracavity matrix of liquid crystals micro-cells deposited on the 1/2-VCSEL structure. One pixel-devices ($1 \mu\text{m} \times 1 \mu\text{m}$) has been already demonstrated [Castany 2012, Belmonte 2015]. They can be used with large modes (area $> 30\,000 \mu\text{m}^2$) in order to limit the diffraction effect. Another possibility would be to control the OAM in the spontaneous emission seeding, this has been investigated theoretically in [Williams 2014].

Appendices

Jones vectors table and Jones matrices of polarizing optics

A.1 Jones vectors

Table A.1 shows Jones vectors corresponding to different polarization states.

A.2 Jones matrices

A.2.1 A wave plate

The Jones matrix for a wave plate, in the general case (see Fig A.1) is given as:

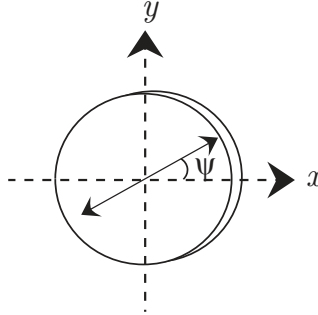


Figure A.1: Schematic of a wave plate, ψ is the orientation angle of the incident waves' electric field.

$$R(-\psi) \begin{pmatrix} \exp(-j\Gamma/2) & 0 \\ 0 & \exp(j\Gamma/2) \end{pmatrix} R(\psi), \quad (\text{A.1})$$

where $R(\psi)$ and Γ are the coordinate rotation matrix, and phase retardation. They are given as:

$$R(\psi) = \begin{pmatrix} \cos(\psi) & \sin(\psi) \\ -\sin(\psi) & \cos(\psi) \end{pmatrix} \quad (\text{A.2})$$

$$\Gamma = \frac{2\pi}{\lambda} (n_s - n_f) d, \quad (\text{A.3})$$

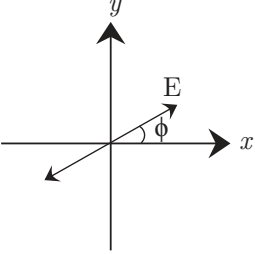
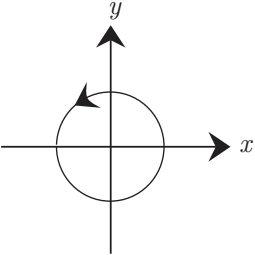
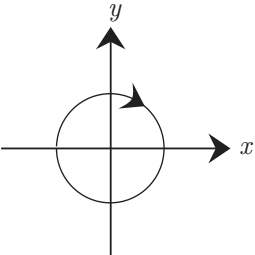
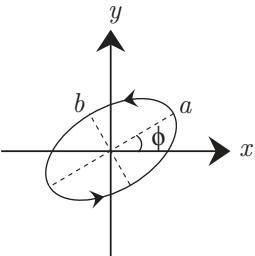
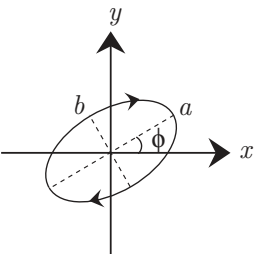
Polarization state	Jones Vector
	$\begin{pmatrix} \cos(\Phi) \\ \sin(\Phi) \end{pmatrix}$
	$\frac{1}{\sqrt{2}} \begin{pmatrix} 1 \\ -j \end{pmatrix}$
	$\frac{1}{\sqrt{2}} \begin{pmatrix} 1 \\ j \end{pmatrix}$
	$\begin{pmatrix} a \cos(\Phi) + jb \sin(\Phi) \\ a \sin(\Phi) - jb \cos(\Phi) \end{pmatrix}$
	$\begin{pmatrix} a \cos(\Phi) - jb \sin(\Phi) \\ a \sin(\Phi) + jb \cos(\Phi) \end{pmatrix}$

Table A.1: Jones Vectors of different polarization states

where n_s and n_f are the refractive indices of the slow and the fast axis of the waveplate, respectively, and d is the width of the plate. After substitution, equation A.1 becomes:

$$\begin{pmatrix} \exp(-j\Gamma/2) \cos(\psi)^2 + \exp(j\Gamma/2) \sin(\psi)^2 & -j \sin(\Gamma/2) \sin(2\psi) \\ -j \sin(\Gamma/2) \sin(2\psi) & \exp(-j\Gamma/2) \sin(\psi)^2 + \exp(j\Gamma/2) \cos(\psi)^2 \end{pmatrix} \quad (\text{A.4})$$

A.2.2 A polarizer

The Jones matrix for a polarizer, in the general case (see Fig A.2) is given by:

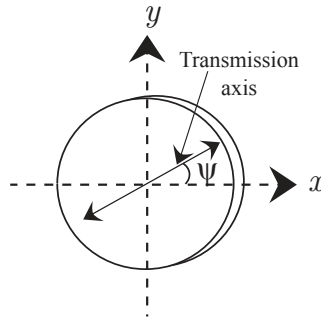


Figure A.2: Illustration of a polarizer with ψ the orientation angle of the transmission axis.

$$\begin{aligned} R(-\psi) T \begin{pmatrix} 1 & 0 \\ 0 & 0 \end{pmatrix} R(\psi), \\ = T \begin{pmatrix} \cos(\psi)^2 & \cos(\psi) \sin(\psi) \\ \sin(\psi) \cos(\psi) & \sin(\psi)^2 \end{pmatrix} R(\psi), \end{aligned} \quad (\text{A.5})$$

The factor T with $0 \leq T \leq 1$ denotes the amplitude transmission of the polarizer. A Brewster plate (see Fig 1.13) is equivalent to a polarizer with $T = 2n_p/(n_p^2 + 1)$ is amplitude transmission due to reflection at the interface air/plate. n_p is the refractive index of the plate.

Derivation of Lamb model coefficients for dual transverse modes

The goal of this appendix is to derive the coefficients of Eq 1.66 from dual-mode rate equations given as:

$$\begin{aligned} \frac{dE_i}{dt} &= -\frac{\gamma_{c_i}}{2}E_i + \frac{B^*}{2} \iint_{r,\theta} N(r,\theta)E_t U_i^*(r,\theta)e^{-j\Delta_i t} drd\theta \\ \frac{dN(r,\theta)}{dt} &= \rho(r,\theta) - \gamma_e N(r,\theta) - BN(r,\theta)|E_t|^2, \end{aligned} \quad (\text{B.1})$$

where E_i is the complex electric field of the i^{th} mode and $U_i(r,\theta)$ its spatial pattern, Δ_i is the frequency detuning between the mode $U_i(r,\theta)$ and the central frequency. $N(r,\theta)$ is the population inversion spatial distribution, γ_{c_i} is the resonator i^{th} mode photon decay rate, and γ_e the population inversion relaxation rate, $\rho(r,\theta)$ is the normalized pump-intensity distribution, and B^* is the complex gain term given by: $B^* = B(1 + j\alpha_h)$ where B is the Einstein coefficient for stimulated emission, and α_h in the Henry factor. Finally E_t denotes the total electric field, and is given by: $E_t = \sum_{i=1,2} E_i U_i(r,\theta)e^{-j\Delta_i t}$.

In a class-A laser $\frac{dN(r,\theta)}{dt} = 0$ we can then write the population inversion expression as

$$N(r,\theta) = \frac{\rho(r,\theta)/\gamma_e}{1 + \frac{B}{\gamma_e}|E_t|^2} \quad (\text{B.2})$$

This equation describes the saturation of the population inversion by the total intensity $|E_t|^2$. $(B/\gamma_e)^{-1}$ is called the saturation intensity I_{sat} . By replacing N in the rate equations (Eq B.1) one obtains:

$$\frac{dE_i}{dt} = -\frac{\gamma_{c_i}}{2}E_i + \frac{B^* \rho(r,\theta)}{2\gamma_e} \iint_{r,\theta} \frac{E_t U_i^*(r,\theta)e^{-j\Delta_i t}}{1 + \frac{B}{\gamma_e}|E_t|^2} drd\theta \quad (\text{B.3})$$

In small saturation approximation one can write $N(r,\theta)$ using the first order Taylor expansion. In what follows we write the complex electric field in terms of the envelope A_i and the phase ϕ_i : $E_i = A_i e^{-j\phi_i}$ and neglect cross-terms. By letting

Appendix B. Derivation of Lamb model coefficients for dual transverse modes

$C^* = C(1 + j\alpha_h) = (\rho B^*)/(2\gamma_e)$ we obtain¹

$$\begin{aligned} \frac{dA_{1,2}}{dt} - j\frac{d\phi_{1,2}}{dt}A_{1,2} = A_{1,2} \left[-\frac{\gamma_{c_{1,2}}}{2} + C^* \iint |U_{1,2}|^2 drd\theta - 2C^* \frac{B}{\gamma_e} A_{2,1}^2 \iint |U_{1,2}|^2 |U_{2,1}|^2 drd\theta \right] \\ - A_{1,2}^3 \left[2C^* \frac{B}{\gamma_e} \iint |U_{1,2}|^4 drd\theta \right] \end{aligned} \quad (\text{B.4})$$

In order to obtain the intensity equations we multiply left and right hand sides of the equation by $2A_{1,2}$:^{2, 3}

$$\begin{aligned} \frac{dI_{1,2}}{dt} = I_{1,2} \left[-\gamma_{c_{1,2}} + 2C \iint |U_{1,2}|^2 drd\theta \right] - I_{1,2}I_{2,1} \left[2C \frac{B}{\gamma_e} \iint |U_{1,2}|^2 |U_{2,1}|^2 drd\theta \right] \\ - I_{1,2}^2 \left[2C \frac{B}{\gamma_e} \iint |U_{1,2}|^4 drd\theta \right] \end{aligned} \quad (\text{B.5})$$

By comparing Eq B.5 and Eq 1.66 we obtain the coefficients given in Eq 1.69, 1.70, 1.71.

¹We dropped the spatial dependence (r, θ) notation for simplicity

² $\frac{dI_{1,2}}{dt} = 2A_{1,2} \frac{dA_{1,2}}{dt}$.

³We also obtain the phase equations, but we don't need them here.

Bibliography

- [Albrecht 2003] H E Albrecht, N Damaschke et C Tropea. Laser Doppler and Phase Doppler measurement techniques. Springer, 2003.
- [Alford 2002] William J. Alford, Thomas D. Raymond et Andrew A. Allerman. High power and good beam quality at 980 nm from a vertical external-cavity surface-emitting laser, 2002.
- [Allen 1992] L Allen, M W W Beijersbergen, R J C Spreeuw et J P P Woerdman. Orbital angular momentum of light and the transformation of Laguerre-Gaussian laser modes. *Physical Review A*, vol. 45, no. 11, pages 8185–8189, 1992.
- [Andersen 2006] M. Andersen, C. Ryu, Pierre Cladé, Vasant Natarajan, A. Vaziri, K. Helmerson et W. Phillips. Quantized Rotation of Atoms from Photons with Orbital Angular Momentum. *Physical Review Letters*, vol. 97, no. 17, page 170406, oct 2006.
- [Arbenz 2012] P Arbenz, D Kressner et DMETH Zürich. Lecture notes on solving large scale eigenvalue problems, 2012.
- [Aspnes 1982] D. E. Aspnes. Local-field effects and effective-medium theory: A microscopic perspective. *American Journal of Physics*, vol. 50, no. 8, page 704, aug 1982.
- [Bachalo 1984] W. D. Bachalo. <title>Phase/Doppler Spray Analyzer For Simultaneous Measurements Of Drop Size And Velocity Distributions</title>. *Optical Engineering*, vol. 23, no. 5, page 235583, oct 1984.
- [Baili 2008] G. Baili, J. Lahitte, M. Alouini, D. Dolfi, J.-P. Huignard et F. Bretenaker. Experimental investigation of noise reduction in an opto-microwave link based on highly-dispersive low-loss fiber. *The European Physical Journal Applied Physics*, vol. 44, no. 1, pages 65–70, jul 2008.
- [Bar-Ad 1992] S. Bar-Ad et I. Bar-Joseph. Exciton spin dynamics in GaAs heterostructures. *Physical Review Letters*, vol. 68, no. 3, pages 349–352, jan 1992.
- [Beck 2010] Rainer J Beck, Jonathan P Parry, William N MacPherson, Andrew Waddie, Nick J Weston, Jonathan D Shephard et Duncan P Hand. Application of cooled spatial light modulator for high power nanosecond laser micromachining. *Optics express*, vol. 18, no. 16, pages 17059–65, aug 2010.
- [Bekshaev 2008] A. Bekshaev, M. Soskin et M. Vasnetsov. Paraxial Light Beams with Angular Momentum. arXiv:0801.2309, page 87, jan 2008.

- [Belmonte 2015] Carlos Belmonte, Leszek Frasunkiewicz, Tomasz Czyszanowski, Hugo Thienpont, Jeroen Beeckman, Kristiaan Neyts et Krassimir Panajotov. Optimization of electrically tunable VCSEL with intracavity nematic liquid crystal. *Optics express*, vol. 23, no. 12, pages 15706–15, jun 2015.
- [Berg-Johansen 2015] Stefan Berg-Johansen, Falk Töppel, Birgit Stiller, Peter Banzer, Marco Ornigotti, Elisabeth Giacobino, Gerd Leuchs, Andrea Aiello, Christoph Marquardt, T Falk, Birgit Stiller, Peter Banzer, Marco Ornigotti, Elisabeth Giacobino, Gerd Leuchs, Andrea Aiello et Christoph Marquardt. Classically entangled optical beams for high-speed kinematic sensing. at <<http://arxiv.org/abs/1504.00697>>, apr 2015.
- [Bernard 1961] Maurice G. A. Bernard et Georges Duraffourg. Laser Conditions in Semiconductors. *physica status solidi (b)*, vol. 1, no. 7, pages 699–703, 1961.
- [Beth 1936] Richard A Beth. Mechanical Detection and Measurement of the Angular Momentum of Light. *Physical Review* *Physical Review*, vol. 50, page 115, 1936.
- [Biermann 2003] Mark L Biermann, Matthew Walters, James Diaz-Barriga et W S Rabinovich. Characterization of optical anisotropy in quantum wells under compressive anisotropic in-plane strain. *Journal of Physics D: Applied Physics*, vol. 36, no. 20, pages 2446–2450, oct 2003.
- [Bishop 2004] Alexis I. Bishop, Timo A. Nieminen, Norman R. Heckenberg et Halina Rubinsztein-Dunlop. Optical Microrheology Using Rotating Laser-Trapped Particles. *Physical Review Letters*, vol. 92, no. 19, page 198104, may 2004.
- [Bisson 2004] Jean François Bisson, Akira Shirakawa, Youhei Sato, Yuri Senatsky et Ken Ichi Ueda. Near-field diffractive optical pumping of a laser medium. *Optical Review*, vol. 11, no. 6, pages 353–357, 2004.
- [Bisson 2005] J. F. Bisson, Yu Senatsky et Ken Ichi Ueda. Generation of Laguerre-Gaussian modes in Nd:YAG laser using diffractive optical pumping. *Laser Physics Letters*, vol. 2, no. 7, pages 327–333, 2005.
- [Bohren 2008] Craig F. Bohren et Donald R. Huffman. *Absorption and Scattering of Light by Small Particles*. John Wiley & Sons, 2008.
- [Boutami 2007] S Boutami, B Benbakir, X Letartre, J L Leclercq, P Regreny et P Viktorovitch. Ultimate vertical Fabry-Perot cavity based on single-layer photonic crystal mirrors. *Optics express*, vol. 15, no. 19, pages 12443–9, sep 2007.
- [Bozinovic 2013] Nenad Bozinovic, Yang Yue, Yongxiong Ren, Moshe Tur, Poul Kristensen, Hao Huang, Alan E Willner et Siddharth Ramachandran. Terabit-scale orbital angular momentum mode division multiplexing in

- fibers. *Science* (New York, N.Y.), vol. 340, no. 6140, pages 1545–8, jun 2013.
- [Brunel 2014] Marc Brunel, Huanhuan Shen, Sébastien Coëtmelec, Gérard Gréhan et Tony Delobel. Determination of the Size of Irregular Particles Using Interferometric Out-of-Focus Imaging. vol. 2014, 2014.
- [Burger 2015] L Burger, I Litvin, S Ngcobo et A Forbes. Implementation of a spatial light modulator for intracavity beam shaping. *Journal of Optics*, vol. 17, no. 1, page 15604 (7pp), 2015.
- [Cai 2006] Wenshan Cai, Uday K. Chettiar, Alexander V. Kildishev et Vladimir M. Shalaev. Optical Cloaking with Non-Magnetic Metamaterials. *Nature Photonics*, vol. 1, pages 224–227, 2006.
- [Cai 2010] W. Cai et V. Shalaev. *Optical metamaterials: Fundamentals and applications*. Springer, 2010.
- [Cai 2012] Xinlun Cai, Jianwei Strainng, J Strain Michael, Benjamin Johnson-Morris, Jiangbo Zhu, Marc Sorel, Jeremy L. O’Brien, Mark G Thompson et Siyuan Yu. Integrated Compact Optical Vortex Beam Emitters. *Science*, vol. 338, no. October, pages 363–367, 2012.
- [Calvez 2009] Stephane Calvez, Jennifer E. Hastie, Mircea Guina, Oleg G. Okhotnikov et Martin D. Dawson. Semiconductor disk lasers for the generation of visible and ultraviolet radiation. *Laser and Photonics Reviews*, vol. 3, no. 5, pages 407–434, 2009.
- [Castany 2012] Olivier Castany et Laurent Dupont. Collective constructions with micro-bricks. Application to the fabrication of liquid crystal micro-cells. *Journal of Micromechanics and Microengineering*, vol. 22, no. 12, page 125009, dec 2012.
- [Chard 2009] S. P. Chard, P. C. Shardlow et M. J. Damzen. High-power non-astigmatic TEM00 and vortex mode generation in a compact bounce laser design. *Applied Physics B*, vol. 97, no. 2, pages 275–280, jul 2009.
- [Chelkowski 2009] Simon Chelkowski, Stefan Hild et Andreas Freise. Prospects of higher-order Laguerre-Gauss modes in future gravitational wave detectors. *Physical Review D*, vol. 79, no. 12, page 122002, jun 2009.
- [Chen 2001] Y F Chen, Y P Lan et S C Wang. Generation of Laguerre-Gaussian modes in fiber-coupled laser diode end-pumped lasers. *Appl. Phys. B.*, vol. 72, pages 167–170, 2001.
- [Cheng 2009] Wen Cheng, Joseph W Haus et Qiwen Zhan. Propagation of vector vortex beams through a turbulent atmosphere. *Optics express*, vol. 17, no. 20, pages 17829–36, oct 2009.

- [Coldren 2012] Larry a. Coldren, Scott W. Corzine et Milan L. Mašanović. Diode Lasers and Photonic Integrated Circuits. John Wiley & Sons, Inc., Hoboken, NJ, USA, mar 2012.
- [Columbo 2012] L Columbo, M Brambilla, M Dabbicco et G Scamarcio. Self-mixing in multi-transverse mode semiconductor lasers: model and potential application to multi-parametric sensing. *Optics express*, vol. 20, no. 6, pages 6286–305, mar 2012.
- [Courtial 1998] J. Courtial, D. A Robertson, K. Dholakia, L. Allen et M. J Padgett. Rotational Frequency Shift of a Light Beam. *Physical Review Letters*, vol. 81, no. 22, pages 4828–4830, nov 1998.
- [Damen 1991] T. C. Damen, Luis Via, J. E. Cunningham, Jagdeep Shah et L. J. Sham. Subpicosecond spin relaxation dynamics of excitons and free carriers in GaAs quantum wells. *Physical Review Letters*, vol. 67, no. 24, pages 3432–3435, dec 1991.
- [Decker 2015] Manuel Decker, Isabelle Staude, Matthias Falkner, Jason Dominguez, Dragomir N. Neshev, Igal Brener, Thomas Pertsch et Yuri S. Kivshar. High-Efficiency Dielectric Huygens’ Surfaces. *Advanced Optical Materials*, vol. 3, no. 6, pages 813–820, jun 2015.
- [Diehl 2000] Roland Diehl. High-power diode lasers. Springer, New York, 2000.
- [Dienerowitz 2008] Maria Dienerowitz, Michael Mazilu, Peter J. Reece, Thomas F. Krauss et Kishan Dholakia. Optical vortex trap for resonant confinement of metal nanoparticles. *Optics Express*, vol. 16, no. 7, page 4991, mar 2008.
- [Djordjevic 2010] Ivan B Djordjevic et Murat Arabaci. LDPC-coded orbital angular momentum (OAM) modulation for free-space optical communication. *Optics express*, vol. 18, no. 24, pages 24722–8, nov 2010.
- [Dudley 2012] Angela Dudley, Ruslan Vasilyeu, Vladimir Belyi, Nikolai Khilo, Piotr Ropot et Andrew Forbes. Controlling the evolution of nondiffracting speckle by complex amplitude modulation on a phase-only spatial light modulator. *Optics Communications*, vol. 285, no. 1, pages 5–12, 2012.
- [Durst 1976] F. Durst et M. Zare. Laser Doppler measurements in two-phase flows. In: *The accuracy of flow measurements by laser Doppler methods; Proceedings of the LDA-Symposium*, pages 403–429, 1976.
- [Fabre 2008] Nathalie Fabre, Loïc Lalouat, Benoit Cluzel, Xavier Mélique, Didier Lippens, Frédérique De Fornel et Olivier Vanbésien. Optical near-field microscopy of light focusing through a photonic crystal flat lens. *Physical Review Letters*, vol. 101, no. 7, 2008.

- [Fallahi 2008] Mahmoud Fallahi, Li Fan, Yushi Kaneda, Chris Hassenius, Jörg Hader, Hongbo Li, Jerome V. Moloney, Bernardette Kunert, Wolfgang Stolz, Stephan W. Koch, James Murray et Robert Bedford. 5-W yellow laser by intracavity frequency doubling of high-power vertical-external-cavity surface-emitting laser. *IEEE Photonics Technology Letters*, vol. 20, no. 20, pages 1700–1702, 2008.
- [Fattal 2010] David Fattal, Jingjing Li, Zhen Peng, Marco Fiorentino et Raymond G Beausoleil. Flat dielectric grating reflectors with focusing abilities. *Nature Photonics*, vol. 116, no. May, pages 1–5, 2010.
- [Fox 1961] A. G. Fox et Tingye Li. Resonant Modes in a Maser Interferometer. *Bell Sys Tech. j.*, vol. 40, pages 453–488, 1961.
- [Frougier 2013] J. Frougier, G. Baili, M. Alouini, I. Sagnes, H. Jaffrès, A. Garnache, C. Deranlot, D. Dolfi et J.-M. George. Control of light polarization using optically spin-injected vertical external cavity surface emitting lasers. *Applied Physics Letters*, vol. 103, no. 25, page 252402, 2013.
- [Galajda 2001] Péter Galajda et Pál Ormos. Complex micromachines produced and driven by light. *Applied Physics Letters*, vol. 78, no. 2, page 249, jan 2001.
- [Galajda 2002a] Péter Galajda et Pál Ormos. Rotation of microscopic propellers in laser tweezers. *Journal of Optics B: Quantum and Semiclassical Optics*, vol. 4, no. 2, pages S78–S81, apr 2002.
- [Galajda 2002b] Péter Galajda et Pál Ormos. Rotors produced and driven in laser tweezers with reversed direction of rotation. *Applied Physics Letters*, vol. 80, no. 24, page 4653, jun 2002.
- [Garnache 1999a] A Garnache, A A Kachanov, F Stoeckel et R Planel. High-sensitivity intracavity laser absorption spectroscopy with vertical-external-cavity surface-emitting semiconductor lasers. *Optics letters*, vol. 24, no. 12, pages 826–828, 1999.
- [Garnache 1999b] Arnaud Garnache. Etude et réalisation de nouveaux tps de lasers proches infrarouge pour la spectroscopie d’absorbition intracavité laser. Dynamique des lasers fortement multimodes. PhD thesis, Université Joseph Fourier -Grenoble I, 1999.
- [Garnache 2000] A. Garnache, A A Kachanov et F Stoeckel. surface-emitting semiconductor laser applied to high-sensitivity intracavity absorption spectroscopy. *journal of Optical Society of America B*, vol. 17, no. 9, pages 1589–1598, 2000.
- [Garnache 2002] A. Garnache, S. Hoogland, A. C. Tropper, I. Sagnes, G. Saint-Girons et J. S. Roberts. Sub-500-fs soliton-like pulse in a passively mode-locked broadband surface-emitting laser with 100 mW average power. *Applied Physics Letters*, vol. 80, no. 21, pages 3892–3894, 2002.

- [Garnache 2007] a Garnache, A Ouvrard et D Romanini. Single-Frequency operation of External-Cavity VCSELs: Non-linear multimode temporal dynamics and quantum limit. *Optics express*, vol. 15, no. 15, pages 9403–17, jul 2007.
- [Gibson 2004a] Graham Gibson, Johannes Courtial, Miles Padgett, Mikhail Vasnetsov, Valeriy Pas'ko, Stephen Barnett et Sonja Franke-Arnold. Free-space information transfer using light beams carrying orbital angular momentum. *Opt. Express*, vol. 12, no. 22, pages 5448–5456, nov 2004.
- [Gibson 2004b] Graham Gibson, Johannes Courtial, Miles J. Padgett, Mikhail Vasnetsov, Valeriy Pas'ko, Stephen M. Barnett et Sonja Franke-Arnold. Free-space information transfer using light beams carrying orbital angular momentum. *Optics Express*, vol. 12, no. 22, page 5448, nov 2004.
- [Giuliani 2002] Guido Giuliani, Michele Norgia, Silvano Donati et Thierry Bosch. Laser diode self-mixing technique for sensing applications. *Journal of Optics A: Pure and Applied Optics*, vol. 4, no. 6, pages S283–S294, nov 2002.
- [Golub 1996] G H Golub et C F Van Loan. *Matrix Computations*, volume 10. JHU Press, 1996.
- [Grier 2003] David G Grier. A revolution in optical manipulation. *Nature*, vol. 424, no. 6950, pages 810–6, aug 2003.
- [Gröblacher 2006] Simon Gröblacher, Thomas Jennewein, Alipasha Vaziri, Gregor Weihs et Anton Zeilinger. Experimental quantum cryptography with qutrits. *New Journal of Physics*, vol. 8, no. 5, pages 75–75, may 2006.
- [Gu 2014] Min Gu, Hong Kang et Xiangping Li. Breaking the diffraction-limited resolution barrier in fiber-optical two-photon fluorescence endoscopy by an azimuthally-polarized beam. *Optics letters*, vol. 4, no. 11, page 3627, jun 2014.
- [Haken 1985] H Haken. *Laser Light Dynamics*. North Holland Physics publishing, 1985.
- [Hamazaki 2008] Junichi Hamazaki, Akira Kawamoto, Ryuji Morita et Takashige Omatsu. Direct production of high-power radially polarized output from a side-pumped Nd:YVO4 bounce amplifier using a photonic crystal mirror. *Optics express*, vol. 16, no. 14, pages 10762–8, jul 2008.
- [Harris 1994a] M Harris, Ca Hill, Pr Tapster et Jm Vaughan. Laser modes with helical wave fronts. *Physical review. A*, vol. 49, no. 4, pages 3119–3122, apr 1994.
- [Harris 1994b] M. Harris, C.a. Hill et J.M. Vaughan. Optical helices and spiral interference fringes. *Optics Communications*, vol. 106, no. 4-6, pages 161–166, mar 1994.

- [Harwit 2003] Martin Harwit. Photon Orbital Angular Momentum in Astrophysics. *The Astrophysical Journal*, vol. 597, pages 1266–1270, 2003.
- [Hast 2003] JUKKA Hast. Self-mixing interferometry and its applications in non-invasive pulse detection. PhD thesis, University of Oulu, 2003.
- [He 1995] H. He, M. E. J. Friese, N. R. Heckenberg et H. Rubinsztein-Dunlop. Direct Observation of Transfer of Angular Momentum to Absorptive Particles from a Laser Beam with a Phase Singularity. *Physical Review Letters*, vol. 75, no. 5, pages 826–829, jul 1995.
- [He 2011] Guangyuan He, Jing Guo, Biao Wang et Zhongxing Jiao. Generation of radially polarized beams based on thermal analysis of a working cavity. *Optics express*, vol. 19, no. 19, pages 18302–9, 2011.
- [Hell 1994] Stefan W. Hell et Jan Wichmann. Breaking the diffraction resolution limit by stimulated emission: stimulated-emission-depletion fluorescence microscopy. *Optics Letters*, vol. 19, no. 11, page 780, jun 1994.
- [Hell 2014] Stefan W. Hell. "The Nobel Prize in Chemistry 2014". Nobelprize.org. Nobel Media AB 2014. Web. 7 Jun 2015. <http://www.nobelprize.org/nobel_prizes/chemistry/laureates/2014/>, 2014.
- [Henry 1982] C. Henry. Theory of the linewidth of semiconductor lasers. *IEEE Journal of Quantum Electronics*, vol. 18, no. 2, pages 259–264, 1982.
- [Ho 1990] K. M. Ho, C. T. Chan et C. M. Soukoulis. Existence of a photonic gap in periodic dielectric structures. *Physical Review Letters*, vol. 65, no. 25, pages 3152–3155, 1990.
- [Hodges 1997] S E Hodges, M Munroe, J Cooper et M G Raymer. Multimode laser model with coupled cavities and quantum noise. *journal of Optical Society of America B*, vol. 14, no. 1, page 191, 1997.
- [Hodgson 1997] Norman Hodgson et Horst Weber. *Optical Resonators*. Springer-Verlag, Springer-Verlag London, 1997.
- [Holub 2007] M Holub et P Bhattacharya. Spin-polarized light-emitting diodes and lasers. *Journal of Physics D: Applied Physics*, vol. 40, no. 11, pages R179–R203, jun 2007.
- [Huang 2007] Michael C.Y. Huang, Y. Zhou et Connie J. Chang-Hasnain. A surface-emitting laser incorporating a high-index-contrast subwavelength grating. *Nature Photonics*, vol. 1, no. 2, pages 119–122, feb 2007.
- [Ito 2010] Akihiko Ito, Yuichi Kozawa et Shunichi Sato. Generation of hollow scalar and vector beams using a spot-defect mirror. *Journal of the Optical Society*

- of America. A, Optics, image science, and vision, vol. 27, no. 9, pages 2072–2077, 2010.
- [Jackson 1962] John David Jackson et John D Jackson. classical electrodynamics. Wiley., New York, 1962.
- [Jankiewics 2001] Z Jankiewics et K KOPCZYNSKI. Diode-pumped solid-state lasers. Opto-electronics review, vol. 9, no. 1, pages 13–33, 2001.
- [Joachim 2003] Piprek Joachim. Semiconductor optoelectronic devices. Academic Press, 2003.
- [Joannopoulos 2007] John D Joannopoulos, Steven G. Johnson, Joshua N. Winn et Robert D. Meade. Photonic Crystals Modeling the Flow of Light. Princeton University Press, second edi édition, 2007.
- [Jun 2012] Young Chul Jun, Edward Gonzales, John L Reno, Eric A Shaner, Alon Gabbay et Igal Brener. Active tuning of mid-infrared metamaterials by electrical control of carrier densities. Optics express, vol. 20, no. 2, pages 1903–11, jan 2012.
- [Kane 2005] Deborah .M Kane et K. Alan Shore. Unlocking Dynamical Diversity: Optical Feedback Effects on Semiconductor Lasers, volume 1. John Wiley & Sons, 2005.
- [Karimi 2009] Ebrahim Karimi, Bruno Piccirillo, Lorenzo Marrucci et Enrico Santamato. Light propagation in a birefringent plate with topological charge. Optics Letters, vol. 34, no. 8, page 1225, apr 2009.
- [Khanin 1995] Ya I Khanin. Principles of laser dynamics. Elsevier, 1995.
- [Kim 2007] Ki Sung Kim, Jaeryung Yoo, Gibum Kim, Sangmoon Lee, Soohaeng Cho, Junyoun Kim, Taek Kim et Yongjo Park. 920-nm vertical-external-cavity surface-emitting lasers with a slope efficiency of 58% at room temperature. IEEE Photonics Technology Letters, vol. 19, no. 20, pages 1655–1657, 2007.
- [Kim 2011] J. W. Kim, J. I. Mackenzie, J. R. Hayes et W. A. Clarkson. High-power radially-polarized Er:YAG laser with Laguerre-Gaussian (LG₀₁) mode output. Opt. Express, vol. 19, no. 15, pages 14526–14531, 2011.
- [Kim 2012] Sora Kim, Sanja Hadzialic, Aasmund S Sudbo et Olav Solgaard. Reflectivity and polarization dependence of polysilicon single-film broadband photonic crystal micro-mirrors. Optics express, vol. 20, no. 6, pages 6306–15, mar 2012.
- [Kim 2013] D J Kim, J W Kim et W A Clarkson. Q-switched Nd : YAG optical vortex lasers. Optics Express, vol. 21, no. 24, pages 275–280, 2013.

- [Klar 1999] Thomas A. Klar et Stefan W. Hell. Subdiffraction resolution in far-field fluorescence microscopy. *Optics Letters*, vol. 24, no. 14, page 954, jul 1999.
- [Knöner 2005] Gregor Knöner, Simon Parkin, Norman R. Heckenberg et Halina Rubinsztein-Dunlop. Characterization of optically driven fluid stress fields with optical tweezers. *Physical Review E*, vol. 72, no. 3, page 031507, sep 2005.
- [König 1986] G. König, K. Anders et A. Frohn. A new light-scattering technique to measure the diameter of periodically generated moving droplets. *Journal of Aerosol Science*, vol. 17, no. 2, pages 157–167, jan 1986.
- [Kozawa 2008] Yuichi Kozawa et Shunichi Sato. Single higher-order transverse mode operation of a radially polarized Nd:YAG laser using an annularly reflectivity-modulated photonic crystal coupler. *Optics letters*, vol. 33, no. 19, pages 2278–2280, 2008.
- [Krebs 1996] Olivier Krebs et Paul Voisin. Giant Optical Anisotropy of Semiconductor Heterostructures with No Common Atom and the Quantum-Confined Pockels Effect. *Physical Review Letters*, vol. 77, no. 9, pages 1829–1832, aug 1996.
- [Krebs 1997] O Krebs, W Seidel, J P André, D Bertho, C Jouanin et P Voisin. Investigations of giant ‘forbidden’ optical anisotropy in GaInAs - InP quantum well structures. *Semiconductor Science and Technology*, vol. 12, no. 7, pages 938–942, jul 1997.
- [Krenn 2015] Mario Krenn, Johannes Handsteiner, Matthias Fink, Robert Fickler et Anton Zeilinger. Twisted photon entanglement through turbulent air across Vienna. [arXiv:1507.06551](https://arxiv.org/abs/1507.06551), page 11, jul 2015.
- [Kuznetsov 1999] Mark Kuznetsov, Farhad Hakimi, Robert Sprague et A. Mooradian. Design and characteristics of high-power (>0.5-W CW) diode-pumped vertical-external-cavity surface-emitting semiconductor lasers with circular TEM00 beams. *IEEE Journal on Selected Topics in Quantum Electronics*, vol. 5, no. 3, pages 561–573, 1999.
- [Lacot 1996] E. Lacot, F. Stoeckel, D. Romanim et A. Kachanov. Two Is Enough Dynamics of a Two Modes Laser for Intracavity Laser Absorption. In *Proceedings of European Meeting on Lasers and Electro-Optics CLEOE-96*, pages 155–155. IEEE, 1996.
- [Lacot 2001] E. Lacot, R. Day et F. Stoeckel. Coherent laser detection by frequency-shifted optical feedback. *Physical Review A*, vol. 64, no. 4, pages 1–11, sep 2001.

- [Lalanne 1996] Philippe Lalanne et G. Michael Morris. Highly improved convergence of the coupled-wave method for TM polarization. *Journal of the Optical Society of America A*, vol. 13, no. 4, page 779, 1996.
- [L.Andrews 2008] David L.Andrews. *Structured Light and Its Applications*. Academic Press, 2008.
- [Lang 1980] R. Lang et K. Kobayashi. External optical feedback effects on semiconductor injection laser properties. *IEEE Journal of quantum Electronics*, vol. 16, no. 3, pages 347–355, mar 1980.
- [Langford 2004] N. K. Langford, R. B. Dalton, M. D. Harvey, J. L. O’Brien, G. J. Pryde, A. Gilchrist, S. D. Bartlett et A. G. White. Measuring Entangled Qutrits and Their Use for Quantum Bit Commitment. *Physical Review Letters*, vol. 93, no. 5, page 053601, jul 2004.
- [Lastras-Martínez 2001] L. F. Lastras-Martínez, D. Rönnow, P. V. Santos, M. Cardona et K. Eberl. Optical anisotropy of (001)-GaAs surface quantum wells. *Physical Review B*, vol. 64, no. 24, page 245303, nov 2001.
- [Laurain 2009] A Laurain, M Myara, G Beaudoin, I Sagnes et A Garnache. High power single-frequency continuously-tunable compact extended-cavity semiconductor laser. *Optics express*, vol. 17, no. 12, pages 9503–9508, 2009.
- [Laurain 2010a] A Laurain, M Myara, G Beaudoin, I Sagnes et A Garnache. Multiwatt-power highly-coherent compact single-frequency tunable Vertical-External-Cavity-Surface-Emitting-Semiconductor-Laser. *Opt. Express*, vol. 18, no. 14, pages 14627–14636, 2010.
- [Laurain 2010b] Alexandre Laurain. *Sources laser à semiconducteur à émission verticale de haute cohérence et de forte puissance dans le proche et le moyen infrarouge*. docteur de l’université montpellier ii, Université Montpellier II - Sciences et Techniques du Languedoc -, 2010.
- [Lavery 2013] Martin P. J. Lavery, Fiona C. Speirits, Stephen M. Barnett et Miles J Padgett. Detection of a Spinning Object Using Light’s Orbital Angular Momentum. *Science*, vol. 431, no. August, pages 537–541, 2013.
- [Lei 2015] Ting Lei, Meng Zhang, Yuru Li, Ping Jia, Gordon Ning Liu, Xiaogeng Xu, Zhaohui Li, Changjun Min, Jiao Lin, Changyuan Yu, Hanben Niu et Xiaocong Yuan. Massive individual orbital angular momentum channels for multiplexing enabled by Dammann gratings. *Light: Science & Applications*, vol. 4, no. 3, page e257, 2015.
- [Li 2015] Huanlu Li, David B. Phillips, Xuyang Wang, Ying-Lung Daniel Ho, Lifeng Chen, Xiaoqi Zhou, Jiangbo Zhu, Siyuan Yu et Xinlun Cai. Orbital angular momentum vertical-cavity surface-emitting lasers. *Optica*, vol. 2, no. 6, page 547, jun 2015.

- [Lin 2014] Di Lin, J M O Daniel et W A Clarkson. Controlling the handedness of directly excited Laguerre-Gaussian modes in a solid-state laser. *Optics letters*, vol. 39, no. 13, pages 3903–6, jul 2014.
- [Lorenz 2007] Robert M Lorenz, J Scott Edgar, Gavin D M Jeffries, Yiqiong Zhao, David McGloin et Daniel T Chiu. Vortex-trap-induced fusion of femtoliter-volume aqueous droplets. *Analytical chemistry*, vol. 79, no. 1, pages 224–8, jan 2007.
- [Luneburg 1944] Rudolf Karl Luneburg. *Mathematical theory of optics*. Brown University, Providence, 1944.
- [Mair 2001] A Mair, A Vaziri, G Weihs et A Zeilinger. Entanglement of the orbital angular momentum states of photons. *Nature*, vol. 412, no. 6844, pages 313–6, jul 2001.
- [Mandel 1995] Leonard Mandel et Emil Wolf. *Optical coherence and*. Cambridge University Press, 1995.
- [Marrucci 2006] L. Marrucci, C. Manzo et D. Paparo. Optical Spin-to-Orbital Angular Momentum Conversion in Inhomogeneous Anisotropic Media. *Physical Review Letters*, vol. 96, no. 16, page 163905, apr 2006.
- [Matthews 1974] J.W. Matthews et A.E. Blakeslee. *Defects in epitaxial multilayers*, 1974.
- [Mie 1908] Gustav Mie. Beiträge zur Optik trüber Medien, speziell kolloidaler Metallösungen. *Annalen der Physik*, vol. 330, no. 3, pages 377–445, 1908.
- [Mignot 2008a] Augustin Mignot. Gyrolaser semi-conducteur à cavité externe. PhD thesis, École Polytechnique, 2008.
- [Mignot 2008b] Augustin Mignot, Gilles Feugnet, Sylvain Schwartz, Isabelle Sagnes, Arnaud Garnache, Claude Fabre et Jean-Paul Pocholle. Single-frequency external-cavity semiconductor ring-laser gyroscope. *Optics Letters*, vol. 34, no. 1, page 97, dec 2008.
- [Moharam 1995] M. G. Moharam, Drew a. Pommet, Eric B. Grann et T. K. Gaylord. Stable implementation of the rigorous coupled-wave analysis for surface-relief gratings: enhanced transmittance matrix approach. *Journal of the Optical Society of America A*, vol. 12, no. 5, page 1077, may 1995.
- [Molina-Terriza 2004] G. Molina-Terriza, A. Vaziri, J. Řeháček, Z. Hradil et A. Zeilinger. Triggered Qutrits for Quantum Communication Protocols. *Physical Review Letters*, vol. 92, no. 16, page 167903, apr 2004.
- [Morrissey 2011] F X Morrissey et H P Chou. Mode calculations in asymmetrically aberrated laser resonators using the Huygens-Fresnel kernel formulation. *Optics express*, vol. 19, no. 20, pages 19702–7, sep 2011.

- [Myara 2013] Mikael Myara, Mohamed Sellahi, Alexandre Laurain, Adrien Michon, Isabelle Sagnes et Arnaud Garnache. Noise properties of NIR and MIR VECSELS. SPIE -proceedings, vol. 8606, 2013.
- [Naidoo 2011] D. Naidoo, K. Ait-Ameur, M. Brunel et A. Forbes. Intra-cavity generation of superpositions of Laguerre–Gaussian beams. Applied Physics B, vol. 106, no. 3, pages 683–690, oct 2011.
- [Naidoo 2015] Darryl Naidoo, Filippus S Roux, Angela Dudley, Igor Litvin, Bruno Piccirillo, Lorenzo Marucci, Andrew Forbes, Dipartimento Fisica, Complesso Universitario et Sant Angelo. Controlled generation of higher-order Poincaré sphere beams from a laser. arXiv:1505.02256, pages 1–10, 2015.
- [Ngcobo 2013] Sandile Ngcobo, Igor Litvin, Liesl Burger et Andrew Forbes. A digital laser for on-demand laser modes. Nature communications, vol. 4, no. May, page 2289, jan 2013.
- [Noyan 2015] Mehmet A. Noyan et James M. Kikkawa. Time-resolved orbital angular momentum spectroscopy. Applied Physics Letters, vol. 107, no. 3, page 032406, jul 2015.
- [Okida 2007] Masahito Okida, Takashige Omatsu, Masahide Itoh et Toyohiko Yata-gai. Direct generation of high power Laguerre-Gaussian output from a diode-pumped Nd:YVO(4) 1.3- μm bounce laser. Optics express, vol. 15, no. 12, pages 7616–7622, 2007.
- [Okida 2009] M. Okida, Y. Hayashi, T. Omatsu, J. Hamazaki et R. Morita. Characterization of 1.06 μm optical vortex laser based on a side-pumped Nd:GdVO4 bounce oscillator. Applied Physics B: Lasers and Optics, vol. 95, no. 1, pages 69–73, 2009.
- [Oroszi 2006] László Oroszi, Péter Galajda, Huba Kirei, Sándor Bottka et Pál Ormos. Direct Measurement of Torque in an Optical Trap and Its Application to Double-Strand DNA. Physical Review Letters, vol. 97, no. 5, page 058301, aug 2006.
- [Padgett 2004] Miles J Padgett. The mechanism for energy transfer in the rotational frequency shift of a light beam. Journal of Optics A: Pure and Applied Optics, vol. 6, no. 5, pages S263–S265, may 2004.
- [Park 2000] Min Soo Park, Byung Tae Ahn, Byueng-Su Yoo, Hye Yong Chu, Hyo-Hoon Park et C. J. Chang-Hasnain. Polarization control of vertical-cavity surface-emitting lasers by electro-optic birefringence. Applied Physics Letters, vol. 76, no. 7, page 813, feb 2000.
- [Parkin 2007] Simon J. Parkin, Gregor Knöner, Timo A. Nieminen, Norman R. Heckenberg et Halina Rubinsztein-Dunlop. Picoliter viscometry using optically rotated particles. Physical Review E, vol. 76, no. 4, page 041507, oct 2007.

- [Phillips 2014] D. B. Phillips, M. P. Lee, F. C. Speirits, S. M. Barnett, S. H. Simpson, M. P. J. Lavery, M. J. Padgett et G. M. Gibson. Rotational Doppler velocimetry to probe the angular velocity of spinning microparticles. *Physical Review A - Atomic, Molecular, and Optical Physics*, vol. 90, no. 1, pages 1–5, 2014.
- [Piche 1983] M. Piche, P. Lavigne, F. Martin et P. a. Belanger. Modes of resonators with internal apertures. *Applied optics*, vol. 22, no. 13, page 1999, jul 1983.
- [Picqué 2003] Nathalie Picqué, Guy Guelachvili et Alexander A. Kachanov. High-sensitivity time-resolved intracavity laser Fourier transform spectroscopy with vertical-cavity surface-emitting multiple-quantum-well lasers. *Optics letters*, vol. 28, no. 5, pages 313–315, 2003.
- [Poynting 1909] J. H. Poynting. The Wave Motion of a Revolving Shaft, and a Suggestion as to the Angular Momentum in a Beam of Circularly Polarised Light. *Proceedings of the Royal Society A: Mathematical, Physical and Engineering Sciences*, vol. 82, no. 557, pages 560–567, jul 1909.
- [Putnam 2012] William P. Putnam, Damian N. Schimpf, Gilberto Abram et Franz X. Kärtner. Bessel-Gauss beam enhancement cavities for high-intensity applications. *Optics express*, vol. 20, no. 22, pages 24429–43, oct 2012.
- [Rakic 1998] Aleksandar D. Rakic, Aleksandra B. Djurišić, Jovan M. Elazar et Marjan L. Majewski. Optical Properties of Metallic Films for Vertical-Cavity Optoelectronic Devices. *Applied Optics*, vol. 37, no. 22, page 5271, aug 1998.
- [Rautiainen 2007] J. Rautiainen, A. Härkönen, V-M. Korpijärvi, P. Tuomisto, M. Guina et O. G. Okhotnikov. 2.7 W tunable orange-red GaInNAs semiconductor disk laser. *Optics express*, vol. 15, no. 26, pages 18345–18350, 2007.
- [Raymond 1999] T. D. Raymond, W. J. Alford, M. H. Crawford et A. A. Allerman. Intracavity frequency doubling of a diode-pumped external-cavity surface-emitting semiconductor laser. *Optics letters*, vol. 24, no. 16, pages 1127–1129, 1999.
- [Rosales-Guzmán 2015] Aniceto Belmonte, Carmelo Rosales-Guzmán et Juan P. Torres. A Measure of Flow Vorticity with Helical Beams of Light. at <<http://arxiv.org/abs/1507.07986>>, jul 2015.
- [San-Miguel 1995] San-Miguel, Q. Feng et J. V. Moloney. Light-polarization dynamics in surface-emitting semiconductor lasers. *Physical Review A*, vol. 52, no. 2, pages 1728–1739, 1995.
- [Schroeder 1995] W. Andreas Schroeder, D. S. McCallum, D. R. Harken, Mark D. Dvorak, David R. Andersen, Arthur L. Smirl et Brian S. Wherrett. Intrinsic

- and induced anisotropy of nonlinear absorption and refraction in zinc blende semiconductors. *Journal of the Optical Society of America B*, vol. 12, no. 3, page 401, mar 1995.
- [Schulz 2013] Sebastian A Schulz, Taras Machula, Ebrahim Karimi et Robert W Boyd. Integrated multi vector vortex beam generator Abstract *∴*. *Optics Express*, vol. 21, no. 13, pages 217–223, 2013.
- [Schwartz 2008] Sylvain Schwartz, François Gутty, Gilles Feugnet, Philippe Bouyer et Jean Paul Pocholle. Suppression of nonlinear interactions in resonant macroscopic quantum devices: The example of the solid-state ring laser gyroscope. *Physical Review Letters*, vol. 100, no. 18, pages 1–4, 2008.
- [Seelert 2005] Wolf Seelert, Stuart Butterworth, Juergen Rosperich, Christian Walter, Ruediger von Elm, Vasily Ostroumov, Juan Chilla, Hailong Zhou, Eli Weiss et Andrea Caprara. Optically pumped semiconductor lasers: a new reliable technique for realizing highly efficient visible lasers. *SPIE -proceedings*, vol. 5707, pages 33–37, 2005.
- [Senatsky 2009] Yu Senatsky, A. Shirakawa et K. Ueda. Generation of near diffraction free beams in Yb:YAG laser using an intracavity lens with spherical aberration. In *CLEO/Europe - EQEC 2009 - European Conference on Lasers and Electro-Optics and the European Quantum Electronics Conference*, 2009.
- [Senatsky 2012] Yury Senatsky, Jean François Bisson, Jianlang Li, Akira Shirakawa, Manasadevi Thirugnanasambandam et Ken ichi Ueda. Laguerre-Gaussian modes selection in diode-pumped solid-state lasers, 2012.
- [Shen 2014] Huanhuan Shen. Interferometric out-of-focus imaging and digital holography for the characterization of droplets or bubbles: theory, optical design, characterization of a flow, synchronized experiments. PhD thesis, Université de Rouen, 2014.
- [Shimizu 1988] M. Shimizu, Fumio Koyama et K.enichi Iga. Polarization characteristics of MOCVD grown GaAs/GaAlAs CBH surface emitting lasers. *Jpn. J. Appl. Phys.*, vol. vol. 27, no. no. 9, pages 1774–1775, 1988.
- [Siegman 1986] Anthony E Siegman. *lasers*. University Science Books, 1986.
- [Simmons 1970] Joseph W. Simmons et Mark J. Guttman. *States, waves, and photons: a modern introduction to light*. 1970.
- [Steinkogler 2003] S. Steinkogler, H. Schneider, M. Walther et P. Koidl. Determination of the electron capture time in quantum-well infrared photodetectors using time-resolved photocurrent measurements. *Applied Physics Letters*, vol. 82, no. 22, pages 3925–3927, 2003.

- [Sudo 2006] Seiichi Sudo, Yoshihiko Miyasaka, Koji Kamikariya, Kana Nemoto et Kenju Otsuka. Microanalysis of Brownian Particles and Real-Time Nanometer Vibrometry with a Laser-Diode-Pumped Self-Mixing Thin-Slice Solid-State Laser. *Japanese Journal of Applied Physics*, vol. 45, no. No. 35, pages L926–L928, sep 2006.
- [Sudo 2007] S Sudo, Y Miyasaka, K Nemoto, K Kamikariya et K Otsuka. Detection of small particles in fluid flow using a self-mixing laser. *Optics express*, vol. 15, no. 13, pages 8135–45, jun 2007.
- [Thirugnanasambandam 2010] M. P. Thirugnanasambandam, Yu Senatsky et K. Ueda. Generation of very-high order laguerre-gaussian modes in Yb:YAG ceramic laser. *Laser Physics Letters*, vol. 7, no. 9, pages 637–643, 2010.
- [Torner 2005] Lluís Torner, Juan Torres et Silvia Carrasco. Digital spiral imaging. *Opt. Express*, vol. 13, no. 3, pages 873–881, 2005.
- [Tropper 2006] Anne. C. Tropper et S. Hoogland. Extended cavity surface-emitting semiconductor lasers. *Progress in Quantum Electronics*, vol. 30, no. 1, pages 1–43, jan 2006.
- [Tyler 2009] Glenn A. Tyler et Robert W. Boyd. Influence of atmospheric turbulence on the propagation of quantum states of light carrying orbital angular momentum. *Optics Letters*, vol. 34, no. 2, page 142, jan 2009.
- [Van de Hulst 1991] H C Van de Hulst et R T Wang. Glare points. *Applied optics*, vol. 30, no. 33, pages 4755–63, nov 1991.
- [Van Haeringen 1967] W. Van Haeringen. Polarization properties of a single-mode operating gas laser in a small axial magnetic field. *Physical Review*, vol. 158, no. 2, pages 256–272, 1967.
- [Vaziri 2002] Alipasha Vaziri, Gregor Weihs et Anton Zeilinger. Superpositions of the orbital angular momentum for applications in quantum experiments. *Journal of Optics B: Quantum and Semiclassical Optics*, vol. 4, no. 2, pages S47–S51, apr 2002.
- [Wang 2012] Jian Wang, Jeng-yuan Yang, Irfan M Fazal, Nisar Ahmed, Yan Yan, Hao Huang, Yongxiong Ren, Yang Yue, Samuel Dolinar, Moshe Tur et Alan E Willner. Terabit free-space data transmission employing orbital angular momentum multiplexing. *Nature Photonics*, vol. 6, no. June, pages 488–496, 2012.
- [Williams 2005] Benjamin Williams, Sushil Kumar, Qing Hu et John Reno. Operation of terahertz quantum-cascade lasers at 164 K in pulsed mode and at 117 K in continuous-wave mode. *Optics express*, vol. 13, no. 9, pages 3331–3339, 2005.

- [Williams 2014] Mathew D. Williams, Matt M. Coles, David S. Bradshaw et David L. Andrews. Direct generation of optical vortices. *Physical Review A*, vol. 89, no. 3, page 033837, mar 2014.
- [Wilsem 2001] C Wilsem, H Temkin et LA Coldren. *Vertical-Cavity Surface-Emitting Lasers: Design, Fabrication, Characterization, and Applications*, volume 2001. Cambridge University Press, 2001.
- [Yamada 1989] Minoru Yamada. Theoretical analysis of nonlinear optical phenomena taking into account the beating vibration of the electron density in semiconductor lasers. *Journal of Applied Physics*, vol. 66, no. 1, page 81, jul 1989.
- [Yao 2011] Alison M. Yao et Miles J. Padgett. Orbital angular momentum: origins, behavior and applications. *Advances in Optics and Photonics*, vol. 3, no. 2, page 161, may 2011.
- [Yariv 2007] Amnon Yariv et Pochi Yeh. *Photonics*. Oxford University Press, 2007.
- [Yu 2014] Nanfang Yu et Federico Capasso. Flat optics with designer metasurfaces. *Nature materials*, vol. 13, no. January, 2014.
- [Zeng 2013] Zhaoli Zeng, Shulian Zhang et Yidong Tan. Laser feedback interferometry based on high density cosine-like intensity fringes with phase quadrature. *Optics Express*, vol. 21, no. 8, page 10019, apr 2013.
- [Zhang 1990] Ze Zhang et Sashi Satpathy. Electromagnetic wave propagation in periodic structures: Bloch wave solution of Maxwells equations. *Physical Review Letters*, vol. 65, no. 21, pages 2650–2653, 1990.
- [Zory 1993] I Zory et S Peters. *Quantum well lasers*. Academic Press, 1 edition édition, 1993.
- [Zouhdi 2008] Saïd Zouhdi, Ari Sihvola et Alexey P Vinogradov. *Metamaterials and Plasmonics: Fundamentals, Modelling, Applications - Page 219*. Book, page 306, 2008.
- [Zwillinger 2003] Daniel Zwillinger. BT - CRC Standard Mathematical Tables and Formulae. In *CRC Standard Mathematical Tables and Formulae*, page 367. 2003.

Résumé :

Le but de ce travail de thèse est l'étude et la réalisation de sources lasers de haute cohérence à semi-conducteurs III-V, basées sur la technologie Vertical-External-Cavity-Surface-Emitting-Laser (VECSEL) à puits quantiques (matériaux InGaAs/GaAs/AlGaAs), émettant dans le proche-IR sur des modes transverses du type Laguerre Gauss (LG) et Hermite Gauss (HG) d'ordres supérieurs. Ces modes ont des structures de phase, d'amplitude et de polarisation complexes qui leur vaut souvent l'appellation de 'lumière complexe' ou 'structurée'. Nous mettrons l'accent particulièrement sur les modes LG possédant un moment angulaire orbital, et sur une source contrôlant le spin du photon. Ce type de source laser présente un grand intérêt pour le développement de systèmes ou capteurs optiques dans différents domaines, tels que les télécommunications, les pinces optiques, et le piégeage et le refroidissement d'atomes, ainsi que la métrologie optique. Nous sommes amenés à étudier les modes propres des cavités optiques de haute finesse. Nous décrivons ces modes suivant les trois "axes" définissant l'état de photon: distribution longitudinale (fréquentielle), transverse (spatiale) et de polarisation. Pour chacun de ces trois axes nous étudions les ingrédients physiques qui régissent la formation des modes, et développons les outils théoriques nécessaires à la manipulation et au calcul des états propres dans des cavités modifiées. Dans une seconde étape, puisque la sélection des modes dans une cavité laser passe par l'interaction matière-rayonnement, nous nous penchons sur la dynamique de ces systèmes en écrivant les équations de Maxwell-Bloch pour notre laser. Ces équations nous permettent d'étudier le rôle de la dynamique temporelle dans la sélection des modes lasers et le chemin vers l'état stationnaire. Nous nous appuyons sur ces modèles pour expliquer certaines questions non/mal comprises, et qui mènent parfois à des interprétations erronées dans la littérature scientifique, notamment la sélection spontanée du sens de rotation du front de phase dans les modes vortex.

Une partie de ce travail est consacrée au développement et à la caractérisation d'une technologie à semi-conducteurs III-V, qui permet de sélectionner efficacement un mode laser donné, dans la base propre. Nous développons une approche basée sur des méta-matériaux intégrés à la structure de gain (le 1/2-VECSEL) et qui agit comme un masque de phase et d'amplitude. Nous nous appuyons sur cette technologie pour réaliser une cavité laser qui lève la dégénérescence des modes vortex contrarotatifs et brise légèrement leur symétrie, ces deux étapes sont cruciales pour pouvoir sélectionner la charge et le signe du vortex généré et stabilisé. Afin de contrôler les modes de polarisation nous étudions les propriétés de polarisation de la cavité et du milieu à gain à puits quantique : la biréfringence, le dichroïsme, et le temps de spin flip dans les puits quantiques. Nous exploitons ces paramètres pour générer les états de polarisation désirés : linéaire stable, circulaire avec un moment angulaire de spin contrôlé par le spin de pompage. Enfin, nous présentons la conception et la réalisation d'un capteur laser sous rétro-injection optique (self-mixing) pour la vélocimétrie linéaire et rotationnelle, en utilisant une source laser émettant sur un mode vortex. Ce capteur montre un exemple de mesure inaccessible avec un laser conventionnel. Il tire profit des propriétés uniques des modes vortex pour mesurer simultanément la vitesse linéaire et angulaire des particules. Nous finirons cette partie par l'étude d'un autre design de capteur laser possible pour la granulométrie, utilisant d'autres types de modes laser générés dans ce travail.

Mots-clés: VECSEL, Vortex, OAM, Vélocimétrie, granulométrie, Semi-conducteurs III-V, méta-surfaces, Modes laser, Dynamique laser,

Highly coherent III-V-semiconductor laser emitting phase-, amplitude- and polarization-structured light for advanced sensing applications

Abstract:

The goal of this PhD thesis is to design and develop novel VeCSEL-type III-V semiconductor laser sources, emitting coherent light with structured wavefront.

Light with structured wavefront also known as complex light, presents unique properties and an increasing interest with both applied and fundamental aspects. For example, Laguerre-Gauss modes LG_{0m} - called vortex beams-, which occupy a central place in this work, possess an orbital angular momentum OAM, in addition to the linear one. This property is of high interest in many new applications: ultrahigh resolution imaging, optical tools for biotechnology, laser cooling, atom trapping, optical manipulation, quantum information, etc.

We start the study in chapter 1 by presenting the theoretical tools required to model the formation and the selection of structured light inside a laser cavity that incorporates mode control elements. We will address light eigenmodes calculation and multimode temporal dynamics.

Then in chapters 2 and 3 we develop a novel technology based on dielectric metasurfaces, and sub-wavelength thick metallic layers, integrated on the gain structure of our laser to efficiently select the desired laser modes. Next we show experimental examples of generated structured light, and conduct a characterization study in chapter 4.

The fifth chapter deals with polarization mode selection in a laser. We start by studying the polarization properties of the optical cavity and the quantum-well-based gain medium: the birefringence near the semiconductor surface; the dichroism and the spin-flip time in the quantum wells. We take advantage of these elements to generate and characterize the wanted polarization state: highly coherent linear and circular polarization state carrying a spin angular momentum (SAM) controlled via electronic spin injection.

We end this work by designing and building a self-mixing laser sensor that takes advantage of a developed vortex laser, to measure simultaneously translational and rotational velocities of particles using optical feedback, which is an example of measurements inaccessible using conventional lasers.

Keywords: VECSEL, Vortex, Orbital angular momentum, Velocimetry, III-V semiconductors, meta-surfaces, 2D subwavelength grating, Laser modes, laser dynamics.
